Analysis of Heat Crack Formation in Brake Discs for Heavy-Duty Vehicles

Am Fachbereich Maschinenbau an der
Technischen Universität Darmstadt
zur Erlangung des Grades eines
Doktor-Ingenieurs (Dr.-Ing.)
genehmigte

Dissertation

vorgelegt von

Sami Bilgic Istoc, M.Sc.
aus Mannheim

Berichterstatter:	Prof. Dr. rer. nat. Hermann Winner
Mitberichterstatter:	Prof. Dr.-Ing. Matthias Oechsner
Tag der Einreichung:	12.11.2019
Tag der mündlichen Prüfung:	14.01.2020

Darmstadt 2020
D 17

Preface

This thesis was written during my work as research associate at Institute of Automotive Engineering of Technische Universität Darmstadt within a cooperation project with Knorr-Bremse Systeme für Nutzfahrzeuge GmbH.

Special thanks go to my doctoral supervisor Prof. Dr. rer. nat. Hermann Winner for his excellent supervision of this thesis.

I would like to thank Prof. Dr.-Ing. Matthias Oechsner for co-supervising this thesis.

In the past four years I could always rely on my project partner Wolfgang Pahle from Knorr-Bremse and would therefore like to thank him very much at this point, as well as Jens Fricke, who made the project possible. I would also like to thank the entire Knorr-Bremse team for their outstanding support.

Finally, I would like to thank my family for my excellent education and my girlfriend for her support and understanding.

Sami Bilgic Istoc Darmstadt, 11/2019

Table of Contents

Abbreviations

Abbreviation	Description
CFD	Computational Fluid Dynamics
CDF	Cumulated Density Function
DT	Disc thickness
DTV	Disc thickness variation
FE	Finite Element
HS	Hat side
PS	Piston side
SRO	Side-face runout

Symbols and Indices

Symbol	Unit	Description
A	m^2	Surface area
α	$W \cdot m^{-2} \cdot K^{-1}$	Heat transfer coefficient
c	$J \cdot kg^{-1} \cdot K^{-1}$	Specific heat capacity
ε	%	Strain
ε_R	-/-	Emissivity
k	-/-	Crack count
l	mm	Crack length
λ	$W \cdot m^{-1} \cdot K^{-1}$	Thermal conductivity
m	-/-	Order
m	kg	Mass
N	-/-	Heat crack cycle number
n	-/-	Revolution number
φ	rad, °	Revolution angle
$\dot{q}_{in}$	$W \cdot m^{-2}$	Specific heat flow
$\dot{Q}$	W	Heat flow
r	mm	Radius
s	µm	Coning
$\boldsymbol{\sigma}$	MPa	Stress
σ_B	$W \cdot m^{-2} \cdot K^{-4}$	Stefan-Boltzmann constant
T	°C	Temperature
$\boldsymbol{\xi}$	-/-	Abbreviation for (r, φ, n, N)
z	µm	Friction surface displacement
Δz	µm	Disc thickness
Σz	µm	Side-face runout
ζ	$W \cdot m^{-1} \cdot K^{-1}$	Constant for parameterisation

Index	Description
∞	Infinity
A	Surface
c	Centre
Exp	Experimental
H	Hatside
HS	Hotspot
i	Inner
max	Maximum
min	Minimum
MP	Max Principal
o	Outer
P	Pistonside
pyro	Pyrometer
sim	Simulated

Figures

Tables

Kurzzusammenfassung

Hitzerisse in Bremsscheiben stellen ein häufiges Problem bei der Entwicklung von Bremssystemen für schwere Nutzfahrzeuge dar, da ihr Auftreten bisher nicht vorhergesagt werden kann. Frühere Arbeiten haben sich mit dem Einfluss des Bremsbelags und des Bremsscheibenmaterials auf die Hitzerissbildung beschäftigt. Allerdings streuen diese Einflussfaktoren in der Serie stark und es besteht keine umfassende Modellvorstellung, die die Hitzerissbildung erklärt. Ziel dieser Arbeit ist daher die Untersuchung der Einflüsse auf die Hitzerissbildung, um mithilfe eines erweiterten Wirkmodells die Rissbildung detailliert zu erklären. Dazu wird eine Versuchsreihe auf dem Schwungmassenprüfstand an fünf verschiedenen Bremsscheiben durchgeführt. Unter Beibehaltung der Bremsbelagzusammensetzung und Bremsscheibenlegierung wird die Kühlkanalgeometrie der belüfteten Bremsscheiben variiert, um diesen bisher unzureichend untersuchten Einflussfaktor zu charakterisieren. Ein umfassender Messtechnikansatz erlaubt die kontinuierliche Beobachtung von Scheibenoberflächentemperatur und Scheibenverformung sowie die automatisierte Erfassung der Längen sämtlicher Risse auf der Scheibe nach jedem Bremszyklus. Die Versuchsreihe wird durch Werkstoffuntersuchungen sowie ein Finite-Elemente-Modell ergänzt.

Die Auswertung der Versuche folgt Untersuchungshypothesen, die auf Basis der mithilfe des Stands der Technik formulierten Forschungsfragen gebildet sind. Zentrale Erkenntnis ist, dass die Kühlkanalgeometrie die Rissbildung direkt und indirekt beeinflusst. Zum einen verursachen die Kühlkanalstege Extrusionen an den Reibflächen, die zu Spannungsspitzen führen und schließlich die Risspfade beeinflussen. Damit wachsen Risse schneller durch radial fluchtend angeordnete Kühlkanalstege hindurch als durch leicht versetzte.

Weiterhin wird durch Variation der Kühlkanalsteganordnung in Umfangsrichtung die harmonische Verwellung des Reibrings und damit die Bildung von Hitzeflecken auf der Bremsscheibe gestört. Hitzeflecken verursachen oberflächennahe Gefügeumwandlungen und definieren Rissinitiierungszonen. Entgegen den Aussagen früherer Studien ist zum Risswachstum geöffneter Risse allerdings nicht das lokale Auftreten eines Hitzeflecks erforderlich. Letztlich ist bereits eine konvexe Verformung des Reibrings ausreichend, um lokal verstärktes Risswachstum hervorzurufen. Schließlich bedingt die Ausbildung eines Durchrisses zum Kühlkanal, dass der Reibring an der jeweiligen Stelle sich stark konvex verformt, was die Beanspruchung nochmals verstärkt.

Der Stand der Technik wird durch diese Arbeit erweitert und präzisiert. Hervorzuheben ist die experimentelle Untersuchungsmethodik und die damit gewonnenen Erkenntnisse über den Einfluss der Bremsscheibengeometrie auf die Hitzerissbildung.

Abstract

Heat cracks in brake discs are a frequent problem during development of brake systems for heavy-duty vehicles since their occurrence cannot be predicted. Earlier works have focused on the influence of the brake pad and the brake disc material on heat crack formation. However, these influences vary strongly during series production and no profound causal model explaining the heat crack formation is available. Primary objective of this work is the analysis of influences on heat crack formation in order to explain crack formation by an extended causal model. Accordingly, a series of experiments is conducted with five different brake discs on the dynamometer. While keeping brake pad composition and brake disc material steady, cooling channel geometry of the ventilated brake discs is varied for characterisation of this previously insufficiently examined influence. A profound experimental setup allows for continuous observation of brake disc surface temperature and disc deformation as well as for automatic capturing of lengths of all cracks on the disc after each braking cycle. The experimental series is complemented by material investigations and a Finite Element model.

Experimental evaluation is done based upon experimental hypotheses, which in turn are formulated based on the state of science and technology. Key finding is the fact that cooling channel geometry directly and indirectly influences crack formation. On the one hand, cooling channel pins cause extrusions on the friction surface, leading to stress peaks and finally guide crack paths. Consequently, cracks grow faster through radially aligned cooling channel pins in contrast to radially slightly staggered pins. Furthermore, variation of cooling channel pin arrangement in circumferential direction distorts evolution of harmonic waviness of the friction ring and therefore evolution of hotspots. Hotspots cause surface near microstructural transformations and define crack initiation zones. In contradiction to findings of previous studies, local presence of a hotspot is not required for propagation of open cracks. In fact, a convex deformation of the friction ring is sufficient for locally intensified crack growth. Finally, formation of a through-thickness crack reaching the cooling channel causes strongly convex deformation of the friction ring at the respective position, which intensifies load over again.

State of science and technology is extended and specified. Experimental methodology and gathered findings on the influence of brake disc geometry on the heat crack formation merits special mention.

1 Introduction

This dissertation focuses on the analysis of the formation of heat cracks in brake discs for heavy-duty vehicles. Brake discs analysed in this work are ventilated standard neck brake discs for air disc brakes for the rear axle of the tractor of 40-ton-truck-trailer combinations made from grey cast iron. Primary objective of this work is the deduction of an extended causal model explaining the heat crack formation in brake discs. Therefore, a series of experiments on the dynamometer is combined with material experiments and analysis using a Finite Element (FE) model.

1.1 Motivation

Heat cracks in brake discs for heavy-duty vehicles often cause delays during the development of new brake systems, since their occurrence is not predictable yet. Numerous influences contribute in a complex manner to the formation of heat cracks (cf. chapter 2). For that reason, similar brake discs perform entirely differently in the heat crack test on the dynamometer, a mandatory certification test for brake system manufacturers. The heat crack test consists of several hundreds of drag brakings at full speed and medium torque, causing the formation of hotspots, thermomechanical damage and finally heat cracks. Previous studies (cf. subchapter 2.3) have presented several influences regarding brake pad and brake disc composition on the heat crack formation. However, brake pad and disc material vary in series production, producing different results of the heat crack test for different batches. Furthermore, none of the previous studies has presented a causal model that entirely explains the formation of heat cracks. Since the problem is too complex to be modelled entirely numerically, methodology with experimental focus is chosen and described in the next subchapter.

1.2 Methodology

In order to compose a new model describing the formation of heat cracks, state of science and technology is evaluated first. Therefore, existing general studies about grey cast iron brake discs are discussed along with studies dedicated to identify influences on the heat crack formation in brake disc. Existing knowledge is combined into a basic causal model, which allows for identification of knowledge gaps. Based on identified knowledge gaps of the state of science and technology, research objectives are derived, which are used in turn for derivation of experimental hypotheses. Based on hypotheses, a methodological experimental approach is deducted with a new experimental setup that has not been used in previous stud-

ies, and experiments on five brake discs are carried out. The first of the tested discs is considered a pre-test in order to observe new, previously unobserved phenomena that contribute to new hypotheses. Accordingly, the pre-test is used for recursion of the hypothesis body. Only the final hypothesis body is presented in chapter 3. Parallel to the experiments, a FE model is implemented that gives additional results about underlying processes contributing to crack formation that cannot be observed in experiments. By evaluation of the results and hypotheses, a profound causal model is composed and compared with the basic causal model. An overview of the general methodology of this is given in Figure 1-1.

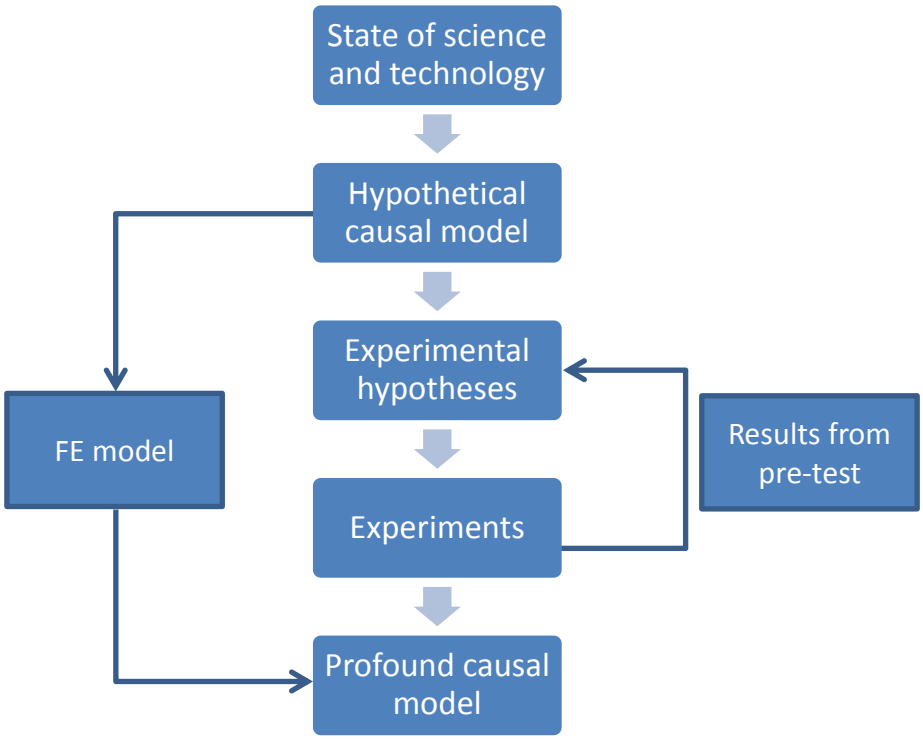

Figure 1-1: General methodology

2 State of Science and Technology

In this chapter, the state of science and technology regarding heat cracks in brake discs and related phenomena is discussed. After a brief overview of the heat crack test, thermomechanical and fracture mechanical basics are presented for introduction and classification of the problem. Subsequently, known influences on the heat crack formation in brake discs are summarised. In the end of this chapter, known influences are combined into a basic causal model that is used for the derivation of research objectives.

2.1 The Heat Crack Test

Heat cracks form in brake discs after repeated, severe thermomechanical loadings. For this reason, a test procedure forcing the brake disc into heat cracking has to consist of numerous brakings with sufficient power in order to heat up the brake disc significantly. Brake system manufacturers use various test programs on the dynamometer in order to test the resistance of their brake discs against heat cracks. Especially for passenger cars, stop brakings from high velocities are preferred, since passenger cars reach higher speeds while having a smaller mass compared to commercial vehicles.[1] Brakes for commercial vehicles are usually tested by application of drag brakings, either at medium speed for several minutes or at maximum speed for roughly one minute.[2,3,4] Brezolin and Soares have shown that crack growth rates rise by 9 times when drag brakings are combined with stop brakings compared to the application of drag brakings only.[3] The loadings of the dynamometer experiments conducted in this work consist of 40-seconds drag brakings at maximum speed, which allows for comparison with the results of Le Gigan.[5]

In all heat crack tests conducted in this work, the brake disc rotates constantly at a speed equivalent to 85 km/h, which results in 428 revolutions per minute (rpm), which equals 7.13/s. Braking periods take turns with cool down periods. After 40 seconds braking time with a constant brake torque of 2800 Nm, the brake disc is cooled down under air with cooling air until an average surface temperature of 50 °C has been reached. Then, the next heat

[1] Mackin, T. J. et al.: Thermal cracking in disc brakes (2002).

[2] Collignon, M. et al.: Failure of truck brake discs (2013).

[3] Brezolin, A.; Soares, M. R.: Influence of Friction Material Properties (2007).

[4] Le Gigan, G. et al.: Disc brakes for heavy vehicles (2015).

[5] Le Gigan, G.: Dissertation, On improvement of cast iron brake discs (2015).

crack cycle starts with the consecutive braking. After a few cycles, fissures form on the friction ring surface. Cracks open up and start growing. For most manufacturers, 500 consecutive heat crack cycles have to be completed without the occurrence of a through-thickness crack, which is defined as a crack that has propagated from the friction ring surface into the cooling channel. Then, the brake disc has passed the heat crack test.

During each braking period, the brake disc heats up, reaching surface temperatures of over 800 °C.[6] Since the heat is generated by friction between brake disc and brake pad in a short time period, strong thermal gradients of several hundred degrees form on the friction ring surfaces and inside the friction rings. These thermal gradients cause the fundamental stresses leading to the formation of heat cracks. In the next subchapter, the basics regarding thermal cracking are discussed for the specific load case of the heat crack test.

2.2 Thermomechanical and Fracture Mechanical Basics

2.2.1 Classification of the load situation

In order to understand the underlying processes leading to cracking, the load situation of the heat crack test has to be identified. Consequently, thermomechanical and fracture mechanical basics will be discussed in this section.

Since the load is applied cyclically, categorisation of the heat crack test can be done in terms of a fatigue test. Literature differentiates between low cycle fatigue (LCF, up to approx. 10^4 load cycles), high cycle fatigue (HCF, up to approx. 10^6 load cycles) and ultra high cycle fatigue (up to appox. 10^8 load cycles), dependent on the number of load reversals until failure.[7] Damage from LCF usually results in numerous cracks on the surface of the part, while damage from HCF mostly causes a single crack only.[7] Additionally, crack growth under LCF load often involves plastic deformations.[8] During the heat crack test, thermomechanical stresses due to inhibited thermal expansion and mechanical stresses caused by the brake torque are superposed. The number of cycles regarding the thermomechanical stresses is around 500, as this is the maximum number of heat crack cycles a brake disc has to withstand in order to pass the test. Regarding tangential stresses caused by the brake torque, the number of load reversals is much higher for each segment of the brake disc, around $1.4 \cdot 10^5$ cycles, assuming a rotational speed of 428 rpm and a braking time of 40 s. This would classify the

[6] Le Gigan, G. et al.: Disc brakes for heavy vehicles (2015).

[7] Richard, H. A.; Sander, M.: Ermüdungsrisse (2012).

[8] Bathias, C.; Pineau, A.: Fatigue of materials and structures (2010).

load situation as LCF (number of test cycles) with superimposed HCF (number of revolutions). However, the resultant crack distribution usually shows multiple cracks on the surface and calculations made by several authors indicate that plastic deformations are dominant in each heat crack cycle.[9,10] For that reason, the load situation will be subsequently categorised as LCF. Furthermore, it is assumed that thermomechanical stresses are the primary reason for heat cracks and the additional load from the brake torque can be neglected. Nonetheless, it should be noted that during each heat crack cycle not only mechanical but also thermal load is reversed, since the brake disc heats up and cools down entirely in each heat crack cycle. Consequently, the problem can be categorised as thermomechanical fatigue (TMF), too.

2.2.2 Grey Cast Iron as Brake Disc Material

Brake discs for heavy-duty vehicles are usually made from cast iron, most commonly grey cast iron, also known as lamellar graphite cast iron (GJL), whose material characteristics show some special issues in comparison to common steel alloys.[11] Less common are brake discs made from nodular or spheroidal graphite cast iron (GJS) and vermicular graphite cast iron (GJV).[12] Generally, the graphite microstructure has a major influence on two material characteristics: thermal conductivity and tensile strength resp. fatigue characteristics.[13] Since graphite conducts heat better compared to iron, thermal conductivity is dependent on shape and length of the graphite flakes.[14] On the other hand, graphite flakes act as voids in the structure, which results, in contrast to steels, in anisotropic deformation behaviour under compression and tension.[15] While graphite transfers compressive stresses, it both acts as a void and inhibits lateral contraction of the iron voids under tensile stresses. Therefore, compressive strength of GJL is usually around four times higher than its tensile strength.[15] For the same reason, the stress-strain curve of GJL is slightly non-linear just after the application of small tensile stresses below the elastic limit.[16]

Furthermore, material characteristics of GJL are strongly temperature dependent. One of the studies that have evaluated the deformation behaviour of GJL at different temperatures has

[9] Rashid, A.; Stromberg, N.: Sequential simulation of thermal stresses (2013).

[10] Gao, C. H. et al.: Stress Analysis of Thermal Fatigue Fracture (2007).

[11] Baumgartner, H. et al.: Nutzfahrzeugbremsen (2012), p. 212.

[12] Goo, B.-C.; Lim, C.-H.: Thermal fatigue (2012).

[13] Lee, Y. M. et al.: Influence of Microstructure (2006).

[14] Hecht, R. L. et al.: The effect of graphite flake morphology (1999).

[15] Berns, H.; Theisen, W.: Eisenwerkstoffe (2008).

[16] Fang, L. Y. et al.: Der Elastizitätsmodul von graphitischen Gußeisen (1998).

been conducted by Pevec et al.[17] They reported strong decrease of strength parameters at high temperatures (500-700 °C) in comparison to room temperature (RT). This way, tensile strength lowered from 280 MPa (RT) to 225 MPa (500 °C) to 50 MPa (700 °C). That means that the material is able to maintain its strength more or less until around 500 °C have been reached and then rapidly loses its carrying capacity with further rising temperature. Meanwhile, at 500 °C the maximum number of cycles until failure is reduced to 50 % of the original value at RT.[17]

The general behaviour of GJL is naturally affected by the amount of alloying elements, too. Ankamma[18] gives an overview of the effect of alloying elements on the strength of GJL. Chrome, Cooper, Tin and Boron strengthen the alloy in small amounts, although Boron already weakens the alloy if amounts exceed 0.02 %.[18] Molybdenum also increases high-temperature strength of grey cast iron, in spite of lowering thermal conductivity.[19] Finally, a higher amount of carbon improves the thermal strength of brake discs, because the advantage of the enhanced thermal conductivity outnumbers the disadvantage of lower thermal strength due to the higher porosity.[20]

2.2.3 Modelling of Grey Cast Iron

The preceding section showed that GJL has special characteristics that have to be considered when simulating the material behaviour. Especially anisotropic, nonlinear deformation behaviour in tension and compression, as well as fatigue behaviour in cyclic loading situations have to be modelled. For that reason, established material models suitable for modelling of GJL are briefly summarised in this section.

Chaboche[21] introduced basic constitutive equations for general description of plastic deformation behaviour. Nonetheless, Chaboche's model is not suitable for modelling of GJL because it cannot reproduce porous behaviour induced by the graphite flakes. Damage based material models have been established for this use case and are based on assumptions made by Gurson.[22] Several models have adopted Gurson's considerations later, such as the damage

[17] Pevec, M. et al.: Elevated temperature low cycle fatigue (2014).

[18] Ankamma, K.: Effect of Trace Elements (2014).

[19] Maluf, O. et al.: Effect of Alloying Elements (2009).

[20] Brecht, J.; Egner-Walter, A.: Influence of Material Selection (1998).

[21] Chaboche, J. L.: Viscoplastic constitutive equations (1977). Quoted after Chaboche, J. L.: A review (2008).

[22] Gurson, A. L.: Continuum Theory of Ductile Rupture (1977).

model by Tveergaard and Needleman.[23] Koetniyoum et al. and Augustinus et al. designed models to calculate stresses in brake discs.[24,25]

Seifert and Riedel have presented a model for fatigue life assessment of cast iron parts under TMF.[26] Later, Metzger and Seifert presented a model suitable to assess TMF behaviour of cast iron cylinder heads under combined LCF and HCF load.[27] It has been adopted by Le Gigan et al. in order to simulate the TMF behaviour of a brake disc segment in the heat crack test.[28] It allows fatigue life assessment of brake disc segments up to the point where a crack opens, being not able to calculate crack propagation.[29]

Recently, Metzger and Seifert have presented a model to describe the micromechanical material behaviour of GJL.[30] It is based on micrographs of specimens, which suit as master for remodelling material structure, and allow for precise re-enactment of material behaviour. However, such micromechanical models are in all likelihood not suitable for modelling an entire brake disc during the heat crack test, since the computational effort would probably be too high.

2.2.4 Crack Formation and Crack Propagation

On a microscale, every engineering material is defective respectively not free of damage. Defects are, amongst others, voids, dislocations, and grain boundaries, which lead, in loading situations, to microscopic plastic deformations and micro cracks. In multi-phase materials, cracks on a microscale form by void nucleation and void coalescence. This is the case for GJL, where the voids nucleate around the graphite lamellae. In alternating load situations, a fissure forms on the surface by surface wrinkling, which is induced by ex- and intrusions on the surface. These processes are summarised by the terms damage and fatigue.[31]

After micro-cracks or voids have coalesced, macro-crack formation occurs. Crack initiation is defined as the transition from a stationary crack or void to an instationary crack, i.e. the beginning of crack propagation. The term fatigue crack growth refers to crack propagation under alternating load. As soon as the crack has opened on the surface, three types of cracks

[23] Gross, D.; Seelig, T.: Bruchmechanik (2016), p. 341.

[24] Koetniyom, S. et al.: The development of a material model (2002).

[25] Augustins, L. et al.: Constitutive model for flake graphite (2016).

[26] Seifert, T.; Riedel, H.: Mechanism-based fatigue life prediction (2010).

[27] Metzger, M.; Seifert, T.: A Mechanism-Based Model (2012).

[28] Le Gigan, G. et al.: Modelling of grey cast iron (2016).

[29] Le Gigan, G.: Dissertation, On improvement of cast iron brake discs (2015), p. 29.

[30] Metzger, M.; Seifert, T.: Computational assessment (2015).

[31] Gross, D.; Seelig, T.: Bruchmechanik (2016).

are distinguished by the displacement of the surface. Mode I crack growth refers to opening mode, which is caused by tensile stresses being normal to the crack plane. Mode II crack growth means sliding mode, caused by shear stresses being parallel to the crack plane and perpendicular to the crack front and finally Mode III, tearing mode, induced by shear stresses parallel to the crack plane and to the crack front.[32]

2.3 Known Influences

In this subchapter, known influences on the crack formation in brake discs are discussed. As described before, most studies have focused on the influence of brake pad and disc material. Some authors presented results giving indications of thermal influences and very few authors described geometric influences on crack growth.

2.3.1 Influence of Brake Pad

The friction material of the brake pad influences heat crack growth rate in brake discs, as Brezolin concludes in his dissertation.[33] In one of his studies[34], which has already been cited in subchapter 2.1, he discusses the influence of the brake pad material properties on – manually measured – crack growth rates, distinguishing heat crack testing by application of drag brakings from application of combined drag and stop brakings, by comparison of three different friction materials. By application of the combined test, a monotonic dependence of crack growth rates from compressibility and thermal conductivity has been evaluated. The more compressible and thermally conductive the brake pad, the lower the crack growth rates. For the drag braking test, results less clearly indicate a monotonic dependence, since two materials with similar thermal conductivity and compressibility cause different crack growth rates. However, a third material being less compressible and thermally conductive compared to the other materials causes the highest crack growth rates in the drag braking test.

A higher pad compressibility might cause a more even surface pressure distribution between brake pad and brake disc, resulting in a lower crack growth rate. Although this relationship has not been explained experimentally yet, simulations and experiments carried out on a rail brake disc showed that maximum circumferential stresses and crack initiation occur on the same position as where the maximum surface pressure arises.[35] For rail vehicles, brake pads

[32] Richard, H. A.; Sander, M.: Ermüdungsrisse (2012).

[33] Brezolin, A.: Dissertation, Estudo de Geração de Trincas Térmicas (2007).

[34] Brezolin, A.; Soares, M. R.: Influence of Friction Material Properties (2007).

[35] Kim, D.-J. et al.: Thermal stress analysis (2008).

with small springs beneath multiple pad segments, which distribute the surface pressure more uniformly, are commonly used.[36]

Nonetheless, pad compressibility and other friction material properties change in the course of the heat crack test due to wear. This effect has been documented by Le Gigan et al.[37], who have tested two brake pads showing similar properties before the heat crack test. After the test, compressibility of both brake pads differed by 52 % between each other. This indicates that friction material properties do not necessarily change equivalently during the heat crack test. For that reason, friction materials that apparently show the same properties before the heat crack test might change their properties differently during the heat crack test, resulting in differently influencing the brake disc's crack growth behaviour in the test. This circumstance is not taken into account by Brezolin et al., since no characterisation of the brake pad's properties is carried out after the heat crack test.

In another study by Le Gigan et al.[37], influence of friction material properties on crack growth is evaluated as well. However, dependence of crack growth rates from brake pad compressibility is neither explicitly confirmed nor is a correlation between brake pad wear and crack growth rates described. Nevertheless, usage of another pad causing higher disc wear results in higher crack growth rates. Similarly, a brake pad with doubled thermal conductivity and lower compressibility causes both lower maximum temperatures on the brake disc and a higher disc life. For that reason, Le Gigan et al. conclude that brake disc life is, in terms of pad influence, mainly dependent on the thermal conductivity of the brake pad rather than on its compressibility.

2.3.2 Influence of Brake Disc Material

As mentioned in section 2.2.2, graphite lamellae influence the characteristics of grey cast iron and thereby the resistance of brake discs against heat cracks. Shape and size of the graphite lamellae are primarily influenced by alloying elements and the casting process. These influences of the heat crack formation in GJL brake discs are discussed in this section.

According to Yamabe et al.[38], crack growth rates are directly influenced by the size of the graphite lamellae on the one hand, which can be refined by inoculation with cerium, and the amount of nickel in the alloy on the other hand. The finer the graphite lamellae and the higher the nickel amount, the lower the crack growth rates, since crack propagate along the graphite lamellae on a microscopic scale. That way, a disc alloy with 1.25 % nickel causes roughly four times lower crack growth rates compared with a zero nickel alloy. Since nickel is an

[36] Wirth, X.: Bremsbelag (1995).

[37] Le Gigan, G. et al.: Disc brakes for heavy vehicles (2015).

[38] Yamabe, J. et al.: Development of Disc Brake Rotors (2003).

expensive alloying element, the melt can be inoculated with cerium in order to achieve similarly low crack growth rates with less nickel (0.019 % cerium and 0.3 % nickel for 2.5-times reduced crack growth rates). It should be noted that Yamabe et al. tested samples in brake disc-like shape but not complete brake systems on the dynamometer.

A similar effect accounts for usage of GJV instead of GJL. A comparison between GJL and GJV material samples has been carried out by Lim and Goo.[39] Applying pure HCF-loads to tensile specimens, GJV samples reach nearly twice the lifetime of GJL samples. While performing a TMF test, crack initiation occurs 2.14 times later for GJV specimens as with GJL specimens, although GJV specimens feature a thermal conductivity reduced by 40 %. Nevertheless, transferability of the results to full brake discs has not been shown by the authors.

Influence of graphite microstructure on crack growth is evaluated for full brake discs by Collignon et al.[40] and Cristol et al.[41]. Both studies assess the suitability of grey cast iron with a graphite structure refined by nitrogen enrichment and grey cast iron with a microstructural gradient. Therefore, Collignon et al. conduct experiments on the dynamometer, applying stop and deceleration brakings, while Cristol et al. test the same materials on a self-developed fatigue-testing machine for brake disc segments. The material with a microstructural gradient is constructed in such a way that the length of the graphite flakes increases in the depth direction of the disc, while the graphite flakes near the surface are shorter than 100 µm and in deeper layers are about 300 µm long. Contrary to the results of common grey cast iron, this material does not show any extrusions on the surface after the braking tests. The same accounts relatively for the brake disc made of grey cast iron that has been enriched with nitrogen. In addition, Cristol et al. demonstrate a similar behaviour in case of thermomechanical fatigue on the testing machine. According to them, grey cast iron with microstructural gradients combines two advantages: on the one hand, forwarding of the crack front is hampered by the shorter graphite flakes. On the other hand, the austenite dendrites located in between the graphite flakes near the surface stop the crack propagation.

Regheere et al.[42] continue the test series of Collignon et al. and Cristol et al. by extending them to GJS with various tensile strengths (EN-GJS-450 up to 600) and other advanced alloys, e.g. GJS with 4 % aluminium added. In comparison to common GJL, most advanced alloys endure more cycles on the brake disc segment-testing machine. For GJS, maximum crack length goes down with increasing tensile strength. GJS with aluminium added shows the highest resistance against TMF in the test.

[39] Lim, C.-H.; Goo, B.-C.: Development of compacted vermicular graphite cast iron (2011).

[40] Collignon, M. et al.: Failure of truck brake discs (2013).

[41] Cristol, A. et al.: Improvement of truck brake disc lifespan (2014).

[42] Regheere, G. et al.: Thermocracks (2013).

Not only length, shape, and type of graphite flakes influences crack formation, but also their distribution homogeneity in circumferential direction, which in turn can be improved by smooth cool down after casting.[43]

2.3.3 Thermal Influences

Thermal influences discussed in this section are not actual influences as they have been described in the preceding sections. Thermomechanical processes that contribute to crack formation are discussed here.

The basic process that causes TMF and therefore cracking of the brake disc has been explained with the help of several Finite-Element Simulations. During braking, the brake disc heats up unevenly, resulting in a rather cool neck and an overheating in radial centre positions of the friction ring, i.e. thermal gradients on the friction surface in radial direction (hotbands) and circumferential direction (hotspots). Hotspots and hotbands usually occur asymmetrically on both friction rings, i.e. at the hotspot-/hotband location of the one side is no hotspot-/hotband on the other side and vice versa, which flips in each braking cycle.[44] Thermal gradients cause non-uniform thermal expansion, which in turn cause compressive stresses in circumferential direction that are high enough to induce plastic deformations.[45] When cooling down, thermal expansion vanishes, forcing the formerly plastic compressed elements into circumferential residual tensile stresses.[46] By cyclic repetition of this process, crack formation and growth starts.[47] Stresses are highest at the surface, since the temperatures are highest there. For that reason, first fissures form on the brake disc's friction ring surface.[48]

In addition to this, Brezolin[49] stated that hotspot temperatures over 750 °C caused microstructural transformation from pearlite to martensite, which would provide the base for cracks at the respective location. These locations would suffer from higher fatigue, since the microstructural transformation towards martensite would cause a growth in volume and hardness. For railway steel brake discs, the formation of martensite is considered to be accelerating crack formation due to its increased hardness.[50]

---

[43] Okamura, T.; Imasaki, M.: Increasing Thermal Strength (2009).

[44] Sardá, A.: Dissertation, Wirkungskette der Entstehung von Hotspots (2009).

[45] Rashid, A.; Stromberg, N.: Sequential simulation of thermal stresses (2013).

[46] Gao, C. H. et al.: Stress Analysis of Thermal Fatigue Fracture (2007).

[47] Dufrénoy, P. et al.: Damage mechanisms (2002).

[48] Collignon, M.: Dissertation, Compréhension des mécanismes de dégradation (2013).

[49] Brezolin, A.: Dissertation, Estudo de Geração de Trincas Térmicas (2007).

[50] Li, Z. et al.: Analyzing the mechanisms of thermal fatigue (2015).

Crack growth might be accelerated as well by residual tensile stresses from the casting process, which can be reduced by annealing, resulting in reduced coning and a more uniform stress distribution.[51] Another effect of heat treatment is reduced crack growth after a bedding procedure. This has been shown by Mace et al.[52], who have observed enforced forming of ferrite after bedding, which reduces crack propagation due to its ductile behaviour.

As mentioned before, not only hotbands but also hotspots influence the stress state in the brake disc during the heat crack test. The influence of hotspots has been investigated by Le Gigan et al.[53]. They observed that hotspots would, dependent on the brake disc, either migrate slowly in circumferential direction over the friction ring surface in the course of the heat crack test or stay at fixed circumferential positions throughout the entire test. The brake discs that showed a fixed hotspot pattern endured less cycles in the heat crack test until a through-thickness crack occurred. The same accounts for radially fixed hotbands. Furthermore, at the positions of large cracks, distinctive hotspots have formed. Additionally, the authors state that cracks would stop propagating after a hotspot had moved away from the respective crack location. Moreover, according to the authors, hotbands on the piston side would form at radial centre or inner position due to coning. As in all other discussed studies, crack growth was measured manually.

2.3.4 Geometric Influences

For ventilated brake discs, temperature and stress distribution during braking and cool down is influenced by the geometry of the disc. For that reason, crack formation might be influenced as well by geometry.

Maximum temperatures depend among others on the cooling power of the cooling channel of the brake disc. Common hat brake discs for heavy-duty vehicles can be grouped into three different geometry types: ventilated brake discs with round or elliptical pins connecting the friction rings, which provide the highest cooling power, ventilated brake discs with straight vanes, which provide medium cooling power and solid brake discs, which provide lowest cooling power.[54] Even higher cooling power is achieved with new, experimental disc geometries, e.g. the wire-woven bulk diamond brake disc, which connects both friction rings through a porous wire mesh and results in 15-25 % lower temperatures at the end of long duration (5500 s) drag brakings.[55] Influence on crack formation is not evaluated in experimental studies.

---

[51] Shin, M. W. et al.: The Effect of Residual Stress (2013).

[52] Mace, G. et al.: Characterisation of Material Transformation (2006).

[53] Le Gigan, G. et al.: Disc brakes for heavy vehicles (2015).

[54] Tirović, M.: Energy thrift (2009).

[55] Mew, T. D. et al.: Transient thermal response (2015).

Le Gigan et al. have presented a numerical study on the effect of cooling channel geometry on fatigue behaviour of brake discs.[56] By application of a hotband pattern to simulate thermal load, cyclic damage by alternating stresses have been evaluated for different cooling channel geometries in terms of maximum endurable cycles until failure, i.e. cracking. The number of cooling channel pin rows is varied between three and seven rows. In addition to this, pin width and length is varied. Cooling channel vane geometry is varied as well. Five consecutive braking cycles are simulated. Only a 5°-segment of the brake disc has been modelled and applied with a single hotband. Results indicated that vanes provide a longer lifetime for the brake disc compared to pins. For pins, the optimum number of rows seems to be three in case the mass has to be constant. If mass is not a constraint, seven rows of pillars indicate to be the optimum solution in terms of fatigue life. However, the study does account for general hotspot patterns on full discs. Furthermore, no crack propagation is simulated.

Generally, crack propagation has been simulated only in very few studies, which are discussed in the next section.

2.3.5 Crack Growth Simulation for Brake Discs

Wu et al.[57] have simulated crack propagation for a segment of a steel railway brake disc. Therefore, the position of crack initiation is manually defined based on experimental observation of the hotspot formation. On that position, a crack of 2 mm length is inserted into the FE model. Consecutively, crack propagation is calculated for that single crack using the extended Finite Element Method (XFEM). However, no validation is carried out. Only temperature distribution is compared with experimental data. Nevertheless, the authors give a forecast on the brake disc's life.

Similarly, Caprioli et al.[58] as well as Peng et al.[59] simulate crack propagation in railway wheel treads made from steel, using a different approach than Wu et al. In the first step, they calculate temperatures and stresses in the part using a FE-model. In the second step, they estimate crack growth by calculating stress intensity factors using Paris' Law (Caprioli et al.) or the Frost-Dugdale-Equation (Peng et al.). Both do indeed not compare their results with experimental data and simulate one crack only.

None of the authors of the discussed studies has simulated crack growth for cast iron brake discs yet. Nevertheless, crack growth has been simulated for cast iron exhaust manifolds by

[56] Le Gigan, G.: Improvement in the brake disc design (2017).

[57] Wu, S. C. et al.: Thermal crack growth-based fatigue life prediction (2016).

[58] Caprioli, S. et al.: Thermal Cracking of a Railway Wheel Tread (2012).

[59] Peng, D. et al.: A study into crack growth (2012).

Ktari et al.[60] Equally to Caprioli et al. and Peng et al., they calculate stresses and temperatures in a FE analysis. Crack growth is calculated analytically using the J-Integral, since crack growth estimation using stress intensity factors is not a valid method for plastic crack propagation, as it is the case for grey cast iron. As a result, it is shown that crack growth rates go up with increasing crack distance. Furthermore, they model more than one crack and show the effect of the interaction of two cracks with each other. Moreover, they have validated their model based upon experimental data.

2.4 Synthesis of the State of Science and Technology into a Basic Causal Model

Based on the findings of other authors that have been described in the preceding sections, a basic causal model is synthesised, which explains the formation of heat cracks according to the state of science and technology. Therefore, different sources are logically combined into chains of effects, generating a broader view on the topic compared to a single study covering a single influence only.

In order to structure the model, the process of crack formation is broken down into the balance of stress versus strength. This is done to structure and classify influences rather than providing a model suitable for calculation of crack propagation, since numerous factors contributing to crack growth are left out. On the stress side, influences raising or lowering the overall stress level line up. On the strength side, influences raising or lowering strength of the brake disc come together. This means in an abstracted and simplified manner that cracks will initiate and propagate faster if influences raising the stress side intensify and propagate slower if influences raising the strength side intensify, and vice-versa. Several alloying elements might lower the strength of the material of the brake disc. This has been shown for carbon, which is responsible for forwarding the crack along the graphite flakes (cf. section 2.3.2). Contrary, molybdenum is known to strengthen the alloy. Influence of other alloying has not been discussed in relation to GJL brake discs. In addition to this, tensile strength of GJL lowers with increasing temperature, e.g. due to the formation of a hotspot, resulting in a more ductile material behaviour. Meanwhile, a higher tensile strength of an alloy results in a higher hardness, which is supposed to be detrimental to the fracture toughness, since high hardness often causes the material to be more brittle.

Stress level is mainly influenced by residual stresses forming out of plastic compression during cooling in each braking cycle (cf. section 2.3.5). The cyclic change from tensile to compressive plastic deformation causes fatigue on a micro level, softening the material (cf. section 2.2.2). The plastic compression itself is generated by non-uniform heating of the friction surface during braking, which can be broken down to the formation of hotspots and

[60] Ktari, A. et al.: Numerical computation (2011).

hotbands (cf. section 2.3.3). Hotspots either show up on fixed positions for the entire test or migrate in circumferential direction over the friction surface, which might cause excessive stresses in case of fixation on the respective locations. Both hotspots and hotbands might be attenuated by a higher thermal conductivity of brake pad and the brake disc material. Moreover, a higher pad compressibility might cause a more even temperature distribution as well (cf. section 2.3.1). The disc's thermal conductivity is increased with several alloying elements, such as copper. Since graphite flakes conduct heat better than the iron structure, thermal conductivity rises with longer graphite lamellae, which is in turn affected by the amount of nickel and cerium in the alloy (cf. section 2.3.2). Hotbands might form narrower if higher coning amplitudes are reached in the test. Disc coning can be reduced by heat treatment, i.e. annealing. Finally, at hotspot locations, temperatures over 750 °C are reached, resulting in possible microstructural transformations due to overheating. These microstructural transformations are known to cause hardening of the friction surface (cf. section 2.3.3).

Regarding geometric influences (cf. section 2.3.4), the findings of Le Gigan et al. and Mew et al. cannot be included into the causal model at this point, since the relation of geometric influences to other influences has not been discussed yet.

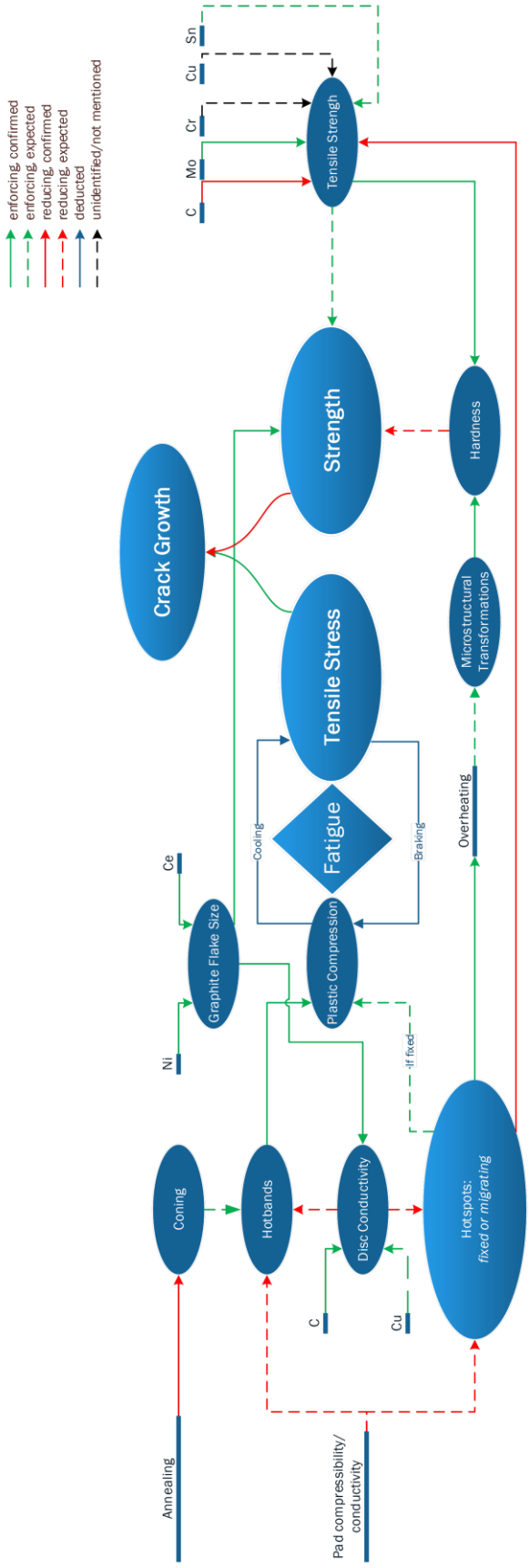

Figure 2-1: Basic causal model based on the state of science and technology

2.5 Derivation of Research Objectives

The basic casual model constructed in the preceding subchapter gives several indications about the focuses of works of earlier authors and helps identifying remaining knowledge gaps in terms of the development of a profound model explaining the heat crack formation in brake discs.

The influence of the brake disc material has been broadly discussed, considering alloying elements and graphite flake size. This way, optimised GJL alloys have been found increasing the cracking resistance of brake discs either by lowering load amplitudes due to better thermal conductivity or by slowing down crack propagation under equally high loadings compared to former alloys. Consequently, further investigations varying the brake disc would rather not deliver unexpected results solving the heat crack problems, at least if a material comparably cheap to GJL is demanded.

The same accounts for the brake pad properties, which are influenced by its composition. Since a higher thermal conductivity reduces the formation of hotspots and hotbands and therefore lowers stresses induced by thermal gradients on the friction surface of the brake disc, brake pads should feature a high thermal conductivity. Similarly, the brake pad's compressibility should be rather high, although this influence is not as clear as the influence of the brake pad's thermal conductivity. Nonetheless, the influence of the brake pad on the heat crack formation has been broadly discussed.

Several studies have already discussed thermal influences on the heat crack formation in brake discs, usually in the context of the formation of hotspots. Some of them, e.g. Le Gigan et al. stated that their results were not clear, for example the influence of the fixation of hotspots. Other studies observed microstructural transformations but have not discussed their influence on crack growth based on experimental results gathered with GJL brake discs. Nevertheless, influence of microstructural transformations towards a martensitic microstructure on crack growth have been discussed for railway brake discs made of steel. Furthermore, none of the mentioned studies has evaluated the effect of hotspot and hotband formation and migration on crack growth in a quantitative manner during the test, i.e. considering crack growth rates. Additionally, disc surface topology effects like side-face runout (SRO) and disc thickness variation (DTV) have so far only been discussed in relation to the formation of hotspots. It has not been evaluated yet, whether a direct link exists between the formation of SRO, DTV and heat cracks.

Finally, none of the mentioned studies has investigated the influence of the brake disc design on the formation of heat cracks in experimental series. Nonetheless, a numeric study by Le Gigan has proposed that the cooling channel geometry might influence the cracking resistance of the brake disc.

Consequently, research objectives for this work are derived based on the identified knowledge gaps in the state of science and technology. First, thermal influences are grouped

as a research objective. On the one hand, this covers the effect of microstructural transformation, induced by hotspots or hotbands. On the other hand, this covers the effect of hotbands and hotspots on the heat crack formation in general and covers questions about effect of migration of hotspots as well. Another thermal topic that has been neglected so far covers the transition from fissures to an open crack, whether hotspots are involved in crack opening, crack propagation or both issues.

Second, the direct influence of disc deformation on the heat crack formation has not been evaluated yet and therefore constitutes another research objective. This includes the influence of coning as deflection of the friction surface on the occurrence of extreme temperatures and the initiation and propagation of heat cracks. In addition to this, the influence of SRO and DTV as local deformation on crack growth and the formation of hotspots is covered. Lastly, the design of the cooling channel is investigated regarding its influence on the propagation of heat cracks.

The third group of research objectives deals with heat crack growth in brake discs in general, covering all influences that affect crack growth in relation to the crack location and the point in time in the course of the test, completing causal chains leading from influencing factors such as deformation and hotspots to crack propagation.

In the next chapter, hypotheses are formulated based on the research objectives stated here. These hypotheses hypothetically answer the identified knowledge gaps. Additionally, the presented research objectives are used in the subsequent chapter to derive the methodological approach for the investigations carried out in this work.

3 Hypotheses and Explorative Assumptions

In this chapter, hypotheses are derived based on the research objectives closing the knowledge gaps of the state of science and technology. Additionally, phenomena observed during the preliminary investigation contribute to the formulation of new explorative assumptions that do not arise from the state of science and technology. According to this, hypotheses on microstructural transformations as well as the connection between hotspots, fissures, and open cracks cover thermal influences. Hypotheses describing the influence of the cooling channel design, coning and SRO relate to the research objectives formulated in terms of the influence of deformation on crack growth. Finally, hypotheses on crack growth in general complete this chapter.

3.1 Crack Propagation and Basic Assumptions

According to the basic causal model based on the state of science and technology (cf. subchapter 2.4), the significant stress leading to crack growth results from a plastic compression with a subsequent transformation of the compressive stresses into residual tensile stresses during cool-down. Simultaneously, an open crack causes stress relief at the surface. On the one hand, the crack might close under compressive stress and on the other hand, the tangential tensile stress near the crack shores is close to zero, which means that the crack is a discontinuity. It is therefore assumed that the formation and opening of cracks slows crack growth, from which the following hypotheses and explorative assumptions are derived:

3.1.1 Crack Closure

According to the basic causal model (cf. subchapter 2.4), circumferential compressive stresses are present at the end of each braking cycle. Due to asymmetrical behaviour of GJL under compressive and tensile stresses (cf. section 2.2.2) and linear thermal expansion, compressive stresses at the end of the braking must be of higher level compared to tensile stresses that cause cracking. Since these stresses are oriented perpendicularly to the radially oriented cracks, they should compress the cracks, putting their shores together and causing crack closure. Accordingly, the following hypothesis is formulated:

Hypothesis 1.1: Open cracks close during each heat crack cycle due to compressive circumferential stresses.

Le Gigan et al. reported that cracks cause local hotspots,[61] acting as a thermal barrier regardless if closed or open. Even if they do not act as a thermal barrier, they should not cause a local lowering of temperature, since this would indicate that the crack remained open. According to this, it is **predicted** that cracks are visible in the hotspot pattern as local narrow hotspots or alternatively are not visible, as they do not act as a thermal barrier. If cracks were visible as local narrow cool spots, they would remain open wide enough that the cooler inside of the friction ring is captured by the thermographic camera at the end of the braking period, which would falsify hypothesis 1.1.

3.1.2 Residual Tensile Stresses

The basic causal model (cf. subchapter 2.4) indicates that residual tensile stresses remain on the friction ring surface after cool-down, as they have originated from prior plastic compression due to non-uniform thermal expansion. As the friction surface is hotter than the inside of the friction ring during braking, compressive stresses should be concentrated on the friction surface.

Hypothesis 1.2: Stresses on the friction surface are exclusively compressive at the end of the braking period.

They should transform into residual tensile stresses, which results in the **prediction** that residual stresses on the friction surface are tensile only after cool-down. Hypothesis 1.2 would be falsified, if compressive stresses or no tensile stresses were measured on the fiction surface after the heat crack test.

3.1.3 Stress relief by crack opening

As tangential stresses are zero on the crack shore and the crack acts as a discontinuity, its opening reliefs its ultimate surrounding. However, it is unclear how the stress relief at the crack location lowers tension for adjacent cracks. An adjacent crack is defined as a crack that is located closer than 12°, as this is the angular segment between cooling channel pins (see assumptions made in subchapter 3.4):

Assumption 1.3: Crack opening of an adjacent crack causes stress relief at already open cracks.

Consequently, it is **predicted** that crack growth rates at adjacent cracks reduce after a crack has opened up. Assuming a measurement deviation of -3 mm for the crack detector (cf. section 4.1.4) and an average crack propagation rate of a crack becoming the through thickness crack with a length of 75 mm after 500 cycles of 0.15 mm/cycle, at least 20 consecutive cycles have to be observed each for determination of crack growth rate changes. If crack

[61] Le Gigan, G.: Dissertation, On improvement of cast iron brake discs (2015).

growth rate of an adjacent crack accordingly rose during the next 20 cycles in comparison to the last 20 cycles before the opening, assumption 1.3 would be falsified.

Continuing this thought, cracks might propagate slower at the end of the test in comparison to the beginning of the test, as a vast number of cracks lowers the actual load level:

Assumption 1.4: Heat crack propagation rates slow down at the end of the test as the number of cracks increases and they relief each other.

Accordingly, it is **predicted** that crack propagation rates of cracks that have grown during the entire test are highest at the beginning of the test. Furthermore, ratio of crack count divided by medium length of cracks should remain constant when the crack opening rate remains constant. If these cracks grow faster at the end of the test in comparison to their growth rate at the beginning of the test, assumption 1.4 would be falsified.

3.1.4 Crack Length vs. Crack Count

Continuing the thought made by assumption 1.3, either few long cracks or many short cracks would form on a brake disc during the heat crack test, as the opening of a new crack would slow down crack propagation at adjacent cracks. Nevertheless, since the braking energy per cycle stays constant in the course of the test, the ratio between crack count and average crack length might approach a constant value defined by the friction pairing after numerous cycles:

Assumption 1.5: Friction pairing characteristics determine the ratio between crack opening and crack growth.

Accordingly, it is **predicted** that the ratio between crack count and average crack length approaches a certain, nearly constant value, which is specific to friction pairing. As long cracks reach the cooling channel more easily when they start growing from radial centre position, formation many small cracks might delay the formation of a through-thickness crack. Since very small cracks cannot be detected by the heat crack detector (cf. section 4.1.4), the heat crack cycle is taken as start for evaluation, in which the ratio reaches the value of ratio of the last cycle for the first time. Assumption 1.5 will count as falsified, if the ascent of a straight regression line over the remaining cycles from the start cycle on is higher than the standard deviation of the ratio between crack count and average crack length (cf. appendix A.2.4).

3.2 Microstructural Transformations

On the one hand, microstructural transformations to martensite have been assumed to be a preceding step before crack formation starts.[62,63] On the other hand, it was stated that microstructural transformations to martensite in steel discs could probably suppress crack growth.[64] Microstructural gradients in GJL might also influence crack formation (cf. section 2.3.2). Based on these statements, hypotheses are formulated here explaining the underlying processes in connection with microstructural transformations.

3.2.1 Crack Initiation and Propagation

As several authors stated, microstructural transformations to martensite are the origin of crack formation.[62,65] Cracks would initiate and propagate due to microstructural transformations in the friction ring. Furthermore, they assume that a coarse microstructure enforces crack propagation (cf. section 2.3.2). Accordingly, the following hypotheses are formulated, assuming the original pearlitic microstructure of the brake disc transforms into a different microstructure:

Hypothesis 2.1: Cracks are caused by microstructural transformations.

According to hypothesis 2.1, it is **predicted** that cracks should only initiate on spots where a microstructural transformation has taken place during previous cycles. If a crack initiates on a position that has not undergone microstructural transformations, hypothesis 2.1 would be falsified.

Hypothesis 2.2: Cracks grow due to microstructural transformations along the crack path.

If microstructural transformations are a necessary condition for crack propagation, cracks are **predicted** to grow only through areas that have previously undergone microstructural transformations. If a crack grows through a region where no microstructural transformation has taken place, hypothesis 2.2 would be falsified.

3.2.2 Hardness of Transformed Material

According to Brezolin[62], material that has undergone microstructural transformations to martensite due to overheating is harder than the original disc material. To evaluate the extent of microstructural transformations, the following hypotheses and assumptions are formulated:

---

[62] Brezolin, A.: Dissertation, Estudo de Geração de Trincas Térmicas (2007).

[63] Li, Z. et al.: Analyzing the mechanisms of thermal fatigue (2015).

[64] Raninger, P. et al.: Understanding the cracking resistance (2016).

[65] Li, Z. et al.: Analyzing the mechanisms of thermal fatigue (2015).

Hypothesis 2.3: Overheating causes microstructural transformations that are harder and more brittle than the original disc material.

Consequently, it is **predicted** that areas that have undergone overheating are harder compared to areas that have not undergone microstructural transformations. This would result in an increased hardness at radial centre position compared to radial outer and inner position, as temperatures are usually highest at a central hotband during the heat crack test. Furthermore, microstructural transformations should be found in the respective area. If hardness was higher in areas that have not undergone overheating or no microstructural transformations were found, hypothesis 2.3 would be falsified.

During the pre-test, friction surface at radial centre position was found to be heat tinted, which is an indication for surface oxidations that are known to be harder than the original material. As cracks preferably started growing from radial centre position, a link between surface oxidations and crack initiation might exist:

Assumption 2.4: Surface oxidations serve as crack initiation spots.

In this case, it is **predicted** that micro-cracks are present at oxidised structures in areas where cracks have opened up during the heat crack test. If no micro-cracks were found in such an area, assumption 2.4 would be falsified.

Finally, as known from basic fracture mechanics, graphite lamellae might cause porosity inside the friction ring (cf. section 2.2.4):

Assumption 2.5: Porosity around graphite lamellae causes crack initiation.

Accordingly, it is **predicted** that material around graphite lamellae is either extraordinarily soft after void nucleation or, if oxidised, extraordinarily hard and brittle. If no such soft or hard graphite lamellae were found in an area that has undergone microstructural transformations, assumption 2.5 would be falsified.

3.3 Dependencies between Hotspots, Fissures, and Open Cracks

Le Gigan et al.[66] have assumed that the manifestation of hotspots would cause higher crack growth rates and therefore the formation of long cracks at the fixed hotspot positions. However, influences on the opening of cracks have not been discussed yet. The following hypotheses are formulated in order to validate the findings of Le Gigan et al. and clarify the process of the evolution of long cracks in relation to presence of hotspots:

[66] Le Gigan, G.: Improvement in the brake disc design (2017).

3.3.1 Hotspots as Crack Propagation Accelerator

Based on the statements mentioned above, the following hypothesis is formulated:

Hypothesis 3.1: Local hotspots boost crack growth of open cracks.

Accordingly, it is **predicted** that as soon as a hotspot has moved away from a crack location, its growth rate will reduce. If a crack grew faster after a hotspot has moved away from its position, hypothesis 3.1 would be falsified.

3.3.2 Hotspot Depth

As described before, hotspots have been observed as accelerators for crack growth rates. This is consistent with the basic causal model, which indicates that strong thermal gradients cause strong compressive stresses and therefore strong crack growth. Continuing the thought forward, deep cracks would require thermal gradients and temperature levels comparable to hotspot temperatures deeply intruding inside the friction ring:

Hypothesis 3.2: For formation of a deep crack, thermal gradients and high temperature level comparable to hotspots on the friction surface are required as well in depth.

Accordingly, it is **predicted** that cracks only grow into depths that are affected by a hotspot, i.e. where the temperature level is equal or above the temperature level of the edge of the hotspot on the friction surface. If cracks grew in depths that are not affected by a hotspot, hypothesis 3.2 would count as falsified.

3.3.3 Hotspot Fixation by Through-Thickness Crack

In addition to the above mentioned statements, Le Gigan et al. observed that through-thickness cracks cause fixated hotspots at their location, which turn out to be exceptionally hot.[67] Furthermore, the link between the formation of SRO and the formation of hotspots has been reported.[68] Building upon this, the following hypothesis is formulated:

Hypothesis 3.3: A through-thickness crack causes an instability in the friction ring and therefore creates a fixed hotspot at its location.

Consequently, the formation of strongly convex SRO is **predicted** at the location of the through-thickness crack at the end of the test. Additionally, peak temperatures should occur at the location of the through-thickness crack. If either no convex SRO formed at the location of the through-thickness crack or peak temperatures were observed at a different location at the end of the test, hypothesis 3.3 would be falsified.

---

[67] Le Gigan, G. et al.: Disc brakes for heavy vehicles (2015).

[68] Sardá, A.: Dissertation, Wirkungskette der Entstehung von Hotspots (2009).

3.3.4 Crack Opening by Hotspots

Brezolin stated that hotspot indicated microstructural transformations would be the origin of fissure formation.[69] Le Gigan et al. observed that crack would grow faster if a hotspot were present.[70] However, crack opening, i.e. the transformation from a fissure to an open crack is not discussed by both studies explicitly:

Hypothesis 3.4: Hotspots are required for crack opening.

Consequently, the location of hotspots is predicted to define the location of crack opening zones. If multiple cracks opened up at location where no hotspot was present before, hypothesis 3.4 would be falsified.

3.4 Influence of Cooling Channel Design

During pre-test (cf. subchapter 4.4), DTV has been observed. The order of the identified DTV matches the number of cooling channel pins in circumferential direction of the examined brake disc (cf. subchapter 4.2). This effect has not been discussed yet, neither its influence on the formation and propagation of heat cracks. Based on this observation, explorative assumptions are made.

3.4.1 Extrusions by Cooling Channel Pins

Since the DTV order matches the order of the cooling channel pins, it is assumed that they cause extrusions on the friction surface. Extrusions have been observed to rise after cool-down. On the one hand, temperature variation inside the friction ring due to heat transfer into the cooling channel pins might cause thermal expansion of the friction ring:

Assumption 4.1: Cooling channel pins cause an inhomogeneous temperature distribution on friction surface during the entire braking and cool-down period, which causes disc thickness variations due to thermal expansion.

In this case, it is **predicted** that a temperature amplitude of the order corresponding to the order of cooling channel pins is present during braking and cool-down that follows DTV of the respective order, i.e. when temperature amplitude rises, DTV amplitude rises and vice versa. If temperature amplitudes of the order corresponding to the order of cooling channel pins monotonically fell during cool-down, assumption 4.1 would be falsified, as DTV amplitudes rise during cool-down.

---

[69] Brezolin, A.: Dissertation, Estudo de Geração de Trincas Térmicas (2007).

[70] Le Gigan, G. et al.: Disc brakes for heavy vehicles (2015).

On the other hand, structure-mechanical effects could cause this extrusion. In case assumption 4.1 is falsified, the following assumption remains:

Assumption 4.2: Due to structure-mechanical effects, cooling channel pins cause extrusions on the friction surfaces during the cool-down period after each heat crack cycle.

Accordingly, it is **predicted** that rising DTV corresponding to the respective cooling channel pin order can be observed during each cool-down period. Otherwise, assumption 4.2 would be falsified as well.

3.4.2 Stress Increase by Extrusion

If assumption 4.1 was falsified and assumption 4.2 held true, extrusions on the friction surface would not be caused by thermal expansion but rather by stresses. Accordingly, shear stresses would rise in between the extrusions:

Assumption 4.3: Cooling channel pin extrusion causes shear stresses on the friction ring surface.

Consequently, it is **predicted** that the maximum effective stress level should occur in between cooling channel pins on the friction ring surface. As stresses cannot be measured with the experimental setup used in this work while the test is running, the FE-Model is used for evaluation of assumption 4.3. If no local effective stress maxima are present in between cooling channel pins, this would contradict assumption 4.3.

3.4.3 Crack Guiding

If assumption 4.2 and assumption 4.3 held true, structure-mechanical effects would cause stresses on the friction surface. Continuing this thought, this might influence crack paths, as shear stresses in between the cooling channel pin extrusions increase effective stress level in between them:

Assumption 4.4: Cracks are guided by cooling channel pins and therefore grow in between them.

In this case, it is **predicted** that cracks would grow faster through radially aligned cooling channel pins in comparison to radially staggered pins, as they could grow straight instead of growing staggered. If cracks grew equivalently fast or faster in areas where pins are radially staggered in comparison to areas where pins are aligned, hypothesis 4.4 would be falsified.

3.4.4 Asymmetric Extrusion

Brake discs observed in this work connected asymmetrically to the brake discs neck, i.e. only the HS is connected to the neck. This type of brake disc shows generally more crack

growth on the HS compared to the PS. If crack growth was also influenced by cooling channel pin extrusions (assumption 4.4) and extrusions were caused by structure-mechanical effects (assumption 4.2), asymmetric neck connection might cause asymmetric pin extrusion as well:

Assumption 4.5: Due to structure-mechanical effects, cooling channel pins cause stronger extrusions on the HS compared to the PS.

Accordingly, it is **predicted** that amplitudes of the extrusion caused by cooling channel pins are generally higher on the HS in comparison to the PS. Assumption 4.5 counts as falsified, if the amplitude of the extrusion caused by cooling channel pins after a heat crack cycle is higher on the PS compared to the HS.

3.4.5 Softening of the Friction Ring

If cooling channel pin extrusions are caused by structure-mechanical effects and amplitudes vary between braking and cool-down in each heat crack cycle, friction surface might be affected by cyclic damage. In case the brake disc material softens under cyclic loading as observed for similar materials,[71] softening of the friction ring might be the result:

Assumption 4.6: Cyclic cooling channel pin extrusions cause softening in the friction ring.

Accordingly, it is **predicted** that DTV amplitudes vary cyclic with each heat crack cycle and the material softens under cyclic loading. If the material hardened under cyclic loading in low cycle fatigue tests or DTV amplitudes did not vary cyclically during the heat crack test, assumption 4.6 would be falsified.

3.5 Influence of Disc Coning and Hotbands

Coning is only discussed in connection with residual stresses from the casting process. Its direct effect on heat crack formation is still unclear. Consequently, it will be evaluated how disc surface temperature and crack formation are influenced by coning. Since one-hotband and two-hotband cases alternate during the heat crack test in connection with the coning, hypotheses dealing with hotbands are formulated accordingly.

[71] Pevec, M. et al.: Elevated temperature low cycle fatigue (2014).

3.5.1 Stress Concentration by Hotbands

Le Gigan et al. stated that hotbands accelerate crack growth.[72] However, it was not stated explicitly that they would cause a stress concentration at the hotband radius after cool-down. For evaluation, the following hypothesis is formulated:

Hypothesis 5.1: Highest stresses occur at the location of the hotband after cool-down.

Hotbands generally show up in one- and two-hotband cases. It is **predicted** for the two-hotband case that highest stresses after cool-down would be present at radial inner and outer position. As stresses cannot be measured with the experimental setup (cf. subchapter 4.1), only indication for contradiction against the hypothesis is evaluated using the FE model (cf. chapter 6). If highest stresses occur at radial centre position after cool-down of a braking with a two-hotband case, this will contradict hypothesis 5.1.

3.5.2 Influence on Coning

During the pre-test, alternation of maximum coning amplitude has been observed. It appears to alternate in the same manner as the one- and two-hotband cases alternate. Accordingly, it is assumed that coning amplitude is affected by hotband formation:

Assumption 5.2: Due to thermal expansion, formation of a single hotband on the HS amplifies coning, formation of a single hotband on the PS reduces coning.

Accordingly, it is **predicted** that coning is generally higher in cycles where one hotband forms on the HS compared to cycles, where two hotbands form on the HS. If coning is higher during the majority of cycles where two hotbands form on the HS, assumption 5.2 would be falsified.

3.5.3 Influence of Coning

A higher coning amplitude results in a stronger skewing of the brake disc. Assumedly, this results in a less uniform surface pressure distribution and finally in a stress concentration. This might also accelerate crack growth:

Assumption 5.3: Discs showing high coning amplitudes fail earlier in the heat crack test.

Consequently, it is **predicted** that the higher the average coning is during a heat crack test, the lower is the number of cycles until occurrence of a through-thickness crack in the respective test, as coning amplitude varies strongly during the test and therefore cannot be compared to crack growth rates in each cycle directly. If one brake disc, which shows higher

[72] Le Gigan, G. et al.: Disc brakes for heavy vehicles (2015).

average coning compared to another brake disc, endures more cycles in the heat crack test compared to the latter brake disc, this will contradict assumption 5.3.

3.6 Influence of SRO

Recent studies have discussed the influence of SRO on the formation of hotspots.[73] The same accounts partly for the influence of hotspots on heat crack formation.[74] However, influence of SRO on crack propagation has not been evaluated yet. Furthermore, the interaction between these effects has not been discussed in depth. So, the following hypotheses and assumptions are formulated:

3.6.1 Formation of Hotspots

According to Sarda[75], hotspots originate from SRO due to locally enforced friction. To evaluate this hypothesis, it is re-formulated:

Hypothesis 6.1: Convex SRO in hot state determines hotspot positions.

Accordingly, it is **predicted** that hotspot positions and positions of convex SRO in hot state match during the entire test. If hotspots formed at positions where no convex SRO in hot state is present or vice versa, hypothesis 6.1 would be falsified.

If hotspots originate from SRO, not only SRO in hot state but also SRO in cold state should determine hotspot positions. Continuing this thought, SRO in hot state should form out of SRO in cold state:

Hypothesis 6.2: SRO in hot state is an amplification of SRO in cold state.

Consequently, it is **predicted** that SRO in hot and cold state match. If coherence between them is low or phase of dominant order differs, hypothesis 6.2 would be falsified.

3.6.2 Influence of SRO on Crack Growth

As described above, influence of hotspots on crack growth and influence of SRO on hotspots has been evaluated in previous studies. Still, a direct influence of SRO on crack growth has

[73] Sardá, A.: Dissertation, Wirkungskette der Entstehung von Hotspots (2009).

[74] Le Gigan, G. et al.: Disc brakes for heavy vehicles (2015).

[75] Sardá, A.: Dissertation, Wirkungskette der Entstehung von Hotspots (2009).

not been found yet. If hotspots form in zones of convex[76] SRO in hot state and hotspots accelerate crack growth, convex SRO might accelerate crack growth as well:

Hypothesis 6.3: Local convex SRO in hot state accelerates crack growth.

Accordingly, it is **predicted** that longest cracks propagate in zones of convex SRO in hot state. If longest cracks were present in zones of concave SRO or zones of neutral SRO, hypothesis 6.3 would be falsified.

Furthermore, as locally enforced friction is assumed for zones of rising, convex SRO,[77] cracks might preferably grow on these positive slopes as well, which specifies hypothesis 6.3 more precisely:

Hypothesis 6.4: Longest cracks propagate preferably in zones of convex SRO in hot state on positive slopes.

If hypothesis 6.4 held true, if longest cracks would be found in zones of convex SRO in hot state on positive slopes. Otherwise, hypothesis 6.4 would falsified, if longest cracks were found in zones of concave SRO.

Continuing this thought, concave SRO might inhibit crack formation, as the friction surface is arched inwards and therefore might suffer from less friction from the brake pad. Furthermore, as no hotspots are assumed to form in these areas (hypothesis 6.1) and hotspots might be responsible for crack opening (hypothesis 3.4), it is **predicted** that crack opening might not happen at all in zones of concave SRO in hot state:

Assumption 6.5: Concave SRO in hot state inhibits crack opening.

Assumption 6.5 would be falsified, if cracks opened up in zones of concave SRO in hot state.

If assumption 6.5 was falsified, crack might still open up in zones of concave SRO in hot state. Nevertheless, they might still be inhibited from growing strongly:

Assumption 6.6: Concave SRO in hot state reduces crack growth.

Accordingly, it is **predicted** that less crack grow occurs in zones of concave, SRO in hot state in comparison to zones of convex, SRO in hot state. Assumption 6.6 would count as falsified, if less crack growth occurred in zones of convex, SRO in hot state in comparison to zones of concave, SRO in hot state.

---

[76] Convex refers to the brake disc's friction surface being arched outwards (e.g. a dent), concave refers to the brake disc surface being arched inwards (e.g. a hole).

[77] Sardá, A.: Dissertation, Wirkungskette der Entstehung von Hotspots (2009).

3.6.3 Evolution of SRO

Here, several considerations regarding the bending stiffness of the friction ring and its influence on SRO are made. Assuming a constant bending force, probably induced by asymmetrical hotspot distribution[78] or inaccuracies from manufacturing,[79] a lower circumferential bending stiffness would cause higher SRO amplitudes. Based on this, several assumptions are formulated, which consider influences on the bending stiffness of the friction ring. Firstly, it is known that GJL materials similar to the material used for the brake discs used in this work softens[80] due to damage under cyclic loading:

Assumption 6.7: As the brake disc gets softer, SRO amplitudes amplify in the course of the test.

Consequently, it is **predicted** that SRO amplitudes monotonically rise in the course of the test, as the load situation remains steady. If SRO amplitudes decreased in the course of the test, hypothesis 6.7 would count as falsified.

Besides softening, several other influences might degrade bending stiffness of the friction ring. As through-thickness cracks grow deeply inside the friction ring and by definition reach at least at one position from the friction surface to the cooling channel, they might also degrade bending stiffness:

Assumption 6.8: Through-thickness cracks decrease bending stiffness of the friction ring.

Accordingly, it is **predicted** that the amplitude of convex SRO in hot state rises monotonically on the location of the through-thickness crack at the end of the test. If no convex SRO was present at the position of the through-thickness crack at the end of the test, hypothesis 6.8 would be falsified.

Finally, cooling channel layout might influence bending stiffness as well, as the second moment of area is theoretically changed by arranging pins with more or less spacing. A higher circumferential pin density increases circumferential bending stiffness. Consequently, SRO order might be influenced as well, if a periodic variation of the bending stiffness around the circumference by periodic variation of the circumferential pin spacing is present:

Assumption 6.9: A periodic variation of the circumferential cooling channel pin spacing inhibits formation of SRO in hot state.

Consequently, it is **predicted** that a brake disc designed with periodically varying circumferential pin spacing with an order that does not match the common order of the brake disc design with constant pin spacing, shows a different order of harmonic SRO compared to the

[78] Sardá, A.: Dissertation, Wirkungskette der Entstehung von Hotspots (2009).

[79] Könning, M.: Dissertation, Simulation von Heißrubbeln im Gesamtbremssystem (2017).

[80] Pevec, M. et al.: Elevated temperature low cycle fatigue (2014).

common order. If two discs that only vary in pin spacing showed the same order of harmonic SRO, assumption 6.9 would be falsified.

4 Methodological Approach

In order to analyse the formation of heat cracks in brake discs for heavy-duty vehicles, a profound methodological approach is required. This arises from the research objectives stated before, evaluating the influence of disc deformation, design, and thermal effects on cracking and the process of heat crack formation itself. Consequently, dynamometer experiments are combined with material investigations as well as numerical studies. By combination of these different methods, they complement one another.

4.1 Experimental Setup at the Dynamometer

As described before, an experimental setup is required that is suitable for the evaluation of quantities related to disc deformation, disc temperatures and cracks on the disc's friction surface.

4.1.1 General Definitions

In order to compare experimental data from different instruments with each other, all quantities are evaluated in a disc-fixed cylinder coordinate system r, φ, z. r is oriented in radial direction of the disc, φ equals the revolution angle and is oriented in rotation direction of the disc. The z-axis is pointing towards the hat side of the disc from the disc centre. The disc rotates in negative φ-direction, so the coordinate system is left handed and oriented fixed on the disc. As the disc rotates continuously, φ is defined as the current twist between the brake disc and the dynamometer and determined based on the unwrapped, total revolution angle:

$$\varphi = \mathrm{mod}\left(\varphi_{\mathrm{unwrap}}, 2\pi\right) \tag{4.1}$$

Accordingly, current revolution n within the heat crack cycle N is calculated by ceiling the total revolution angle divided by 2π:

$$n = \left\lceil \frac{\varphi_{\mathrm{unwrap}}}{2\pi} \right\rceil \tag{4.2}$$

With the start of a new brake actuation, i.e. increment of N, n is reset to 1 in order to compare different heat crack cycles with each other. For the coordinate tuple (r, φ, n, N), an abbreviation is used:

$$\boldsymbol{\xi} = (r, \varphi, n, N) \tag{4.3}$$

Some quantities are evaluated at fixed radial positions, inner radius of the friction ring $r_{\mathrm{i}} = 138.5$ mm, centre radius of the friction ring $r_{\mathrm{c}} = 172$ mm, and outer radius of the friction ring $r_{\mathrm{o}} = 205.5$ mm. The friction ring width is 85 mm. Accordingly, abbreviations are used:

$$\boldsymbol{\xi}_{\mathrm{i/c/o}} = \left(r_{\mathrm{i/c/o}}, \varphi, n, N\right) \tag{4.4}$$

For simplification, the displacement of the friction ring surfaces is evaluated relatively to the inertial displacement at the beginning of the heat crack test. With the initial thickness d_0 of the brake disc at the beginning of the test, the displacement of the hat side $z_{\mathrm{H}}(\boldsymbol{\xi}_{\mathrm{i/c/o}})$ and piston side $z_{\mathrm{P}}(\boldsymbol{\xi}_{\mathrm{i/c/o}})$ is defined:

$$z_{\mathrm{H}}(\boldsymbol{\xi}_{\mathrm{i/c/o}}) = z\left(\boldsymbol{\xi}_{\mathrm{i/c/o}}\right) - \frac{d_0}{2}, \tag{4.5}$$

$$z_{\mathrm{P}}(\boldsymbol{\xi}_{\mathrm{i/c/o}}) = z\left(\boldsymbol{\xi}_{\mathrm{i/c/o}}\right) + \frac{d_0}{2}, \tag{4.6}$$

with $z_{\mathrm{P}} < z_{\mathrm{H}}$. An overview of the coordinate system and the sensor positions is given in Figure 4-1.

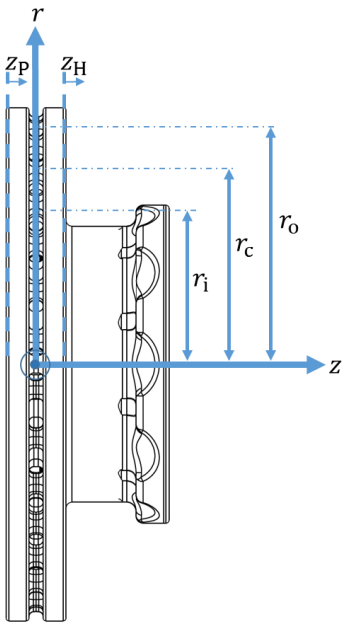

Figure 4-1: Coordinate system and sensor positions

4.1.2 Measurement of Disc Deformation

Considering disc deformation related quantities, disc coning as well as SRO and DTV have to be monitored during the entire heat crack test. This requires a sensor setup that is capable of capturing the deflection of both friction ring surfaces for hat and piston side simultaneously at different radial positions. In general, optical and capacitive sensor systems are used to capture disc deformation on the dynamometer. Optical systems were used, for example, by Okamura[81] by application of two high-speed laser profilometers on HS and PS. High-

[81] Okamura, T.: Interactive Effects of Thermal Deformation (2016).

speed laser profilometers capture the deflection of the friction surface in line mode. In contrast to this, capacitive sensor system, which were used for example by Sardá,[82] capture deflection only at one radial point per sensor simultaneously. Hence, the radial resolution of laser profilometers is higher compared to capacitive sensors. Nevertheless, since evaluation of SRO and DTV is usually done for fixed radii,[83] capacitive sensors are considered sufficient for the present task. For evaluation of average disc coning, sensors at two different radial positions are sufficient as well. Moreover, optical systems might be distorted by the varying reflectivity caused by the relatively strong brake pad abrasion on the friction surface during the heat crack test.

Consequently, a capacitive sensor setup is chosen. It consists of three sensor pairs, capturing the deflection of HS and PS simultaneously at three different radial positions, at inner, centre, and outer radius of the friction surface. Three radii have been chosen, since hotbands usually occur either on radial centre position, or simultaneously at radial inner and outer position, i.e. on three possible radii.[84] This allows for comparison of SRO/DTV with thermal influences. For additional evaluation, another capacitive sensor detects deflections of the friction ring in radial direction, i.e. monitors changes in the disc's diameter. The sensors run at a sampling rate of 10 kHz, which results in a resolution of roughly 1400 samples per revolution. This discretisation equals around 1 mm on the circumference and is therefore sufficient for the detection of geometry induced surface topology distortions, since the smallest geometric elements of the brake disc are cooling channel pins with a diameter of at least 12 mm. The resolution of the capacitive sensors is 200 nm on a measurement range of ± 2 mm. Active measuring area is a circle with a diameter of 7.9 mm.

For further evaluation, disc displacement at the friction ring surface is defined as $z_{\mathrm{H/P}}(\boldsymbol{\xi}_{\mathrm{i/c/o}})$ for HS and PS. By addition or subtraction, SRO $\Sigma z(\boldsymbol{\xi}_{\mathrm{i/c/o}})$ and disc thickness (DT) $\Delta z(\boldsymbol{\xi}_{\mathrm{i/c/o}})$ is calculated:

$$\Delta z(\boldsymbol{\xi}_{\mathrm{i/c/o}}) = z_{\mathrm{H}}(\boldsymbol{\xi}_{\mathrm{i/c/o}}) - z_{\mathrm{P}}(\boldsymbol{\xi}_{\mathrm{i/c/o}}) \tag{4.7}$$

$$\Sigma z(\boldsymbol{\xi}_{\mathrm{i/c/o}}) = \frac{z_{\mathrm{H}}(\boldsymbol{\xi}_{\mathrm{i/c/o}}) + z_{\mathrm{P}}(\boldsymbol{\xi}_{\mathrm{i/c/o}})}{2} \tag{4.8}$$

Coning is calculated as mentioned by reading out sensors at radial inner and outer position:

$$s(N) = \max_{n}\left(\overline{z_{r_{\mathrm{o}},\mathrm{H}}(n,N)} - \overline{z_{r_{\mathrm{i}},\mathrm{H}}(n,N)}\right) - \min_{n}\left(\overline{z_{r_{\mathrm{o}},\mathrm{H}}(n,N)} - \overline{z_{r_{\mathrm{i}},\mathrm{H}}(n,N)}\right), \tag{4.9}$$

with $\overline{z_{r_{\mathrm{i/o}},\mathrm{H}}(n,N)}$ being the average displacement of the HS in respect of φ at radial inner/outer position. Since coning in cold state of the respective cycle is subtracted from the maximum coning value, coning is defined as skewing during one braking cycle here. An

[82] Sardá, A.: Dissertation, Wirkungskette der Entstehung von Hotspots (2009), p. 43.

[83] Okamura, T.: Interactive Effects of Thermal Deformation (2016).

[84] Le Gigan, G. et al.: Disc brakes for heavy vehicles (2015).

alternative method for calculating coning, which takes both friction ring sides into account is described in appendix A.1.1.

4.1.3 Measurement of Friction Surface Temperature

Primary requirements for the thermal measurement setup are the ability to detect hotspots and hotbands, as well as the measurement of the maximum disc surface temperatures during braking and cool down for both HS and PS. Consequently, the measurement of the entire friction surface temperature has to be validated regarding accuracy and precision of the measurement. A thermographic camera is used, measuring temperatures on both friction surfaces simultaneously using a mirror system as it has been used by several authors before.[85,86] Contrary to the cited authors, both friction surfaces are monitored through mirrors. The camera runs in line mode and scans 320 temperature points in radial direction at once. The line rate is synchronised to the rotation of the dynamometer, maintaining a line rate of 1024 samples per revolution. Recording starts with the beginning of each braking cycle and lasts for 60 seconds (45 seconds in the experiment with the *Reference* disc), 20 seconds (5 seconds) longer than the actual braking period. The camera generates a thermographic image for HS and PS for each revolution n in polar coordinates $T(\boldsymbol{\xi})$ with a resolution of around 64 pixels in radial direction and 1024 pixels in angular direct. The calibration of the thermographic camera is valid in the range between 350 °C and 700 °C, which roughly covers the temperature distribution on the friction surface at the end of each braking period (cf. chapter 5). Nonetheless, higher temperatures up to 800 °C are still measured.

The results of the thermographic camera measurement depend on the emissivity of the friction surface and the reflectance of the mirrors. Emissivity on the friction surface might change due to oxidisation or the accumulation of brake pad abrasion. Similarly, the mirrors get usually slightly covered with brake dust in the course of the heat crack test, which might reduce their reflectance. However, accurate readings are required for the evaluation of temperature dependent microstructural transformations.

In order to calibrate the thermographic camera measurement, a pyrometer and two sliding thermocouples are used. The pyrometer measures temperature on a fixed radius, quickly reacting on temperature gradients. It monitors the brake disc directly, i.e. not trough a mirror, and operates in a wavelength range that is less emissivity dependent in comparison to the thermographic camera. Nevertheless, the temperature level measured by the pyrometer is still dependent on emissivity of the friction surface. For that reason, two sliding thermocouples are used as well, which measure an average temperature $\bar{T}_{\mathrm{H/P}}(\boldsymbol{\xi}_{\mathrm{c}})$ on a fixed radius r_{c} on HS and PS, which equals the centre position of the displacement sensors. The measurement of a thermocouple does not depend on emissivity. However, it flattens the temperature

[85] Sardá, A.: Dissertation, Wirkungskette der Entstehung von Hotspots (2009).

[86] Le Gigan, G. et al.: Disc brakes for heavy vehicles (2015).

profile since it is not able to quickly react to steep temperature gradients due to its own thermal capacity. Nonetheless, it provides the most accurate, stationary friction surface temperature. This makes it exceptionally feasible for tracking the friction surface temperature during cool down, when the entire friction surface maintains an even temperature distribution.

Figure 4-2 shows the comparison of the temperature readings acquired by thermographic camera, the pyrometer and the thermocouples. While the stationary temperature of the pyrometer matches the temperature of the thermocouples quite well, the thermographic camera tends to underestimate high temperatures and overestimate low temperatures. However, no dependency of the accuracy of the camera from the heat crack cycle N is found, which indicates that a possible coverage of the mirrors with brake dust does not influence measurement accuracy in the course of the test.

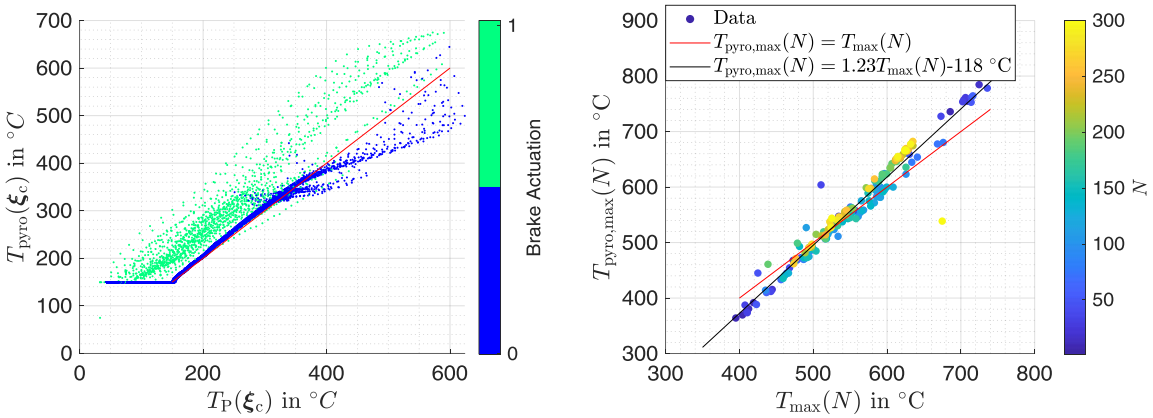

Figure 4-2: Comparison of temperature readings, pyrometer vs. thermocouples (left) and pyrometer vs. thermographic camera (right), showing the straight line of best fit between readings of pyrometer and camera including the equation of the line of best fit

4.1.4 Observation of Crack Growth

In earlier studies, crack growth was not evaluated for all cracks in each heat crack cycle. In fact, crack lengths were recorded by manual inspection in intervals of numerous heat crack cycles, usually 50 to 100. For that reason, an eddy-current heat crack detector has been developed by Wiegemann et al.[87] It scans the entire friction surface for heat cracks at the end of the cool-down period of each heat crack cycle. In order to do that, eddy-current-differential-probes scan both HS and PS simultaneously in rings, differing in the radius by 1.5 mm each. This way, crack lengths of all cracks can be recorded for the first time systematically in each of the heat crack cycles with a radial resolution of 1.5 mm. The angular number of samples is $2 \cdot 10^4$ for each of the rings. Manual estimation of accuracy of the crack detector

[87] Wiegemann, S.-E. et al.: Automatic Heat Crack Detection (2016).

showed that cracks are measured too short occasionally, resulting in a measurement deviation between 0 mm and -3 mm. A minimum crack length of roughly 3 mm is required in order to be detected by the heat crack detector. Consequently, crack growth rates of all cracks ($\frac{\mathrm{d}l}{\mathrm{d}N}(\varphi, N)$) are calculated dependent on the heat crack cycle number N. For the first time, this allows for direct comparison of the spatio-temporal distribution of crack growth with deformation and thermal quantities as well as tracking of the length of single cracks.

In conclusion, all measured quantities are available for evaluation at least once per heat crack cycle. Moreover, temperature distribution is available during the entire braking period as well as for the beginning of the cool down period. Surface topology is available throughout the entire heat crack test, the same accounts for the temperature readings of the thermocouples and the pyrometer. The experimental setup is summarised in Table 4-1.

Table 4-1: Overview of the experimental setup

Quantity	Symbol	Instrument	Coverage	Measurement period	Measurement Range
Crack length	$l(\varphi, N)$	Crack detector	All cracks, entire friction surface	End of each cool-down	$l \geq 3$ mm
Surface topology	$z_{\mathrm{H/P}}(\boldsymbol{\xi}_{\mathrm{i/c/o}})$	Capacitive sensors	3 radii on HS/PS each	Permanent during the test	$-2\ \mathrm{mm} \leq z_{\mathrm{H/P}} \leq 2\ \mathrm{mm}$
Temperature distribution	$T(\boldsymbol{\xi})$	Thermographic camera	Entire friction surface	Permanent during braking, 5-20 s during cool-down	$350\ °\mathrm{C} \leq T(\boldsymbol{\xi}) \leq 750\ °\mathrm{C}$
Temperature	$T_{\mathrm{pyro}}(\boldsymbol{\xi}_{\mathrm{c}})$	Pyrometer	Fixed radius on PS	Permanent during the test	$150\ °\mathrm{C} \leq T_{\mathrm{pyro}}(\boldsymbol{\xi}_{\mathrm{c}}) \leq 900\ °\mathrm{C}$
Temperature	$T_{\mathrm{H/P}}(\boldsymbol{\xi}_{\mathrm{c}})$	Thermocouples	Fixed radius on HS/PS	Permanent during the test	$-260\ °\mathrm{C} \leq T_{\mathrm{H/P}}(\boldsymbol{\xi}_{\mathrm{c}}) \leq 1370\ °\mathrm{C}$

4.2 Experiments on the Dynamometer

The experiments conducted in this work are designed to check the hypotheses and cover the research objectives formulated before. These are grouped into the influence of disc geometry, thermal and deformation phenomena. For that reason, influence of brake pad and brake disc material is minimised by maintaining the same pad material and disc alloy throughout the series of experiments. Since brake pads are sintered and brake discs are casted, variation of the properties is still inevitable. Consequently, properties of all test specimens are evaluated before the test.

In order to test the experimental setup and to identify phenomena that have not been described by earlier studies for further observation in subsequent experiments, a pre-test is carried out. Some of the assumptions formulated in chapter 3 are based on the observations made in this preliminary investigation. During the subsequent series of experiments, the brake disc is geometrically varied based on a commonly used brake disc considered as reference. The variations cover the friction surface and the cooling channel. Since these geometric variations force changes in the thermal and deformation behaviour of the brake disc as well, all hypotheses and research objectives are covered by the series of experiments discussed in this chapter.

All dynamometer experiments are carried out on a full-scale dynamometer at Knorr-Bremse SfN GmbH. Generally, the brake system of Knorr-Bremse type SN7 is used in connection with series brake pads of type Ferodo 4550, only the brake disc is varied in between the experiments. The compressibility of the brake pads is measured before the test according to ISO 6310[88] with a test load of 5 MPa on one half of the brake pad's friction surface and is given in µm.

4.2.1 Test Procedure of the Heat Crack Test

The test procedure for all dynamometer experiments described here follows the general heat crack test of Knorr-Bremse for brake discs designed for wheels with 22.5" rim diameter. In order to pass the test, 500 consecutive heat crack cycles have to be completed. Occurrence of a through-thickness crack terminates the test. Each cycle consists of a 40 s drag braking with a constant brake torque of 2800 Nm at 428 rpm, which refers to a drag braking at 85 km/h. Torque is measured and controlled by the dynamometer with a torque bar. Revolution speed is kept constant during the subsequent cool-down period, which lasts around 20 minutes (cf. chapter 5). The subsequent heat crack cycle is started when the condition $\bar{T}_{\mathrm{H/P}}(\boldsymbol{\xi}_{\mathrm{c}}) \leq 50$ °C is met. During cool-down, the brake disc is actively cooled by air on the test bench with an air speed of $9\,\frac{\mathrm{m}}{\mathrm{s}}$ and an air flow of $1.69\,\frac{\mathrm{m}^3}{\mathrm{s}}$. During braking, the cooling air flow is reduced to $0.5\ \frac{\mathrm{m}^3}{\mathrm{s}}$. Before the actual heat crack test starts, a bedding program is applied, consisting of stop brakings starting from 60 km/h with rising brake pressures by 1 bar each up to 9 bar.

4.2.2 Preliminary Investigation

The preliminary investigation, i.e. the pre-test is carried out with reduced experimental instrumentation regarding simultaneous operation of the instruments. A similar brake system

[88] ISO: 6310 Compressive strain test methods (2009).

of a different manufacturer is used, and 150 heat crack cycles are observed. Results are discussed in the next chapter.

4.2.3 Reference Brake Disc ("*Reference*")

A complete heat crack test is carried out with a brake disc for the Knorr-Bremse brake system SN7, which acts as reference for the subsequent experiments, hereinafter referred to as *Reference* disc. Additionally, most material experiments are conducted with the *Reference* brake disc in order to model the brake disc numerically (cf. chapter 6). For the material characterisation, an identical brake disc, which has been produced in the same batch, is used as well for identification of the characteristics before the test.

The brake disc is a ventilated hat brake disc for the rear axle of the tractor unit of a 40-ton truck with pins connecting both friction rings. Other connection types, e.g. vanes are not considered in the experiments. It is made from high carbon cast iron with a tensile strength greater than 180 MPa. The outer diameter of the brake disc is 430 mm and the weight is roughly 33 kg. The layout of the cooling channel pins is drawn in Figure 4-3. Pins are arranged in four rows with 30 pins on the circumference each, with even and odd rows ordered staggered. Thickness of both friction rings is 16.5 mm each, $z_{\mathrm{H}} - z_{\mathrm{P}} = 45\ \mathrm{mm}$.

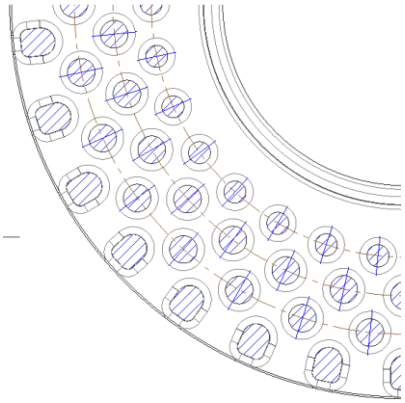

Figure 4-3: Layout of the cooling channel of the *Reference* brake disc

300 heat crack cycles have been achieved with the *Reference* brake disc when a through-thickness crack terminated the test. Tensile strength of the brake disc was 241 MPa and compressibility of the brake pads was 109 µm before the test started.

4.2.4 Brake Disc with Variably Arranged Cooling Channel Pins ("*Variable*")

For determination of the influence of the cooling channel design on the heat crack propagation, as well as on thermal and deformation behaviour of the brake disc, a brake disc with variably arranged cooling channel pins is tested, hereinafter referenced as *Variable* disc. The

number of pins on the circumference increases in each of the four rows with increasing radius: 28 pins on the inner row, 29 pins on the central inner row, 30 pins on the central outer row and finally 31 pins on the outer row (cf. Figure 4-4). This way, all possible combinations of cooling channel pin arrangements are tested on a single brake disc, starting from radially aligned pins via slightly intersecting pins towards staggered pins and back to aligned pins. A practical aim of the test is to determine the optimal cooling channel pin arrangement. The design of the *Variable* disc has become the fundament of a patent application. The heat crack test with the *Variable* brake disc ended after 500 heat crack cycles with a through-thickness crack. Tensile strength of the brake disc was 216 MPa and compressibility of the brake pads was 105 µm before the test started.

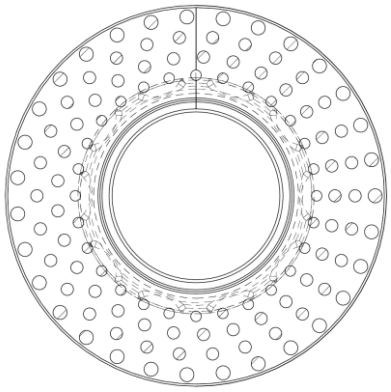

Figure 4-4: Cooling channel layout of the "*Variable*" brake disc

4.2.5 Brake Discs with Optimised Cooling Channel ("*Constant*" and "*Periodic*")

Based on the results of the heat crack test with the *Variable* brake disc (cf. subchapter 5.3), two additional cooling channel designs have been created. The design of these brake discs has become the fundament of a patent application as well. The cooling channel pins are arranged slightly intersecting in radial direction in a way that any radial line intersects with at least one cooling channel pin (Figure 4-5). The number of cooling channel pins in circumferential direction is constantly 30. The aim of the cooling channel design with slightly intersecting pins is to slow down a crack as it reaches the projected pin edge on the friction surface (cf. hypotheses in 3.4).

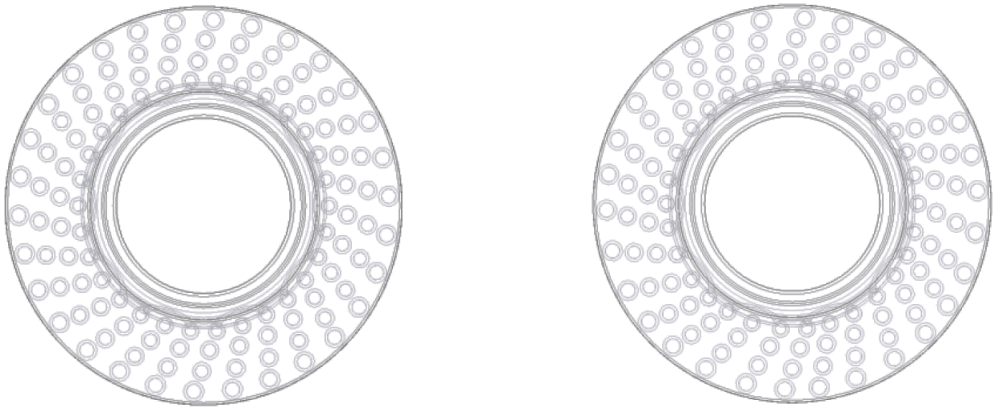

Figure 4-5: Cooling channel layout of the *Constant* brake disc (left) and the *Periodic* brake disc (right)

The design of the optimised disc exists in two variations: without a periodical variation of the angular cooling channel pin spaces ("*Constant*", Figure 4-5 left) and with variation ("*Periodic*", Figure 4-5 right). According to the hypotheses formulated in subchapter 3.4, the periodical variation should influence the formation of SRO, because it is assumed to influence the angular warping stiffness. The order of the periodic variation is chosen to seven, since the *Reference* brake disc and their derivatives are known to develop six hotpots respectively SRO of order six in the heat crack test. Hence, the predetermined periodic variation with the order of seven should interfere with the "natural" order of six and therefore reduce amplitudes of SRO and hotspots.

The heat crack test with the *Constant* (*Periodic*) brake disc ended after 500 (460) heat crack cycles with a through-thickness crack. Tensile strength of the brake disc was 266 MPa (266 MPa) and compressibility of the brake pads was 99 µm (114 µm) before the test started. Both "optimised" brake discs were casted from the same ladle.

An overview of the conducted heat crack test experiments is given in Table 4-2.

Table 4-2: Overview of the dynamometer experiments

Brake disc	Tensile strength in MPa	Pad Compressibility in µm	$N_{\max}$	Aim of the test
Reference	241	109	300	Reference
Variable	216	105	500	Optimal pin arrangement
Constant	266	99	500	Optimal pin arrangement
Periodic	266	114	460	Influence of periodic pin spacing

4.3 Material Experiments with the Probed Brake Discs

Material experiments are carried out for two reasons: first, they complement the experiments on the dynamometer and therefore make up the causal model or simply fill knowledge gaps that cannot be considered through dynamometer experiments. Second, they are required to identify the parameters for accurate modelling of the brake disc numerically. For that reason, material characteristics as well as deformation behaviour is evaluated with a *Twin* of the *Reference* disc, i.e. a disc that has been casted simultaneously from the same ladle, hereinafter referred to as *Twin* disc. Cyclic LCF tests simulate the loadings during the heat crack test. They serve for both modelling and explaining the behaviour of the GJL alloy during the heat crack test. Specimens out of the *Twin* disc are used for material characterisation for modelling. Microstructural analyses are carried out in order to deal with the hypotheses formulated in 3.2. Finally, the analysis of residual stresses serves for comparison of the stress state of the disc before and after the heat crack test.

4.3.1 Cyclic LCF Tests

Cyclic LCF tests are carried out on specimens cut out of the *Twin* disc, which has been casted from the same ladle as the *Reference* brake disc tested on the dynamometer. For that reason, the material behaviour of the *Twin* disc is nearly identical to the *Reference* disc. Hourglass shaped specimens are used and cut out of the friction ring in circumferential orientation to keep the direction of the loading the same in the LCF and the heat crack test. For the reduction of test duration, 10 cycles are applied to the specimens with dwell. The latter cycles are pure LCF without dwell, i.e. triangular load reversals. All LCF tests are strain controlled. The initial dwell cycles are designed to simulate the loadings during the heat crack test (Figure 4-6). To simulate the loading situation during braking, the specimen is compressed and held in maximum compression for approximately 40 seconds. Afterwards, to simulate cool down, the specimen is torn to maximum tension and held for 120 seconds. Then, the cycle starts over by compressing the specimen again. The maximum strain amplitudes are chosen based on a previously conducted tensile test that was run until rupture of the specimen. Accordingly, maximum strain amplitudes are chosen in order to deform the specimen significantly plastically in each of the cycle while maintaining a damage reserve in a way that at least 10 cycles are achievable.

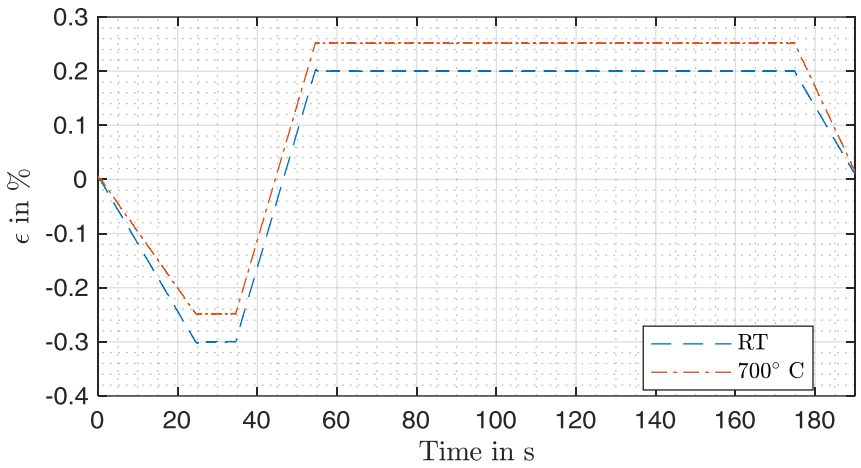

Figure 4-6: Controlled strain during the first part of the cyclic LCF test, with dwell

The test is conducted isothermally at room temperature as well as at 700 °C. 700 °C equals roughly the maximum temperature that is reached in hotspots.[89] Still, 700 °C is lower than the austenizing temperature of 727 °C.

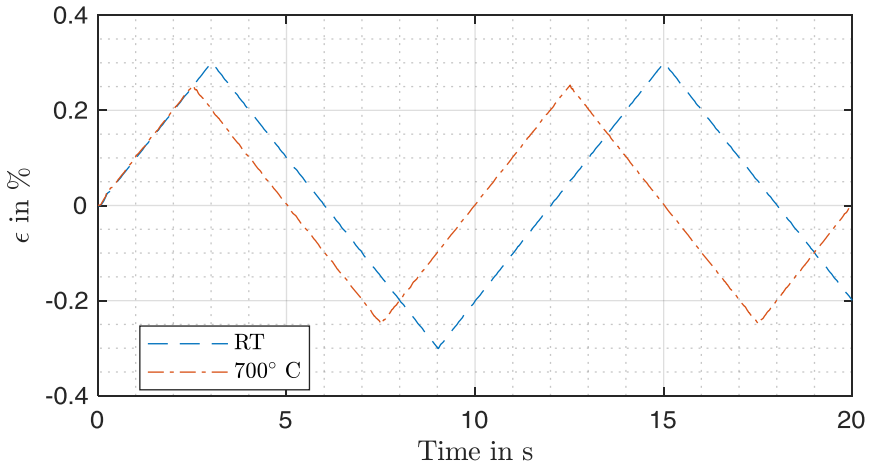

Figure 4-7: Controlled strain during the second part of the cyclic LCF test, pure LCF without dwell

For room temperature, generally higher strain rates are applied, except for the maximum tensile strain amplitudes of the dwell cycles (compare Figure 4-6 and Figure 4-7), since the maximum tensile strength is assumed to be higher at room temperature compared to 700 °C. The pure LCF tests have been similarly conducted for GJL brake disc specimens by Pevec et al.,[90] who did not include dwell in their experiments. Strain rates are constant for both samples at room temperature and 700 °C.

[89] Le Gigan, G. et al.: Disc brakes for heavy vehicles (2015).

[90] Pevec, M. et al.: Elevated temperature low cycle fatigue (2014).

4.3.2 Determination of Material Characteristics

Material characteristics of the *Twin* Disc are evaluated in a series of experiments for the finite element model. Specimens are cut out of the friction ring of the *Twin* disc. Thermal diffusivity is measured using laser flash analysis, specific heat capacity using dynamic difference calorimetry. After identification of the density of the specimens, thermal conductivity is calculated using density, thermal diffusivity and specific heat capacity for room temperature and 700 °C. All experiments are carried out under argon atmosphere.

Thermal expansion is evaluated using thermomechanical analysis. A cylindrical specimen, which has been cut out of the friction ring of the *Twin* disc, is placed a heated surface under argon atmosphere. Subsequently, thermal expansion is continuously evaluated in the temperature range between 20 °C and 770 °C.

In comparison to steel alloys, only few values can be found for GJL in previously published works, for example in the VDI Heat Atlas.[91]

4.3.3 Microstructural Analysis

In order to identify and classify microstructural transformations for evaluation of the hypotheses formulated in 3.2, polished micrographs are made out of specimens that have been cut out of the *Reference* brake disc after the heat crack test. For comparison with the original microstructure, a specimen is cut out of the neck of the brake disc, where temperatures stay low compared to the friction surface during the heat crack test. The remaining specimens are cut out of the friction surface on and off a location where a hotspot formed during the test as well as close to the through-thickness crack. The exact sample taking points are described in section 5.2.4. In order to make the microstructure visible, micrographs are etched. The original microstructure has been determined by the disc manufacturer as pearlitic.

4.3.4 Evaluation of Hardness Increase

Since overheating of the friction surface usually changes the surface hardness, a hardness increase indicates that overheating took place at the respective positions of the friction surface. For that reason, a hardness map of the friction surface is built by indentation measurement. The original surface hardness has been determined by the manufacturer and is used for evaluation of the hardness increase. Since hardness measurements by indentation always indicate the average hardness of the material penetrated by the indenter, two different methods are applied: measurement according to Brinell as well as according to Vickers. For the

[91] Ullrich, C.; Bodmer, T.: Thermophysikalische Stoffwerte (2019).

Brinell method, a relatively high indentation force of 187.5 kilopond[92] (kp) is used in conjunction with a bigger indenter (HBW5/187.5). Surface hardness measurements according to Brinell have also been carried out by the manufacturer for reference. The Vickers method is applied with a much smaller indentation force of 1 kp (HV1) and therefore returns hardness of the surface near layers.

The entire friction surface of the *Reference* brake disc is measured at around 150 measurement positions using the Brinell-method, while the measurement using the Vickers-method is carried out only on a segment where the through-thickness crack occurred, which is also used for the microstructural analysis described in the previous section. Measurement positions are chosen based on the crack and hotspot pattern: positions of hotspots are compared to positions of cracks and positions that have potentially not undergone severe loadings.

4.3.5 Evaluation of Hardness inside the Friction Ring

In order to determine hardness of the microstructure inside the friction ring at various depths, nano indentation tests[93] are made with the specimens used for microstructural analysis of the *Reference* disc (cf. section 4.3.3). Indentation force is set to 20 mN, which results in an intrusion depth of roughly 500 nm[94]. On the one hand, measurement paths going in axial direction inside the friction ring are evaluated, beginning from the friction ring surface with a sampling point at each 30 µm. On the other hand, microstructure is characterised by indentation measurements in different microstructural areas, e.g. on graphite lamellae. This way, microstructural influences on crack formation, e.g. micro-crack formation in brittle areas, are evaluated.

4.3.6 Analysis of Residual Stresses

For identification of the influence of residual stresses, X-ray diffraction measurements are carried out on the *Reference* and the *Variable* brake disc. The *Reference* disc is measured three times: after casting, before the heat crack test and after the heat crack test. The *Variable* disc is measured only once after the heat crack test for validation of the method. Measurement positions are chosen before the test, which makes it impossible to consider the crack or hotspot distribution for determination of ideal measurement positions. Three measurement positions are set on HS and PS each with an angular offset of 100° in between the measure-

[92] For historical reasons the indentation force is given in kiloponds, 1 kp = 9.81 N

[93] DIN: 14577 Instrumentierte Eindringprüfung (2015).

[94] According to DIN EN ISO 14577-1, intrusion depths greater 200 nm are classified as micro hardness. Since measuring process is in accordance with nano indentation, the measurement principle is referenced here as nano indentation.

ment positions. The rather odd offset is chosen since hotspots and other phenomena are usually distributed evenly on the friction surface. Additionally to the three angular measurement positions, two more measurement positions are set next to one of the three positions with radial offset. Residual stresses are directly evaluated on the friction surface, i.e. none of the upper surface layers have been removed before measurement.

4.4 Exemplary results from pre-test

In this subchapter, results from pre-testing the experimental setup are presented. Since the experimental setup presented in the beginning of this chapter has not ever been used before, evaluation techniques are formulated in the subsequent section partially based on the results from pre-testing. Furthermore, phenomena that have been observed during pre-testing for the first time and are not part of the concurrent state of science and technology, contribute to the hypotheses presented in the previous chapter.

Cycles 1 until 155 have been observed with alternating experimental setup. In this subchapter, readings from thermal and deformational observation are presented, since the heat crack detector has been assessed in a previous study[95].

4.4.1 Thermal Observation

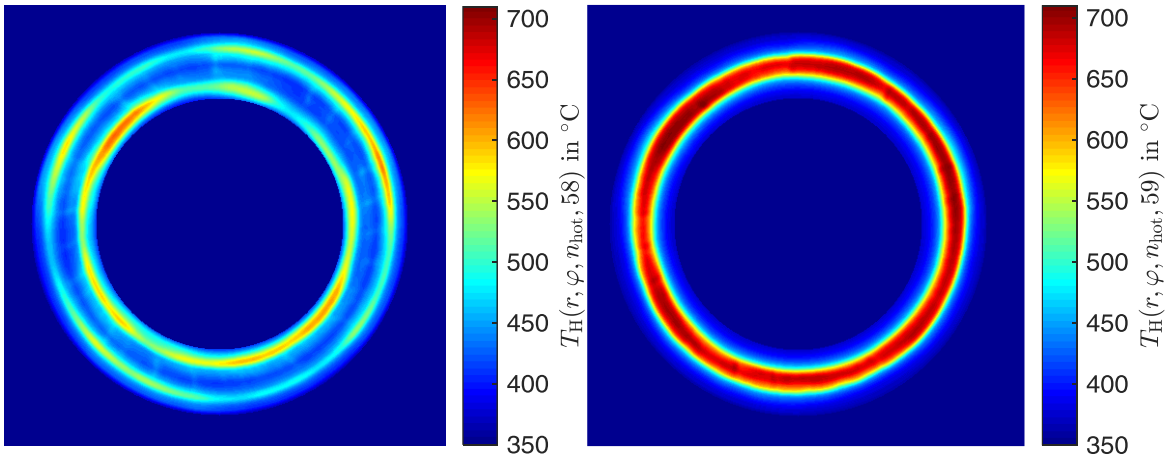

Figure 4-8: Temperature distribution on the friction surface of the HS; two-hotband case in the 58th cycle (left) and one-hotband case in the 59th cycle (right)

Figure 4-8 shows two thermal images of the HS of the disc, taken at the end of each braking period in two subsequent cycles. In the 58th cycle, two hotbands show up, while in the 59th cycle only one, central hotband shows up. The alternation of the one- and two-hotband case

[95] Wiegemann, S.-E. et al.: Automatic Heat Crack Detection (2016).

is typical and has been discussed partially by several authors before.[96,97] Since the heat is more concentrated in the one-hotband case, peak temperatures are higher. While for the one-hotband case all hotspots occur on one radius, hotspots are distributed on two radii in the two-hotband case. If hotspot movement should be tracked comparably to the results of Le Gigan et al.[97] in a pattern figure, it has to be chosen, whether hotspots from a single hotband or from both hotbands are tracked in the two-hotband case. Since hotspots would be left out if a fixed radius would be chosen, maximum temperature from each angular segment is chosen for processing of hotspot pattern (cf. section 4.5.1). The angular number of hotspots, i.e. the dominant hotspot order, stays similar during the two subsequent brakings. This suggests that the occurrence of hotspots is linked to the formation of SRO and/or DTV. For that reason, a discrete Fourier transformation is applied to the hotspot pattern in order to identify dominant hotspot orders.

Generally, temperatures in hotspot areas reach over 700 °C (Figure 4-8 right). This is sufficiently high to engage temperature-induced microstructural transformations (cf. subchapter 3.2). In addition to this, temperature gradients seem to be higher in radial direction than in circumferential direction, which indicates that hotbands contribute more to circumferential stresses than hotspots. This will be discussed in connection with the findings of the main tests in chapter 7.

[96] Sardá, A.: Dissertation, Wirkungskette der Entstehung von Hotspots (2009).

[97] Le Gigan, G. et al.: Disc brakes for heavy vehicles (2015).

4.4.2 Observation of Disc Surface Topology

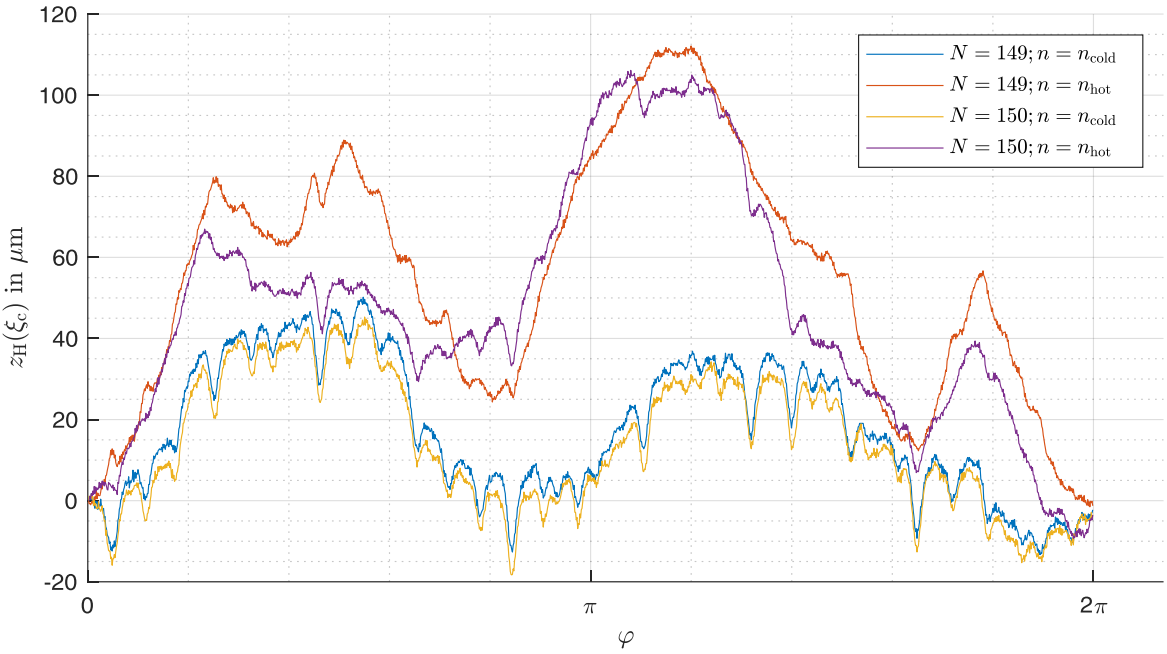

Figure 4-9: Surface topology in the centre of the hat side in cold and hot state; preliminary investigated brake disc; figure with zero-point suppression

A comparison of the surface topology in cold and hot state for two subsequent brakings is shown in Figure 4-9. In cold state, surface topology seems not to change qualitatively. However, amplitudes are slightly lower during the second braking in comparison to the first on. Contrary, amplitudes rise in hot state differently in the first and second braking, still resulting in generally higher amplitudes for both brakings. While the surface topology is rather even and mostly consists of two wide peaks in cold state, it becomes rather non periodic in hot state, showing several, partially narrower peaks. This indicates again that the formation of hotspots, which changes during two subsequent cycles (cf. Figure 4-8) is linked to the morphism of the surface topology. Numerous periodic inverted peaks are distinctively visible in cold state. Their appearance is rather odd, since they partially vanish in hot state. As they appear periodic, a spectrogram of the surface topology is made for the two examined brakings (Figure 4-9).

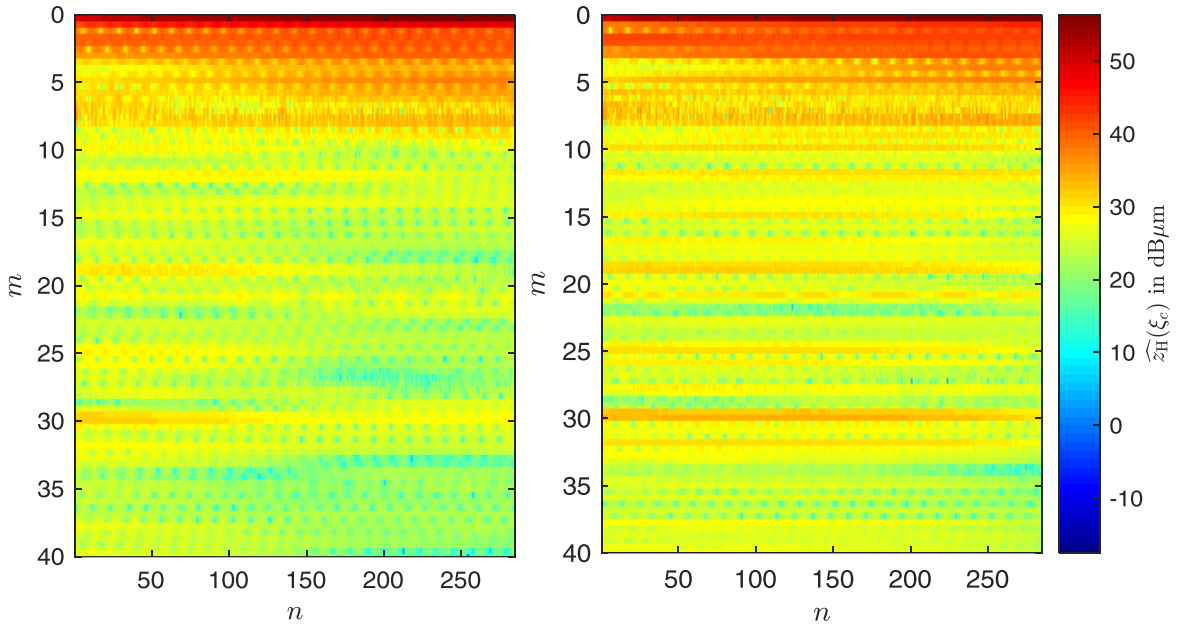

Figure 4-10: Power spectral density of the surface topology of the HS during the 149th (left) and 150th (right) braking; preliminary investigated brake disc

The spectrogram shows numerous amplitudes of lower order which rise during the braking period, i.e. with rising temperature. Additionally, several orders that are not induced by the brake disc itself but by non-rotating parts of the dynamometers are visible, which have been identified during the assessment of the displacement sensor setup (cf. appendix A.6.2). However, the 30th order progresses differently during the braking in comparison to the other orders. Its amplitude nearly vanishes during braking 149 and lowers in the course of braking 150. This effect might be caused by the cooling channel geometry, since the observed brake disc is constructed with 30 cooling channel vanes in circumferential direction. For that reason, modifications to the cooling channel are made in the subsequent tests.

4.5 Evaluation Methods

In this subchapter, evaluation methods that are used for post-processing of experimental raw data are presented. It should be mentioned that instruments on the dynamometer have been positioned manually regarding revolution angle. Accordingly, deviations of roughly $\varphi = \pm 2°$ have to be kept in mind when talking about spatial correlation.

4.5.1 Condensing of Information into Patterns and Trends

Since $\boldsymbol{\xi} = (r, \varphi, n, N)$ depends on four independent variables and therefore cannot be plotted in regular figures, comparison between observed quantities $\Xi(\boldsymbol{\xi})$ requires a condensing of information by reduction of independent variables. Accordingly, two reduction methods are used: by elimination of r and subsequently n by maximisation, pattern figures $\Xi_{\max}(\varphi, N)$

are deducted, which results in a 2-dimensional image with φ to the right, N going down and the actual quantity being color-coded. In order to eliminate the independent variable n, two situations are distinguished: first, the revolution featuring the hottest disc temperature, usually the last revolution of the braking. It is selected by maximisation for each heat crack cycle individually:

$$n_{\mathrm{hot}}(N) = \underset{n}{\operatorname{argmax}}\, T(\boldsymbol{\xi}) \tag{4.10}$$

Second, the revolution featuring the coldest disc temperature, which is defined as the last revolution before the subsequent braking starts:

$$n_{\mathrm{cold}}(N) = \max\big(n(N)\big) \tag{4.11}$$

In order to compare the evolution of hotspots, for each angular position φ maximum temperature is searched during $n_{\mathrm{hot}}(N)$:

$$T_{\max}(\varphi, N) = \max_{r}(T(r, \varphi, n_{\mathrm{hot}}(N), N) \tag{4.12}$$

Alternatively, temperature at the radius featuring peak temperature can be used for generation of the hotspot pattern:

$$T^{*}_{\max}(\varphi, N) = T\left(\underset{r}{\operatorname{argmax}}\big(T(r, \varphi, n_{\mathrm{hot}}(N), N)\big), \varphi, n_{\mathrm{hot}}(N), N\right) \tag{4.13}$$

However, in case peak temperature occurs on a radius that differs to the radius of the remaining hotspots, remaining hotspots are not considered. Still, temperature patterns $T^{*}_{\max}(\varphi, N)$ are attached in the appendix (cf. Figure 8-2, Figure 8-3, Figure 8-4 and Figure 8-5).

Display of hotspot patterns for tracking of hotspot movement has been proposed by Le Gigan et al. before.[98] However, they used mean temperature of the respective angle for comparison. This evaluation method skips some hotspots in contrast to evaluation of maximum temperature. An example for left out hotspots using the calculation method by Le Gigan et al. is given by the *Constant* disc (Figure 4-11).

[98] Le Gigan, G. et al.: Disc brakes for heavy vehicles (2015).

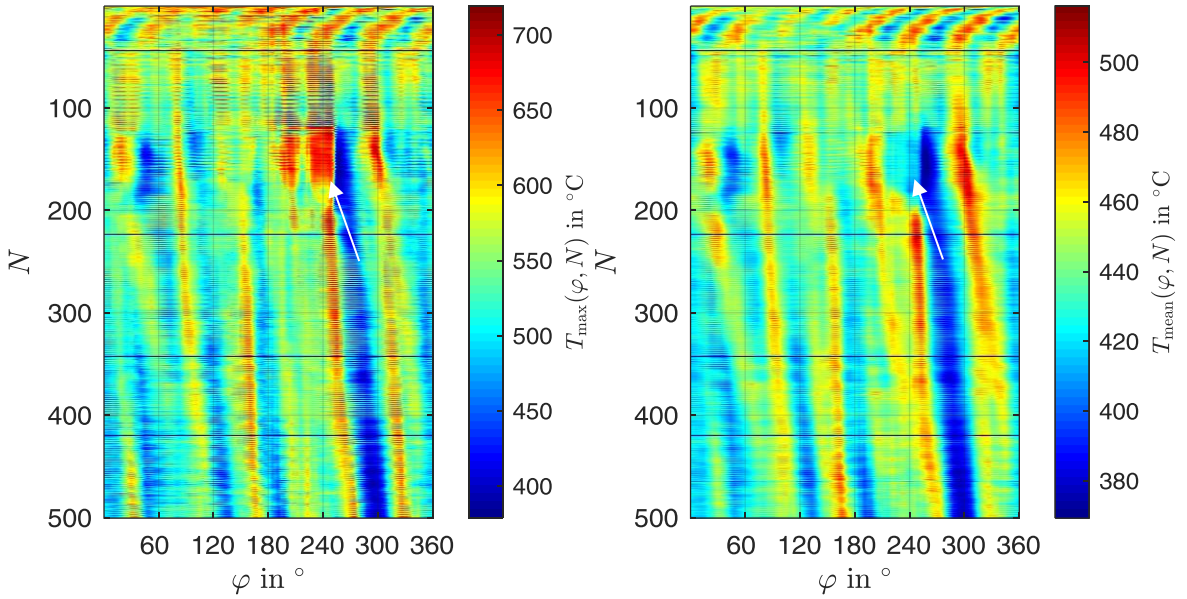

Figure 4-11: Comparison of methods for generation of hotspot patterns: calculation using maximum temperatures (left) vs. calculation using mean temperatures as proposed by Le Gigan et al. (right), leaving out a broad hotspot; data from the *Constant* disc

Similarly, disc thickness and SRO patterns are generated:

$$\Delta z_{\mathrm{hot/cold}}\left(r_{i/c/o}, \varphi, N\right) = \Delta z\left(r_{i/c/o}, \varphi, n_{\mathrm{hot/cold}}, N\right) \tag{4.14}$$

$$\Sigma z_{\mathrm{hot/cold}}\left(r_{i/c/o}, \varphi, N\right) = \Sigma z\left(r_{i/c/o}, \varphi, n_{\mathrm{hot/cold}}, N\right) \tag{4.15}$$

To generate crack patterns, raw crack lengths from the crack detector are plotted onto a mesh with an angular width of 0.1°. The average width of an open crack has been manually measured 1.5 mm on r_c. For that reason, a crack is plotted into a mesh position, if its detected angular centre is closer than 0.25° to the mesh position. This way, crack pattern $l(\varphi, N)$ is available for comparison.

For further compression, a reduction by φ is applied using maximisation, resulting in a trend figure of the peaks of an observed quantity $\Xi(\boldsymbol{\xi})$:

$$\Xi_{\mathrm{peak}}(N) = \max_{\varphi}\left(\Xi_{\mathrm{max}}(\varphi, N)\right) \tag{4.16}$$

4.5.2 Fourier Transformation and Filtering

For visualisation of phenomena that occur bound to a specific order, e.g. hotspots, Discrete Fourier Transformation (DFT) is applied to the observed quantities. Application of DFT to a quantity $\Xi(\boldsymbol{\xi})$ allows for evaluation of the amplitude spectrum $\hat{\Xi}(\boldsymbol{\xi})$ and phase spectrum $\Delta\Xi(\boldsymbol{\xi})$ of the respective quantity. In order to minimize the Leakage-effect, signals are split into segments with a length of exactly one revolution. If not mentioned, no window functions are used.

For smoothing of noisy signals, filters are applied. In contrast to regular low pass filters, the Savitzky-Golay-Filter provides smoothing of the data while maintaining peaks of the signal by polynomial regression.[99] Based on the signal characteristic, order m_f and frame length l_f are chosen. An overview on figures containing data filtered with Savitzky-Golay-Filters and chosen filter parameters is given in Table 4-3

Table 4-3: Filter parameters for figures containing signals filtered with Savitzky-Golay-Filters

Figure	m_f	l_f	Comment
Figure 5-2	3	15 cycles	Additional "phase unwrap" to avoid signal jumps of $\pm 2\pi$
Figure 5-4	0	10 cycles	Oscillation around a nearly constant value
Figure 5-9	3	101 cycles	Temperature data unfiltered
Figure 5-18	1	12.6°	Filtered gradient calculated from filtered SRO

Crack lengths of the longest cracks (Figure 5-7) are filtered using a maximum filter, since crack length is repeatedly underestimated by the crack detector due to friction dust:

$$l_{\max}(\varphi, N) = \max(l(\varphi, 1..N) \tag{4.17}$$

Finally, for correlation of average temperature of the friction ring surface with surface topology data, median filters for one revolution are applied to the pyrometer signal. Median filters are less sensitive signal peaks like hotspots compared to mean filters.

4.6 Scope and Requirements for the Finite Element Model

On the one hand, the FE model should provide additional information on the underlying processes leading to crack growth that cannot be evaluated in experiments. On the other hand, it should suit as a basic estimation tool for evaluation and comparison of the resistance of brake disc designs against cracking. Requirements are derived based on these aims and the state of science and technology regarding FE models simulating the heat crack test.

Stresses cannot be measured during the heat crack test using the experimental setup presented above. Since cracks are caused by stresses, their evaluation is required for complementation of the causal model. Still, qualitative reproduction of stresses is sufficient in order to complement the model. Accordingly, the first target requirement is formulated:

[99] Savitzky, A.; Golay, M. J.: Smoothing and Differentiation of Data (1964).

Requirement 1: Calculation of stress distribution on the friction ring surface and inside the friction ring

In order to fulfil this major target requirement, the model has to fulfil several necessary requirements. Since stresses are mostly caused by non-uniform thermal expansion, temperature distribution in the friction rings has to be calculated:

Requirement 1.1: Reproduction of temperature distribution on the friction ring surface

In order to fulfil requirement 1.1, several minor requirements have to be fulfilled:

Requirement 1.1a: Reproduction of the heat flow inside the friction ring by braking

Requirement 1.1b: Calculation of heat transfer inside the friction ring

Requirement 1.1c: Calculation of heat losses from the cooling channel

Requirement 1.2: Reproduction of uniaxial stress-strain behaviour

In order to fulfil requirement 1.2, a validated material model for GJL designed and parameterised by Fraunhofer IWM Freiburg is used.[100] Parameterisation and comparison is done using experimental data from the LCF tests with the *Twin* disc (cf. section 4.3.1). Requirement 1.1a is fulfilled by a deconvolution algorithm for calculation of heat flow based on temperature distribution during the heat crack test (cf. section 6.2.2). Requirement 1.1b is addressed by measurement of temperature dependent heat transfer coefficient of the *Twin* disc (cf. section 4.3.2). In order to fulfil requirement 1.1c a CFD model is used (cf. section 6.2.1).

For estimation of cracking resistance of brake disc design, comparison of three influences is necessary: first, it should be estimated when cracks initiate first, i.e. the number of cycles until failure for each element. This is done by fatigue life estimation:

Requirement 2: Estimation of fatigue life of friction surface elements

Moreover, as a through-thickness crack is defined as a crack that has reached the cooling channel, cracks initiating on the inner or outer radius can become a through-thickness crack faster than cracks initiating on centre radius. Accordingly, the third requirement is formulated:

Requirement 3: Determination of crack initiation zones

Finally, as through-thickness cracks usually form as large cracks, crack growth has to be estimated as well. This is necessary, since crack growth rates vary strongly during the test (cf. e.g. Figure 5-7):

Requirement 4: Estimation of crack growth rates

Remaining requirements 1-4 are discussed in subchapter 7.4.

[100] Metzger, M.: Mikrostruktur- und mechanismusbasierte Werkstoffmodelle (2016).

5 Results

In this chapter, results from the dynamometer experiments are presented. First, phenomena occurring in all experiments are described entirely. Results specific to the respective brake disc design are described afterwards in separate subchapters. Each of the subchapter is structured in sections related to the described phenomena – mostly to disc surface temperature, deformation and crack formation. Results from the experiment with the *Reference* brake disc are presented first, since this brake disc is considered reference. Subsequently, results from the experiments with the *Variable, Constant* and *Periodic* disc are presented. Unless otherwise stated, evaluations are discussed for the HS of the brake disc, since that side generally suffers more from cracking than the PS.[101] None of the through thickness-cracks observed in the test series was found on the PS, and longest cracks were found on the HS as well.

5.1 Common Phenomena

Since all brake discs of the main test series show similar behaviour, common phenomena are described in this subchapter. This includes comparison of peak surface temperature, hotspot migration and cooling times as well as coning and surface topology. Finally, general cracking behaviour is evaluated.

[101] Le Gigan, G. et al.: Disc brakes for heavy vehicles (2015).

5.1.1 Friction Surface Temperature

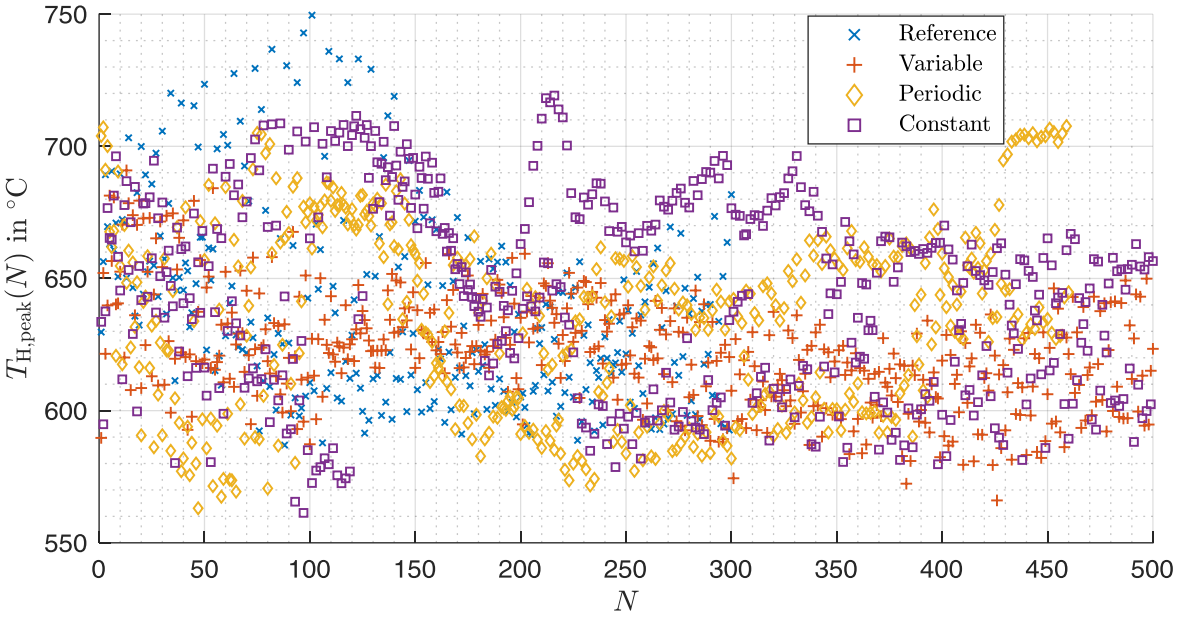

Figure 5-1: Peak temperatures in each heat crack cycle

Figure 5-1 shows the peak temperature reached on the HS in each heat crack cycle. Generally, it alternates in each of the cycles between a high level of 650 to 750 °C and a low level of 550 to 650 °C. The alternation is highest for $N < 100$, resulting in a narrowing envelope in the course of the test. The highest temperatures are reached with the *Reference* brake disc, followed by the *Constant* brake disc. The *Variable* brake disc shows the most even peak temperature progression, the *Constant* and the *Periodic* disc show partially wave like progression of the peak temperature. In general, all discs reach temperatures sufficiently high to trigger microstructural transformations. The peak temperatures of the *Reference* and the *Periodic* brake disc extraordinarily rise during the last cycles of the test. This might be caused by the through-thickness crack that occurred in both discs directly *before* the location of the peak temperature, i.e. during each revolution the brake pad first runs over the crack and then over the hotspot (cf. Figure 8-6 and Figure 8-9):

$$\varphi\left(T_{\mathrm{H,peak}}(N)\right) - \varphi_{\mathrm{Crack}} \approx 15° \tag{5.1}$$

Additionally, at the location of the peak temperature, strongly convex SRO occurs in the last cycles (cf. Figure 5-10, Figure 5-16 and Figure 5-13 for the *Reference* disc, Figure 5-37, Figure 5-39 and Figure 5-44 for the *Periodic* disc). This indicates a break in the brake disc's stability caused by the through thickness crack and therefore an extreme deformation, which in turn results in a temperature peak at the location of the crack. Furthermore, opening of the through-thickness crack shows deep intrusion into the material, supporting the hypothesis on instability of the friction ring (cf. Figure 8-25).

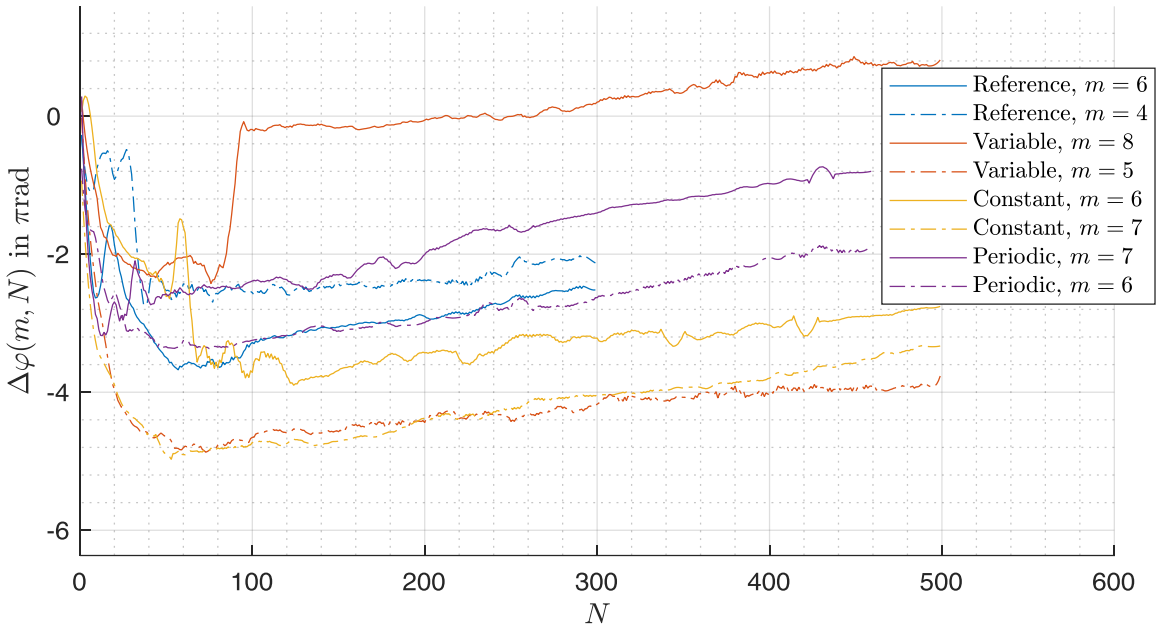

Figure 5-2: Filtered[102] phase shift of dominant and subordinate hotspot orders of all 4 brake discs

Since hotspots usually occur periodically, a dominant order can be identified. In the subsequent sections, the respective order of the hotspots for the specific brake disc as well as the hotspot evolution will be described. However, during all conducted tests, hotspots migrated similarly over the friction surface against and in rotational direction. The phase shift of the dominant and subordinate hotspot order is drawn in Figure 5-2. For all brake discs, a fast migration behaviour against the rotational direction of the disc is visible during $N < 50$. This fast migration slows down approaching $N \approx 50$ and transforms afterwards into a slow migration behaviour in the opposite direction, i.e. in rotational direction of the brake disc. The migration speeds match for all brake discs. The fast hotspot migration speed is roughly 10 times higher than the slow migration speed.

[102] Using a Savitzky-Golay-Filter on the unwrapped signal, cf. section 4.5.2

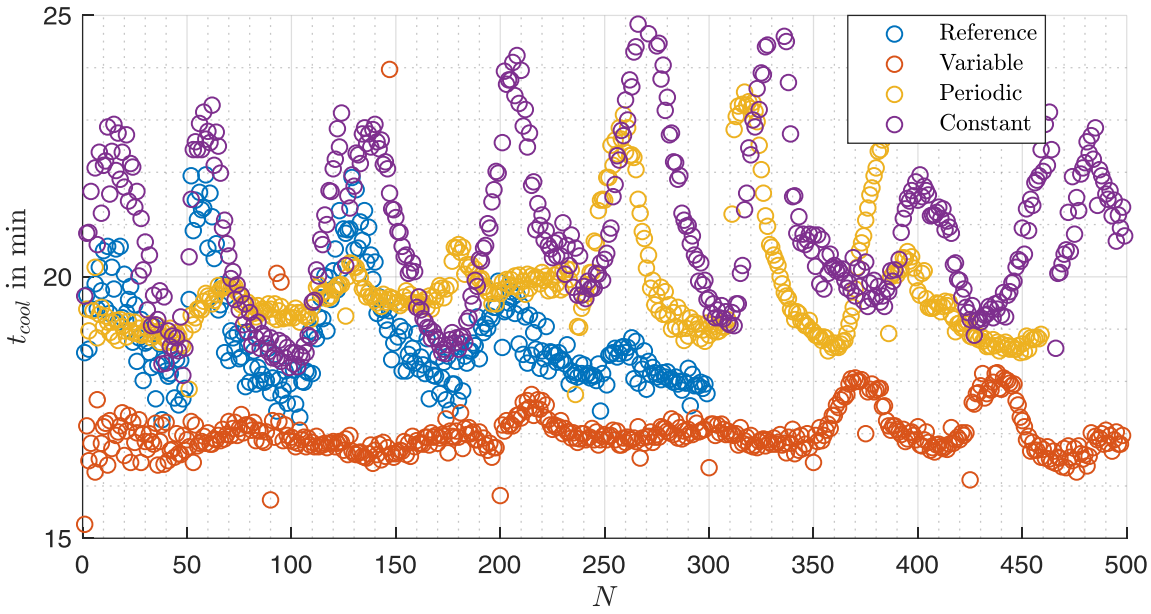

Figure 5-3: Cool-down duration in each heat crack cycle for all tested brake discs

Cool-down duration usually varies in the course of the heat crack test (Figure 5-3). Especially for the *Constant* brake disc, parabolic variations of the cooling times occur, while the longest cooling times occur around the cycles, when inspection breaks have been made during the test ($N = \{50; 125; 200; 270; 330; 390; 465\}$). For the *Periodic* disc, parabolic variations mainly occur during the second half of the test. Here, the longest cool-down times do not necessarily occur around the cycles of the inspection breaks ($N = \{50; 125; 175; 235; 310; 385\}$). The same accounts for the *Reference* brake disc (inspection break after $N = \{50{,}200{,}250\}$). The *Variable* brake disc does not show any variation of the cooling time for $N < 350$ and only slight variations afterwards. It also shows the lowest cooling times. Since *Constant* and *Variable* disc show the same lifetime but different cooling times, cooling time seems not to have an influence on crack growth.

Furthermore, no correlation between cooling times and maximum average surface temperature could be found (coefficient of determination nearly 0 %, cf. Figure 8-10). Although the highest peak temperatures were measured with the *Reference* brake disc, the *Periodic* and *Constant* brake disc show higher cooling times. For that reason, cooling time is obviously not linked to other evaluated quantities related to the friction surface.

5.1.2 Friction Surface Topology and Disc Deformation

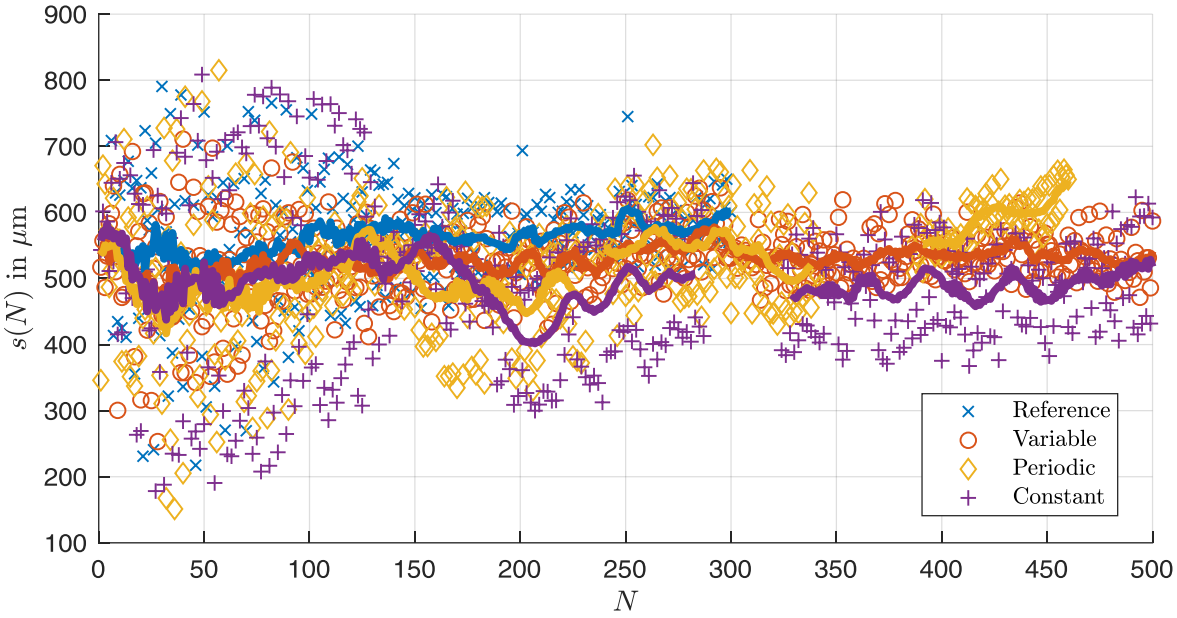

Figure 5-4: Evolution of disc coning of all tested brake discs; drawn-through: moving average

In subchapter 2.3, disc coning was identified as a possible influence on crack formation. Figure 5-4 shows the evolution of disc coning during the heat crack test. Disc coning deviates for $N < 150$ in general more around a mean value, which is constant during the test. After $N > 150$, variation stays generally lower, which correlates with the variation of the peak temperatures (Figure 5-1). Both quantities are plotted against each other in Figure 5-5. For the *Variable* brake disc, the coefficient of determination is lowest ($R^2 = 4\ \%$), for the *Constant* disc it is highest ($R^2 = 47\ \%$). However, variation of both coning and peak temperature is lowest for the *Variable* disc. During the second half of the test, coefficient of determination is generally higher for all discs, up to 78 % for the *Constant* disc. The link between peak temperature level and coning level might be the alternating hotband cases: if one hotband appears on the HS, temperatures are higher for the HS and so is the coning. If two hotbands appear on the HS, temperatures are lower and coning is lower as well.

In general, mean values of coning are similar for all brake discs: the *Reference* disc shows the highest average coning (561 µm) and the shortest lifetime ($N_{\max} = 300$), the average coning of the *Variable* disc is 528 µm and its lifetime is nearly twice as high ($N_{\max} = 500$). The *Periodic* disc has a slightly lower average coning value of 522 µm and a slightly lower lifetime of $N_{\max} = 460$, while the lowest average coning value has been measured for the *Constant* disc with 494 µm ($N_{\max} = 500$), which is the only disc in the test series without a through-thickness crack. Accordingly, a high coning value might reduce disc lifetime. Still, since geometry of the discs has changed, influence of coning on crack formation remains mostly unanswered.

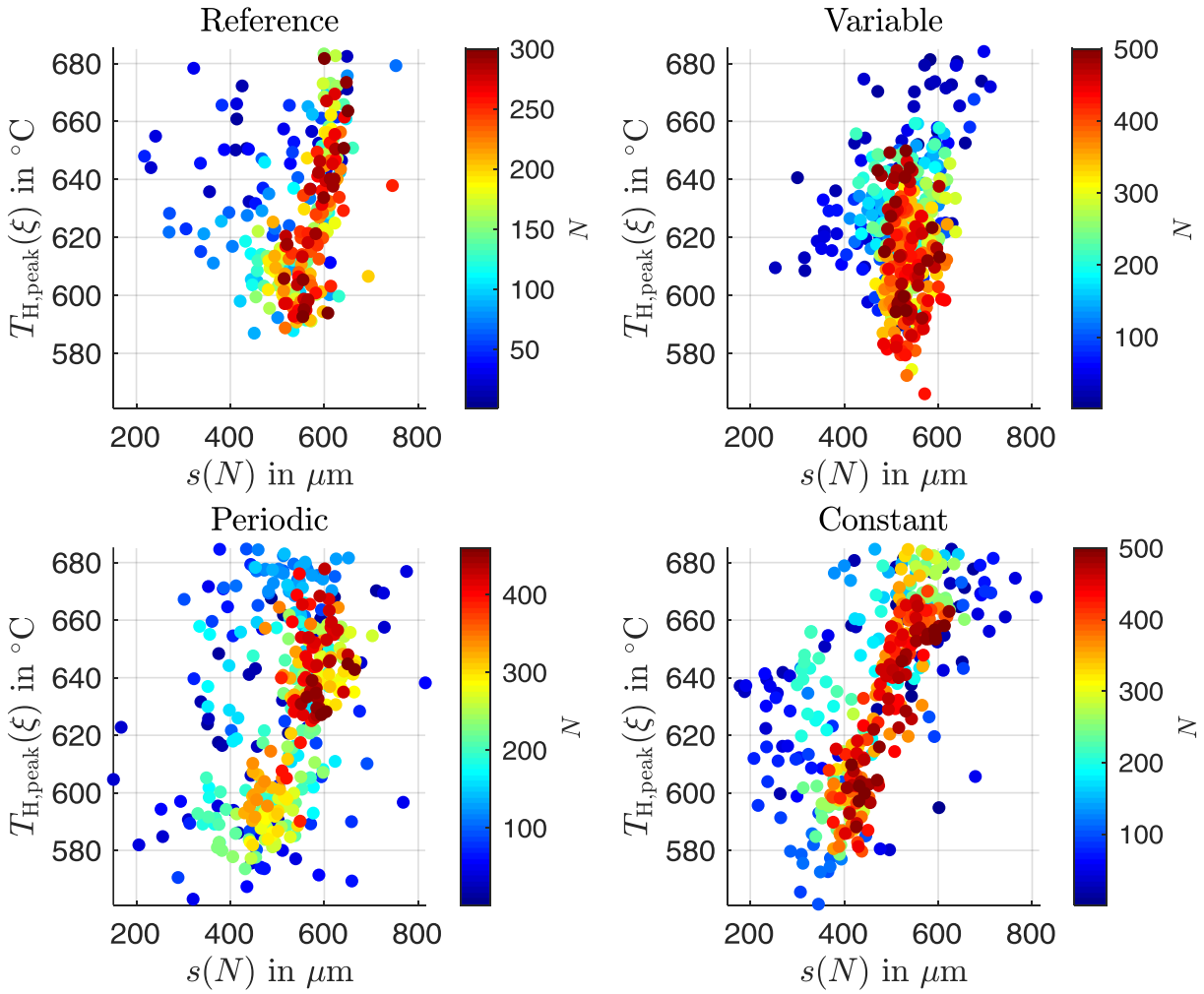

Figure 5-5: Peak temperature vs. disc coning for all brake discs, test progress colour-coded

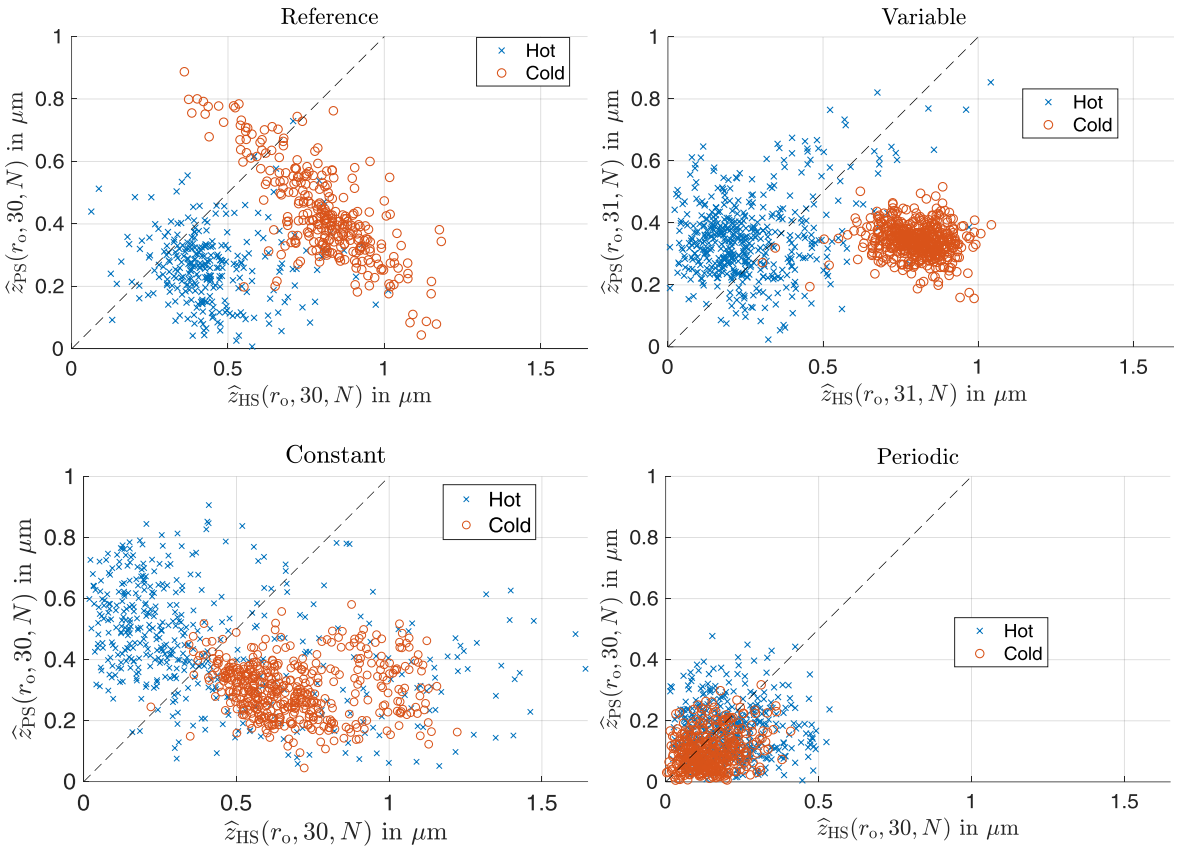

Figure 5-6: Amplitude of the extrusion of the HS vs. the PS at radial outer position for the respective cooling channel pin order; top left: *Reference* brake disc;[103] top right: *Variable* brake disc;[103] bottom left: *Constant* disc; bottom right: *Periodic* disc

During the pre-test, a surface deformation of 30$^{\mathrm{th}}$ order, matching the number of cooling channel pins in circumferential direction, has been observed. Figure 5-6 shows the extrusion amplitudes of the respective order for all main tests. While amplitudes vary a lot in hot state, amplitudes after cool-down for the *Reference*, *Variable* and *Constant* disc are higher and more concentrated at the HS compared to the PS. The amplitude of the HS is not only higher compared to the piston side in cold state. Rather is the overall amplitude, i.e. the sum of both amplitudes of HS and PS higher in cold state compared to hot state. This is consistent with the findings of the pre-test, where amplitudes lowered during the braking period. The overall evolution of the amplitude of the cooling channel pin extrusion will be discussed in the sections 5.2.2 and 5.3.2. The *Periodic* disc does not show any amplitude of the respective order above noise level.

[103] Bilgic Istoc, S.; Winner, H.: A New Model (2018).

5.1.3 Crack Formation

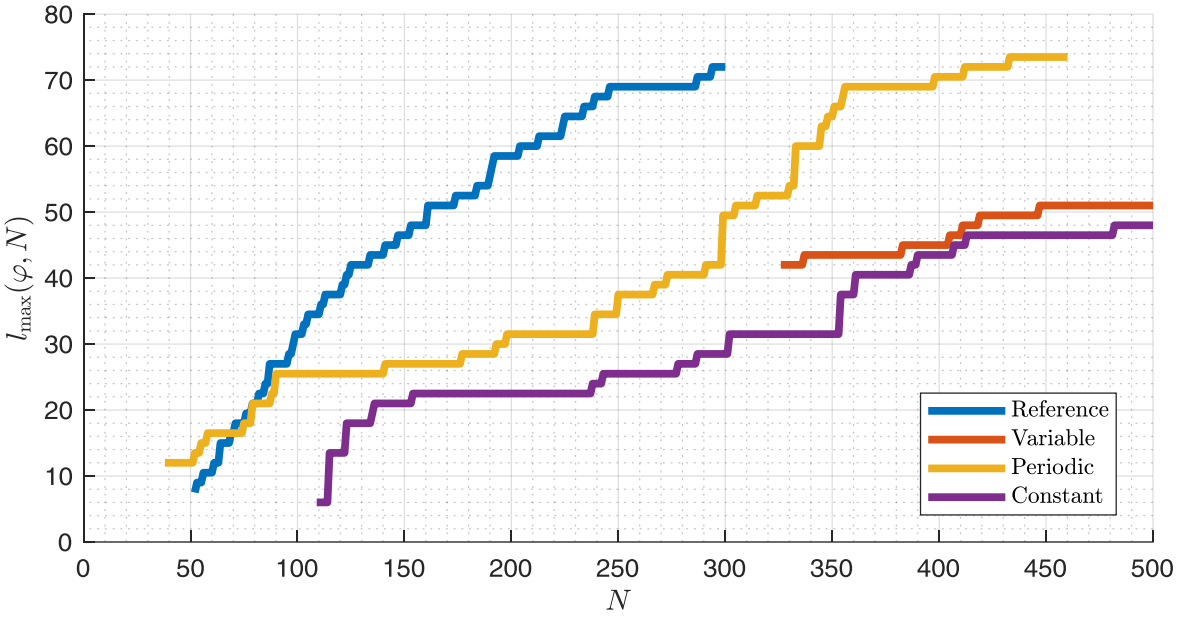

Figure 5-7: Evolution of lengths of the longest cracks of each of the tested brake discs

Crack length evolution of each of the longest cracks for all four tested discs is shown in Figure 5-7. For the *Reference* and the *Periodic* brake discs, maximum lengths of the (through-thickness) cracks reached over 70 mm, while crack lengths of the *Variable* and *Constant* disc did not exceed 51 mm. For the *Reference* brake disc, a crack growth speed is constantly degressive in the course of the test. It can be well fitted to a logarithmic curve ($R^2 = 94.2\ \%$). Crack growth speeds of the *Constant* and *Variable* disc are rather constant throughout the test, although crack growth rates lower for $N > 425$ for them as well. Additionally, highest crack growth rates have been recorded for both *Variable* and *Constant* disc at the beginning of the test. The longest crack of the *Variable* disc shows up after $N = 325$, since it formed by unification of two smaller cracks. The *Periodic* disc shows a rather irregular cracking behaviour. After the crack growth rate of its longest crack has been degressive in the first half of the test, it is rising rapidly again around $N \approx 300$. This rise might be caused due to an inspection break of one week, which has been applied to the *Periodic* disc after $N = 235$. The slowdown of the crack growth speeds might be caused by several reasons. First, the width of the friction rings of 84 mm is limiting the maximum detectable crack size. The crack detector is not able to detect fissures closer than 3 mm to the edge of the friction surface. For that reason, cracks that start growing into the cooling channel stop growing from the perspective of the crack detector. Second, the growth and opening of cracks might lower tensions in the friction ring, which causes reduction to crack growth speeds of longer cracks. However, mean crack length rises steadily throughout the entire test (cf. Figure 8-11).

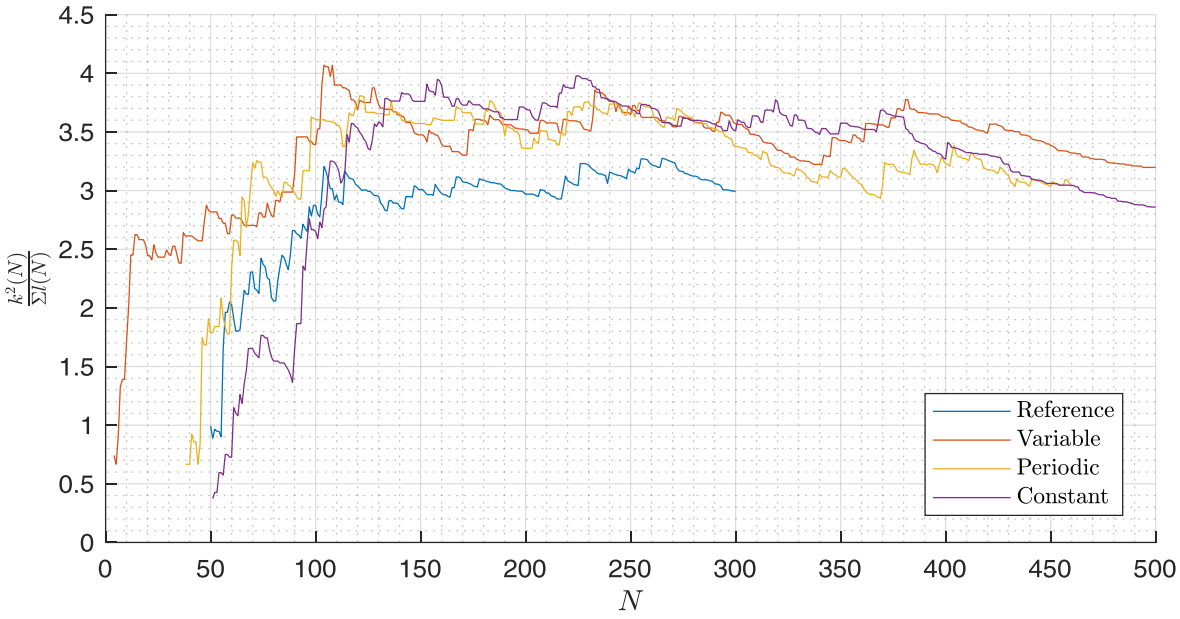

Figure 5-8: Crack count divided by mean crack length for all tested brake discs

Nevertheless, number of cracks ($k(N)$) divided by mean crack length $\frac{\Sigma l(N)}{k(N)}$ is nearly constant after $N > 100$ for all brake discs (coefficient of variation 4-8 %, Figure 5-8). Since mean crack length rises constantly, number of cracks rises as well in a similar manner. $\frac{k^2(N)}{\Sigma l(N)}$ is lowest for the *Reference* brake disc, while the remaining discs maintain a similar level, which is roughly 20 % higher compared to the *Reference* disc (3.05 vs. 3.40-3.52). Especially at the end of the test, $\frac{k^2(N)}{\Sigma l(N)}$ reduces. Since $\bar{l}(N)$ grows steadily, even at the end of the test, this indicates a stagnation of crack openings at the end of the test, which is the case for all discs except for the *Periodic* disc (cf. Figure 8-12). It is not clear, whether the lower level of $\frac{k^2(N)}{\Sigma l(N)}$ for the *Reference* brake disc has caused the early failure in the heat crack test after $N = 300$. However, it seems to be plausible, since a low level of $\frac{k^2(N)}{\Sigma l(N)}$ indicates that cracks rather continue grow instead of the enforced opening of new cracks. A high number of smaller cracks might be positive for the respective brake disc in terms of reaching a longer lifetime. For all discs, ascent of a regression line of $\frac{k^2(N)}{\Sigma l(N)}$ as described in section 3.1.4 is lower or equally high compared to standard deviation (cf. appendix A.2.4).

Figure 5-9 shows approximated crack growth rates and maximum temperatures at the positions of the two longest cracks for the *Reference* brake disc (top) and the *Constant* brake disc (bottom). Especially during the first cycles, maximum temperature and crack growth rate seem to be linked to each other, since they both start rather high at the beginning of the test. However, temperature does not seem to be the only influence on crack growth speeds, as deviations of the two curves from each other are rather high.

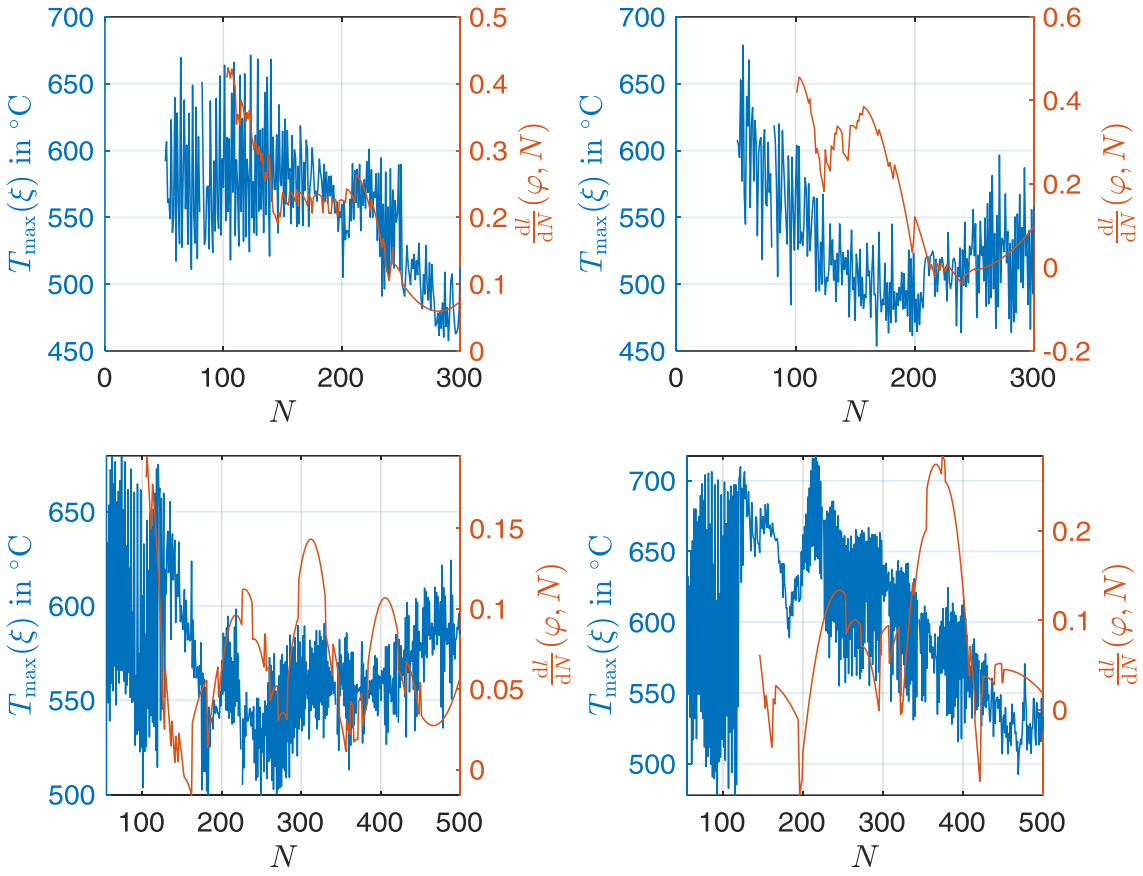

Figure 5-9: Approximated crack growth rates and temperature evaluated at the same positions for the two longest cracks of the *Reference* brake disc (top) and the *Constant* disc (bottom)

5.2 *Reference* Brake Disc

In this subchapter, results from the heat crack test with the *Reference* brake disc are presented. As the *Reference* brake disc is considered as reference, the regular behaviour of a commonly used brake disc for heavy-duty vehicles in the heat crack test is shown. Nevertheless, the focus of this chapter is set on general friction surface temperature evolution, especially considering hotspots, disc friction surface topology and crack formation. As SRO and DTV have been discussed in relation to heat crack formation, their evaluation stands next to the further investigation of the extrusion of cooling channel pins on the friction surface as introduced in the last sections. Crack growth is set in relation to the above-mentioned quantities, and finally, results from the material experiments top off this subchapter providing a deep and broad insight into the underlying processes leading to crack growth.

5.2.1 Friction Surface Temperature

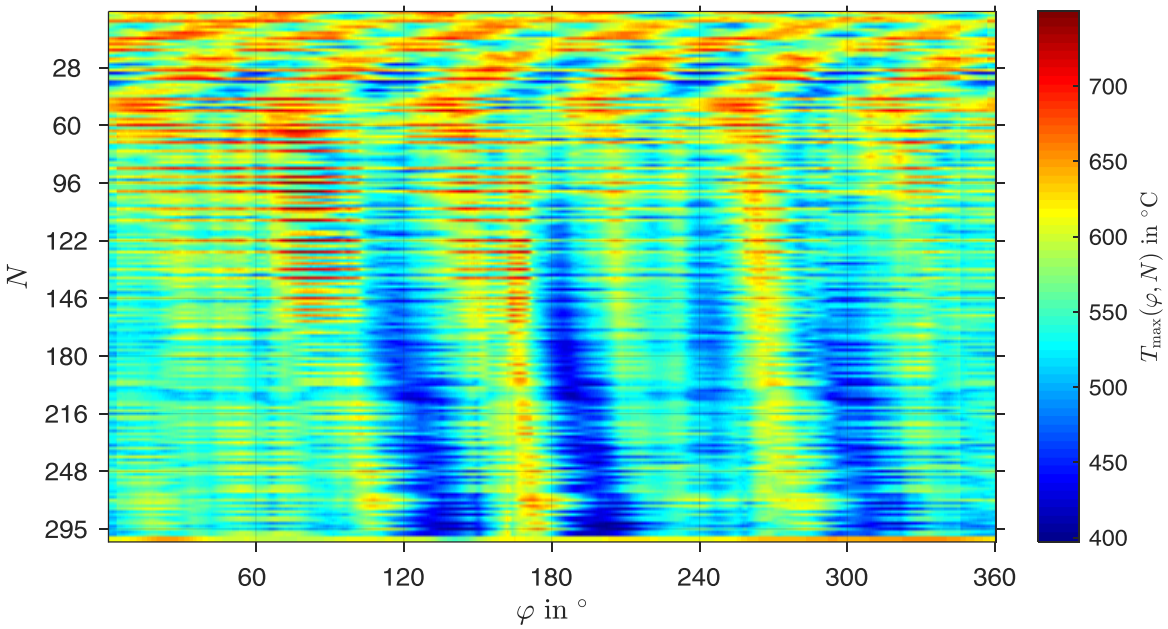

Figure 5-10: Hotspot pattern of the *Reference* brake disc[104]

The hotspot pattern of the *Reference* brake disc is shown in Figure 5-10. For $N < 50$, six harmonic hotspots quickly migrate over the friction surface against the rotational direction of the brake disc (cf. also Figure 5-2). Afterwards, the dominant hotspot order reduces from 6 to 4. Simultaneously, the entire hotspot pattern slowly migrates in opposite direction. For $N < 50$, hotspots reach similar temperature peaks in one cycle. Afterwards, temperature peaks are distributed less even on the brake disc's surface. At $\varphi \geq 180°$, a hotspot is nearly fixated, directly next to two large cracks. This hotspot is the hottest one in the second half of the test. Although it is partly fixated, it broadens in rotational direction, following the overall migration pattern. Between $50 < N < 150$, a broad hotspot forms at $70° < \varphi < 80°$. It vanishes in the course of the test after $N = 150$ and moves away in rotational direction. At $\varphi = 150°$, the crack, which becomes in the end of the test the through-thickness crack, is visible as a cool spot. The same accounts for $\varphi = 246°$, where a large crack becomes visible as a cool spot in the hotspot pattern. Again, next to the large crack, at $\varphi \approx 270°$ a broad hotspot moves away from the crack location.

[104] Bilgic Istoc, S.; Winner, H.: The Influence of SRO and DTV (2018).

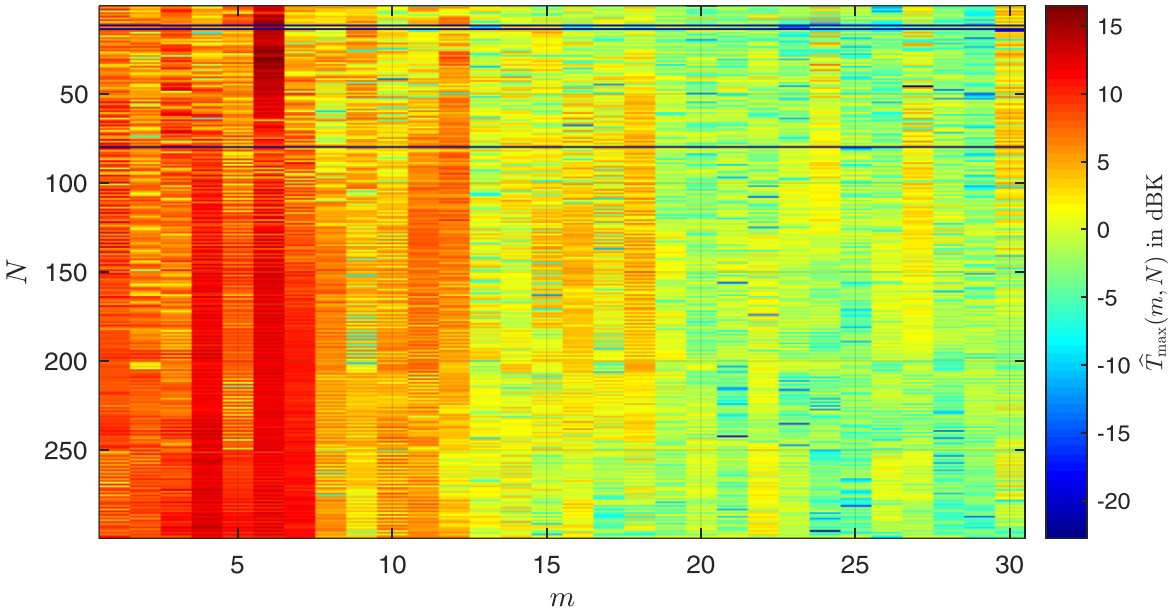

Figure 5-11: Amplitude spectrum of the hotspots

At the beginning of the test, 6 harmonic hotspots form. These quickly migrating hotspots are clearly distinguishable in the amplitude spectrum (Figure 5-11) with a maximum amplitude of 16.5 dBK. For $N > 50$, the dominant 6th order fades off, resulting in a blurry mixture of different orders from the 1st to the 7th order. Additionally, an 11th and 12th order fades in with rather low amplitude. The origin of these amplitudes cannot be explained at this point, although they might be overtones of the 6th order hotspots. In addition to this, a 4th order starts to fade in, which turns out to have a similarly high amplitude as the 6th order for $N > 150$. In the end of the test, the 6th and 4th amplitude are accompanied by a 7th amplitude, which has smoothly faded in from $N > 150$.

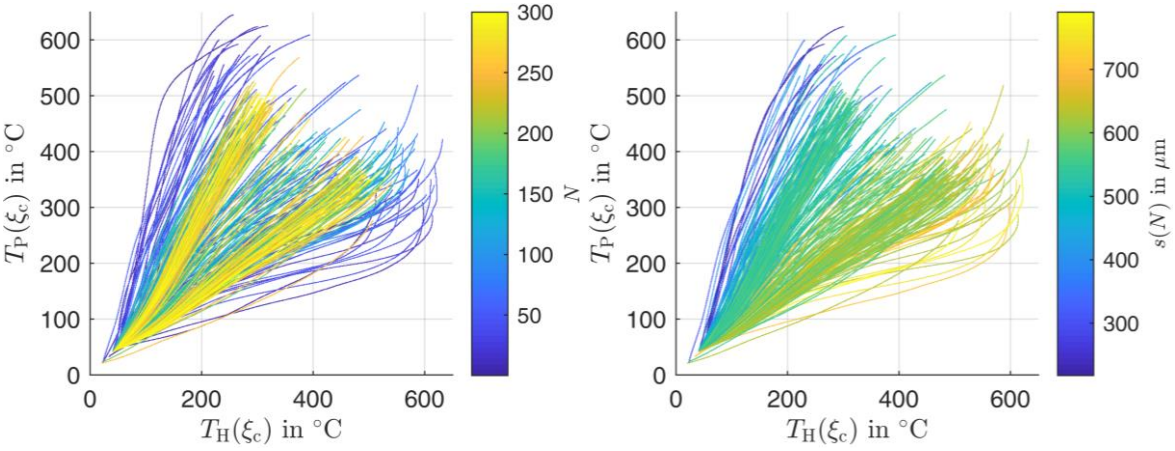

Figure 5-12: Average friction surface temperature measured by the thermocouples of the piston side vs. the hat side during braking; heat crack cycle (left) and coning (right) color-coded; temperature data from sliding thermocouples[105]

[105] Bilgic Istoc, S.; Winner, H.: Heat cracks in brake discs (2018).

Similarly to the alternation of the two- and one-hotband case on one friction surface, the hotband distribution alternates simultaneously on the opposite side. This phenomenon is expressed by the alternation of the ratio of average temperature on HS and PS (Figure 5-12 left). If the average temperature is high on the HS (i.e. one hotband on HS), the temperature is low on the PS (i.e. two hotbands on PS) and vice-versa. It should be noted that average temperatures are evaluated at radial centre position. This deviation of the average temperatures is strongest for $N < 50$. Whenever extreme average temperatures occur on one side ($T(\xi_c) > 500\,°C$), the temperature rise on the respective side slows down, which results in a bended curve in the plot. For $N > 50$, average temperatures of HS and PS approximate each other, although deviations of around 50 % are still present for the last cycles of the test. Around $N \approx 150$, average temperatures for HS and PS are almost equal.

The assumption made in section 5.1.2 that the level of peak temperatures on the HS and disc coning are linked to each other, are now confirmed (Figure 5-12 right). In those cycles where average temperature of the HS is higher compared to the PS, higher coning values occur compared to the opposite case. Furthermore, the stronger the deviation of the average temperatures, the stronger the deviation of the disc coning from the mean value.

In conclusion, the general thermal behaviour of a brake disc has been shown in this section. 6 harmonic hotspots with an amplitude of 16.5 dBK form during $N < 50$, where the average temperatures of HS and PS deviate most from each other. The former 6 hotspots transform into a mixed pattern of 6^{th} and 4^{th} order as the test continues, and the average temperatures approximate each other. In general, temperature distribution gets more even in the course of the test. Cracks become visible and fixate hotspots next to them in rotational direction. The overall hotspot pattern still migrates slowly until the end of the test.

5.2.2 Friction Surface Topology and Disc Deformation

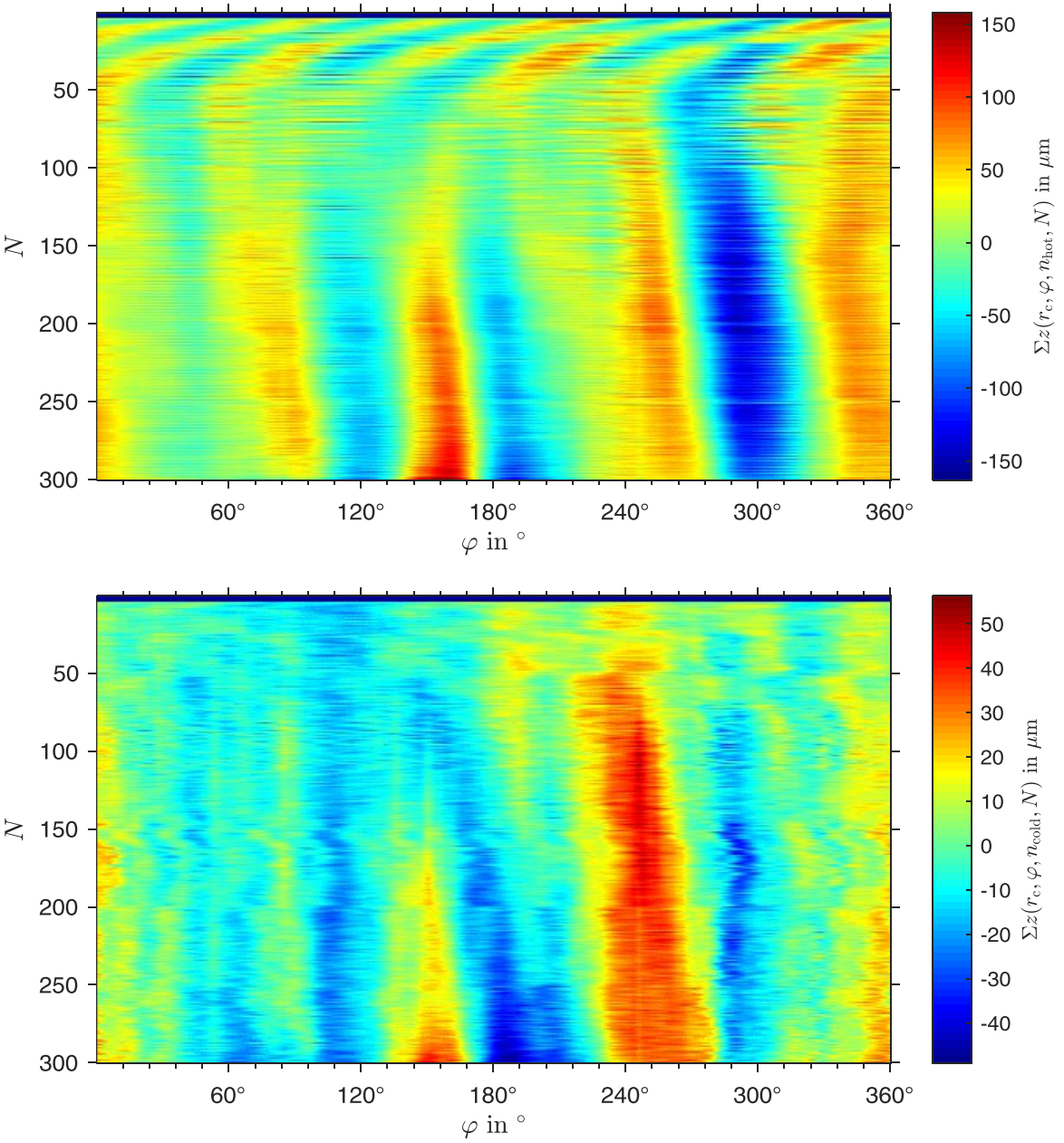

Figure 5-13: SRO pattern of the *Reference* brake disc, evaluated in hot state (top) and cold state (bottom) at radial centre position;[106] different color scale used in hot and cold state for contrast enhancement; both figures with identical color scale are in the appendix (Figure 8-18)

The SRO pattern differs strongly in hot state (Figure 5-13 top), i.e. at the end of the braking period, and cold state (Figure 5-13 bottom), i.e. at the end of the cool-down period. In hot state, the SRO pattern shows convex deformation towards the HS as high values, concave deformation towards HS as low values. For $N < 50$, 6 harmonic convex deformations are visible (dominant order, maximum amplitude of 28.6 µm, cf. Figure 8-19), which align with

[106] Bilgic Istoc, S.; Winner, H.: The Influence of SRO and DTV (2018).

the hotspot pattern (Figure 5-10) and migrate accordingly (cf. Figure 8-17). Again, the amplitude is similar for all of the convex deformations at the beginning of the test. Afterwards, between $50 < N < 150$, only low SRO amplitudes occur. A slight migration pattern in rotational direction, similar to the SRO pattern, becomes visible. In the second half of the test, amplitudes of the pattern are amplified, and cracks become visible in the pattern. They are located at positions of rising convex SRO, e.g. at $\varphi = \{85°; 246°\}$. At the end of the test, two extreme values for SRO are present: the most convex SRO occurs at $\varphi = 150°$, where maximum temperature and the through thickness crack are located. The most concave SRO occurs in an area between $290° < \varphi < 310°$. This "valley" is formed after $N > 50$ and marks the only area of no crack formation. As observed similarly for the hotspot pattern, 4th order becomes dominant in the second half of the test (cf. Figure 8-19).

In cold state (Figure 5-13 bottom), the SRO pattern differs. Although areas of convex and concave SRO basically match, amplitudes are lower (maximum amplitude of 10.2 µm instead of 30.5 µm, cf. Figure 8-20) and dominant orders differ. The most convex SRO is located at $\varphi = 241°$ and the most concave SRO in an area around $\varphi = 180°$. Furthermore, the pattern of quickly migrating hotspots present in the SRO pattern in hot state and the hotspot pattern is mostly missing (amplitude of roughly 3 µm for 6th order, phase varies, cf. Figure 8-17). This indicates that hotspots are not entirely related to SRO in cold state and form dynamically during braking. The same accounts for the SRO pattern in hot state. Especially the six harmonic hotspots are not present in the SRO pattern in cold state. Possible interactions of these phenomena with crack formation are discussed in the next chapter.

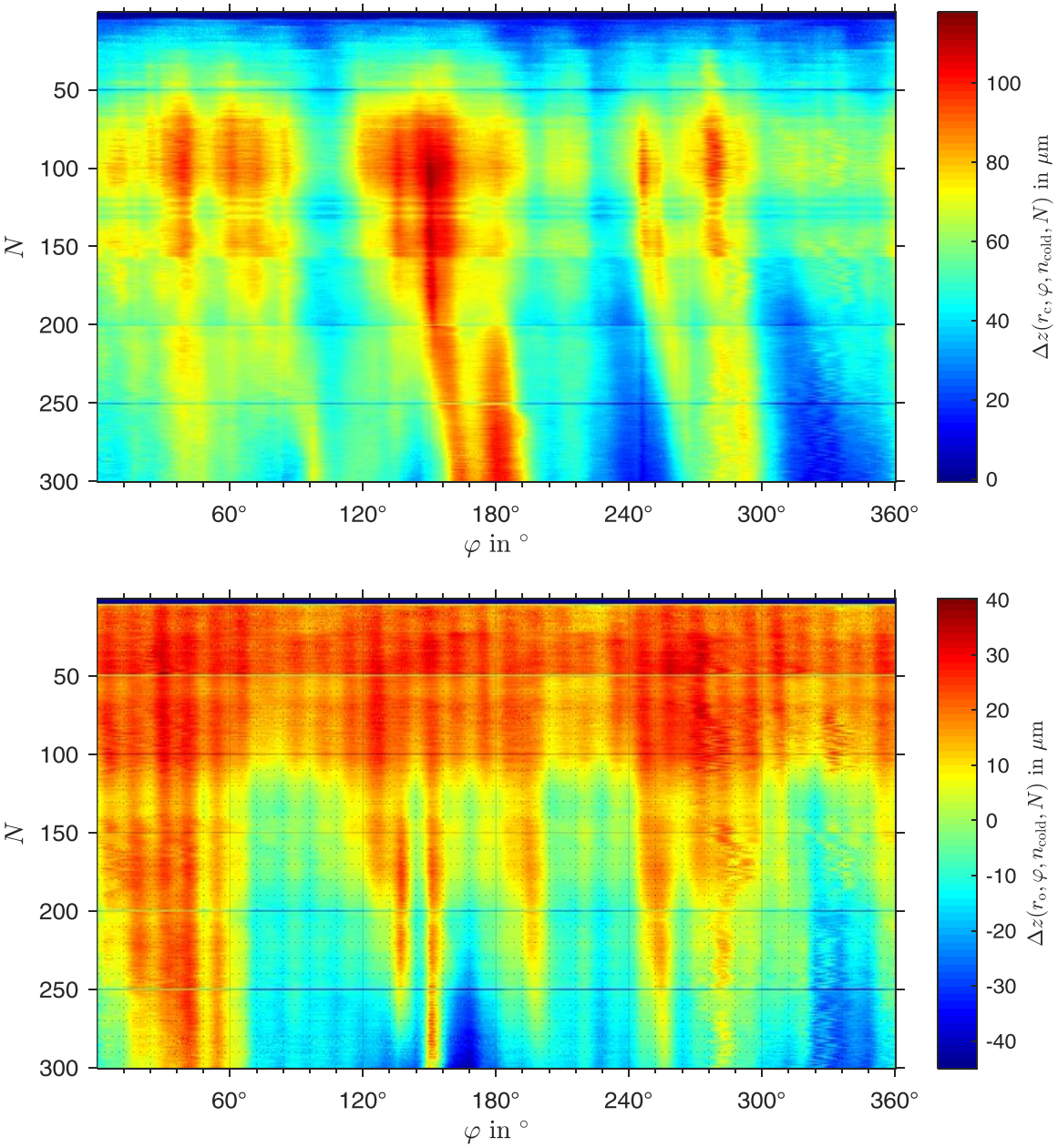

Figure 5-14: DT pattern of the *Reference* brake disc, evaluated in cold state at radial centre (top) and outer (bottom) position;[107] grid lines indicating centre points of cooling channel pins at radial outer position (bottom)

The DT pattern after cool-down at radial centre position is shown in top of Figure 5-14. The brake disc gets thicker during the first 50 cycles, then several narrow dents form, which are grouped in thicker areas. Their form is similar to the cooling channel pins. At the position of the through-thickness crack ($\varphi = 150°$), a single cooling channel pin extrudes extremely during $100 < N < 200$. The single cooling channel pin extrusion happens coincidently with the growth of the through-thickness crack in this area. Afterwards, the dent becomes visible at radial outer position (Figure 5-14 bottom) as the crack continues growing at radial outer

[107] Bilgic Istoc, S.; Winner, H.: The Influence of SRO and DTV (2018).

position. In contrast to radial centre position, the brake disc gets thinner on average by 37.8 µm at radial outer position from the beginning to the end of the test. At radial outer position, the extrusion caused by the cooling channel pins is clearly visible on the entire circumference of the disc. Nevertheless, in cold state, the brake disc is thinner at the angular positions of the cooling channel pins (0°, 12°, 24° …). The extrusion of the cooling channel pins in hot state, when the brake disc is thicker at cooling channel pin positions (convex dents, cf. Figure 8-22), causes consequently concave dents at the cooling channel pin positions after cool-down (cf. also Figure 8-21).

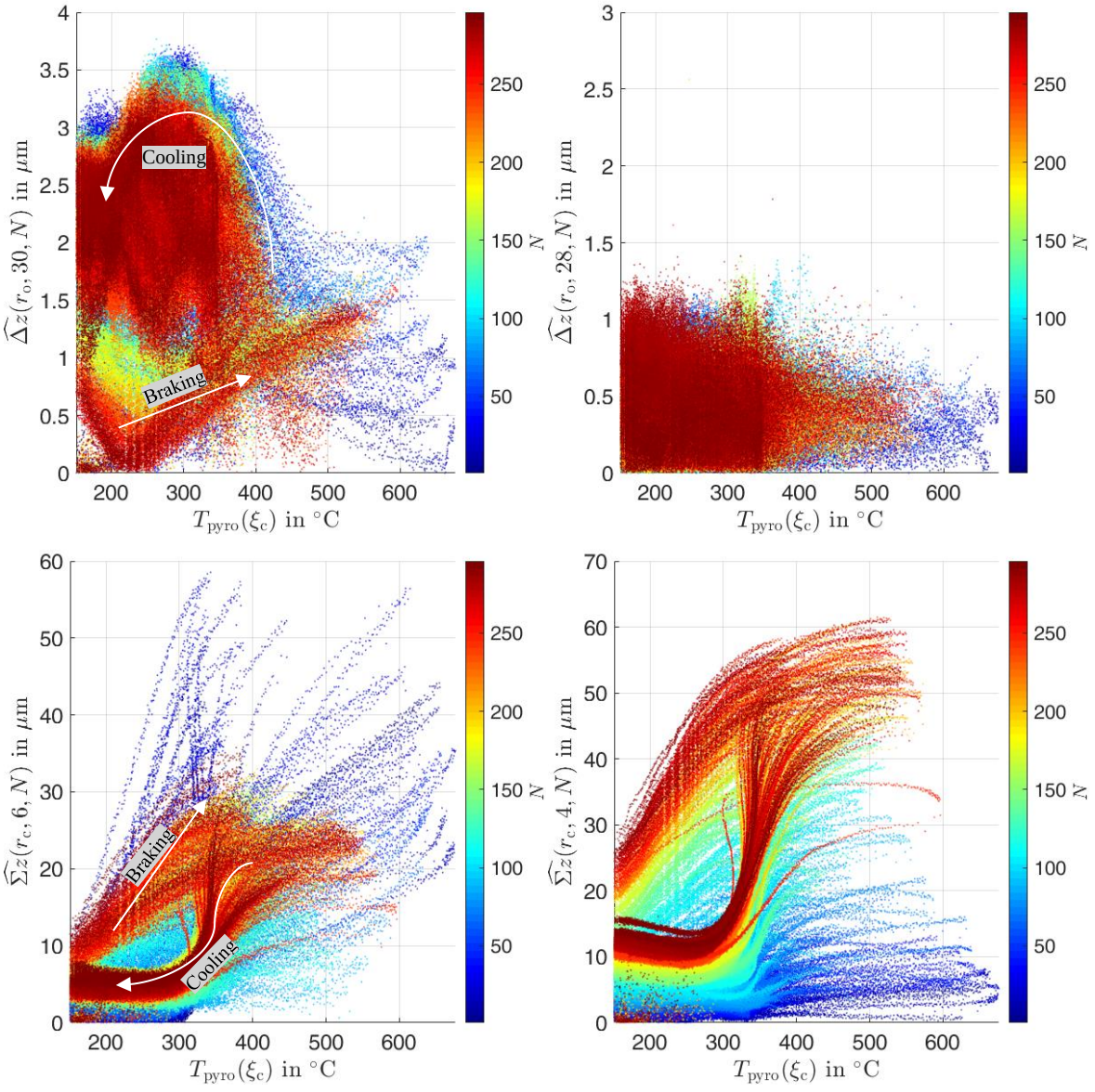

Figure 5-15: Amplitude of DTV (top)/SRO (bottom) at radial outer/centre position vs. temperature; top left: 30th order; top right: 28th order; bottom left: 6th order; bottom right: 4th order

The amplitude of the extrusion caused by the cooling channel pins in relation to the temperature is plotted in Figure 5-15, top left. At the beginning of the braking period, the amplitude of 30th-order DTV is rather low (1 µm). During the braking period, the amplitude lowers

even more and afterwards rises in order to reach a level of around 1.5 µm. During cool-down, the amplitude rises further, reaching a peak of 3 - 3.5 µm when the surface temperature is about 300 °C high. The delay of the cooling channel pin extrusion might be caused by the delayed heat dissipation into the cooling channel pins through the friction ring. Later, the amplitude lowers again. In general, the amplitude lowers in the course of the test. For other orders, e.g. the 28th order shown in Figure 5-15 top right does not show any temperature dependent trend.

For the evolution of the dominant SRO amplitudes, a different behaviour is observed. 6th-order SRO amplitude (Figure 5-15 left) rises during the first cycles to over 50 µm. During cool-down, the amplitude falls rapidly under 10 µm when the surface temperature approaches 300 °C. The general behaviour remains qualitatively steady after $N > 50$, although peak amplitudes are limited to roughly 30 µm. In contrast to DTV, the general amplitude level of SRO rises in the course of the test, except for the drop of the peak levels after $N > 50$. The overall 4th-order SRO amplitude (Figure 5-15 right) rises constantly during the entire test, starting with rather low amplitudes of 10 µm and reaching peaks of over 60 µm at the end of the test.

In conclusion, the brake disc tends to become less stiff in the course of the test. Cooling channel pin induced extrusions lower and SRO rises. SRO in hot state matches the hotspot pattern while SRO in cold state qualitatively and quantitatively differs. Cracks grow in zones of convex SRO formed during braking and dents form at cooling channel pin extrusion positions after cool-down.

5.2.3 Crack Formation

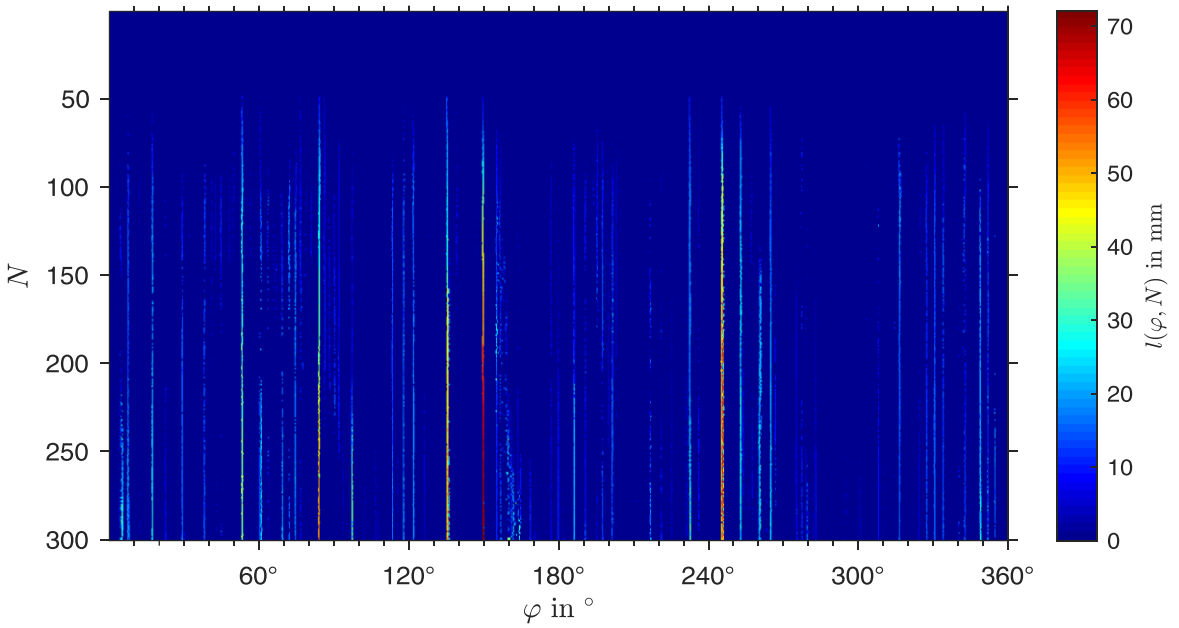

Figure 5-16: Crack pattern of the *Reference* brake disc[108]

The first cracks form after $N > 50$ (cf. Figure 5-16). In general, cracks are not uniformly distributed over the friction ring surface. Moreover, multiple areas of high crack growth and a single area of low crack growth are present on the surface. In $280° < \varphi < 310°$ nearly no cracks are present. This is the exceptionally cool and concave area reported in the last sections. Longest cracks are located at $\varphi = \{150°; 246°; 136°; 85°\}$ in descending order regarding their length (Figure 8-23). The crack at $\varphi = 150°$ becomes the through-thickness crack at the end of the test. It grows steadily from the 52nd heat crack cycle on, being one of the first open cracks. Directly next to it, several smaller cracks open up in the course of the test. The crack opening zones moves in rotational direction, following the migration pattern of the hotspots. The crack at $\varphi = 150°$ keeps growing, although the hotspot has moved away from its position. Nevertheless, strongly convex SRO is present at the crack location, as mentioned before. A similar, migrating crack opening zone is present at $\varphi > 275°$ and $\varphi > 85°$. At the latter one, cracks even close one after another in rotational direction.

[108] Bilgic Istoc, S.; Winner, H.: The Influence of SRO and DTV (2018).

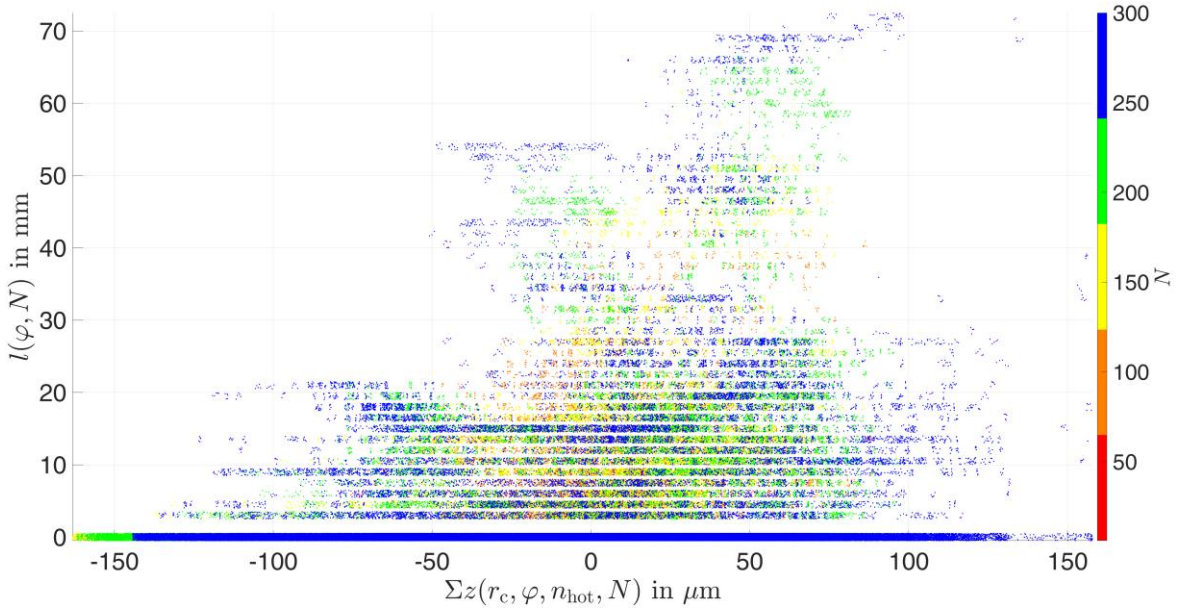

Figure 5-17: Crack lengths vs. SRO in hot state at radial centre position

The relationship between the spatial coherence of long cracks and SRO value is shown in Figure 5-17. No cracks with $l > 55$ mm form in areas of SRO value ≤ 15 µm, which equals the absence of longest cracks in areas of concave SRO. Cracks with $l < 20$ mm are mostly uniformly distributed in areas of concave and convex SRO. Longer cracks occur by trend in areas of convex SRO. In cold state, the through-thickness crack grows in an area of convex SRO (cf. Figure 8-24). For the gradient of SRO, a similar behaviour is observed (Figure 5-18). Most cracks with $l > 40$ mm form in areas of rising SRO, i.e. where the brake pad climbs the hill on the HS.

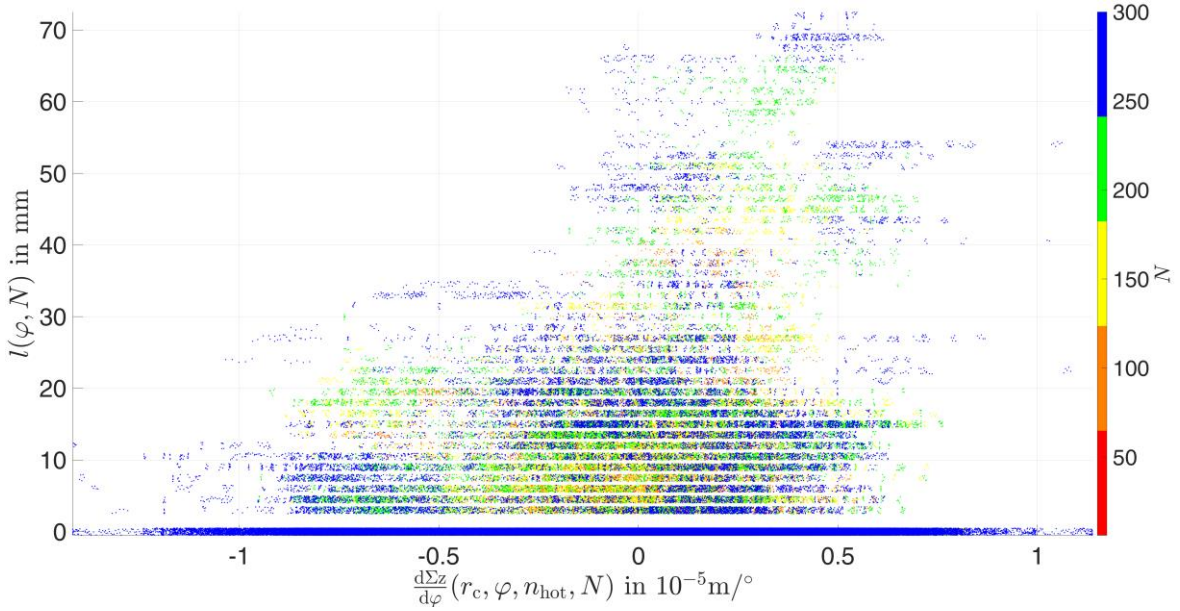

Figure 5-18: Crack lengths vs. gradient of SRO in hot state at radial centre position

In conclusion, cracks form in zones of high SRO values, non-uniformly distributed along the friction surface. The hotspot pattern defines the zones of crack opening.

5.2.4 Microstructural Transformation and Surface Hardness

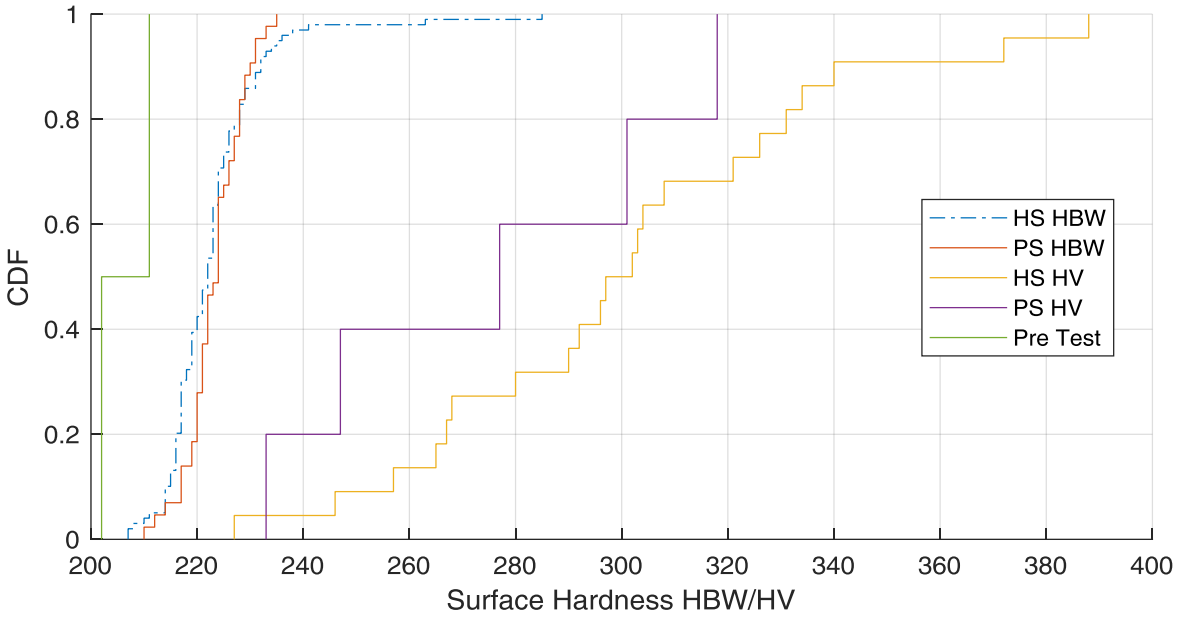

Figure 5-19: CDF of the surface hardness before/after the heat crack test; *Reference* brake disc, hat and piston side

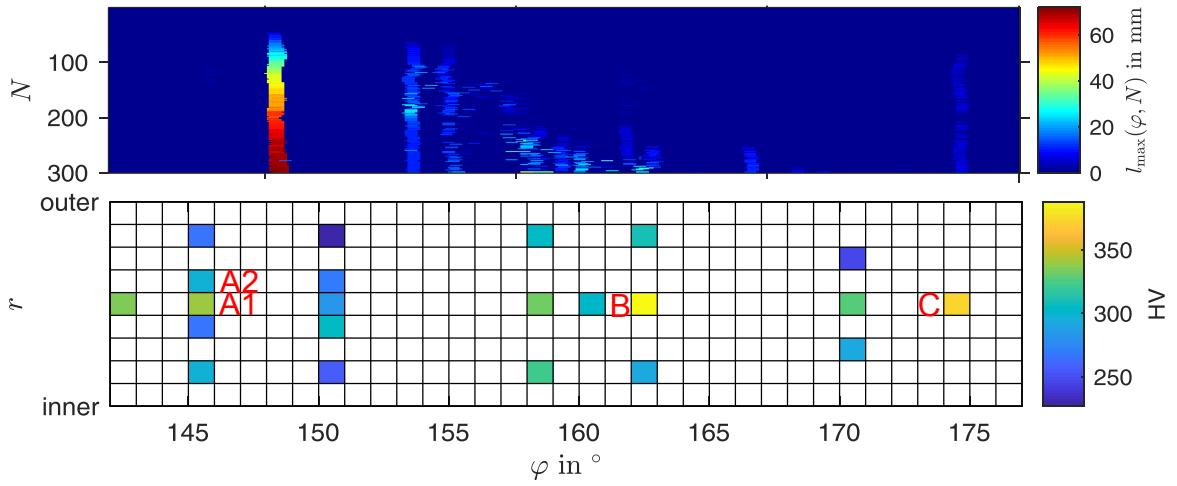

Figure 5-20: Surface hardness of a segment of the *Reference* brake disc, sampling positions for micrograph sections A/B/C marked (bottom); for reference: crack pattern of the respective segment, taken from Figure 5-16 (top)

Before the heat crack test started, the brake disc's surface hardness was 202/211 HBW (cf. Figure 5-19). After completion of the heat crack test, surface hardness increased on 95 % of the measurement positions on both HS and PS. For measurements carried out with the less intrusive Vickers method (HV), the increase in hardness was even higher, namely an average increase of hardness of roughly 10 % (HBW method) and even 40-50 % (PS/HS, HV method). The peak hardness value has been measured on the HS next to sampling position B, being with 388 HV almost twice as high as measured before the test started. This indicates that hardness increased more in surface near layers compared to more deeply located layers.

The peak hardness value is located on radial centre position (cf. Figure 5-20) at sampling point B, where the hottest hotspot of the second half of the test has moved over the surface (cf. Figure 5-10) and multiple smaller cracks opened up one after another (cf. Figure 5-16). In general, hardness is higher in radial centre position compared to radial inner and outer position. However, there appears to be no correlation between hardness and crack length, since surface hardness is higher in the crack-free sampling area C compared to the position of the through-thickness crack, A. Furthermore, local transformation depth and hardness do not seem to correlate as well, since hardness near sampling area A1 is higher compared to hardness near sampling area A2 and no transformation is present in area A1, while deep transformations are present in area A2 (cf. Figure 5-22). Still, it should be noted that transformation depth varies strongly spatially and hardness measurement and micrographs samples are located few millimeters away from each other (see next section).

Polished micrographs provide information about microstructural transformations that cause hardness changes in the observed section. The original microstructure is pearlitic/ferritic, as a sample taken from the unaffected neck area reveals (cf. Figure 5-21 top). The microstructure is homogenous, and no transformations are visible. In sampling area C, microstructural transformations of varying depth are visible (cf. Figure 5-21 centre), ranging from 0 µm to 204 µm, within a radial distance of less than 1 mm. In the transformed areas, the microstructure shows partially carbides. Furthermore, a narrow oxide layer on the surface is visible in detail view. The huge spatial variance of the transformation depth indicates that hotspots are far narrower than previously assumed, since overheating is required for microstructural transformations. In the area of peak hardness (sampling area B), deep transformation of 401 µm is visible (cf. Figure 5-21 bottom). Here, oxidation is more widespread and micro cracks are visible on the oxidised surface. Furthermore, the former pearlitic microstructure has widely transformed into carbides.

Figure 5-21: Polished micrographs of the *Reference* brake disc, overview (left) and detail (right); top: unaffected state, taken from the neck, pearlitic microstructure;[109] centre: area with microstructural transformations of varying depth, taken from a crack-free area (sampling area C), partially carbides present;[110] bottom: deep transformation showing carbides and oxidation (sampling area B)[109]

[109] Bilgic Istoc, S.; Winner, H.: A New Model (2018).

[110] Bilgic Istoc, S.; Winner, H.: Influences, Interactions and Prediction Potential (2019).

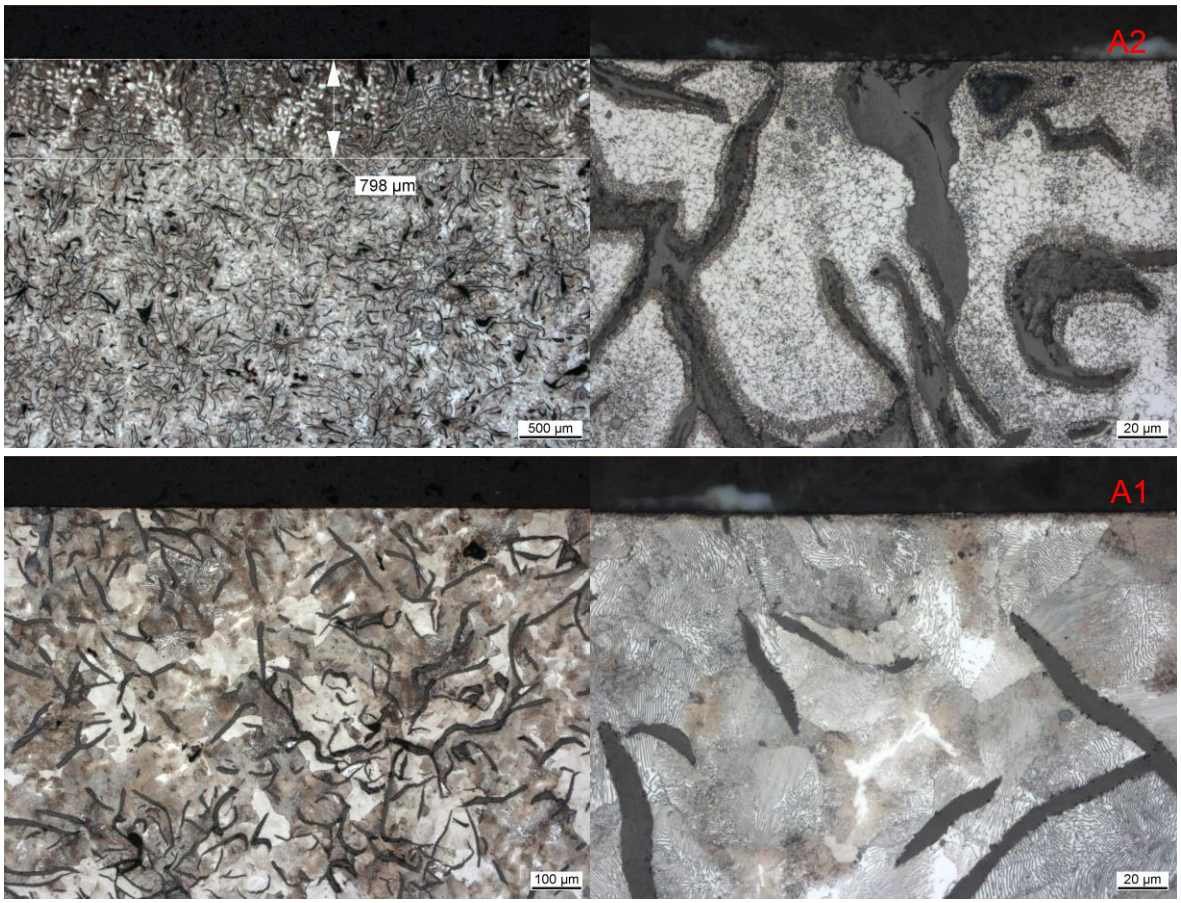

Figure 5-22: Polished micrographs of the *Reference* brake disc, overview (left) and detail (right); top: area A2 with deep microstructural transformation, taken in close proximity to the through thickness crack at $r = 177$ mm, ferrite, spheroidal cementite, carbides; bottom: area A1 with no visible microstructural transformation, taken in close proximity to the through thickness crack at $r = 170$ mm $\approx r_c$, pearlitic microstructure

The deepest transformations have been observed in sampling area A2 (cf. Figure 5-22 top). Microstructural transformations of 798 µm are present at radial centre position, directly next to the through thickness crack. In addition to the other transformations mentioned before, spheroidal cementite is present in the transformed layer. Oxidations around graphite lamellae show micro cracks intruding into the brake disc. The through-thickness crack initiated close to this area (cf. Figure 8-26).

However, in sampling area A1, which is located 7 mm from area A2 in radial direction towards the inside and located directly to the through-thickness crack, no microstructural transformations are visible (cf. Figure 5-22). The microstructure appears to be untouched and is similar to the reference microstructure observed at the neck (dominantly pearlitic). This indicates that cracks, after they have opened up, are able to propagate through areas that have not suffered from any microstructural transformations.

In conclusion, microstructural transformations seem to be responsible for crack initiation. However, they are not a necessary condition for propagation of already opened cracks.

5.2.5 Residual Stresses

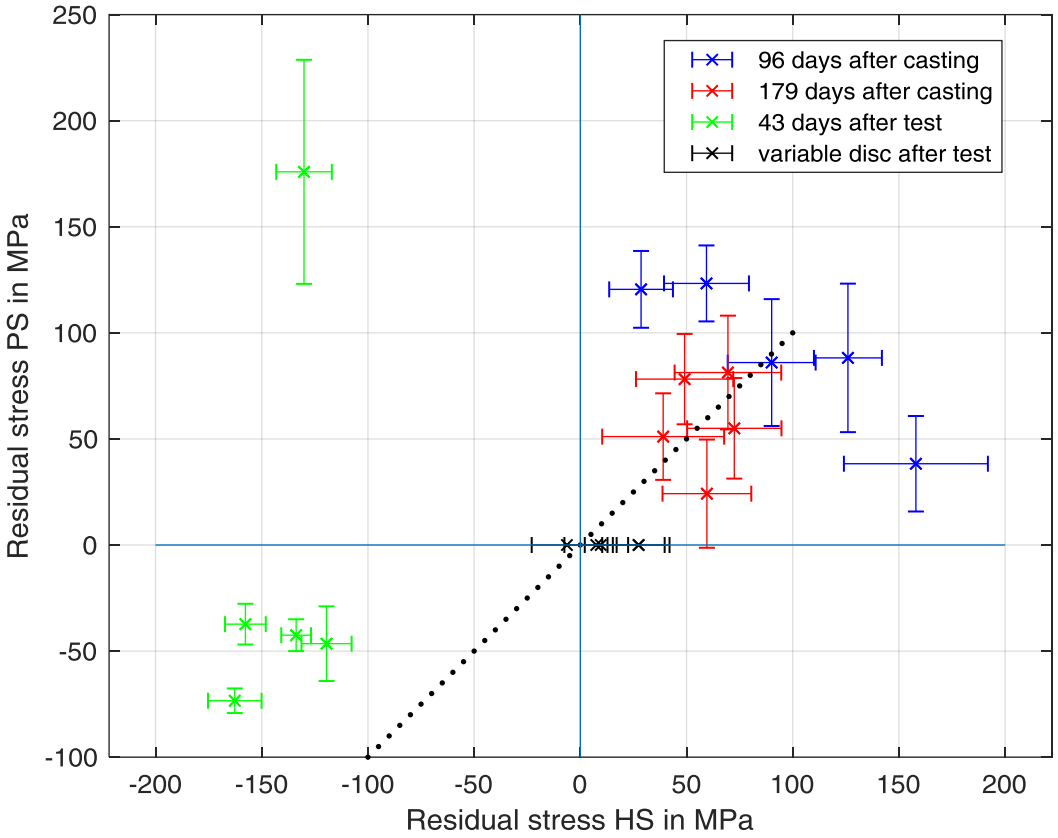

Figure 5-23: Residual stresses of the PS vs. the HS; *Reference* brake disc (blue, red, green) and *Variable* disc (black)

Figure 5-23 shows residual stresses on the surface of HS and PS of the *Reference* brake disc and on the HS of the *Variable* brake disc. The *Reference* brake disc has been observed 96 days after casting, 179 days after casting and 43 days after the subsequent heat crack test. The *Variable* disc has only been observed after the test. In general, residual stresses apparently reduced after casting and are all positive, i.e. tensile stresses. Values for 96 days after casting are on average around twice as high compared to 179 days of casting. This indicates that residual stresses, which remain from the casting process, might reduce during rest of the brake disc. No prevalence towards one of both friction surfaces could be found. However, as it is unclear how residual stresses are able to reduce during rest at room temperature, measurement results are doubted.

After the heat crack test, tensile stresses apparently transformed into compressive stresses. This is not consistent to established models and also contradicts the fact that cracks open up on the brake discs surface in circumferential direction due to circumferential tensile stresses. Now, stresses on the HS are two to three times higher compared to the PS. One value indicates tensile stress on the PS and is considered to be an outlier, since it has been measured directly on a fissure, making it impossible to obtain valid readings. Currently, there is no

explanation why compressive stresses remain on the surface after the heat crack test. Probably a series of high pressure brakings that has been performed after the heat crack test for cleaning of the friction surface has caused compressive stresses.

For that reason, the *Variable* brake disc has been tested regarding residual stresses as well. No high-pressure braking series was applied to the *Variable* brake disc after the test. This time, nearly no compressive stresses could have been measured. All measured stresses are close to zero within measurement tolerance. That means that residual tensile stresses have either reduced since the test has finished, are not evaluable due to friction dust coating, or are not present at the measurement positions. Again, measurement results are doubted as values greatly spread.

5.2.6 Low Cycle Fatigue

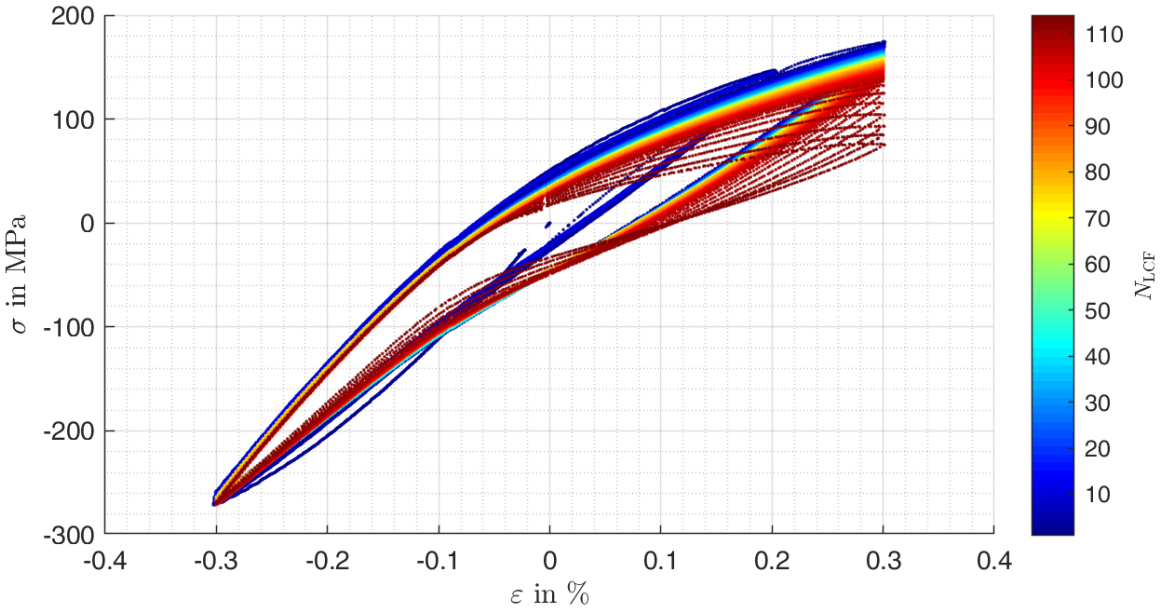

Figure 5-24: Stress-strain curve at room temperature

Stress-strain response at room temperature of the tested specimens made from the *Twin* disc of the *Reference* brake discs is shown in Figure 5-24. It shows non symmetric behaviour in compression and tension typical for GJL (cf. section 2.2.2). Additionally, cyclic fatigue is present and visible as a degradation of the maximum stress level at maximum strain. Degradation of maximum stress level is used for parametrisation of the FE model and plotted over cycle number in Figure 8-27. Stress level is lowering constantly for the first 100 cycles and then abruptly during the last 10 cycles, most probably due to macro crack growth at the specimen.

Stress-strain response at 700 °C is shown in Figure 5-25. At high temperature, material gets softer, resulting in less stress at similar strain levels. In addition to this, relaxation occurs during dwell periods. This way, stress level is reduced to roughly one third in tension and

two thirds in compression. Finally, maximum number of cycles is greatly reduced, and macro crack growth starts much earlier.

Stress-strain curves are used for parameterisation of the material models (cf. section 6.2.3).

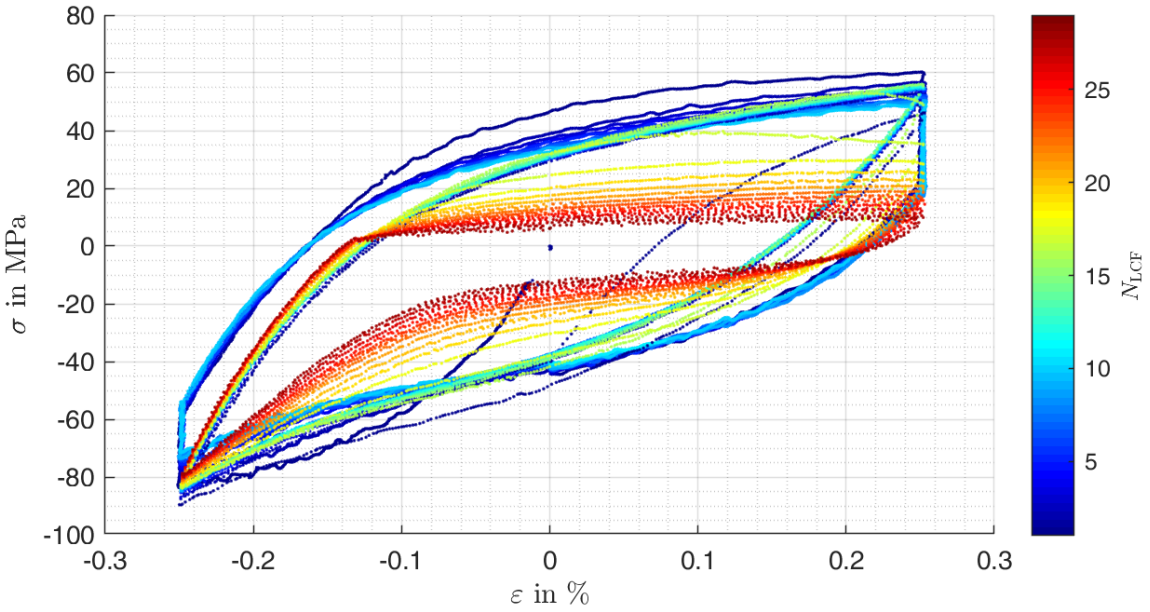

Figure 5-25: Stress-strain curve at 700 °C

5.2.7 Hardness inside the Friction Ring

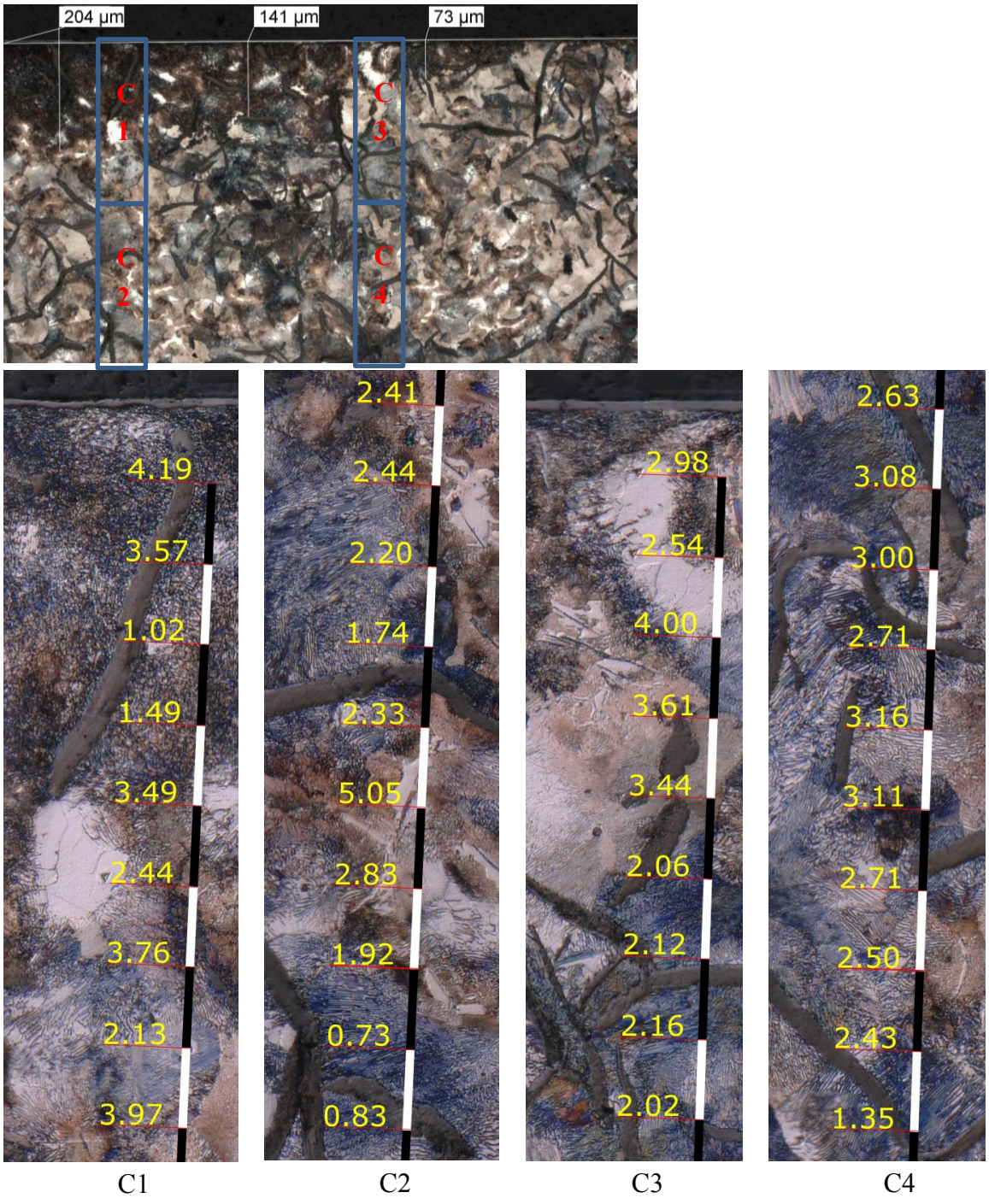

Figure 5-26: Overview of section C indicating positions of hardness measurement paths C1-C4 (top); detail view of hardness measurement paths C1-C4 (bottom left to right) with nano hardness values in GPa; indentation points marked left of numbers;

Hardness is evaluated inside the friction ring based on nano indentation tests along the cross section. Two hardness measurement paths are shown in Figure 5-26, C1/C2 in an area with intermediately deep transformation and C3/C4 in an area with almost no transformation. On both paths, hardness varies depending on the microstructure at the intrusion point. In General, highest hardness (around 4 GPa) is present in surface near, transformed regions (C1,

first two rows; C3 third row). Lower hardness values (around 2.5 GPa) are found at ferrite particles. Lowest hardness values (around 1 GPa) were measured at graphite lamellae, regardless whether they are located in surface near, transformed areas (e.g. third/fourth row of C1) or in deep, untransformed areas (e.g. last two rows of C2). Exceptionally high hardness was found in the 6th row of C2 (5.05 GPa). No indication for soft annealing in deeper layers was found.

In the area with deep microstructural transformation (area A1), various microstructures show different hardness values as well (Figure 5-27). Again, graphite lamellae are partly extraordinarily soft (0.41-0.69 GPa, Figure 5-27 top centre/right). In contrast to this, graphite lamellae surrounded with oxidised material and covered with micro-cracks are extremely hard (5.96-6.76 GPa, Figure 5-27 top left). Oxidation might cause strong brittleness of the regions around the lamellae, resulting in them being the origin of heat crack formation. Again, ferritic parts of the microstructure are quite soft (1.73-2.98 GPa, Figure 5-27 top centre/right). However, remaining cementite parts of the microstructure show equivalently high hardness values.

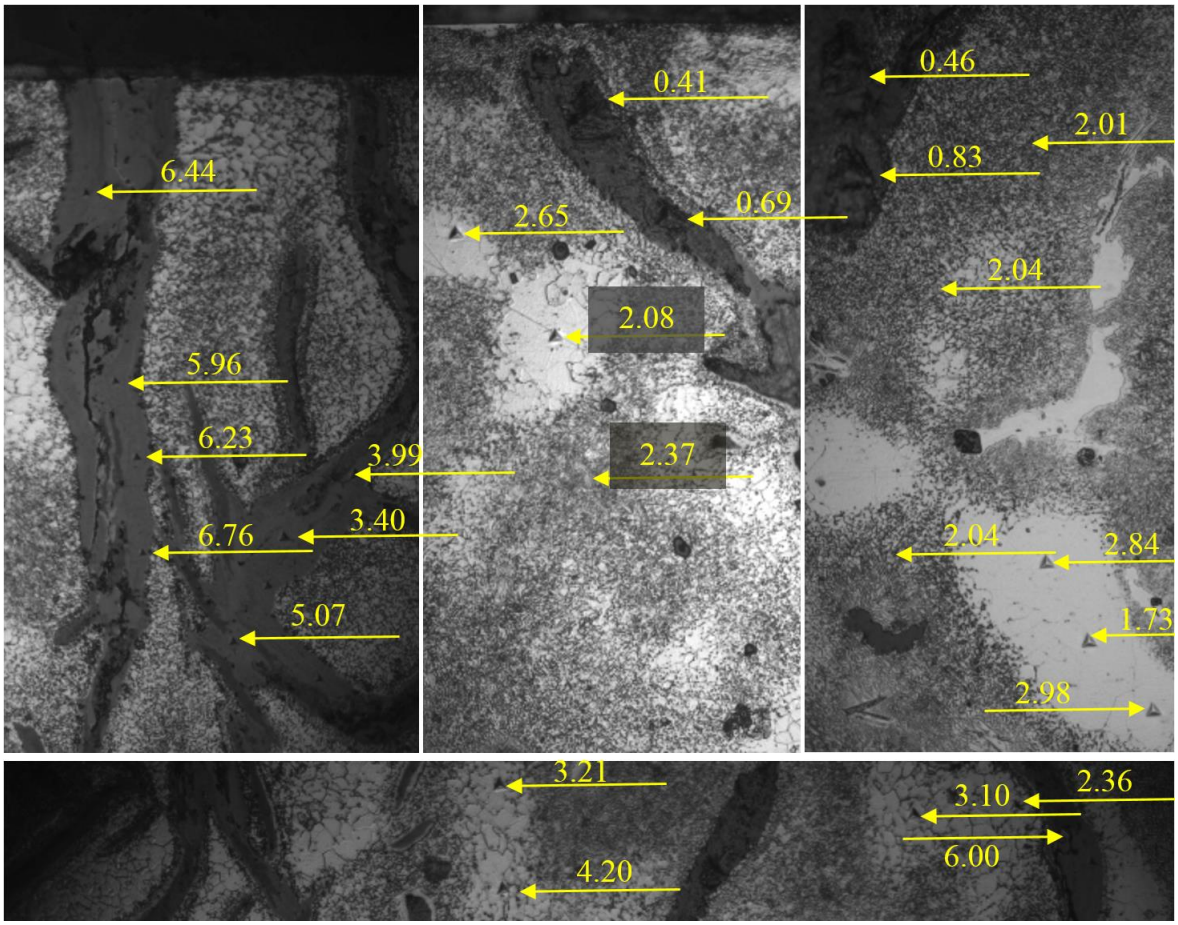

Figure 5-27: Hardness in area A1 (area with deep microstructural transformation); hardness values in GPa

5.3 *Variable* disc

The results obtained by the heat crack test with the *Reference* brake disc indicated that cooling channel pins have an influence on the friction ring surface due to their surface extrusion during cool-down. Since these extrusions might damage the friction ring surface, they might influence the crack formation by guiding the crack path along the projected edges. For that reason, the *Variable* disc is tested. Its design (cf. section 4.2.4) features all possible combinations of cooling channel pin arrangements, from radially aligned to radially staggered pin arrangements. Primary objective of the test is to determine the influence of the radial cooling channel pin arrangement on crack propagation, hotspot formation and disc deformation. Pins of the tested disc are radially aligned at $\varphi = 240°$, staggered at $\varphi = 60°$, slightly shifted in rotational direction from the inside to the outside at $\varphi = 330°$ and slightly shifted against rotational direction from the inside to the outside at $\varphi = 150°$ (cf. also Figure 5-33 bottom).

5.3.1 Hotspot Formation

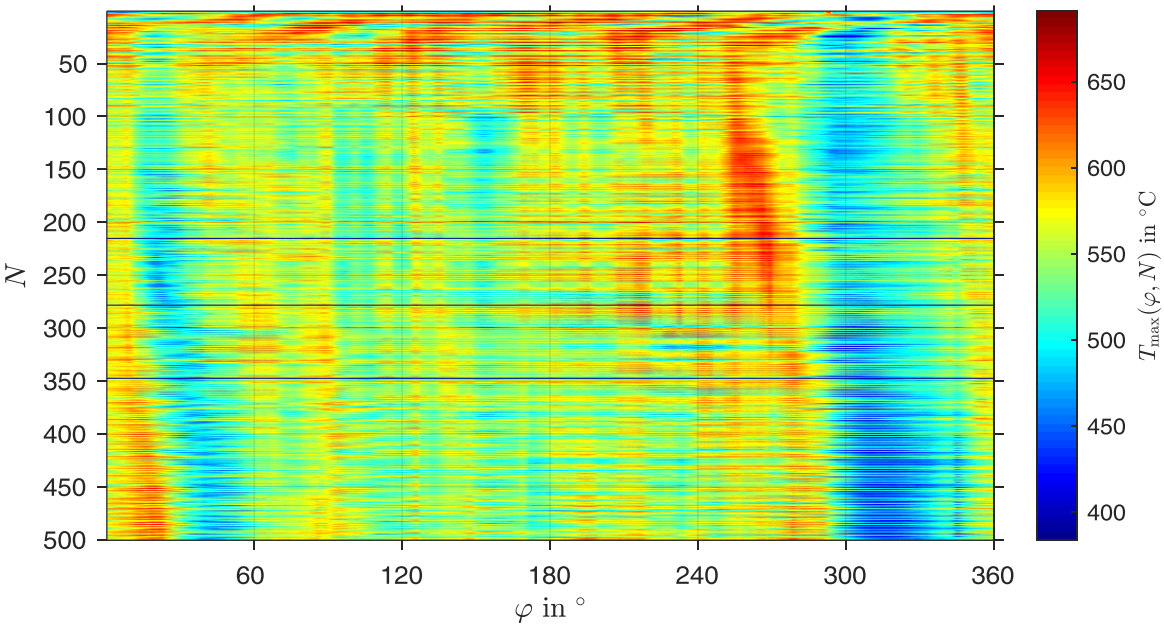

Figure 5-28: Hotspot pattern of the *Variable* disc[111]

Due to the cooling channel pin arrangement, hotspot behaviour of the *Variable* brake disc changed significantly. The hotspot pattern is plotted in Figure 5-28. Up to $N \approx 30$, 5 harmonic hotspots, which is one hotspot less compared to the *Reference* disc, migrate quickly over the friction surface. The migration behaviour is similar to the *Reference* brake disc. However, the movement stops earlier and in one area of the brake disc around $\varphi \approx 260°$ a broad, hot hotspot is present for the rest of the test. Another hotspot comparable to the

[111] Bilgic Istoc, S.; Winner, H.: A New Model (2018).

hotspots of the *Reference* disc considering amplitude, width and migration behaviour migrates from $\varphi = 350°$ to $\varphi = 20°$ during the rest of the test. The other hotspots form as fixed, narrow hotspots, which align with the cooling channel pins. Between $290° < \varphi < 350°$, an exceptionally cool area forms.

Generally, the hotspot spectrum is broader (cf. Figure 5-29) in comparison to the *Reference* brake disc, and a clear, dominant order is missing. Furthermore, the peak amplitude of the harmonic 5th order is with 14.1 dBK only half as high as the harmonic hotspots of the *Reference* brake disc and the remaining hotspot orders are not as distinguishable from each other as observed at the *Reference* disc. However, hotspots of 30th order, which corresponds to the number of cooling channel pins in circumferential direction at radial centre position, is more present in comparison to the *Reference* brake disc.

In conclusion, the cooling channel layout directly influences the hotspot formation. Harmonic hotspots vanish more quickly and mostly transform into narrow, cooler hotspots in between the cooling channel pins in the where they slightly align. A broad and hot hotspot forms in the area, where pins radially align. In the area where pins are arranged staggered, which matches the alignment of the pins of the *Reference* brake disc, hotspots form corresponding to the hotspot formation of the *Reference* brake disc. The area where the pins are aligned and shifted in rotational direction remains exceptionally cool.

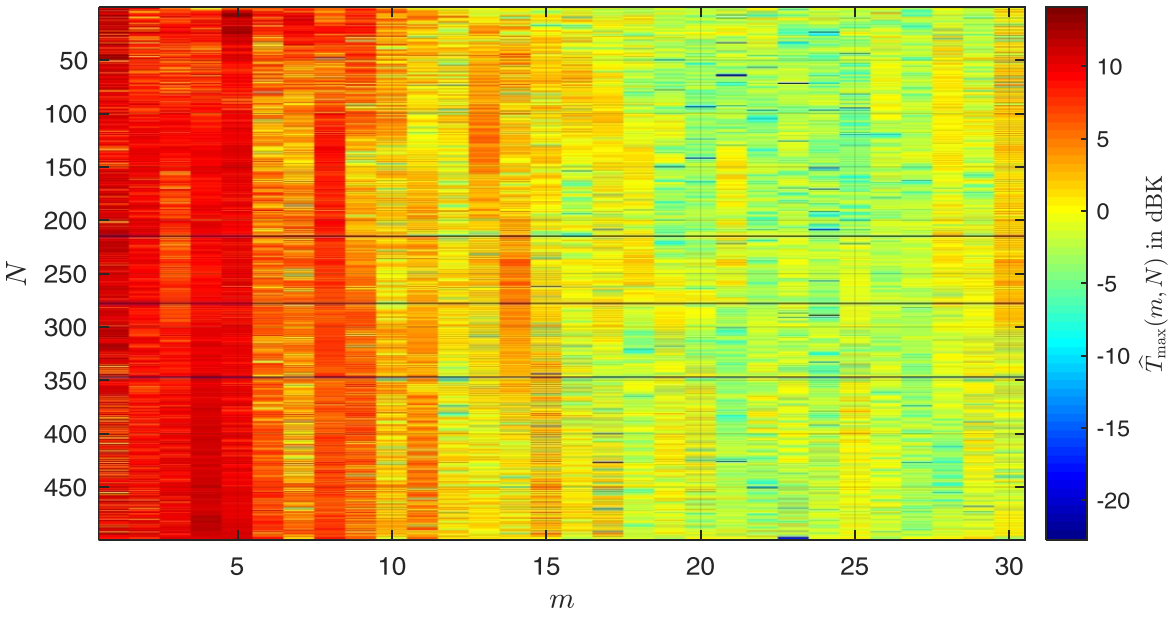

Figure 5-29: Amplitude spectrum of the hotspots

5.3.2 Influence of Cooling Channel Geometry on Friction Surface Topology

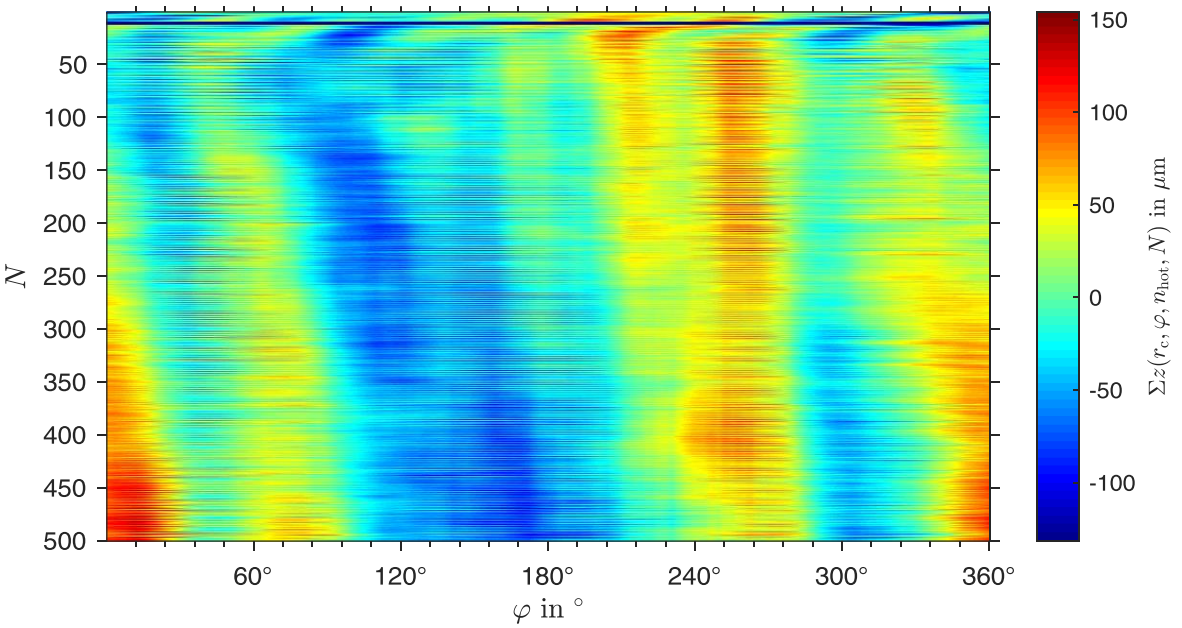

Figure 5-30: SRO pattern of the *Variable* disc, evaluated in hot state at radial centre position

Comparable to the *Reference* brake disc, the SRO pattern of the *Variable* disc (Figure 5-30) is similar to the hotspot pattern and shows the same migration pattern. However, at $\varphi > 240°$, convex SRO seems is fixed and does not move during the test. This area turns out to be exceptionally crack prone (cf. Figure 5-33), which might be related to the fixation of convex SRO. The level of the maximum SRO amplitude is also similar to the *Reference* brake disc. Harmonic SRO at the beginning of the test is weaker in comparison to the *Reference* disc. Highest convex SRO values form around $\varphi \approx 0°$ and even rise in the end of the test.

The disc thickness pattern after cool-down is shown in Figure 5-31. The area around $300° < \varphi < 360°$ roughly maintains its thickness during the entire test. In other areas, cooling channel pins extrude through the surface, resulting in characteristic DTV dents. In contrast to the *Reference* brake disc, high disc thickness is present only in one, coherent area between $60° < \varphi < 290°$. The width of this area shrinks in the course of the test, as the brake disc gets thinner.

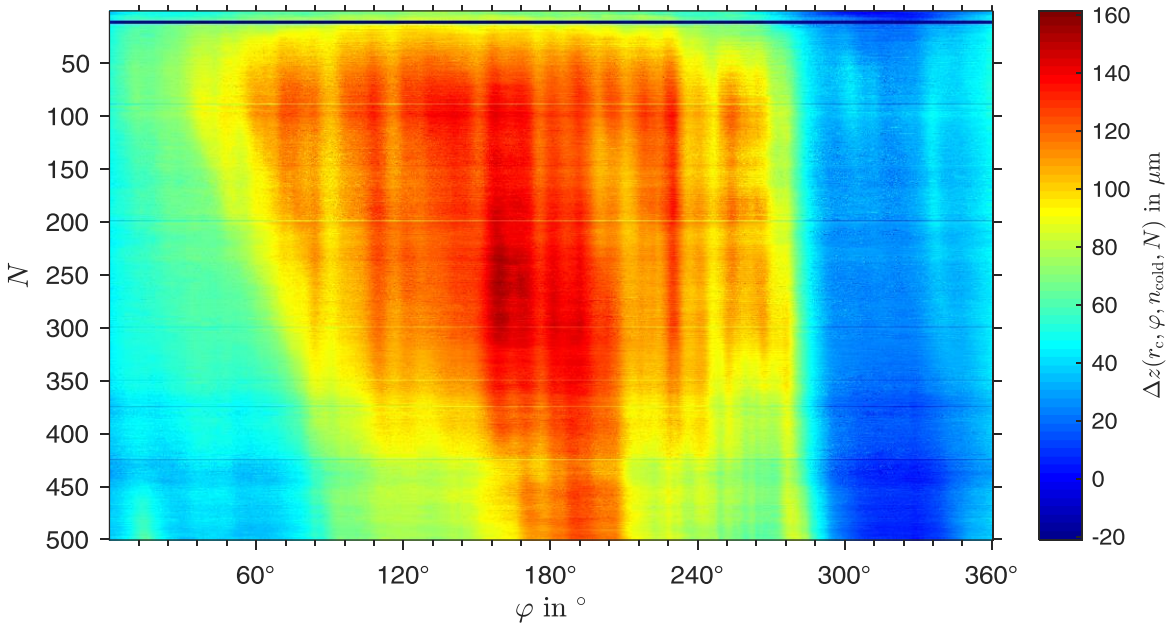

Figure 5-31: DT pattern of the *Variable* disc, evaluated in cold state at radial centre position

At radial outer position, the number of cooling channel pins is 31 for the *Variable* brake disc. Accordingly, the extrusion, seen as dents in the DT pattern, is observable only for the 31st order of DTV, not for the 30th order (Figure 5-32 top). While the 30th order remains beyond 1.6 µm and does not show any characteristic magnification, 31st order DTV of the *Variable* disc shows the same behaviour compared to 30th order DTV of the *Reference* disc. Again, amplitude rises during cool-down to values around 3 µm. During braking, the amplitude remains low. General amplitude level lowers in the course of the test, which can be explained this time by the general shrinkage of the brake disc. Finally, the behaviour of the *Variable* brake disc considering pin extrusion is quite similar to the *Reference* disc regarding amplitude level and evolution.

The evolution of SRO (Figure 5-32 centre) is similar to the *Reference* disc. SRO amplitudes of the 5th order, which corresponds to the harmonic hotspot order, rise almost linearly during braking to maximum amplitudes of 35-40 µm, which is lower than the maximum amplitudes reached by dominant SRO orders of the *Reference* disc of 50-60 µm. Other orders, e.g. the 4th order, reach peak amplitudes of 30-35 µm, which are nearly half as high compared to the *Reference* disc with around 60 µm. Additionally, the rise of the general SRO amplitude level at radial centre position in the course of the test is not as high as it is for the *Reference* disc. However, at radial outer position, a strong trend of general rising of SRO amplitude is visible during the entire test (Figure 5-32 bottom). Again, amplitudes remain lower compared to the *Reference* disc (25-35 µm vs. 45-55 µm). 1st-order SRO rises as well throughout the entire test (cf. Figure 8-30). The general reduction of SRO amplitudes might be caused by the fact that no clear SRO orders form during the test. Amplitudes are more blurry and more evenly distributed instead.

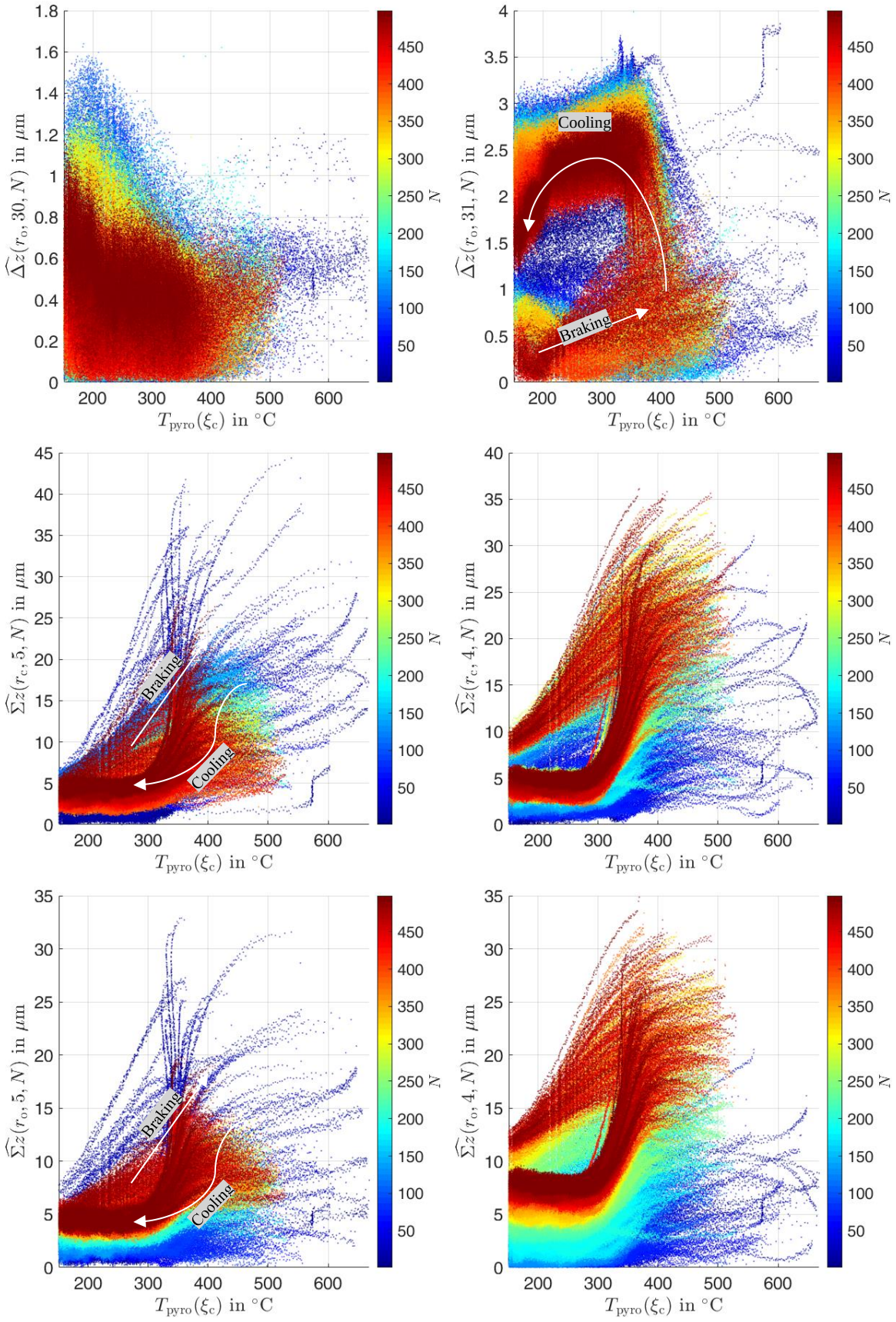

Figure 5-32: Amplitude of DTV (top)/SRO (centre/bottom) at radial outer/centre position vs. temperature; top left: 30th order; top right: 31st order;[112] centre left: 5th order; centre right: 4th order; bottom left: 5th order; bottom right: 4th order

In conclusion, the variable cooling channel pin distribution causes a more blurry SRO pattern compared to the harmonic pattern of the *Reference* disc. The effect of extrusions caused by cooling channel pins during cool-down is confirmed, since the number of cooling channel pins matches the order of DTV on both discs (30th vs. 31st order).

5.3.3 Crack Formation in Relation to Cooling Channel Geometry

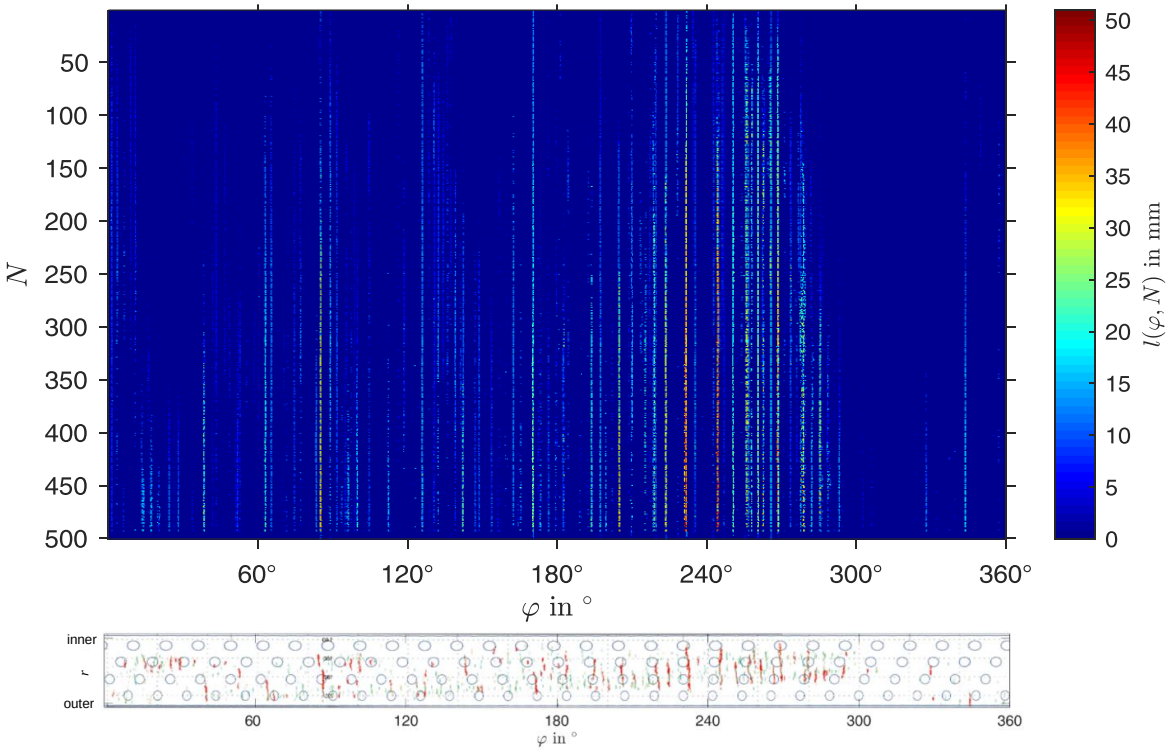

Figure 5-33: Crack pattern of the *Variable* disc (top);[112] overlay of cracks and cooling channel geometry (bottom)

The most obvious effect of the cooling channel pin arrangement is its influence on crack propagation. Although cracks initiate in the very first cycles of the test on the entire friction surface, in the area of radially aligning pins a vast number of cracks initiates (Figure 5-33). Furthermore, longest crack lengths are exclusively reached in this area. As the overlay of cracks and the cooling channel geometry reveals, cracks propagate along the projected edges of the cooling channel pins, supporting the hypothesis that the cooling channel pin extrusion guides the cracks along the friction surface (Figure 5-33 bottom). Longest cracks propagate after the projected pin location in rotational direction, i.e. right of the pins in the figure. However, even in the crack prone area around $\varphi \approx 240°$ where cooling channel pins radially align, crack lengths do not exceed 50 mm, which indicates that reduced temperature and SRO inhibit high crack growth. In the exceptionally cool area between $290° < \varphi < 350°$, nearly no cracks show up. The through-thickness crack forms at radial outside position of

[112] Bilgic Istoc, S.; Winner, H.: A New Model (2018).

the friction ring at $\varphi = 344°$. Its length reaches only 19.5 mm, which is untypical for a through-thickness crack. It occurs again in the area of highest rising convex SRO at the end of the test.

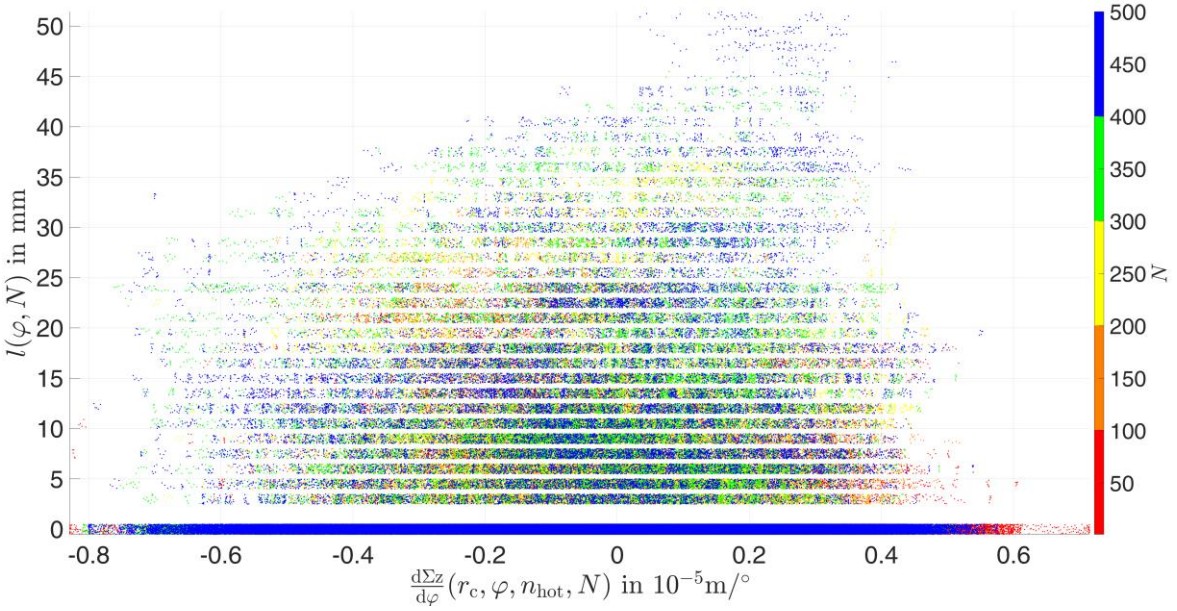

Figure 5-34: Crack lengths vs. gradient of SRO in hot state at radial centre position

In comparison with gradient of SRO, the same correlations for crack lengths are observed as they have been observed for the *Reference* brake disc. Longest cracks are exclusively located in areas of rising convex SRO at radial centre position (Figure 5-34). The same accounts for SRO at radial outer position (cf. Figure 8-31). Again, areas where the brake pad "climbs the hill" seem to be extraordinarily damaged during the heat crack test.

Crack lengths in relation to disc thickness are shown in Figure 5-35. As the brake disc gets thinner in the course of the test, the plot is shifted to the left after each 100 cycles. However, the correlation between crack length and thickness level is lower than the correlation between crack length and level of SRO gradient. Indeed, smaller cracks are located at the thinnest positions of the disc. However, this indicates that the absolute disc thickness does not directly influence crack growth. Its gradient (cf. Figure 8-32) still seems to affect the crack formation, as longest cracks are located in areas of falling thickness, which is consistent to the growth of longest cracks along the edges of extrusion of cooling channel pins (cf. Figure 5-33 bottom).

In conclusion, the results from the heat crack test with the *Variable* disc indicate that crack growth is directly affected by the cooling channel geometry in multiple ways: first, the circumferential continuous change of radial pin arrangement seems to vary the bending stiffness of the friction ring. As a result, SRO occurs less harmonic and higher SRO orders are damped. This results in overall lower temperatures and lower crack growth rates. Second, the cooling channel pin extrusion guides the crack propagation paths, as long cracks grow along the falling edge of dents that are radially aligned due to cooling channel design.

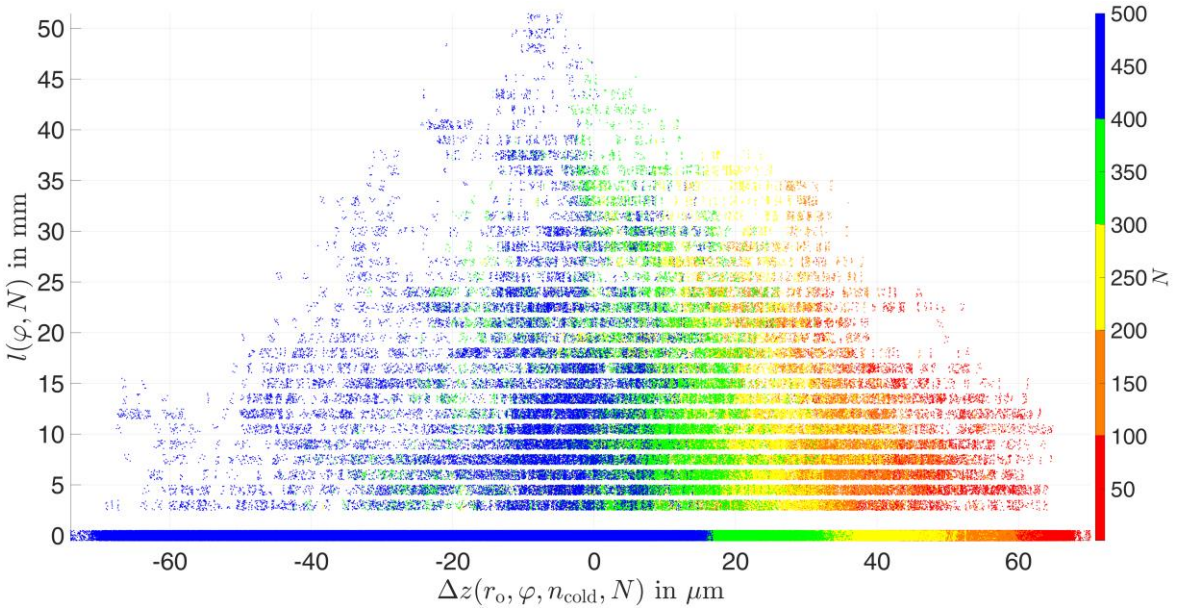

Figure 5-35: Crack lengths vs. DT in cold state at radial outer position

5.4 Brake Discs with Optimised Cooling Channel

Since the results of heat crack test with the *Variable* disc indicated that cooling channel pin arrangement influences crack growth, the brake discs with optimised cooling channel, which are designed based on the pin arrangement that caused least crack growth, are tested. The "*Constant*" disc features constant circumferential angular spacing of the cooling channel pins. They are slightly radially shifted in rotational direction. The "*Periodic*" disc features the same radial shifting. In contrast to the *Constant* disc, the circumferential pin spacing of the *Periodic* disc is varied periodically. Aim of the tests is validation of the findings of the previous tests, especially in terms of pin shifting and crack growth and to investigate on the effect of periodic variance of pin spacing, as this might also change the circumferential bending stiffness observed with the *Variable* disc.

In this chapter, results from both tests are discussed and compared with each other. Since both discs have been casted from the same batch, results are not affected by different material composition.

5.4.1 Influence of Pin Spacing on Hotspot Evolution

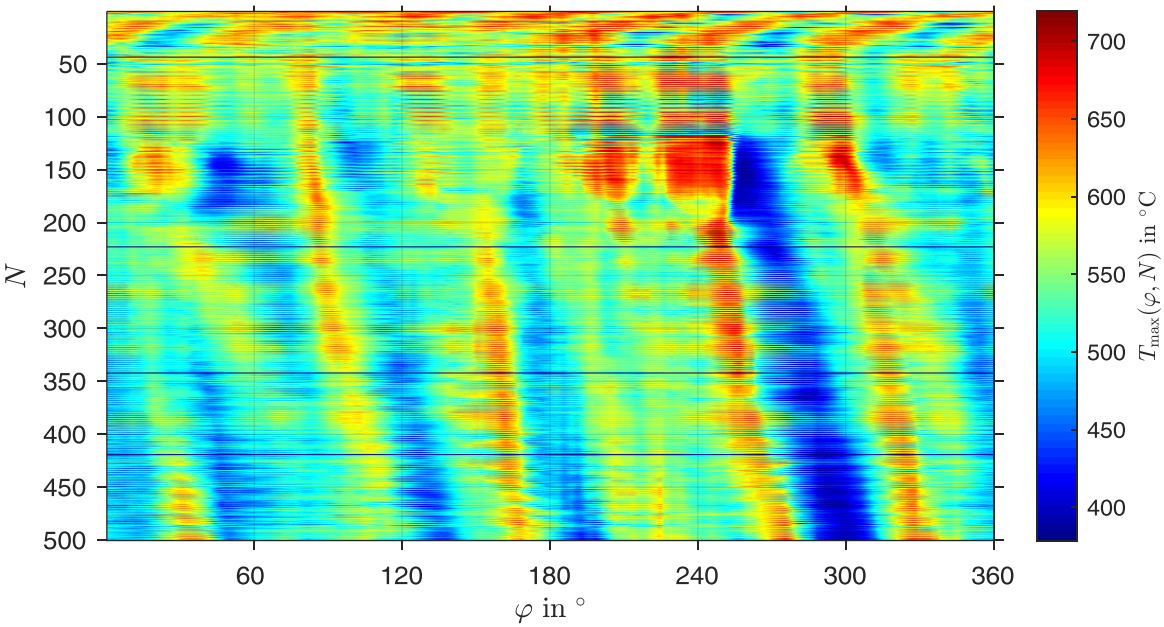

Figure 5-36: Hotspot pattern of the *Constant* disc[113]

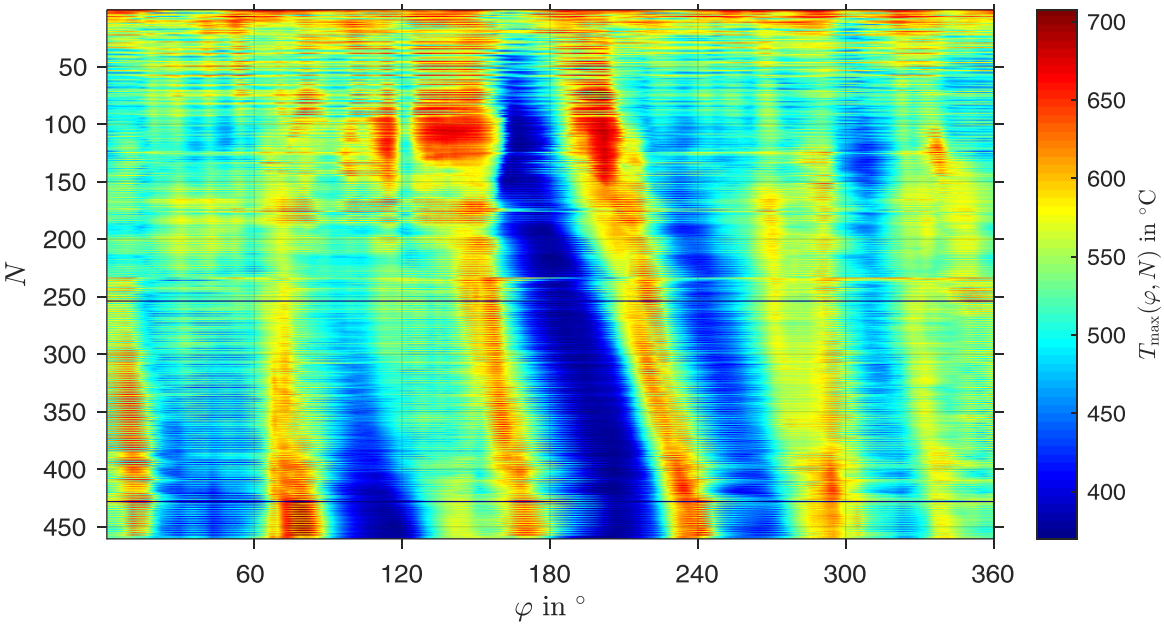

Figure 5-37: Hotspot pattern of the *Periodic* disc

The hotspot patterns of the *Constant* and the *Periodic* disc are shown in Figure 5-36 and Figure 5-37. For $N < 50$, 7 harmonic hotspots form on the *Constant* disc but not on the *Periodic* disc. Afterwards, fixed hotspots form on both discs and start slowly migrating after another 100 cycles. The dominant hotspot order of the *Constant* disc at the end of the test is higher compared to the *Periodic* disc (6^{th} vs. 5^{th} order, cf. Figure 8-33 and Figure 8-34).

[113] Bilgic Istoc, S.; Winner, H.: Influences, Interactions and Prediction Potential (2019).

However, both discs show comparably high maximum amplitudes of roughly 15 dBK like the *Reference* brake disc. In general, the hotspot pattern of both discs is more similar to the hotspot pattern of the *Reference* disc than to the *Variable* disc. Nevertheless, in the hotspot pattern of the *Periodic* disc, similarities to the *Variable* disc exist: cooling channel geometry is visible in the pattern. Furthermore, harmonic hotspots vanish earlier than $N = 50$. Remarkably similar is the hotspot pattern of both discs in the area around the coolest area of the disc. Between $180° < \varphi < 310°$ for the *Constant* disc and $100° < \varphi < 220°$ for the *Periodic* disc, two broad hotspots surround the cool area. These hotspots get narrower and start slowly migrating after $N > 150$. They enclose the cool area until the end of the test and are locations of highest temperature in the middle of the test. The other tested disc features similar hotspot surrounded cool areas, but rather less obvious (*Reference* disc: $240° < \varphi < 360°$; *Variable* disc: $250° < \varphi < 10°$). It is unclear, why these patterns form around one single, cool area. Nonetheless, especially the hotspot left to the cool area marks an area of exceptionally high temperatures and crack growth at all tested discs.

In conclusion, variable pin spacing has a similar effect than variable pin arrangement with constant spacing: harmonic hotspots are suppressed, and cooling channel geometry becomes visible in the hotspot pattern. This might be caused by the effect of cooling channel pin spacing on the bending stiffness of the friction ring and will be discussed further in the next section.

5.4.2 Friction Surface Topology

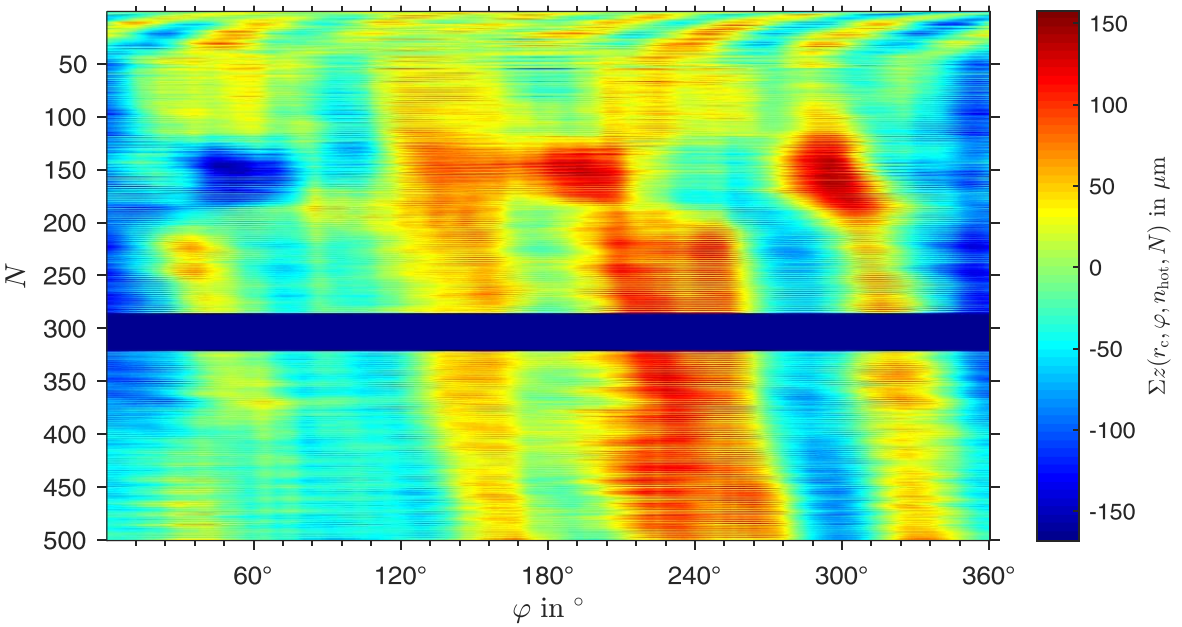

Figure 5-38: SRO pattern of the *Constant* disc, evaluated in hot state at radial centre position[114]

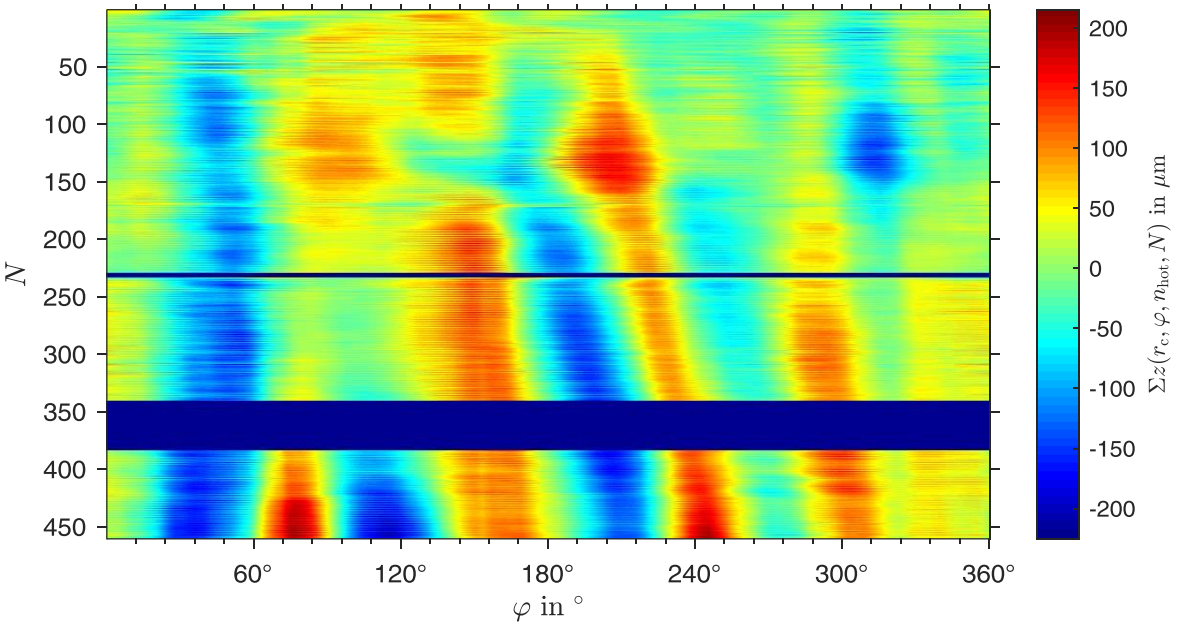

Figure 5-39: SRO pattern of the *Periodic* disc, evaluated in hot state at radial centre position

As observed with the *Reference* and *Variable* disc, the SRO pattern in hot state is similar to the hotspot pattern (cf. Figure 5-38 and Figure 5-39). Harmonic, quickly migrating SRO is visible for the *Constant* disc during $N < 50$. After manifestation of the SRO pattern, an odd shifting of the pattern takes place during $125 < N < 180$ for the *Constant* disc and $100 < N < 150$ for the *Variable* disc. This shifting movement cannot be explained at this point, but

[114] Bilgic Istoc, S.; Winner, H.: Influences, Interactions and Prediction Potential (2019).

it occurs at the same time when broad and hot hotspots form for both discs. Therefore, it might trigger the formation of these extreme hotspots. However, the shifting is not observable with the *Reference* and the *Variable* brake disc.

Nevertheless, at the end of the test, extremely concave SRO values are present at the positions of the through-thickness respectively longest cracks, i.e. at $\varphi > 215°$ for the *Constant* disc and at $\varphi > 65°$ for the *Periodic* disc. Maximum SRO amplitude is higher for the *Periodic* disc compared to the *Constant* disc.

The DT patterns of both discs are quite similar as well (cf. Figure 5-40 and Figure 5-41). Again, the overall disc thickness reduces in the course of the test. However, for the period disc, thicker areas (e.g. at $\varphi \approx 300°$) are present throughout the entire test. Similar to the *Reference* and *Variable* disc, the exceptionally cool area is visible in the DT pattern as a thinner area compared to the rest of the disc. For both the *Constant* and the *Periodic* disc, cooling channel pins are less visible in comparison to the *Reference* and *Variable* disc. At radial outer position, cooling channel pins are more visible, especially for the *Constant* disc (cf. Figure 8-40 and Figure 8-41).

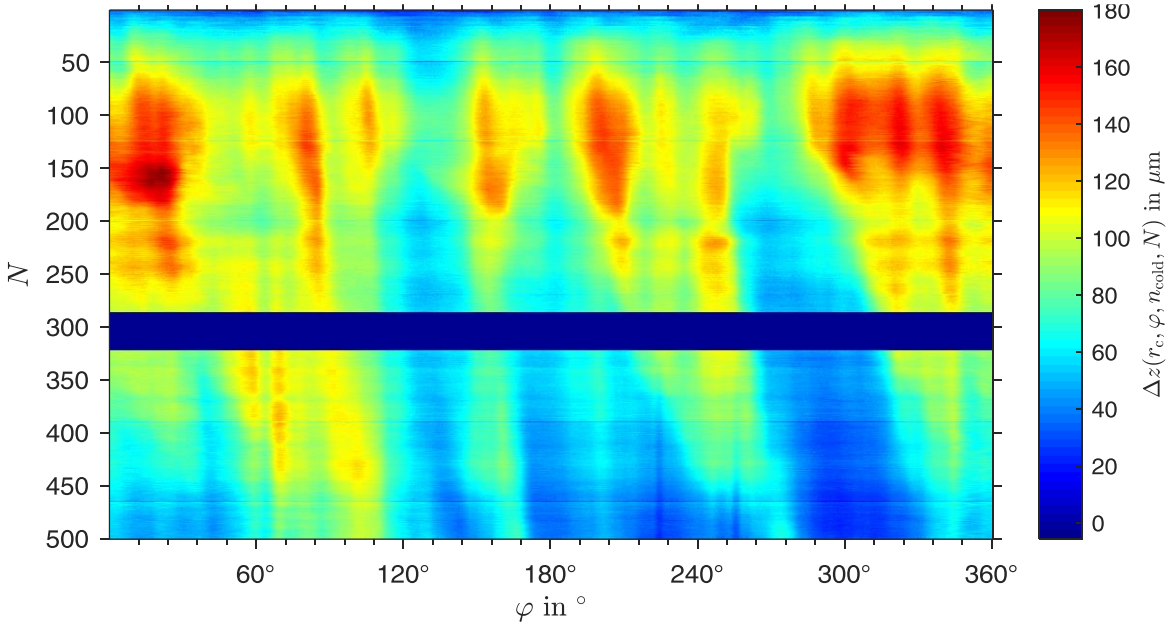

Figure 5-40: DT pattern of the *Constant* disc, evaluated in cold state at radial centre position[115]

[115] Bilgic Istoc, S.; Winner, H.: Influences, Interactions and Prediction Potential (2019).

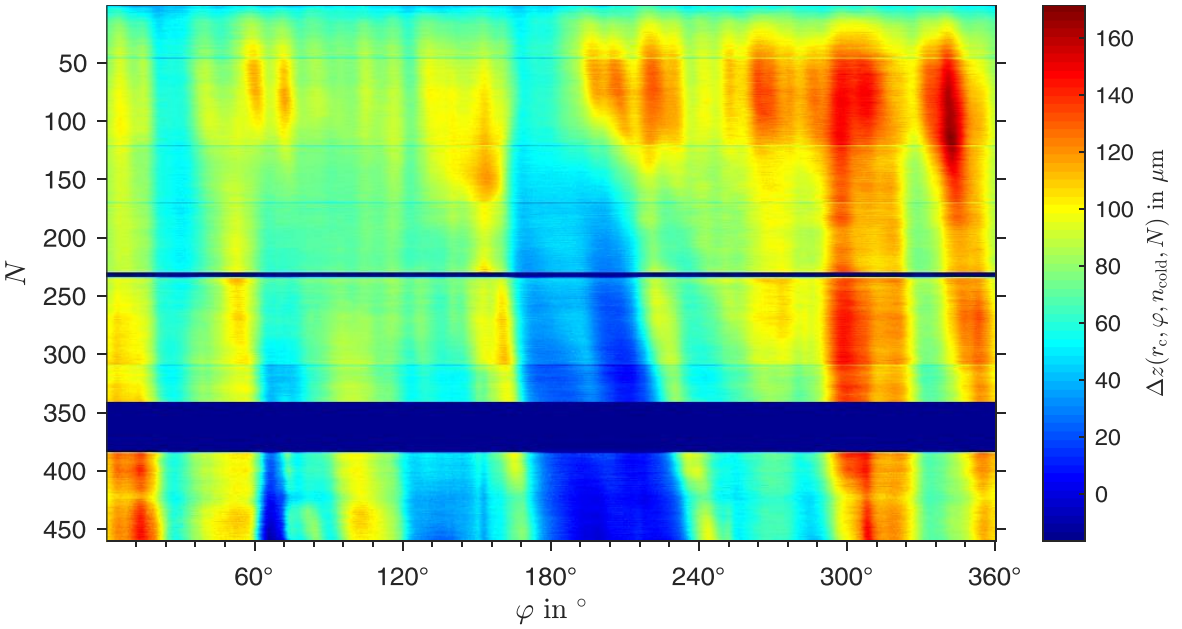

Figure 5-41: DT pattern of the *Periodic* disc, evaluated in cold state at radial centre position

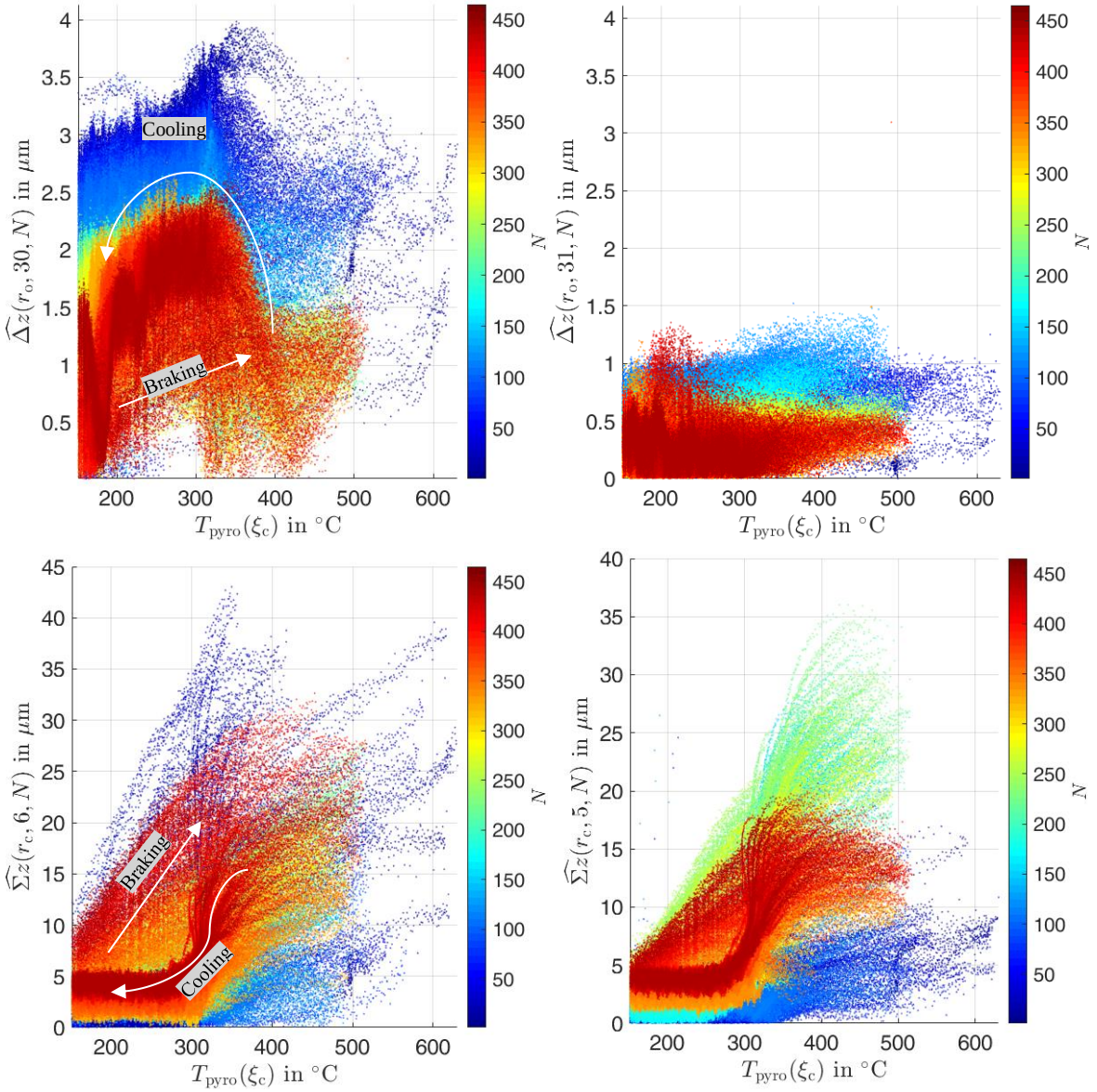

Figure 5-42: Amplitude of DTV (top)/SRO (bottom) at radial outer/centre position vs. temperature, evaluated for the *Constant* disc; top left: 30th order; top right: 31st order; bottom left: 6th order; bottom right: 5th order

Amplitudes of selected DTV and SRO orders vs. temperature for the *Constant* disc are shown in Figure 5-42. The DTV order corresponding to the cooling channel pin number in circumferential direction shows the expected behaviour observed with the other discs regarding rise of the amplitude due to cooling channel pin extrusion during cool down. Again, the 31st order shows no trend over temperature, representing the noise level with 1 µm. 30th-order DTV rises up to 4 µm, with a general amplitude reduction in the course of the test. This is quantitatively and qualitatively comparable to the findings of the *Reference* and *Variable* brake disc and confirms the assumption regarding pin extrusion.

The same accounts for SRO amplitude of the dominant order (6th order). During the first 50 cycles, SRO amplitudes rise up to approximately 40 µm. For $N > 50$, as harmonic SRO vanishes, amplitudes fall abruptly and rise slowly again. Still they do not reach the level of

the first cycles. The subordinate 5th order SRO which rises after $N \approx 50$ shows untypical behaviour: between $180 < N < 250$, amplitudes almost double to 35 µm and fall afterwards to values under 20 µm. SRO amplitudes of the other brake discs rise throughout the entire test. The same behaviour is observed for 1st-order SRO of the *Constant* disc (cf. Figure 8-42). This behaviour cannot be explained. However, 1st-order SRO might be caused mostly due to non-planar mounting of the brake disc and is not necessarily a phenomenon of the heat crack test in general.

In conclusion, the results from the heat crack tests with the *Constant* and the *Periodic* disc confirmed previous findings. Harmonic SRO is damped by periodically varying pin spacing in circumferential direction. Cooling channel pins cause DTV due to extrusions during cool-down.

5.4.3 Crack Formation

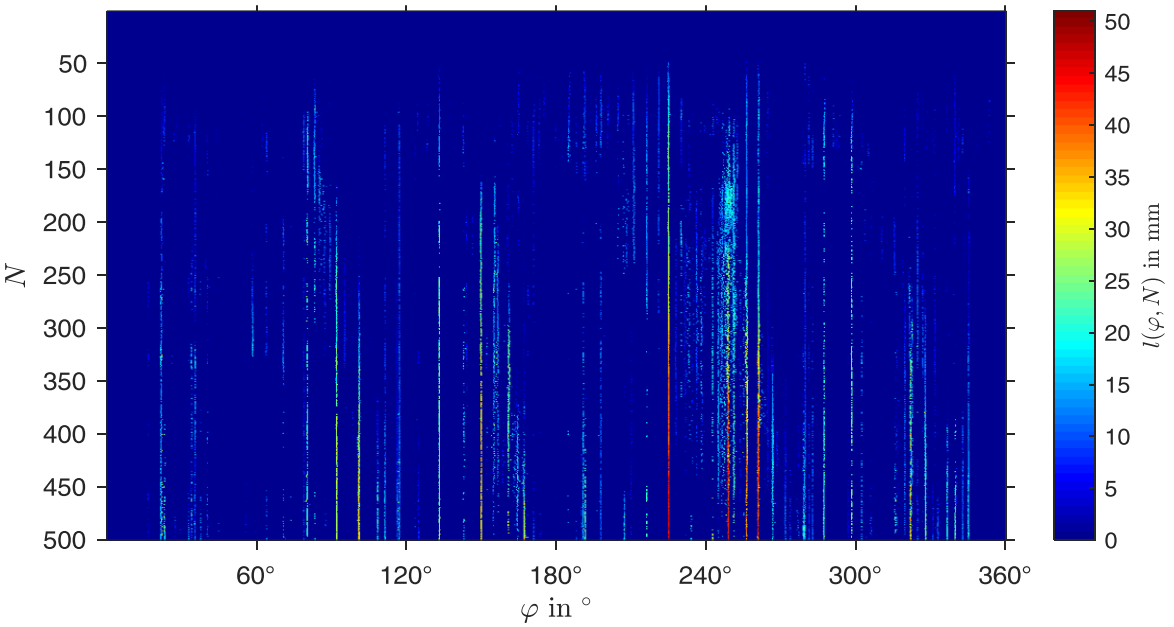

Figure 5-43: Crack pattern of the *Constant* disc[116]

[116] Bilgic Istoc, S.; Winner, H.: Influences, Interactions and Prediction Potential (2019).

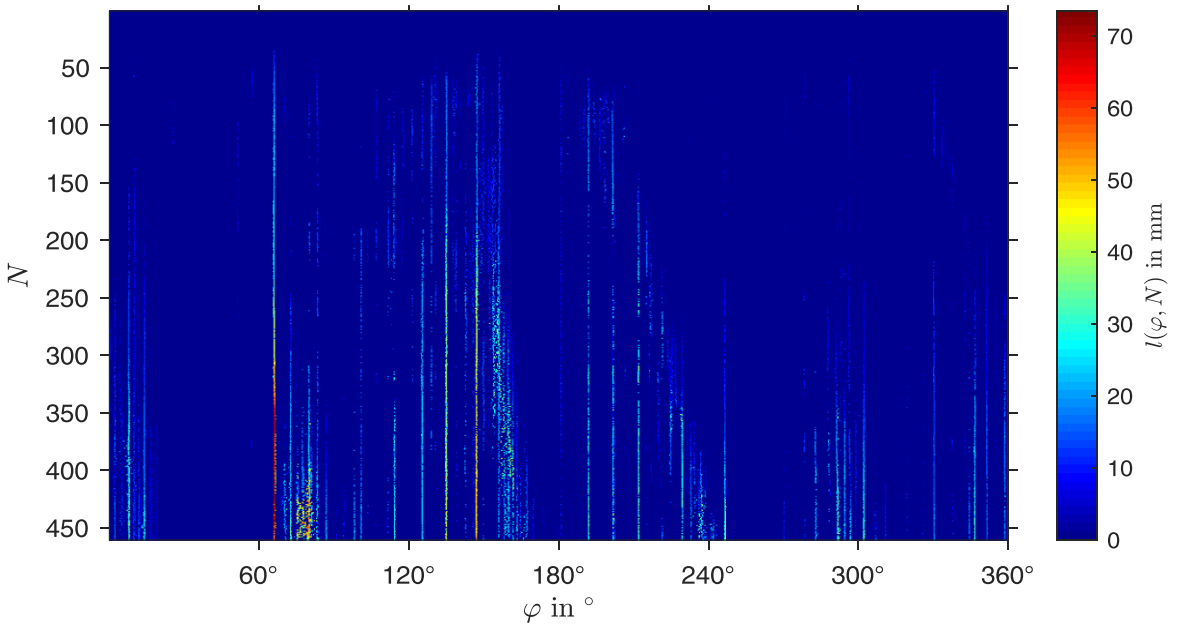

Figure 5-44: Crack pattern of the *Periodic* disc

Crack patterns of the *Constant* and *Periodic* brake disc show same phenomena as observed for the *Reference* and *Variable* disc (cf. Figure 5-43 and Figure 5-44). This includes crack opening zones that migrate along with hotspots, crack prone and crack free areas as well as formation of through-thickness cracks respectively longest cracks in areas of extreme convex SRO. However, especially the crack pattern of the *Constant* disc shows a previously unobserved phenomenon: during the cycles when the shifting in the SRO pattern takes place ($125 < N < 180$), numerous cracks close one after another. As the shifting does not occur in the hotspot pattern, the crack closure might be induced by the SRO shifting, which is a new finding.

At the end of the test, crack lengths of the *Constant* disc stay below 52 mm and no through-thickness crack occurs. Longest cracks of the *Periodic* disc remain at a similar length, although a single crack, which turns into a through-thickness crack, reaches a length of 73.5 mm. The growth behaviour of this crack is quite irregular in comparison to the other cracks observed in this and the other test. Its growth rate is degressive until around $N \approx 250$ and then rises again. This behaviour might be caused by the long inspection break after $N = 235$ for the *Periodic* disc. Presumably, the rest period caused microstructural damage at the crack location.

5.5 Matrix Comparison for all Discs

Table 5-1: Matrix comparison for all tested discs

	Reference	*Variable*	*Constant*	*Periodic*
Pin Arrangement	series	continuously varying	optimised	optimised periodic
Tensile strength in MPa	241	216	266	266
Pad Compressibility in µm	109	105	99	114
N_{max}	300	500	500	460
Through-thickness crack	yes	yes	no	yes
Longest crack length in mm	72	51	48	73.5
Average coning in µm	561	528	494	522
Cool-down duration	slightly varying, medium	constant, low	highly varying, high	highly varying, high
Average of crack count divided by mean crack length	3	3.5	3.5	3.5
Maximum 30^{th}/31^{st} order DTV in µm	3.8	3.7	4	n/a
Maximum harmonic SRO in µm	58.5	44.4	43	n/a
Maximum subordinate SRO in µm	61.5	36.1	35.5	n/a

Table 5-1 shows a matrix comparison for all tested discs. Numbers are rated by color-coding. Influences that are assumed to reduce disc life are colored red, influences that are assumed to increase disc life are colored green. By trend, *Reference* disc shows the worst performance in most categories. It endured the least number of cycles in the heat crack test as well. Still, its tensile strength and pad compressibility are not worst of the test series. Best performance is observed for the *Constant* disc, which also endured most cycles in the test and was the only brake disc remaining free of a through-thickness crack. It still shows the highest DTV amplitude of 30^{th} order. However, DTV amplitude of 30^{th} order is almost evenly high for all tested discs.

In conclusion, this comparison provides a slight indication that evaluated values and disc lifetime correlate with each other. Still, it should be mentioned that a total of four experiments is not sufficient to assume causal connection.

6 Finite Element Analysis of the Heat Crack Test

The observations made in the heat crack tests of the experimental series are used to design and implement a Finite Element (FE) Model that simulates the heat crack test. Since it is considered the reference and most extensively observed brake disc, the *Reference* disc is modelled here. In this chapter, the simulation concept is presented first. Second, modelling principles are discussed. Lastly, results are presented. Validation of the model is discussed in the next chapter.

6.1 Simulation Concept

Based on the requirements formulated in subchapter 4.6 the simulation concept is derived. The simulations concept consists of a computational fluid dynamics (CFD), a thermal and a mechanical model. Their interaction is briefly introduced in Figure 6-1.

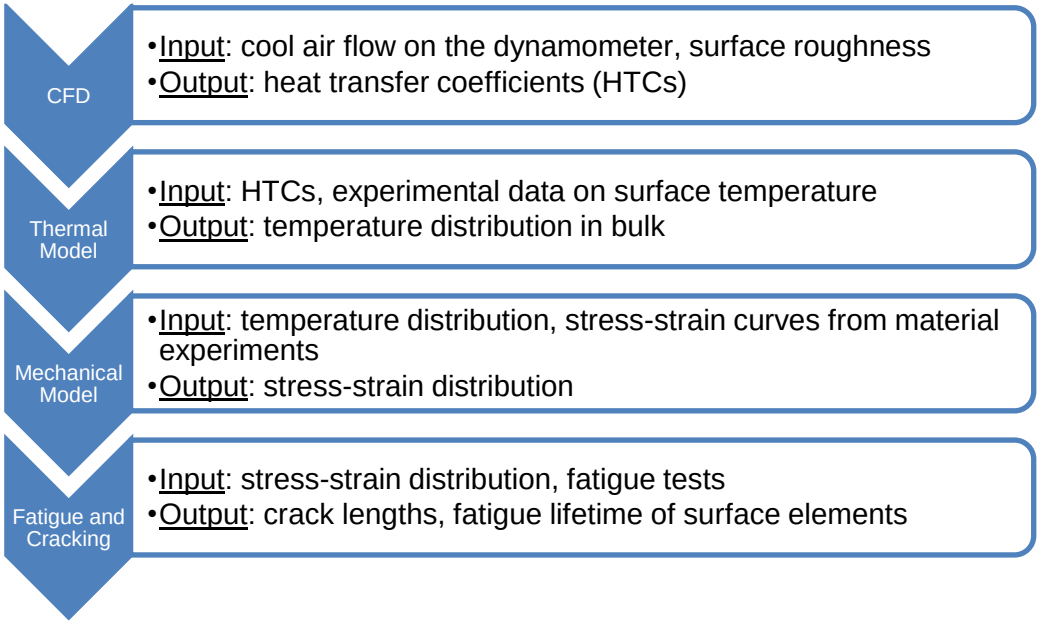

Figure 6-1: Structure of the simulation concept

Since the reproduction of the temperature distribution inside and on the friction rings is required, a heat transfer analysis is conducted. The heat transfer analysis is a transient analysis, since the thermal load changes during the braking period. Therefore, the thermal load is calculated using experimental data from the actual heat crack test. Sinks of the thermal analysis are heat conduction into the neck of the brake disc, radiation to cooler surroundings and

convective losses over the air surrounding the friction rings and streaming through the cooling channel. In order to calculate convective losses, a CFD model is used for calculation of heat transfer coefficients.

With the pre-calculated temperature solution of the heat transfer analysis, the transient mechanical model calculates stress-strain distributions on the entire brake disc. Two different approaches are used for material modelling: first, the standard material model of ABAQUS™ is parameterised, since it allows crack propagation simulation by application of the built-in XFEM routine. Second, a grey cast iron model is parameterised, which features damage and fatigue calculation. It is used to calculate remaining lifetime of friction surface elements. The parameterisation of both material models is based on the material experiments described before, mainly the isothermal compression/tension tests at room temperature and high temperature. Modelling is described in detail in the next subchapter.

6.2 Modelling[117]

6.2.1 Computational Fluid Dynamics Model

Purpose of the CFD model is calculation of temperature dependent HTCs. They are required for the calculation of convective losses in the subsequent heat transfer analysis. Assumptions are a stationary flow around the brake disc and uniform temperature of the brake disc. Analysis is therefore conducted at different, constant temperatures of the brake disc up to 700 °C in ANSYS CFX™. Since the simulation is stationary, the brake disc does not rotate. To simulate rotation, the coordinate system of the control volume directly enclosing the brake disc rotates. Implementation of the model has been carried out in a master thesis.[118]

6.2.2 Thermal Model[119]

Heat transfer analysis is conducted static and transient in ABAQUS™. Convective losses are calculated based on the HTCs calculated in the CFD model described in the preceding section. Uniform HTC for each the cooling channel and the friction surface is assumed and estimated by averaging the calculated HTCs. In addition to this, radiation losses are estimated on the friction surface by assuming an emissivity factor of $\varepsilon_R = 0.64$ for oxidised

[117] Partially described before in Bilgic Istoc, S.; Winner, H.: Simulationskonzept (2018).

[118] Xuan, Z.: Masterthesis, Simulation (2017).

[119] Taken from Bilgic Istoc, S.; Winner, H.: Simulationskonzept (2018).

GJL.[120] Conductive heat transfer inside the brake disc is calculated isotropically using a temperature dependent heat transfer coefficient, which has been determined using laser flash analysis on specimens cut out of the *Twin* disc.

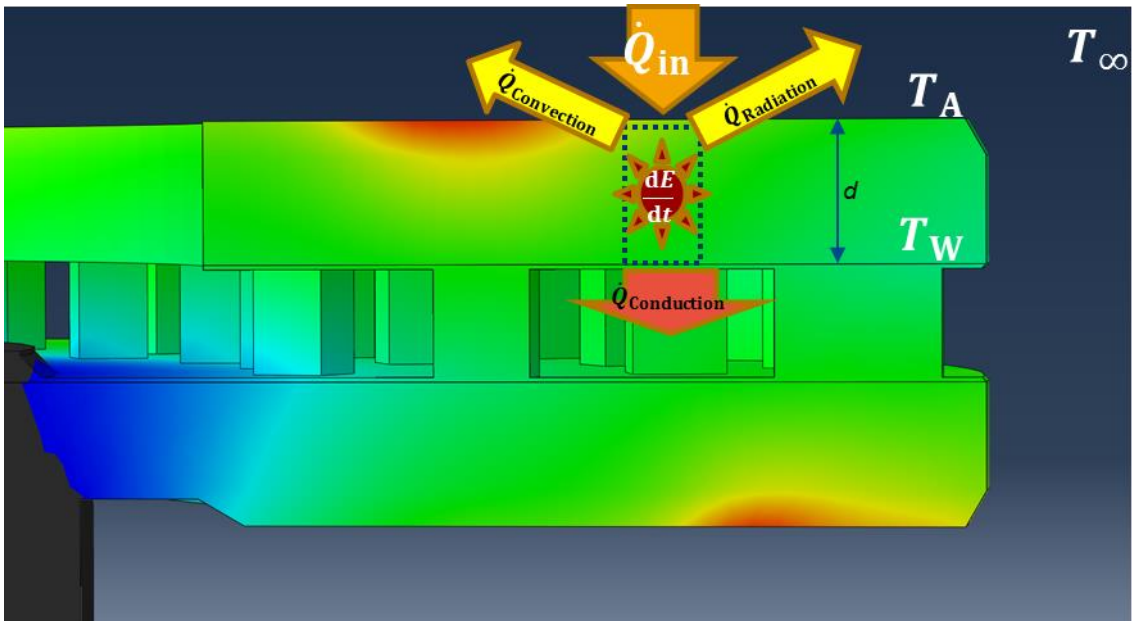

Figure 6-2: Heat sources and sinks in a section of the brake disc. Temperature color-coded (red hot/blue cold)[121]

Heat flow into the friction ring surface is calculated using a deconvolution approach based on measurement data gathered by the thermal camera in the heat crack test of the *Reference* brake disc. Since one thermographic image is available for each revolution, heat flow is recalculated for each revolution. First, a power balance between heat flow $\dot{Q}_{\mathrm{in}}$ and thermal losses $\dot{Q}_{\mathrm{Conduction}}$, $\dot{Q}_{\mathrm{Radiation}}$, $\dot{Q}_{\mathrm{Convection}}$ in the brake disc is formulated (cf. Figure 6-2):

$$\frac{\mathrm{d}E}{\mathrm{d}t} = \dot{Q}_{\mathrm{in}} - \dot{Q}_{\mathrm{Conduction}} - \dot{Q}_{\mathrm{Radiation}} - \dot{Q}_{\mathrm{Convection}} \tag{6.1}$$

System boundaries for the control volume (where system energy E is contained) are the friction surface and the margin towards the cooling channel with d being the thickness of the friction ring. $\dot{Q}_{\mathrm{Conduction}}$ stands for dissipated heat into the cooling channel. Since the ratio between thermal loss in the cooling channel via convective flow and conduction into the cooling channel pins is unknown, $\dot{Q}_{\mathrm{Conduction}}$ accounts for both. Furthermore, it includes conduction into the cooler neck of the brake disc. After inserting friction surface temperature T_{A}, transition temperature to the cooling channel T_{W} and ambient air temperature T_∞ equation 6.1 is reformulated with mass m, specific heat capacity c, thermal conductivity λ, thickness d, Stefan-Boltzmann constant σ_{B}, and heat transfer coefficient α:

[120] Gesellschaft Verfahrenstechnik und Chemieingenieurwesen: VDI-Wärmeatlas (2013), p. 1087.

[121] Bilgic Istoc, S.; Winner, H.: Simulationskonzept (2018).

$$mc\frac{\Delta T}{\mathrm{d}t} = \dot{Q}_{\mathrm{in}} - \frac{\lambda A}{d}(T_{\mathrm{A}} - T_{\mathrm{W}}) - \varepsilon_{\mathrm{R}}\sigma_{\mathrm{B}}AT_{\mathrm{A}}^4 + \alpha A(T_{\mathrm{A}} - T_{\infty}) \tag{6.2}$$

By rearranging of equation 6.2 and assumption of an infinitesimally small friction surface element A, an equation is formulated describing the specific heat flow $\dot{q}_{\mathrm{in}}$ depending on friction surface temperature T_{A}, friction surface temperature of the preceding time step T_{t-1} and a constant ζ, which quantitates losses into the cooling channel $\dot{Q}_{\mathrm{Conduction}}$:

$$\dot{q}_{\mathrm{in}} = \rho dc\frac{(T_{\mathrm{A}} - T_{t-1})}{\mathrm{d}t} + \zeta\, T_{\mathrm{A}} + \epsilon\sigma_{\mathrm{B}}T_{\mathrm{A}}^4 + \alpha(T_{\mathrm{A}} - T_{\infty}) \tag{6.3}$$

As a side condition it assumed that 90 % of the total braking power is distributed uniformly on both friction ring surfaces:[122]

$$\sum \dot{q}_{\mathrm{in}}A \cong \frac{1}{2}\cdot 0{,}9P_{\mathrm{tot}} \tag{6.4}$$

This allows for the determination of the constant ζ, since brake torque and rotational speed are constant during each braking. During the first 10 seconds of the braking period, large amounts of the friction surface temperature is out of the measurement range of the thermographic camera. For that reason, heat flow is estimated in this period using the average heat flow distribution of the remaining 30 seconds braking time.

This way, heat flow is calculated for each revolution based on thermographic measurement data by application of the presented equation. For validation, the temperature evolution at beginning of the cooling period is compared with experimental data. Finally, the approach presented here allows for the simulation of hotspots and hotbands, which is hardly achievable using tribology models.[123]

6.2.3 Mechanical Models

As described before, two mechanical models are implemented. The first one relies on the standard material implementation of ABAQUS™. It is extended by user-subroutines. This way, a different Young's modulus is used for tension and compression, as GJL shows greatly varying stress-strain behaviour in tension and compression (cf. section 2.2.2). Furthermore, the Young's modulus as well as the plastic deformation curves are implemented temperature dependent, with a sampling point at room temperature and 700 °C each. Base for parameterisation is the LCF test described in section 4.3.1. Additional material parameters are chosen based on the tests described in section 4.3.2. The first model does not account for relaxation and cyclic damage. Nevertheless, it allows for application of the XFEM method for crack growth estimation, which will be discussed in section 6.2.4.

[122] Remfrey, J. et al.: Aufbau und Komponenten von Pkw-Bremsanlagen (2017), p. 139.

[123] Könning, M.: Dissertation, Simulation von Heißrubbeln im Gesamtbremssystem (2017).

The second model is based on Metzger and Seifert.[124] It accounts for antisymmetric Young's modulus and plastic deformation behaviour in tension and compression and additionally for relaxation and cyclic damage. Furthermore, it allows lifetime prediction, i.e. estimation of remaining cycles until failure for elements on the friction surface and in the brake disc. Parameterisation of the second model was conducted by Fraunhofer IWM Freiburg.

6.2.4 Crack Propagation Estimation

For estimation of crack initiation and propagation, the XFEM is used in connection with the standard material model implemented in ABAQUS™. Crack initiation criterion is set to maximum principal tensile stress. The criterion is implemented cycle dependent using a user-subroutine, degrading with increasing cycle number in accordance with remaining stiffness evaluated in the LCF tests. As initial criterion, ultimate tensile strength, evaluated in a single tensile stress test, is used. It should be noted that this implementation only serves as a very basic estimation.

6.3 Results

In this subchapter, results obtained by the FE model are evaluated, which contribute to the causal model developed in the next chapter explaining the formation of heat cracks in brake discs. Accordingly, evaluation focuses on the underlying processes that cannot be observed using experimental data gathered during the heat crack tests. All evaluations have been made for the 10th heat crack cycle of the heat crack test with the *Reference* brake disc. Parameters result generation are documented in appendix A.6

[124] Metzger, M.; Seifert, T.: A Mechanism-Based Model (2012).

6.3.1 Hotspot Width vs. Depth

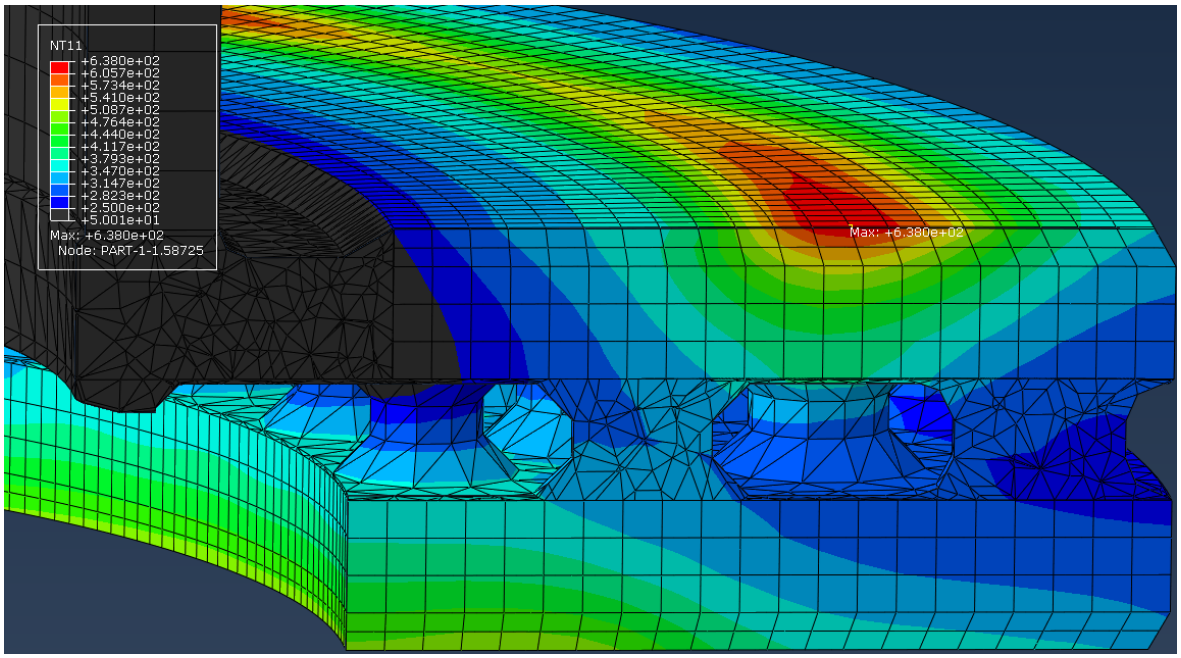

Figure 6-3: Section view of the brake disc showing depth of hotspots (red) and general temperature distribution in the friction ring; N=10, end of braking period

Hotspot distribution and amplitude on the friction ring surface is well known from the experiment series conducted in this work. However, no information on the intrusion depth of a hotspot is available through thermographic images. For that reason, general hotspot depth is evaluated using the FE model. As shown in Figure 6-3 with isothermal lines, hotspots are about three to four times broader compared to their depth. The temperature gradient, averaged over the circumference of the hotband, is $23\,\frac{\mathrm{K}}{\mathrm{mm}}$ in depth direction (cf. Figure 8-44). This indicates that thermal gradients in depth direction of the brake disc induce probably higher thermally induced stresses due to non-uniform thermal expansion in comparison to non-uniform thermal expansion caused by gradients visible on the surface of the brake disc. Furthermore, it shows that hotspots only affect layers near to the surface in terms of extreme overheating. Nevertheless, deeper layers of the friction ring still reach high temperatures around 500 °C, as the model supposes (cf. Figure 6-3).

6.3.2 Cooling Channel Pin Extrusion

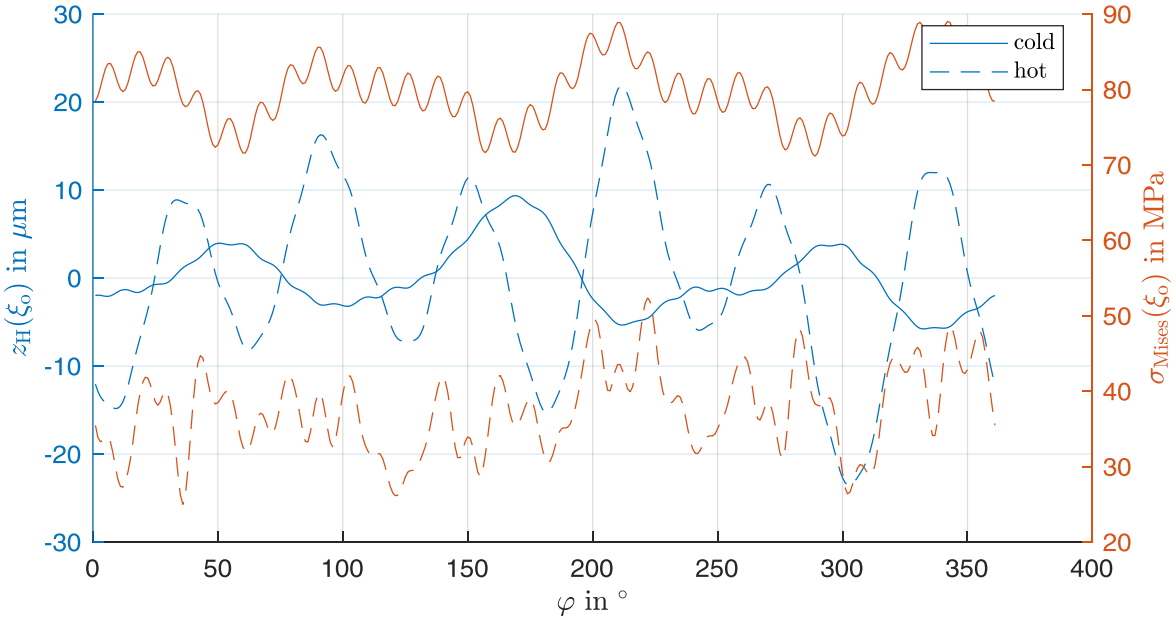

Figure 6-4: Surface topology and Mises stresses on the HS in at the end of the braking period (hot) and after cool-down (cold); $\varphi = 0°$ is set to the centre of a cooling channel pin; *z*-coordinate subtracted by average surface topology values for comparability

The cooling channel extrusion observed in experiments is reproduced in the FE model. Figure 6-4 shows surface topology at radial outer position $z_H(\boldsymbol{\xi}_o)$ and Mises stresses σ_{Mises} on the HS around the circumference of the brake disc in hot and cold state. In hot state, surface topology is dominated by SRO of 6th order due to the hotspots, as it has been observed in the experiment (cf. also Figure 7-4). Amplitudes of the deformation lower after cool-down. In cold state, dents caused by the cooling channel pins become visible. Peaks of the dents are exactly centred in the centre of the cooling channel pins.

Average Mises stress is twice as high in cold state compared to hot state (80 vs. 37 MPa). This is most probably caused by the asymmetric behaviour of GJL in tension and compression. With a shift of 6°, equally to half cooling channel spacing, fluctuations of 30th order occur in the Mises stress in cold and hot state. This indicates that local stress maxima occur in between the cooling channel pins due to their extrusion and confirms the hypotheses formulated based on the experiments. These results are furthermore consistent with the extended crack growth observed with the *Variable* disc at segments, where pins are radially aligned, and cracks could therefore growth straight through in between the cooling channel pins.

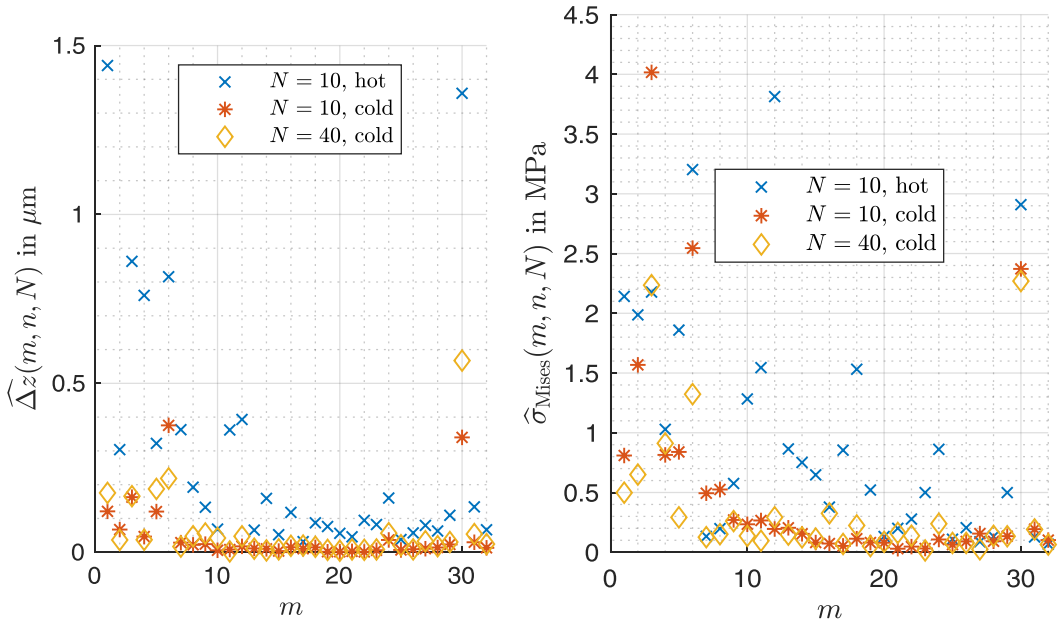

Figure 6-5: DTV (left) and Mises stress (right) amplitudes at the end of the braking period (hot) and after cool-down (cold); evaluated at radial outer position

DFT of the Mises stress signal (Figure 6-5) shows that amplitude level of the stress fluctuation of 30th order caused by the cooling channel pins is around 2.5-3 MPa. This equals 3-8% of the average Mises stress level. Additionally, stress amplitudes of 30th order are similarly high compared to stress amplitudes of 6th order, which is caused by hotspots. However, it should be noted that – in order to be consistent with experimental investigation – evaluation has been done at radial outer position, where hotspots had only a distant effect, since they showed up at radial centre position during the respective braking. As a limitation, it should be noted that DTV amplitudes are 0.3 to 1.4 µm high and therefore around 4 times lower compared to the maximum DTV amplitudes observed in the experiment. To be precise, DTV amplitudes during braking (hot state) match amplitudes of the experiment. They still lower during cool-down, which is inconsistent with the findings of the experiment. If there was be a proportionality between DTV amplitude level of 30th order and stress variation of 30th order, Mises stresses caused by the cooling channel pins would account for roughly one fourth of the average Mises stress level with values around 20 MPa. However, no data is available to support this hypothesis, and there appears to be no direct correlation between DTV amplitude and Mises stress amplitude of 30th order.

6.3.3 Stress Distribution

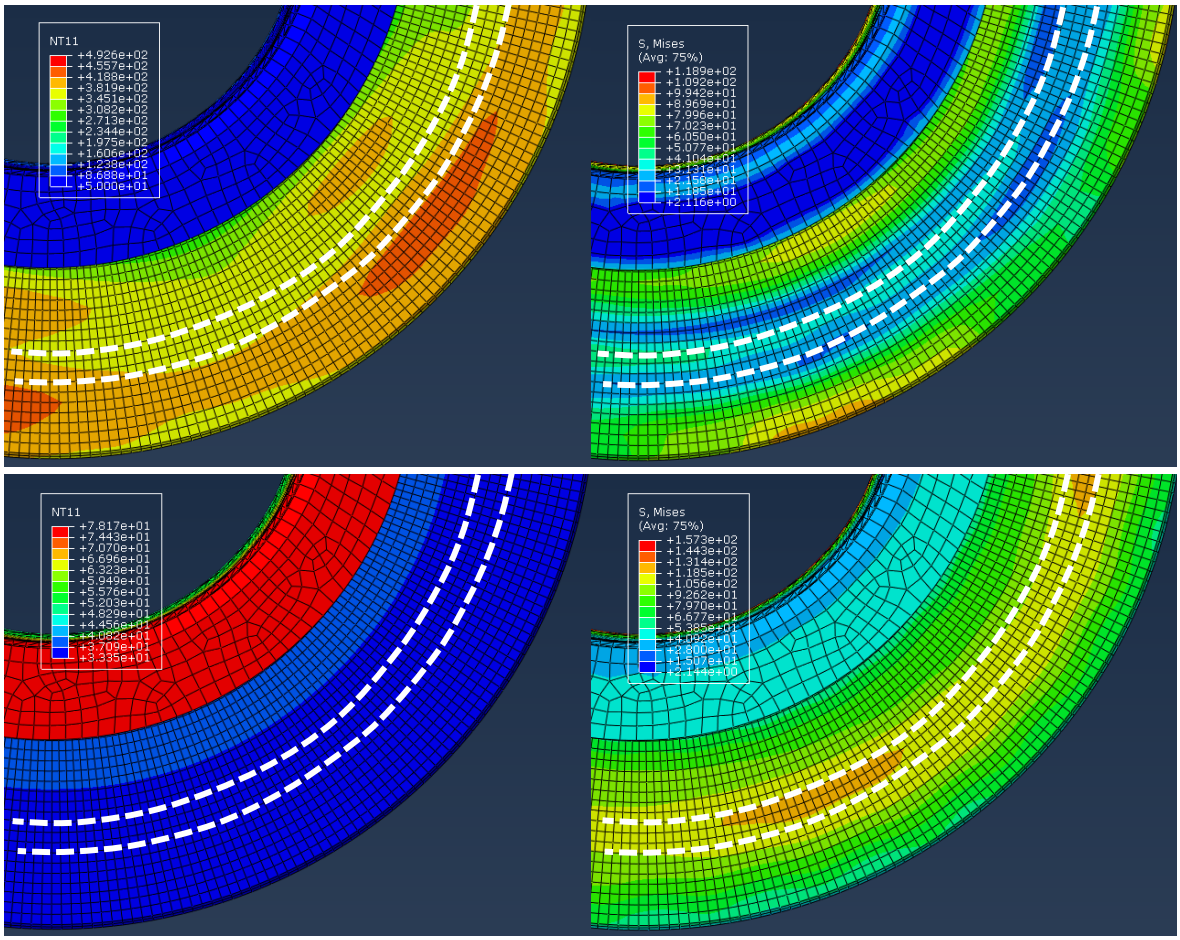

Figure 6-6: Temperature (left) and stress distribution (right) at the end of the braking period (top) and after cool-down (bottom); location of the remaining “stress-band” (bottom right) marked in all images by white stripes.

Figure 6-6 shows temperature and stress distribution during a heat crack cycle that featured a two-hotband case on the HS. During braking, two hotbands form at radial inner and outer position (Figure 6-6 top left). Accordingly, maximum stresses occur at radial inner and outer position (top right). At radial centre position, lowest stresses are present at the end of the braking period. After 20 minutes of cool-down, temperature distribution is flat (bottom left) with approximately 35 °C on the friction ring surface. Nevertheless, stress distribution is not uniform due to residual stresses, as expected (bottom right). Surprisingly, maximum stresses are now located at radial centre position in a narrow “stress-band”, which is highlighted in the figure. Furthermore, locations of peak stresses are phase shifted in comparison to the hotspots located in the two hotbands. According to this, the stress state of the penultimate braking, showing a single hotband at radial centre position has been “conserved” throughout the subsequent heat crack cycle. This behaviour might be caused by the fact, that peak temperatures are higher during one-hotband cycles and therefore residual stresses cannot be compensated by the weaker stresses caused during two-hotband cycles. Moreover, this contributes to the explanation, why heat cracks usually initiate at radial centre positions.

6.3.4 Parameter Sensitivity

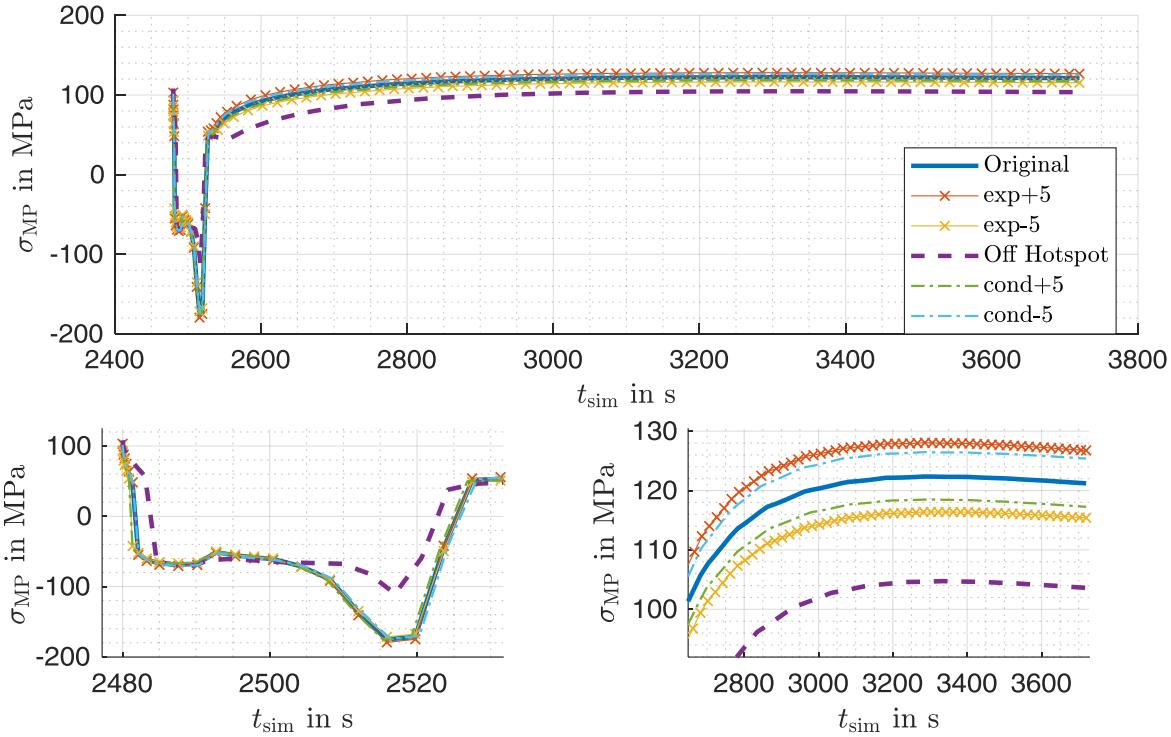

Figure 6-7: Evolution of maximum principal stress at a hotspot position during the entire third heat crack cycle; original stress evolution in comparison with stress evolution of a material model with 5 % increased/decreased thermal expansion coefficient ("exp±5"), 5 % increased/decreased thermal conductivity ("cond±5") and an entirely different heat flow derived from another brake disc, where the hotspot formed at a remote position ("Off Hotspot"); bottom: horizontal zoom over braking period (left) and vertical zoom over cool-down period (right)

For evaluation of parameter sensitivity, Figure 6-7 shows the evolution of maximum principal stress σ_{MP} in the centre of a hotspot for several parametric modifications of the FE model during the third heat crack cycle, i.e. in the timeframe of 2480 s $< t_{sim} <$ 3720 s. In original state, i.e. parameterised according to the actual properties of the tested brake disc, stress is first transformed from tensile to compressive stress during braking, reaching a maximum value of 175 MPa compressive stress. In general, during the last 5 seconds of the braking period, compressive stresses lower slightly. Afterward, compressive stresses rapidly transform into tensile stresses, resulting in a stress level of 50 MPa after 4 seconds of cool-down. During further cool-down, stress in original state reaches a maximum of 122 MPa after 14 Minutes of cool-down. Afterwards, all stresses lower slightly. In the end of the cycle, stresses vary from each other slightly. When thermal expansion coefficient is changed by ±5 %, stresses vary around ±5 % (+4.6 %, −4.8 %) compared to original the stress value. Variation is lower for modification of thermal conductivity, namely ±3 % (+3.5 %, −3.2 %). When applying a different heat flow, resulting in the hotspot being not located at the evaluation position but on radial outer and inner position, degradation of maximum principal tensile stress is 14.5 % at the end of the cycle. These results indicate, that calculated stresses are less sensitive to modifications of material parameters in comparison to load variation.

Finally, modification of thermal conductivity has a lower influence compared to modification of thermal expansion coefficient.

6.3.5 Crack and Fatigue Estimation

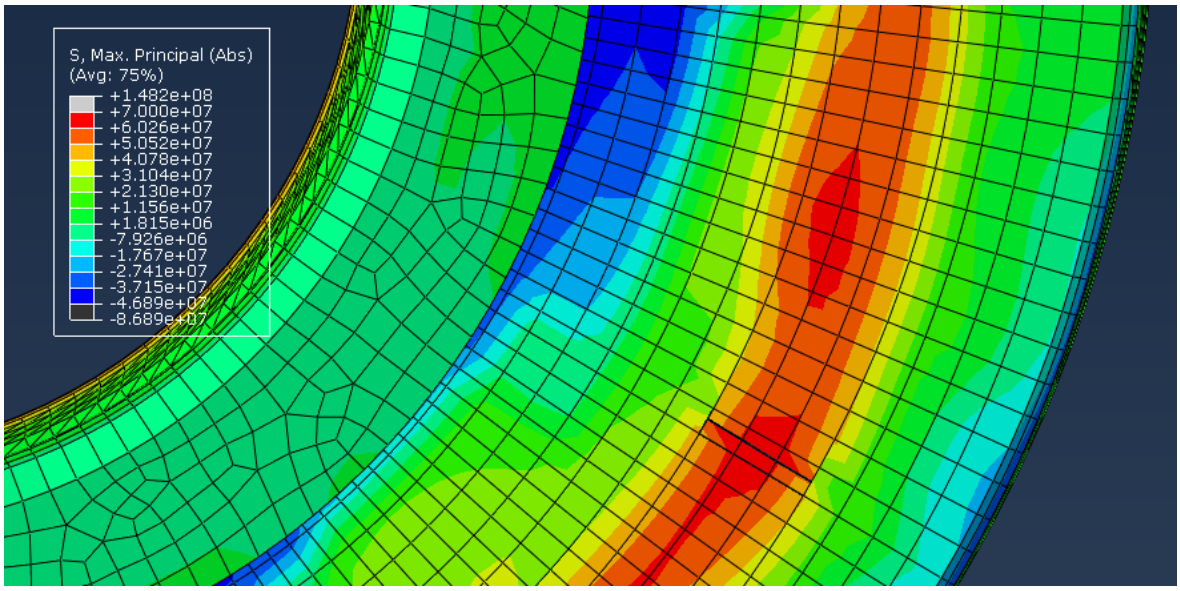

Figure 6-8: Friction ring showing a crack at radial centre position

Figure 6-8 shows the crack calculated using the XFEM model. It initiates during $N = 5$, which is 10 times earlier compared to the experiment ($N = 51$). It grows to its final length after 9 minutes of $N = 10$. Afterwards, its length does not increase anymore. Other cracks remain at radial centre position as well. This behaviour might be caused by the manifestation of "stress-bands", explained in this section. However, overall cracking behaviour could not be validated in terms of crack growth behaviour, most likely due to the rudimental parameterization and the very basic approach. Nevertheless, cracks initiate at radial centre position, which is consistent with experimental results.

In terms of fatigue calculation, results are not valid as well. Calculated cycles until failure are for all evaluated elements greater than 1000, which is not consistent with experimental results. This suggests that crack initiation might be caused by influences that have not been modelled or parameterization is not sufficient as well for the fatigue model. One of the phenomena not modelled might be microstructural transformation in layers close to the surface. In conclusion, results of fatigue calculation do not falsify any hypotheses.

Finally, the results gathered by application of the FE model support the hypotheses based upon experimental data in terms of the effect of cooling channel pin extrusion as well as hotspots, hotbands and the resulting stress state on the friction ring surface.

7 Discussion

In this chapter, results from experimental series and the FE model are discussed. First, results are aggregated in brief before they are utilised to evaluate the hypotheses formulated in chapter 3. Based upon the evaluated hypotheses, identified influences on the heat crack formation are merged into a causal model. Lastly, plausibility of the FE model is checked for assessment of its applicability.

7.1 Aggregation of results

In this subchapter, results from the single experiments and numerical investigation are summarised and set in relation to each other. For that reason, results are set in context and yet prepared for hypothetical evaluation. Accordingly, results related to crack propagation are summed up. Results related to microstructural transformations follow. Finally, hotspot-, cooling channel-, coning- and SRO-related results conclude this subchapter.

Heat crack lengths are evaluated for all tested brake discs. *Reference* and *Periodic* disc failed the test with a through-thickness crack. *Variable* disc achieved 500 cycles, but showed a through-thickness crack after 500 cycles as well. *Constant* disc ran through heat crack test without the occurrence of a through-thickness crack. In general, crack propagation rates lower in the course of the test. An exception to this observation is provided by the *Periodic* disc, for which accelerated crack growth was observed for the longest crack after a rather long inspection break. In addition to this, a balance between the opening of new cracks and growth rates of existing cracks seems to exist. This means that damage in the disc is put either into the opening of new cracks or into prolongation of existing cracks. Some cracks entirely close during the heat crack test if they remain small. However, longest cracks do not fully close even during braking, as they are visible as cool spots in thermographic images. Furthermore, after the heat crack test, no tensile residual stresses have been measured. Still, this might be caused by the fact that residual stresses lower during rest of the disc.

Microstructural transformations are present at various positions with various depth. Transformation depth partly correlates with surface hardness and varies strongly spatially. Accordingly, hotspots do not seem to intrude into the material as deep as they are wide. There appears to be no correlation between surface hardness and crack length at the respective location. Heavily oxidised structures are covered with micro-cracks, especially at the surface. Crack growth could not be validly modelled using the FE model.

Hotspots are present during all conducted heat crack tests. Using the FE model, they are found to be three to four times less deep than wide. These results are confirmed by transformation depth observed in the experiment. During the first cycles, hotspots usually occur

harmonically and transform into blurry hotspots of lower order that migrate slower after $N > 50$. For the period disc, no harmonic hotspots were observed. Harmonic hotspots are partly reduced for the *Variable* disc as well, which indicates that the variation of the cooling channel geometry around the circumference distorts the formation of harmonic hotspots. Crack opening zones migrate together with hotspots. According to this, hotspots are responsible for the opening of heat cracks. When a hotspot moves away, partial closure of small cracks is rarely observable for all discs, frequently for the *Reference* disc. However, after a crack has reached a certain length, it continues growing regardless of the presence of a hotspot at its position. In rotational direction, a hotspot forms after the location of the through-thickness crack. This causes peak temperatures to be located next to the hotspot at the end of the test. However, between peak temperature and endured cycles in the heat crack test is no relation apparent for all discs.

In addition to this, crack growth is directly affected by the cooling channel design. Cooling channel pins extrude through the friction ring surface during braking. During each cool down, convex dents caused by the cooling channel pins transform into concave dents, i.e. the brake disc gets thinner at the pin positions, most probably due to abrasion of the extrusions during braking. This cyclic extrusion causes a stress peak in the gap between them. Most probably due to this stress gap, heat cracks are found to propagate preferably along the edges of cooling channel pins, since longest cracks are present at segments of the *Variable* disc, where pins are radially aligned. The extrusion of cooling channel pins is observed as DTV of 30^{th} order and an amplitude of 4 µm for the *Reference* and *Constant* disc, and DTV of 31^{st} order for the *Variable* disc and thereby corresponds to the order of cooling channel pins. DTV of 30^{th} respectively 31^{st} order reduces in the course of the test, which might be related to a softening of the brake disc.

No relation could be found between value of average coning and number of endured heat crack cycles in the experimental series. Still, higher coning values occur in cycles, when one hotband forms on the HS and two hotbands on the PS. Regardless of the distribution of hotbands, highest stresses occur in radial centre position, where usually one hotband is present. This might be caused by the more uniform temperature distribution that was observed for the two-hotband case in relation to the one-hotband case.

SRO is linked to the formation of hotspots, as it defines hotspot locations as zones of convex SRO. They match hotspot positions in most cases. Accordingly, a dominant, harmonic and high SRO order is present for $N < 50$ and replaced by a lower, blurry subordinate SRO order later. The harmonic order is missing entirely for the *Periodic* disc and partly for the *Variable* disc, consistent to the findings regarding hotspot formation. Furthermore, SRO order is generally lower and more blurry in these tests compared to the *Reference* and the *Constant* disc. The subordinate order grows in the course of the test, as the brake disc gets less stiff. Longest heat cracks are located in areas of rising convex SRO. Heat cracks are absent in areas of concave SRO. The mentioned phenomena do not account for SRO in cold state, which most probably originates from mounting inaccuracies of the brake disc and therefore qualitatively and quantitatively differs from SRO in hot state.

7.2 Evaluation of Hypotheses

In this subchapter, hypotheses are evaluated using the results previously collected. This is structured using the categories introduced before.

7.2.1 Crack Propagation

Hypothesis 1.1: Open cracks close during each heat crack cycle due to compressive circumferential stresses.

Result: Several cracks are visible in the hotspot pattern as cool spots, e.g. the through-thickness crack of the *Variable* disc at $\varphi = 344°$ (cf. Figure 5-28) or the (through-thickness) cracks of the *Reference* brake disc at $\varphi = \{150°; 246°\}$. This indicates that these large cracks are too wide to close entirely during braking. Accordingly, hypothesis 1.1 is falsified.

Conclusion: Compressive circumferential stresses are not high enough to close large, wide cracks entirely. Consequently, crack closure mechanisms, which might slow down crack growth rates, do not apply to the largest cracks. However, smaller cracks might close first, allowing circumferential compressive displacement, as closure of small cracks has been observed as well (cf. e.g. section 5.2.3).

Hypothesis 1.2: Stresses on the friction surface are exclusively compressive at the end of the braking period.

Result: Measurement of residual stresses (cf. Figure 5-23) returned throughout compressive or no residual stresses on the HS of the *Reference* and the *Variable* disc after the heat crack test. Under the assumption that measurement has returned valid results, hypothesis 1.2 is falsified.

Conclusion: The basic model indicating an exclusively compressive stress state on the friction surface could not be confirmed. However, this does not deny the existence of local compressive stresses on the friction surface on the end of the braking period.

Assumption 1.3: Crack opening of an adjacent crack causes stress relief at already open cracks.

Result: The crack pattern of the *Periodic* brake disc (cf. Figure 5-44) shows numerous cracks at $\varphi > 70°$ opening up one after another after $N > 400$. Still, the crack that becomes the through-thickness crack later, remains growing. It grows 3 mm during $400 < N < 420$ compared to 1.5 mm during $360 < N < 400$. Accordingly, assumption 1.3 is falsified.

Conclusion: Stress pattern is more diverse than previously assumed. Stress relief by crack opening is not sufficient for reduction of crack growth rates of adjacent cracks. As crack growth rate even increases, the opening of adjacent cracks does not seem to affect crack propagation of an already open crack at all.

Assumption 1.4: Heat crack propagation rates slow down at the end of the test as the number of cracks increases and they relief each other.

Result: Although crack growth rates of the longest cracks (Figure 5-7) lower in the end of the test, $\frac{k^2}{\Sigma l}$ is degrading during the last 50-100 cycles for all brake discs (Figure 5-8). Crack number also stops increasing at the end of the test as no more cracks open up. As cracks do not additionally close at the end of the test, this indicates that overall crack propagation rates remain at least constant or even increase. Accordingly, longest cracks are not slowed down because of relief due to the opening of additional cracks, but rather because they reach the margin of the friction ring and their continuous growth is not captured by the crack detector anymore. In conclusion, assumption 1.4 is falsified.

Conclusion: The reduction of crack growth rates of the longest cracks at the end of the test is not caused stress relief by a vast number of cracks. This is consistent with assumption 1.3. Alternatively, crack growth rates of longest cracks lower in the end of the test because the load level lowers, e.g. by more even stress distribution or a general softening of the brake disc.

Assumption 1.5: Friction pairing characteristics determine the ratio between crack opening and crack growth.

Result: For all brake discs, the ratio between crack count and average crack length approaches a certain, nearly constant value, which is specific to each disc (Figure 5-8). Highest deviation from a constant value is present for the *Constant* disc (cf. Table 8-1), where deviation is equally high to standard deviation. Accordingly, hypothesis 1.5 is not falsified.

Conclusion: Apparently, the ratio of open cracks and average crack length seems to be constant for each friction pairing. The damage induced during braking might either increase average crack length or crack opening, depending on the disc. Probably, a higher average crack length caused early failure of the *Reference* disc. However, data is not sufficient to evaluate this statement.

7.2.2 Microstructural Transformations

Hypothesis 2.1: Cracks are caused by microstructural transformations.

Result: Polished micrograph sections of the *Reference* disc (cf. Figure 5-21 and Figure 5-22) show microstructural transformations from pearlite to spheroidal cementite and/or ferrite at all positions where cracks have initiated. No transformation is present in an area where a previously opened has grown through. However, this area is not a crack initiation area. Accordingly, hypothesis 2.1 is not falsified.

Hypothesis 2.2: Cracks grow due to microstructural transformations along the crack path.

Result: The through-thickness crack of the *Reference* brake disc initiates in an area with deep microstructural transformation (cf. Figure 8-26 and Figure 5-22 top). However, it grows

through an area that shows no microstructural transformation (cf. Figure 5-22 bottom) and therefore hypothesis 2.2 is falsified.

Hypothesis 2.3: Overheating causes microstructural transformations that are harder and more brittle than the original disc material.

Result: An oxide layer is present at all polished micrograph sections of the *Reference* disc (cf. Figure 5-21 and Figure 5-22) except for the sample taken from the neck, which has not been overheated. Additionally, micro-cracks are visible at oxidised material along graphite lamellae. This indicates that oxidised samples are more brittle. Moreover, all samples showed a higher hardness value compared to the original hardness of the disc (cf. Figure 5-19). Microstructural transformations are also visible in surface near regions at radial centre position. Furthermore, hardness is highest at radial centre position, where the central hotband was present during the test. Accordingly, hypothesis 2.3 is not falsified.

Assumption 2.4: Surface oxidations serve as crack initiation spots.

Result: For the *Reference* brake disc, in areas of deep microstructural transformation (cf. Figure 5-21 and Figure 5-22), micro-cracks are visible along oxidised material around graphite lamellae. However, in sampling area C, only the ultimate surface layer is oxidised. Here, no micro-cracks are visible. Accordingly, assumption 2.4 is falsified and adjusted:

Assumption 2.4a: Surface oxidations along graphite lamellae serve as crack initiation spots.

Assumption 2.4a is not falsified.

Assumption 2.5: Porosity around graphite lamellae causes crack initiation.

Result: As shown in section 5.2.7, material around graphite lamellae is extremely hard when oxidised. Simultaneously, extraordinarily low hardness values were found at graphite lamellae. Furthermore, micro-cracks indicate porosity at the respective positions. Accordingly, assumption 2.5 is not falsified.

Conclusion: Overheating causes microstructural transformations that are harder and more brittle than the original disc material. Furthermore, it causes oxidations on the surface and along graphite lamellae. Material is hardened at overheated areas. This is consistent with the basic causal model. Nevertheless, cracks originate as small fissures at brittle, oxidised material around graphite lamellae on or near the friction surface. Microstructural transformation seem to be a necessary condition for crack opening but not for crack propagation. As soon as a crack has opened up, it can also grow through areas that have not undergone microstructural transformation. This is contradictory to the findings of other authors.

7.2.3 Connection between Hotspots, Fissures, and Open Cracks

Hypothesis 3.1: Local hotspots boost crack growth of open cracks.

During the test of the *Constant* disc, the longest crack of the disc at $\varphi = 226°$ maintains its length of 25.5 mm between $112 < N < 174$ (cf. Figure 5-7). Before this period and especially during this period, a hotspot is located at its position (cf. Figure 5-36). For $N > 175$, the hotspot moves away in rotational direction. Simultaneously, the crack starts growing again. Accordingly, it increases its growth rate although the hotspot has moved away from its location and hypothesis 3.1 is falsified.

Conclusion: Contradictory to statements of other authors and the basic causal model, a hotspot does not necessarily increase crack propagation rates. Moreover, large cracks most probably continue growing, regardless of the presence of a hotspot, because of the general tension friction ring created by hotbands. Accordingly, formation of a hotband might increase crack growth more than formation of a hotspot.

Hypothesis 3.2: For formation of a deep crack, thermal gradients and high temperature level comparable to hotspots on the friction surface are required in depth.

Result: No transformation at depths over 1 mm has been found, not even in areas of highest hardness levels. Accordingly, temperature levels where not as high as they are in hotspot regions on the friction surface. Still, the through thickness crack has grown at least 5 mm deep into friction ring at the respective area (cf. Figure 8-26). Accordingly, hypothesis 3.2 is falsified.

Conclusion: In the same way as hypothesis 3.1 is falsified for surface cracks, hypothesis 3.2 is falsified for deep cracks. Cracks can grow in depths that seems to be not affected by the hotspot, neither by strong thermal gradients nor by microstructural transformations.

Hypothesis 3.3: A through-thickness crack causes an instability in the friction ring and therefore creates a fixed hotspot at its location.

Result: Locations of the peak temperatures are plotted in Figure 8-6 till Figure 8-9 in the appendix. For the *Reference* brake disc, the through-thickness crack is located next to the peak temperature at the end of the test. Same accounts for the *Periodic* disc. Both discs have in common, that they are damaged by a long through-thickness crack at the end of the test, which causes extremely convex SRO at its location. The *Variable* disc has a short through-thickness crack at the end of the test. Peak temperature of the *Variable* disc is located at another position compared to the position of the through-thickness crack. Still, extremely convex SRO is present at the through-thickness crack location of the *Variable* disc. The *Constant* disc has no through-thickness crack, but several long cracks that are located in area of strongly convex SRO but rather not at the position of peak temperature. Taking into account that the through-thickness crack of the *Variable* disc is located at a rather cool position, hypothesis 3.3 is falsified. Peak temperatures at through-thickness crack locations of the *Reference* and *Periodic* disc are most probably caused by extremely convex SRO, which is present at all through-thickness crack locations at the end of the test. Accordingly, hypothesis 3.3 is adjusted:

Hypothesis 3.3a: A through-thickness crack causes an instability in the friction ring, which causes the formation of extremely convex SRO.

Hypothesis 3.3a is not falsified.

Conclusion: As extremely convex SRO forms at each through-thickness crack location at the end of the test but hotspots are not present at each through-thickness crack location at the end of the test, through-thickness cracks most probably cause formation of extremely SRO or are at least linked to its formation. Contradictory to the state of science, formation of through-thickness cracks is not caused by fixed hotspots. Moreover, a fixed hotspot is a phenomenon that might occur at through-thickness crack locations due to extremely convex SRO but is neither a necessary condition nor the origin for through-thickness crack formation.

Hypothesis 3.4: Hotspots are required for crack opening.

Result: For all tested brake discs crack opening zones (cf. Figure 5-16, Figure 5-33, Figure 5-43 and Figure 5-44) and hotpot positions (cf. Figure 5-10, Figure 5-28, Figure 5-36 and Figure 5-37) match entirely. For that reason, hypothesis 3.4 is not falsified.

Conclusion: Hotspots are presumably a necessary condition for crack opening and the formation of fissures, since they provide temperatures sufficiently high for microstructural transformations. This is consistent with the state of science. However, after cracks have reached a certain length, the presence of hotspots is not required for continued or even accelerated crack growth, which renders the state of science more precisely.

7.2.4 Influence of Cooling Channel Design

Assumption 4.1: Cooling channel pins cause an inhomogeneous temperature distribution on friction surface during the entire braking and cool-down period, which causes disc thickness variations due to thermal expansion.

Result: As described before, DTV of 30^{th} respectively 31^{st} order is still present in cold state and even rises during cool-down. During cool-down, temperature variation amplitudes of 30^{th} order fall monotonically for the *Constant* disc, starting from up to 10 K from the beginning of the cool-down period to amplitudes under 1 K 20 seconds later (cf. Figure 8-43). Accordingly, assumption 4.1 is falsified.

Assumption 4.2: Due to structure-mechanical effects, cooling channel pins cause extrusions on the friction surfaces during the cool-down period after each heat crack cycle.

Result: For each of the tested brake discs, DTV of 30^{th} respectively 31^{st} order, corresponding to the number of cooling channel pins in circumferential direction, is present and amplifying during cool-down (cf. Figure 5-15, Figure 5-32 and Figure 5-42). During braking, this phenomenon causes convex dents on the friction ring that transform into concave dents during cool-down. Temperature variations of 30^{th} respectively 31^{st} order rise during braking, but

fall monotonically and rapidly after release of the brake, as the temperature profile homogenizes rapidly (cf. Figure 8-43). Results are confirmed by the FE model, except for the convex/concave formation of the dents, as abrasion is not modelled. Accordingly, assumption 4.2 is not falsified.

Conclusion: Cooling channel pins push through the friction surface, causing extrusion that cannot be explained by thermal expansion during cool-down. These extrusions form as convex dents (thicker areas) during braking and transform into convex dents (thinner areas) during cool-down, most probably due to abrasion during braking. This phenomenon occurs cyclic with each heat crack cycle and has not been described in any earlier studies.

Assumption 4.3: Cooling channel pin extrusion causes shear stresses on the friction ring surface.

Result: Results from the FE model showed a single effective stress peak in between each of the cooling channel pins (cf. Figure 6-4). Accordingly, assumption 4.3 is not falsified.

Assumption 4.4: Cracks are guided by cooling channel pins and therefore grow in between them.

Result: Evaluation of crack paths in relation to cooling channel geometry has been done for the *Variable* disc (cf. Figure 5-33). In this context, all cracks, which became longest cracks at the end of the test, propagate along the projected edge of cooling channel pins. Accordingly, assumption 4.4 is not falsified.

Conclusion: Cooling channel pin extrusions cause shear stresses in between the projected edges of cooling channel pins on the friction surface. These shear stresses provide to the effective stress level, resulting in a stress peak in between each of the gaps. This stress peak is sufficiently high to guide cracks during their propagation. As a result, cracks grow faster through radially aligned pins in comparison to radially staggered pins, as they grow straight in the first case.

Assumption 4.5: Due to structure-mechanical effects, cooling channel pins cause stronger extrusions on the HS compared to the PS.

Result: In hot state, amplitude of extrusion is equally high on the PS compared to the HS for the *Constant* disc (cf. Figure 5-6). However, in cold state, amplitude of extrusion is generally higher on the HS for all discs. Accordingly, assumption 4.5 adjusted:

Assumption 4.5a: Due to structure-mechanical effects, cooling channel pins cause stronger extrusions on the HS compared to the PS in cold state.

Assumption 4.5a is not falsified.

Conclusion: During braking, neck influence seems to be negligible. During cool-down, HS probably suffers from a different thermal and stress state due to heat transfer into the neck while being more constraint. Furthermore, the additional constraint might increase effective stress level inside the friction ring. For that reason, pin extrusions are stronger on the HS compared to the PS after cool-down.

Assumption 4.6: Cyclic cooling channel pin extrusions cause softening in the friction ring.

Result: As DTV amplitudes corresponding to pin extrusions lower in the course of the test, which does not indicate a softening of the friction surface material, cooling channel pins might soften as well. However, results from FE modelling indicate that stress peaks are present in between the cooling channel pins due to their extrusion (cf. Figure 6-4). Since the brake disc material is known to soften under cyclic loading, additional cyclic stresses as induced by the pins cause additional softening on the friction ring. Accordingly, assumption 4.6 is not falsified.

Conclusion: Cyclic softening of the friction ring surface in between the cooling channel pins might additionally influence crack paths, as they grow preferably through weakened material areas. This might contribute to the phenomenon that cracks grow faster through radially staggered pins.

7.2.5 Influence of Disc Coning and Hotbands

Hypothesis 5.1: Highest stresses occur at the location of the hotband after cool-down.

Result: Results of the FE model indicate that highest stresses are concentrated in form of a "stress band" at radial centre position, regardless if a one-hotband case (at radial centre position) or a two-hotband case (at radial inner and outer position) appeared during braking (cf. Figure 6-4). This contradicts hypothesis 5.1 under the assumption that stress calculation of the FE model is correct.

Conclusion: Stresses are generally higher at radial centre position compared to radial outer and inner position, as the stress intensity caused by a single hotband outnumbers reduced stress concentration by two hotbands. This finding is consistent with the observation that cracks initiate at radial centre position and hardness is higher at radial centre position compared to radial inner and outer position. Still, hotbands influence crack formation strongly, which is consistent with the state of science.

Assumption 5.2: Due to thermal expansion, formation of a single hotband on the HS amplifies coning, formation of a single hotband on the PS reduces coning.

Result: For the *Reference* and the *Variable* brake disc, coning value is generally higher if the one-hotband case appears on the HS. However, for the *Periodic* disc, no dependency between hotband case and coning level could be found (cf. Figure 8-39). Nevertheless, this might be caused by the untypical hotspot and hotband formation of the *Periodic* disc. For that reason, assumption 5.2 is not falsified.

Assumption 5.3: Discs showing high coning amplitudes fail earlier in the heat crack test.

Result: According to the findings of section 5.1.2, relatively high average coning levels might reduce disc lifetime. Least cycles were endured by the *Reference* brake disc, which showed highest coning values of the test series. Most cycles were endured, even without a through-thickness crack, by the *Constant* disc, which showed lowest coning values of the

test series. The results do not contradict assumption 5.3. Accordingly, assumption 5.3 is not falsified.

Conclusion: Evaluation of assumption 5.2 and 5.3 relies on relatively few experimental data. Accordingly, reliability of the findings is low.

7.2.6 Influence of SRO

Hypothesis 6.1: Convex SRO in hot state determines hotspot positions

Result: SRO of the *Constant* and *Periodic* disc shifts for 50 cycles each (cf. Figure 5-38 and Figure 5-39). The reason for this shifting movement could not be explained (cf. section 5.4.2). However, it is not present in the hotspot patterns of the *Constant* and *Periodic* disc (cf. Figure 5-36 and Figure 5-37). Accordingly, positions of convex SRO do not match hotspot positions during the entire test and hypothesis 6.1 is falsified.

Hypothesis 6.2: SRO in hot state is an amplification of SRO in cold state.

Result: Comparison of SRO in hot state with SRO in cold state (e.g. Figure 5-13) shows that SRO in cold and hot state differs. Furthermore, dominant order and phase of the order corresponding to the hotspot order differ (Figure 8-17, Figure 8-19 and Figure 8-20). For that reason, SRO in hot state is not a simple amplification of SRO in cold state and hypothesis 6.2 is falsified.

Conclusion: Hotspots are not solely caused by SRO. Additional mechanisms might exist. Still, most hotspots, especially harmonic hotspots at the beginning of the heat crack test, are most likely caused by convex SRO in hot state. Furthermore, hotspots might influence SRO formation during braking as well, as SRO in hot and cold state differs from each other qualitatively.

Hypothesis 6.3: Local convex SRO in hot state accelerates crack growth.

Result: As described in the result chapter, crack growth zones are zones of convex SRO in hot state. Comparison of pattern figures shows that SRO and crack pattern match more compared to SRO and hotspot patterns. However, this statement is not completely valid for the *Periodic* disc (cf. Figure 8-35), as long cracks are present during $300 < N < 350$ in zones of concave SRO. Still, at the end of the test, longest cracks are present in zones of convex SRO, as well for the *Periodic* disc. Accordingly, hypothesis 6.3 is not falsified.

Hypothesis 6.4: Longest cracks propagate preferably in zones of convex SRO in hot state on positive slopes.

Result: For all discs except for the constant disc, longest crack are present in zones of positive SRO gradient (cf. Figure 5-18, Figure 5-34, Figure 8-36). Nevertheless, coefficient of determination between crack length and gradient of SRO is roughly zero ($R^2 = 0.424\ \%$) for the *Constant* disc (Figure 8-38). Moreover, all through-thickness cracks form in areas of convex SRO on positive slopes. Accordingly, hypothesis 6.4 is not falsified.

Assumption 6.5: Concave SRO in hot state inhibits crack opening.

Result: SRO of the *Variable* disc is mostly concave in between $110° < \varphi < 170°$. However, cracks open in this area, especially after $N > 250$. Accordingly, assumption 6.5 is falsified.

Assumption 6.6: Concave SRO in hot state reduces crack growth.

Result: All figures showing crack lengths vs. SRO level indicate that no long cracks are present in areas of concave SRO for all tested discs. Accordingly, assumption 6.6 is not falsified.

Conclusion: Crack growth of already open cracks might be accelerated in areas of convex SRO and reduced in areas of concave SRO. However, crack opening is not caused by convex SRO, which is consistent with the finding that hotspots open cracks (hypothesis 3.4). In addition to this, cracks preferably grow in areas of rising, convex SRO, as friction is most probably increased in these areas.

Assumption 6.7: As the brake disc gets softer, SRO amplitudes amplify in the course of the test.

Result: For all tested discs, SRO amplitudes generally rise in the course of the test in a manner that the entire curve is amplified slightly cycle-by-cycle (cf. Figure 5-15, Figure 5-32 and Figure 5-42). As a limitation, during $N < 50$, amplitude of harmonic SRO order, which corresponds to the order of quickly migrating, harmonic hotspots, is additionally amplified and exceeds remaining SRO amplitudes. For that reason, assumption 6.7 is adjusted:

Assumption 6.7a: As the brake disc gets softer, non-harmonic SRO amplitudes amplify in the course of the test.

Assumption 6.8: Through-thickness cracks decrease bending stiffness of the friction ring.

Result: This behaviour has been observed for all through-thickness cracks, regardless of their length. Accordingly, assumption 6.8 is not falsified.

Assumption 6.9: A periodic variation of the circumferential cooling channel pin spacing inhibits formation of SRO in hot state.

Result: *Constant* and *Periodic* disc are identical except for the cooling channel pin spacing in circumferential direction. Still, SRO order changes, as the *Periodic* disc shows no harmonic SRO and different SRO orders in general as well. Accordingly, hypothesis 6.9 is not falsified. Furthermore, *Periodic* disc shows no harmonic SRO and harmonic hotspots during $N \leq 50$. The same accounts partially for the *Variable* disc, whose cooling channel pin arrangement changes on the circumference as well. For that reason, assumption 6.10 is formulated:

Assumption 6.10: A periodic variation of the circumferential cooling channel pin spacing in circumferential direction suppresses formation of harmonic SRO and hotspots at the beginning of the heat crack test.

Assumption 6.10 is not falsified.

Conclusion: SRO is affected by several influences regarding bending stiffness. Due to softening of the material in the course of the test, SRO-amplitudes rise. Second, a through-thickness crack causes an instability of the friction ring and therefore degrades bending stiffness. Finally, by variation of pin spacing, counter-periodicity inhibits the formation of harmonic SRO and therefore the formation of hotspots.

7.3 Combination of the Identified Influences into a Causal Model

Based on the results and evaluated hypothesis of this work, a new causal model is deducted correcting and extending the basic causal model presented before. Additionally, objective evidence of the identified influences is discussed. The hypothesis/assumption number is indicated after each statement in brackets.

The basic model is extended by a quantity that has not taken into account before in the context of heat crack formation in brake disc: deformation in relation to cooling channel geometry. Cooling channel design directly affects formation of SRO and DTV in the heat crack test (4.2, 6.9). This affects both areas of crack growth due to SRO formation (6.3, 6.4) and local crack paths (4.4) due to DTV formation: cooling channel pins extrude during each heat crack cycle through the friction ring surface (4.2). This causes a DTV amplitude corresponding to the order of the cooling channel pins with a peak amplitude of 4 µm. During braking, extrusion of pins is convex, during cooling concave (i.e. intrusion). The cyclic extrusion causes shear stresses in between the cooling channel pins and finally results in stress peaks in between the cooling channel pins (4.3). Accordingly, cracks propagate preferably through these stress peaks, i.e. in between cooling channel pins (4.4). Furthermore, pin arrangement in radial direction affect crack growth rates: cracks are slowed down as soon as they “hit” the projected edge of a cooling channel pin. If pins are radially aligned, relatively long cracks in the heat crack test occur. If pins are slightly staggered, relatively short cracks are the result. Fully staggered pin arrangement causes relatively long cracks as well. This causal chain is fully backed by experimental findings, except for the resulting stress state, which is only indicated by the FE model. Still, these findings have been presented for the first time in this work, which makes confirmation in future works necessary for extended reliability.

SRO is influenced by cooling channel pin arrangement as well as inaccuracies of the brake disc itself and its mounting. For that reason, SRO cannot be fully reproduced by FE models. SRO in hot state is not an amplification of SRO in cold state (6.2). SRO in hot state has an influence on crack growth rates. In areas where concave SRO forms, only small cracks are present (6.6), although concave SRO does not inhibit crack opening (6.5). Longest cracks are present in areas where convex SRO forms (6.3). Cracks trend to grow in areas where SRO rises, i.e. a positive slope is present (6.4). Convex SRO in hot state mostly occurs at positions where hotspots are present (6.1). However, in rare cases hotspots also form without

presence of convex SRO and convex SRO forms without presence of hotspots. SRO can be partially suppressed by periodic variation of cooling channel pin arrangement along the circumference (6.9). In the course of the test, most SRO amplitudes rise (6.7). As soon as a through-thickness crack forms, strongly convex SRO forms at the position of the through-thickness crack, most probably due to loss of structural integrity of the brake disc (6.8). This causal chain is mostly backed by experimental findings. However, evidence for correlation of crack growth at positive slopes as well as conjunction of hotspots and SRO is lower. As reported for the influence of cooling channel pin arrangement on crack propagation, influence of SRO on heat crack formation has been presented for the first time in this work, requiring confirmation in future works.

Two forms of hotspots are distinguished: harmonic hotspots, which quickly migrate over the friction surface during the first 50 cycles of the test and are characterised by a clearly dominant, relatively high order. They transform into subordinate hotspots, which migrate slower during remaining cycles of the test and are characterised by a blurry mixture of lower orders. Harmonic hotspots are suppressed by circumferentially varying cooling channel pin arrangement. From the basic causal model, hotspots are known to cause plastic compression during braking and therefore cyclic damage, being the main influence of the formation of heat cracks. It was found that stress state on the friction surface is not entirely compressive during braking (1.2). Moreover, influence of hotspots is considered differently and more detailed here. Hotspots cause overheating and therefore microstructural transformations. Microstructural transformations are – as hotspots are – limited to ultimate surface layers and spatially greatly varying in their depth. Furthermore, surface near oxidations along graphite lamellae are covered with micro-cracks, which most probably are the origin of heat crack formation (2.4, 2.5), as they initiate in microstructural transformed areas (2.1), which are harder and more brittle than the untouched disc material (2.3). In short, hotspots are necessary for crack opening (3.4). Contrary to previous findings of other authors, local presence of a hotspot is neither necessary for the formation of a long heat crack (3.1) nor for a through-thickness crack (3.3). Cracks can moreover grow in depths that are not affected by a hotspot (3.2). Neither is presence of microstructural transformations required for crack propagation through the respective area (2.2). However, short cracks might close after a hotspot has moved away from their location. Still, large cracks remain open during braking regardless of compressive stresses (1.1). Furthermore, crack opening does not necessarily slow down crack growth rates of adjacent cracks (1.3, 1.4). Still, the ratio of crack count to medium crack length seems to be constant and specific to the friction pairing (1.5).

Instead, hotbands are most likely the dominant influence on crack growth of opened cracks, along with convex SRO. They cause most stresses at radial centre position in case one hotband is present (5.1). In case two hotbands are present on the inner and outer radius during braking, stresses are still highest at radial centre position after cool-down since a single hotband is hotter and therefore causes higher residual tensile stresses. For that reason, most

cracks start growing at radial centre position. Shape and intensity of hotbands might be influenced by the brake pad. However, influence of the brake pad is not part of this work. It is further unclear, if coning has an influence on crack formation (5.2, 5.3).

The causal chain regarding the influence of hotspots is mostly backed by experimental findings. Limitations are the unclear conjunction of transformation depth and surface hardness as well as the unknown delay between overheating by a hotspot and initiation of crack growth, since the crack detector does not detect cracks smaller than 3 mm. Finally, the causal chain regarding the influence hotbands partially consists of assumptions deducted by experimental results, partially of assumptions based on the findings of the FE model. Still, influence of hotspots on crack opening and growth has been identified clearly, correcting the state of science.

In conclusion, the new causal model is summarised graphically in Figure 7-1.

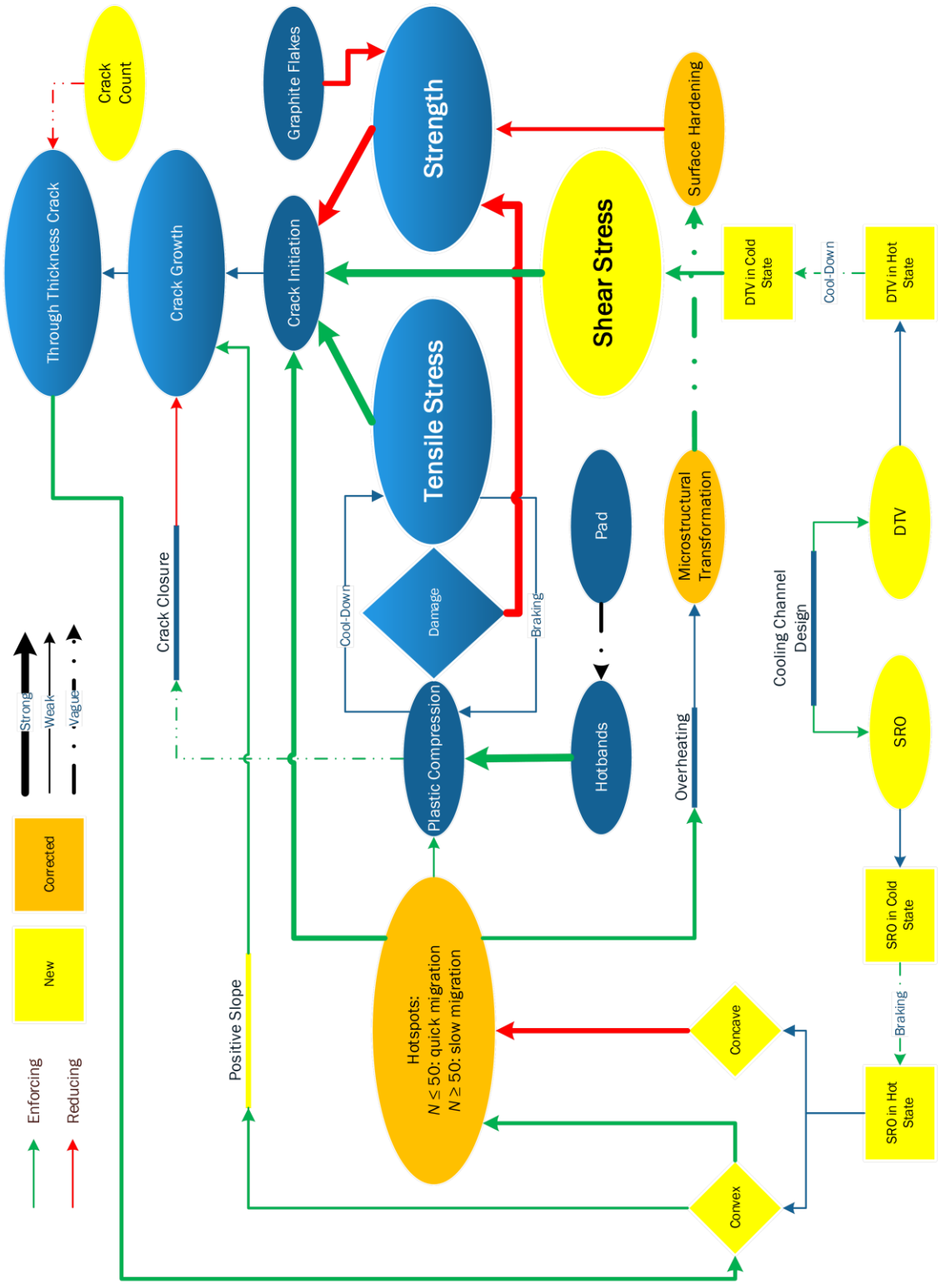

Figure 7-1: New causal model deducted in this work

7.4 Check on Plausibility and Applicability of the FE Model

In order to evaluate the plausibility of the results of the FE model, comparison between simulated and experimental data is made. Since no experimental data on stresses is available, evaluation focuses on temperature and deformation. Crack related quantity have already been checked in the preceding chapter.

Temperature distribution on the HS at the end of a braking period is shown in Figure 7-2 for simulation (left) and actual measured data (right). In general, temperature distributions are similar to each other regarding number of hotspots and hotbands. However, several differences between model and experiment are present. First, maximum temperatures are measured higher than calculated. Second, average temperature of the model is slightly higher compared to the measurement by the thermographic camera. These deviations might be caused due to the one-dimensional heat transfer assumed by the deconvolution approach. Accordingly, narrow and high hotspots are flattened and get wider during calculation, since heat dissipates to the ultimate surrounding of the hotspot. Finally, temperatures on the inner radius of the friction ring are cooler than 350 °C, which is the lower limit of the measurement range of the thermographic camera. It is unclear, whether temperatures are actually lower in this area or heat dissipation into the neck of the brake disc is not sufficiently considered by the deconvolution approach. However, temperatures on the PS, which has no connection to the neck, are partially lower than 350 °C as well, indicating that actual values are lower and not captured by the thermographic camera. In brief, temperature gradients regarding hotspots are generally underestimated by the model, making it rather conservative.

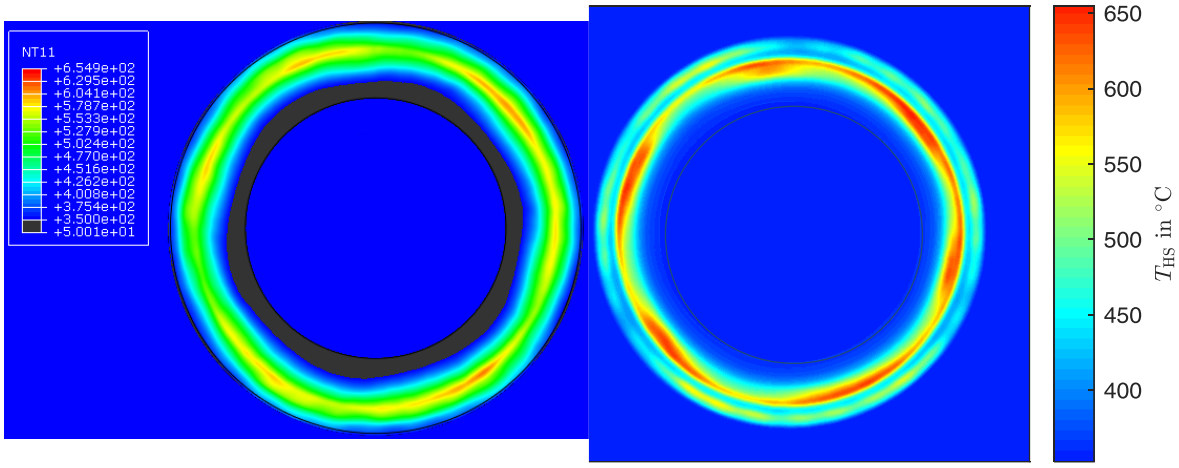

Figure 7-2: Simulated temperatures (left) and measured temperatures (right) at the end of the first braking period of the heat crack test with the *Reference* disc; temperatures in °C

Comparison of hotspot-temperature T_{HS} and cooling rates (bottom) during the first five seconds of the cool-down period is shown in Figure 7-3. As peak temperature is lower in the simulation, simulated cool-down temperature is shifted about 50-70 K beneath measured

temperature. Still, temperature-dependent cool-down rates are overestimated in the simulation, especially at high temperature. Later, cool-down rates align slightly. The overestimation of cool-down rates at high temperatures might be caused due to overestimated radiation losses. 100 °C is reached after 525 s of cool-down in simulation, in the actual experiment after 601 s (cf. Figure 8-45). On semi-logarithmic scale both cool-down temperature curves appear as mostly straight lines after a few seconds of cool-down (Figure 8-45). Gradient of simulated temperature straight line is steeper. In conclusion, convective heat losses are slightly overestimated as well.

However, requirement 1.1 is still fulfilled, as the temperature distribution is reproduced based on experimental results.

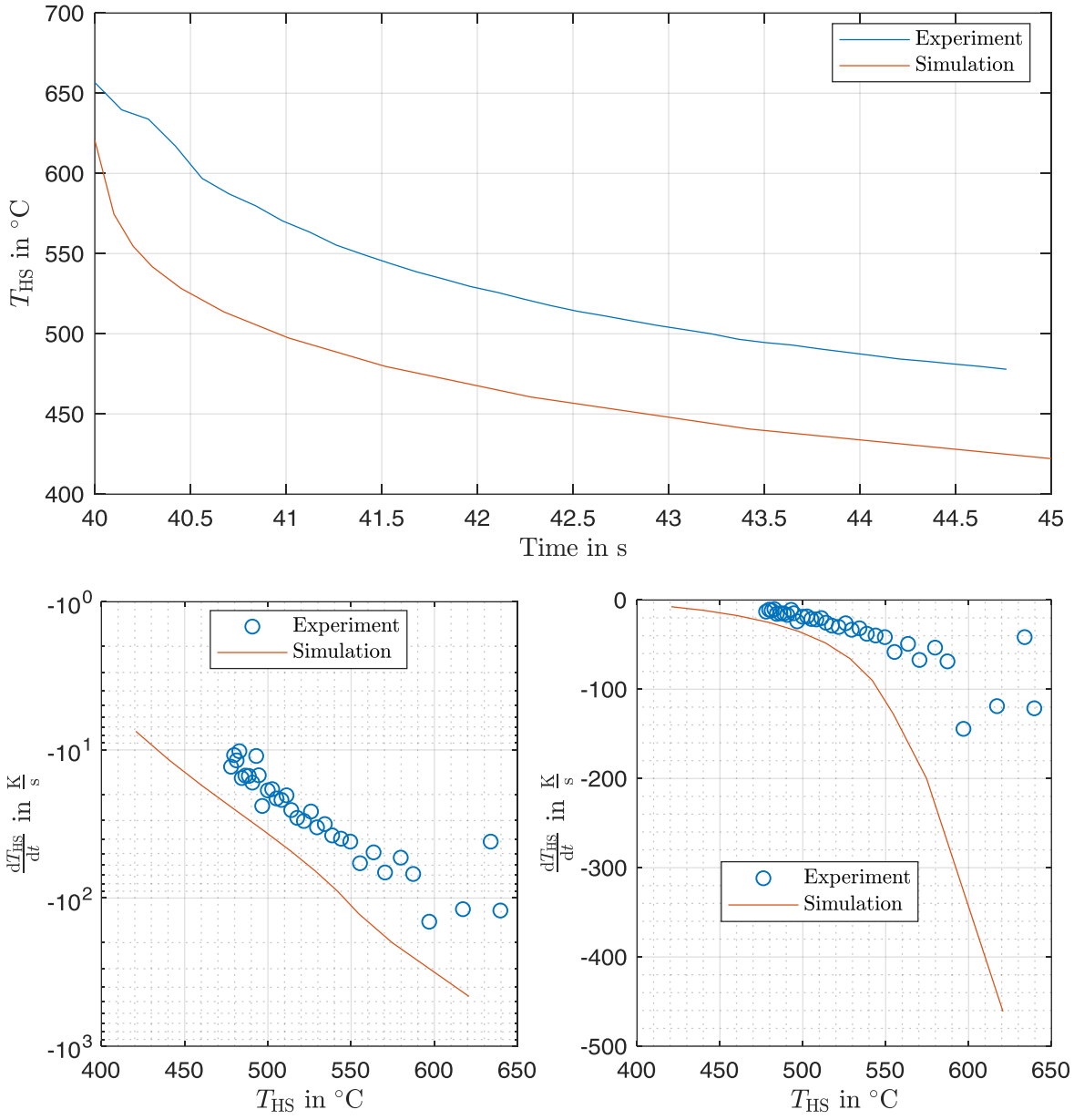

Figure 7-3: Comparison of hotspot-temperature (top) and cooling rates (bottom) during the first cool-down of the *Reference* brake disc; semi-logarithmic (left) vs. linear (right)

In terms of deformation, cooling channel pin induced DTV amplitude of 30th order has already been compared to experimental results in section 6.3.2. A comparison between SRO in model and experiment is shown in Figure 7-4.

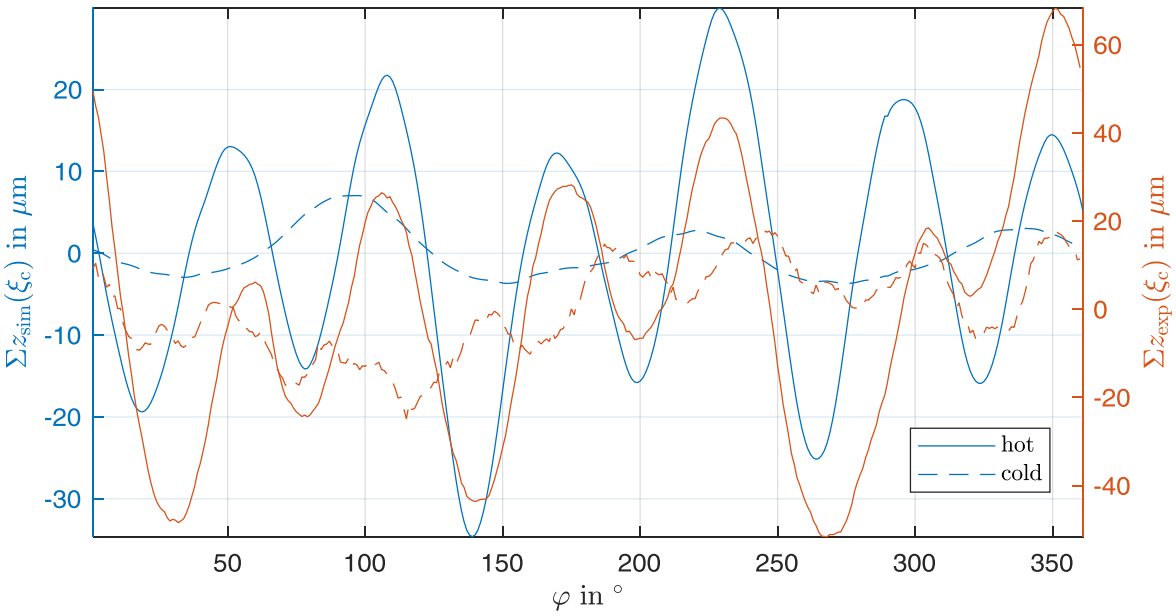

Figure 7-4: Comparison between simulation and experiment for SRO in hot and cold state

SRO in hot state is generally higher compared to SRO in cold state for both simulation and experiment. In addition to this, SRO in hot state is dominated by a 6th order (simulation: 18.8 µm), caused by the hotspots. Phase delay between 6th-order hotspots and SRO is 15.3° in the simulation, 16.6° in the experiment. However, amplitude of measured 6th-order SRO is more than two times higher (40.6 µm) than amplitude of calculated SRO. In cold state, deviation is higher, since SRO in the experiment is dominated by a first order, which is most probably caused by non-planar mounting of the brake disc to the dynamometer. Furthermore, SRO in cold state mostly consists of a 3rd order (3.64 µm) in simulation, in the experiment besides the dominant 1st order of a 7th order (5.39 µm).

In conclusion, dominant SRO order and phase match in hot state, but amplitudes are too low in the model. In cold state, SRO amplitudes differ completely. Deviations might be caused by inaccuracies of the real specimen.

Finally, applicability of the FE model is evaluated. Temperature distribution is reproduced by the model, although peak temperatures are underestimated, and cooling rates are slightly overestimated (requirement 1.1). Stress distribution is supposedly correct (requirement 1), since the stress-strain response is modelled accurately under unilateral loading (requirement 1.2, cf. Figure 8-46 until Figure 8-49). Crack and fatigue calculation do not provide valid results in terms of crack length and fatigue life estimation (requirements 2 and 4). However, crack initiation zones match experimental results (requirement 3). Accordingly, the model is suitable for comparison of the temperature and stress distribution for the modelled brake disc, as well as for basic comparison between brake disc designs. However, two issues limit the applicability of the FE model as a forecast tool for prediction of the result of the heat

crack test: first, formation of hotspots and the general thermal load distribution can only be calculated by the model based on experimental data. This limits its applicability to new brake discs designs with different hotspot formation behaviour. Second, crack growth rates are dependent on the crack path. Since no valid crack growth simulation is available for calculation of crack paths, crack length prediction is not possible.

8 Conclusion and Outlook

In this work, a basic causal model has been derived based on the state of science and technology. Based on this model, research objectives have been formulated based on knowledge gaps. These include influence of the non-uniform temperature distribution, microstructural transformations and disc deformation. Hypotheses have been formulated, which are suitable to derive a new, profound causal model explaining the formation of heat cracks in brake discs for heavy-duty vehicles.

Five heat crack tests have been observed using an extensive experimental setup. The methodology has several unique features. First, the usage of an automated crack detector, allowing for systematic observation of crack lengths of all cracks during the entire experiment. Second, usage of displacement sensors at high sampling rate for comparison of crack formation with deformation of the friction ring. Finally, numerous material experiments with a *Twin* disc and an additional FE model providing an insight into the stress state on and inside the brake disc. The extended experimental setup allows for several new evaluation methods. The most outstanding is the comparison of crack, temperature and deformation patterns.

Several brake disc designs have been tested, while material and pad influence have been kept as a minimum. A *Reference* brake disc provided results on the general behaviour of a brake disc in the heat crack test. Additionally, it has been modelled for FEA and material experiments have been conducted at the *Reference* disc itself and its *Twin* disc. This makes the *Reference* disc the most comprehensively investigated disc in comparison to the state of the art. In addition to this, a heat crack test with a brake disc with circumferentially varying cooling channel pin arrangement that showed the influence on pin arrangement to crack path guiding for the first time. Based on the findings of the first experiments, two brake discs with an optimised cooling channel have been tested. One of these discs, which features periodically varying circumferential pin spacing, suppresses the formation of harmonic hotspots. The improved brake disc designs endured more heat crack cycle in comparison to the *Reference* disc.

Experimental results have been used for composition of a new causal model. The new model extends the basic model and corrects it partially. Key findings, which have not been or not correctly been discussed in literature before, are as follows: first, the cooling channel design directly affects crack propagation due to surface extrusions caused by the cooling channel pins. Second, the influence of hotspots on growth rates of open cracks introduced in literature has been re-evaluated: hotspots define crack initiation zones due to microstructural transformations. Their presence is not a necessary condition for continuous crack growth, as soon as a crack has reached a certain length. The phenomenon that peak temperatures occur at the position of long or through-thickness cracks made by other authors is caused by extremely convex SRO at the through-thickness crack location, most probably caused by structural

instability of the friction ring. Finally, general causal chain of crack formation behaviour has been described in a new level of detail, starting from micro-cracks over crack initiation to the occurrence of through-thickness cracks. Furthermore, it evaluates the size of each influence.

The FE model provides additional information on temperature and stress distribution on and in the friction rings. It relies on a new deconvolution approach for reproduction of the temperature distribution based on experimental data and confirms experimental results. However, it is not suitable for prediction of crack growth or brake disc life. Accordingly, future works should focus on the development of a FE model capable of predicting the formation of hotspots in the first place and afterwards focus on the prediction of general crack formation.

Furthermore, several experimental observations conducted in this work did not deliver clear results: first, results of measurement of residual stresses were greatly varying. Therefore, their validity is concerning. Second, depth of microstructural transformation and local surface hardness did not appear to be related to each other, although expected. Third, the relation between SRO and DTV in cold and hot state was observed, but could not be explained.

Although several works by other authors have discussed the influence of brake pads, future studies might improve the new model composed in this work by repeating tests with different friction couplings. Moreover, results are only valid for the heat crack test procedure described in this work. Other test procedures, e.g. stop-brakings, might produce different results when mechanical stresses outperform thermomechanical stresses. Finally, some of the hypotheses might be falsified by additional experiments. Five tested brake discs, which are quite similar, e.g. cooling channel pins instead of vanes, are sufficient for falsification of hypotheses but rather not sufficient to state that hypotheses will not be falsified by experiments with other brake disc types.

A Appendix

A.1 Additional Evaluation Methods

A.1.1 Alternative Calculation Method for Disc Coning

For generation of results in this work, calculation method $s(N)$ introduced in section 4.1.2 is used. However, as this does only take the HS into account, an alternative calculation method is presented here, calculating coning $s^*(N)$ based on the average displacement of the centreline of both friction rings:

$$s^*(N) = \frac{\overline{z_{r_c,\mathrm{H}}\left(n\left(\underset{n}{\operatorname{argmax}}\left(z_{r_c,\mathrm{H}}\right)\right),N\right)} + \overline{z_{r_c,\mathrm{P}}\left(n\left(\underset{n}{\operatorname{argmax}}\left(z_{r_c,\mathrm{P}}\right)\right),N\right)}}{2} - \frac{\overline{z_{r_c,\mathrm{H}}\left(n\left(\underset{n}{\operatorname{argmin}}\left(z_{r_c,\mathrm{H}}\right)\right),N\right)} + \overline{z_{r_c,\mathrm{P}}\left(n\left(\underset{n}{\operatorname{argmin}}\left(z_{r_c,\mathrm{P}}\right)\right),N\right)}}{2} \tag{8.1}$$

This calculation method takes both friction rings into account and is less sensitive to the formation of hotbands, since they usually do not occur on simultaneously on the same radius on both friction rings. However, regardless of calculation method, coning values reside in the same sequence, i.e. high coning values remain high coning values and low coning values remain low coning values. Comparison between calculated coning values is shown in Figure 8-1 exemplarily for the *Reference* and the *Variable* disc. The coefficient of determination is 90.3 % for the *Reference* disc and 75.9 % for the *Variable* disc, although $s(N)$ is higher than $s^*(N)$ for the *Reference* disc.

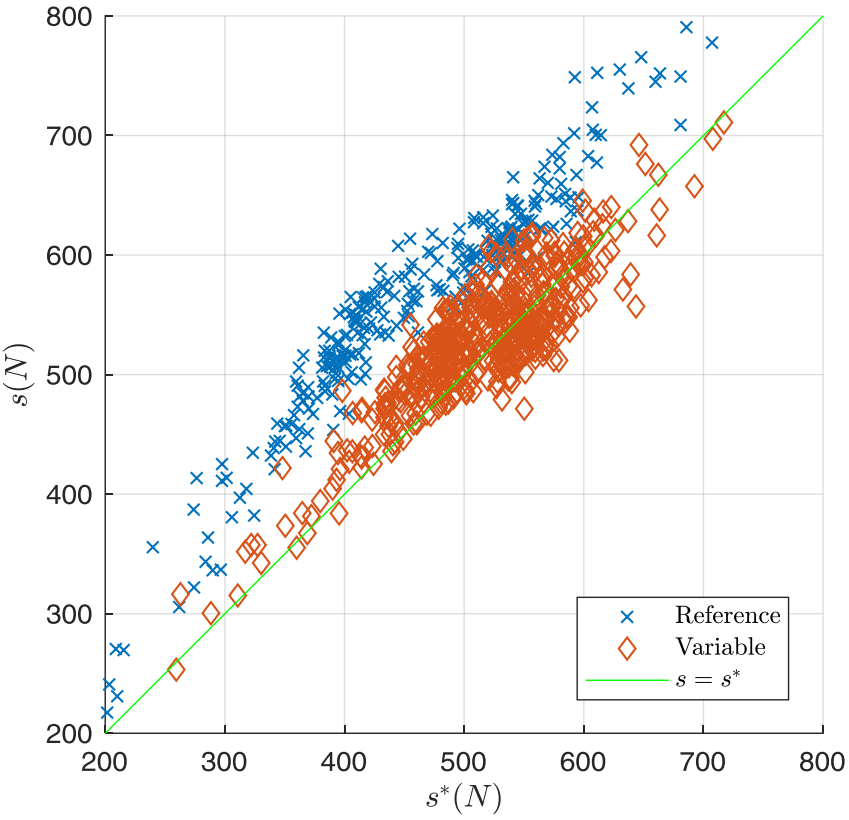

Figure 8-1: Coning of the *Reference* and the *Variable* disc as calculated in the result chapter $s(N)$ vs. alternative calculation method $s^*(N)$

A.1.2 Hotspot Pattern Using Alternative Evaluation Method

As described in 4.5.1, hotspot patterns can also be generated using an alternative method by extracting temperatures at the radius featuring peak temperature. These hotspot patterns are shown in the following figures for reference.

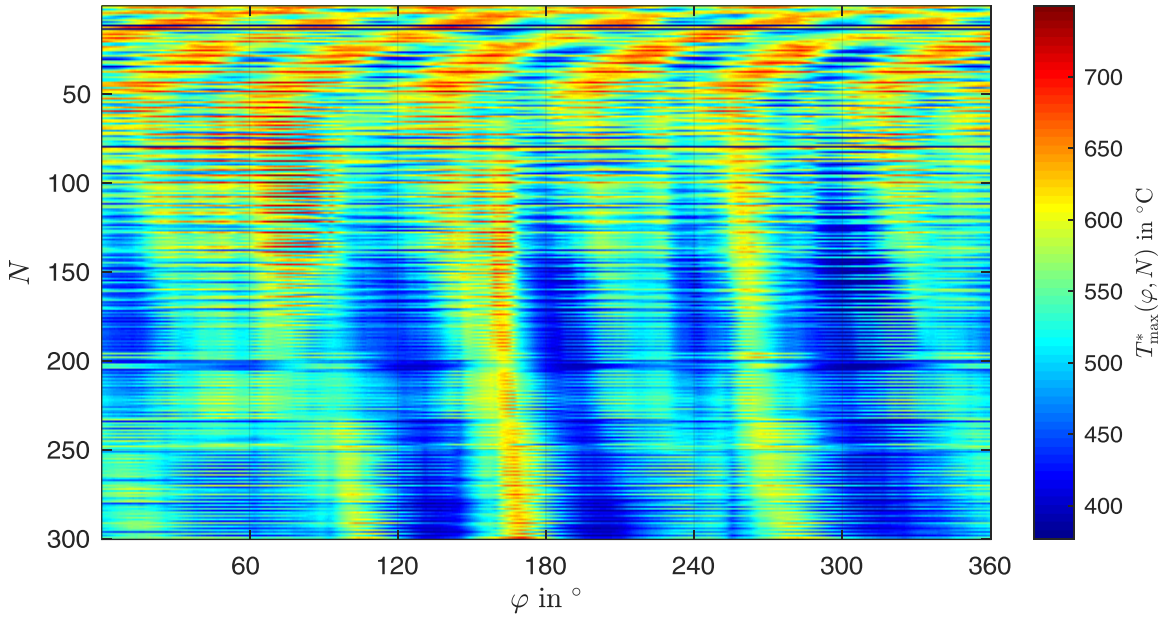

Figure 8-2: Hotspot pattern of the *Reference* brake disc using an alternative evaluation method

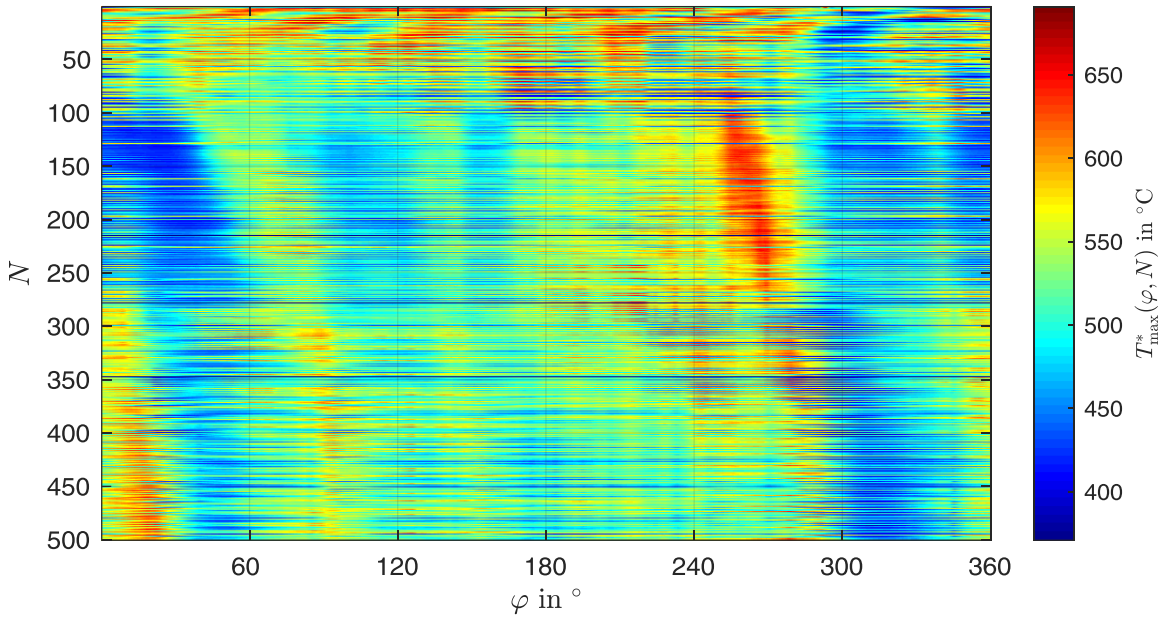

Figure 8-3: Hotspot pattern of the *Variable* brake disc using an alternative evaluation method

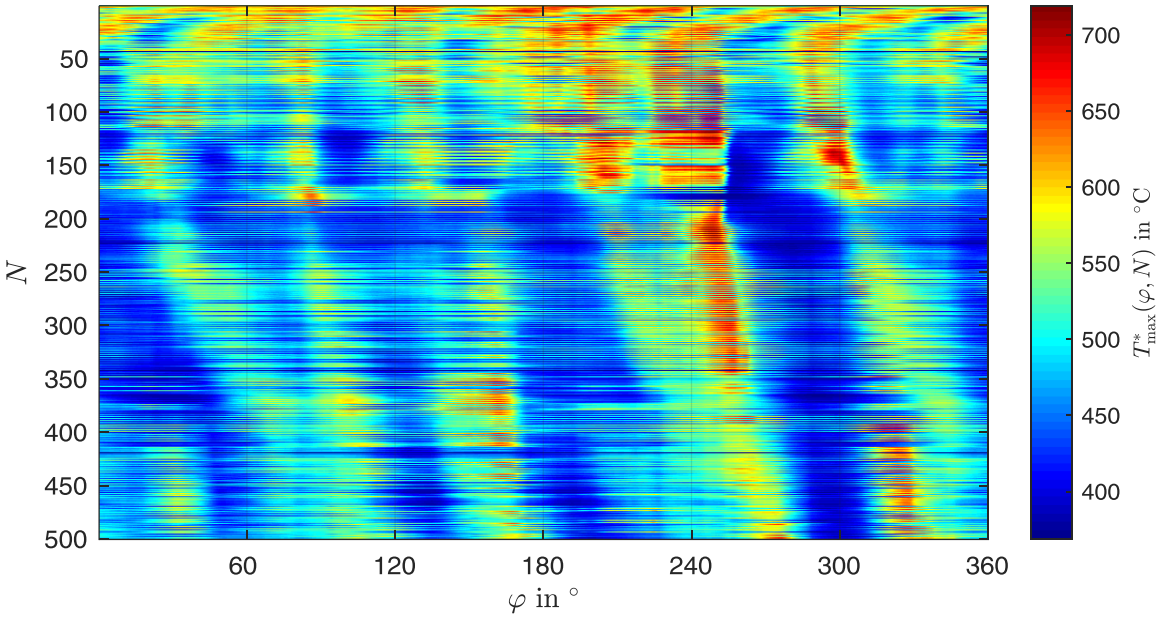

Figure 8-4: Hotspot pattern of the *Constant* brake disc using an alternative evaluation method

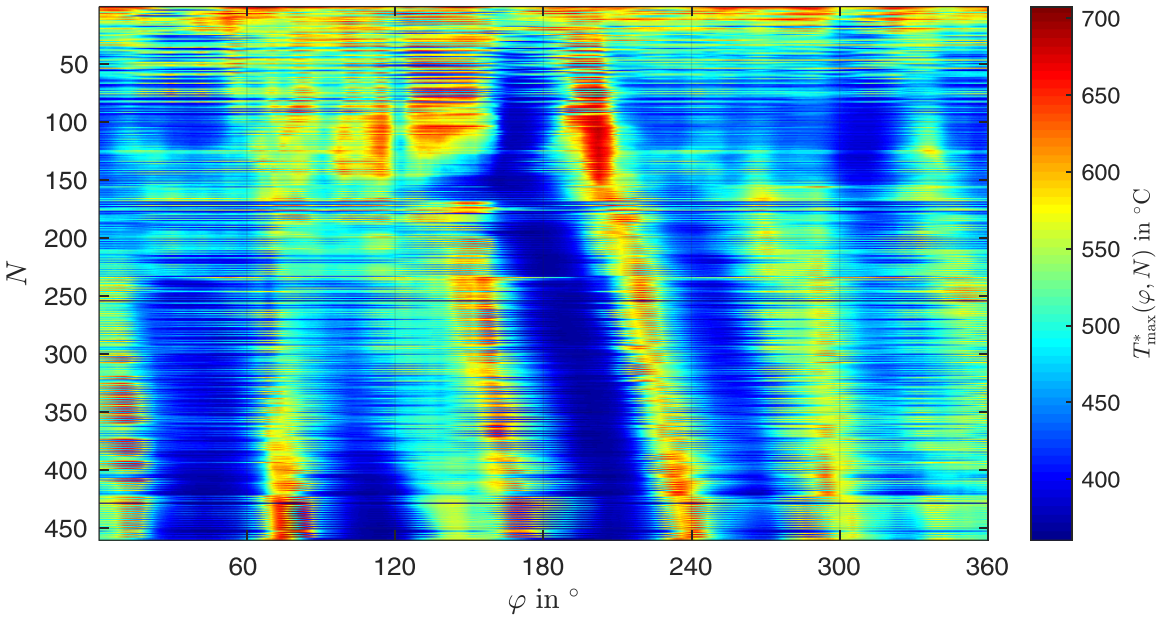

Figure 8-5: Hotspot pattern of the *Periodic* brake disc using an alternative evaluation method

A.2 Additional Evaluations Regarding Common Phenomena

A.2.1 Location of Peak Temperature

The thermographic image taken during the revolution in which the peak temperature of the respective heat crack cycle occurred (n_{hot}) is used for determination of angular position $\varphi\left(T_{\mathrm{H,peak}}(N)\right)$ and radial position $r\left(T_{\mathrm{H,peak}}(N)\right)$ of the peak temperature.

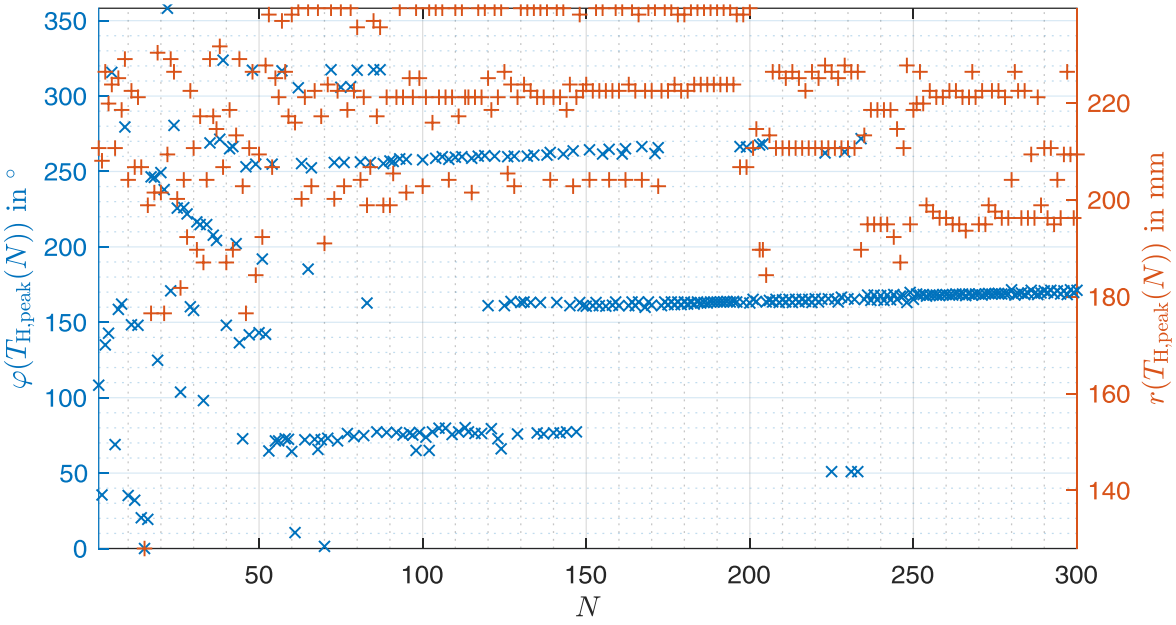

Figure 8-6: Angular and radial location of the peak temperature of the *Reference* brake disc; radial location values are partly biased due to malfunction of the thermographic camera; through-thickness crack at $\varphi = 150°$

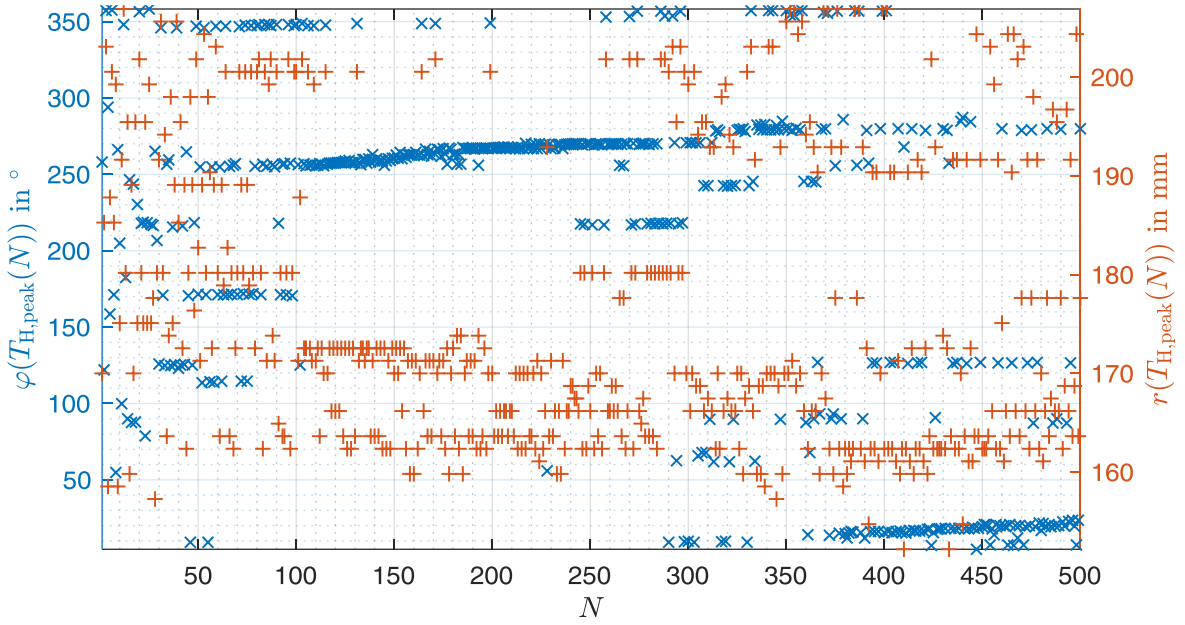

Figure 8-7: Angular and radial location of the peak temperature of the *Variable* disc; through-thickness crack at $\varphi = 344°$

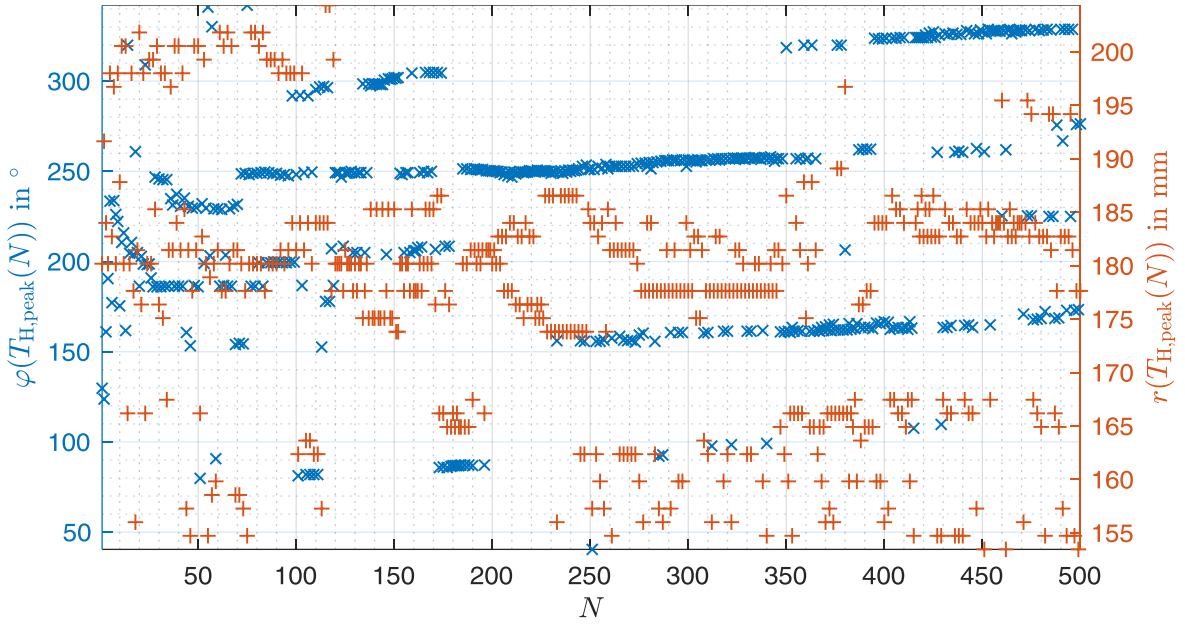

Figure 8-8: Angular and radial location of the peak temperature of the *Constant* disc; longest cracks at $\varphi = \{226°; 250°; 261°; 257°\}$

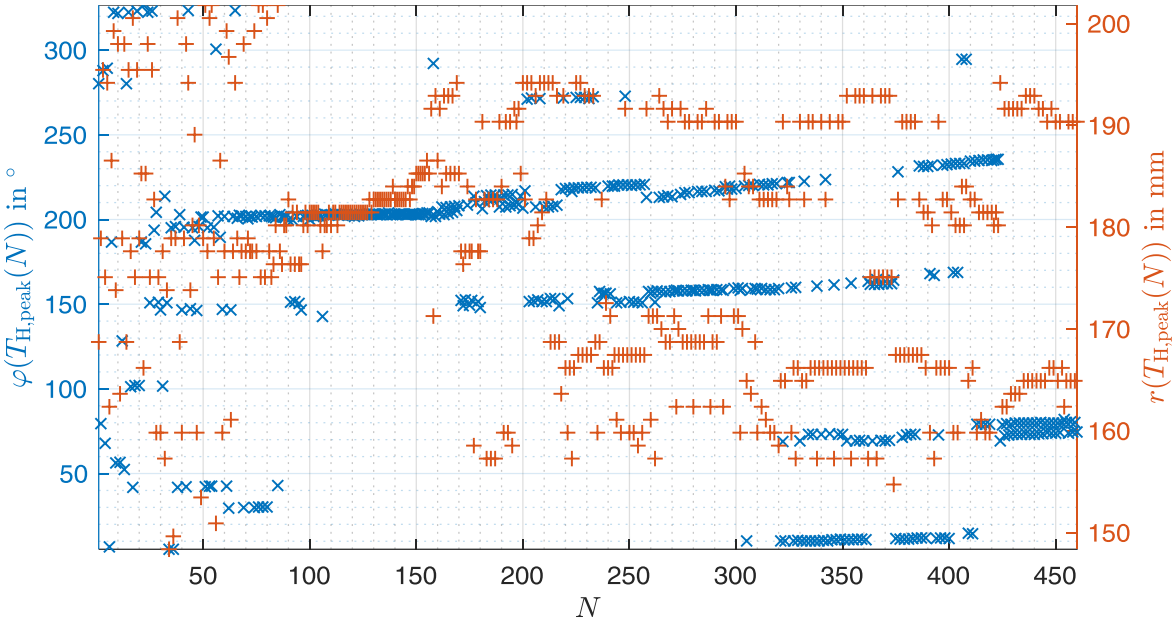

Figure 8-9: Angular and radial location of the peak temperature of the *Periodic* disc; through-thickness crack at $\varphi = 67°$

A.2.2 Cool-Down Duration vs. Maximum Temperature

Figure 8-10 shows cool-down durations taken from Figure 5-3 plotted vs. maximum temperature measured by the thermocouple $\max\left(T_{\mathrm{H}}(\xi_{\mathrm{c}})\right)$ in each heat crack cycle N. In addition

to this, the coefficient of determination, i.e. the squared correlation coefficient is shown on top of each of the plots. No correlation is apparent.

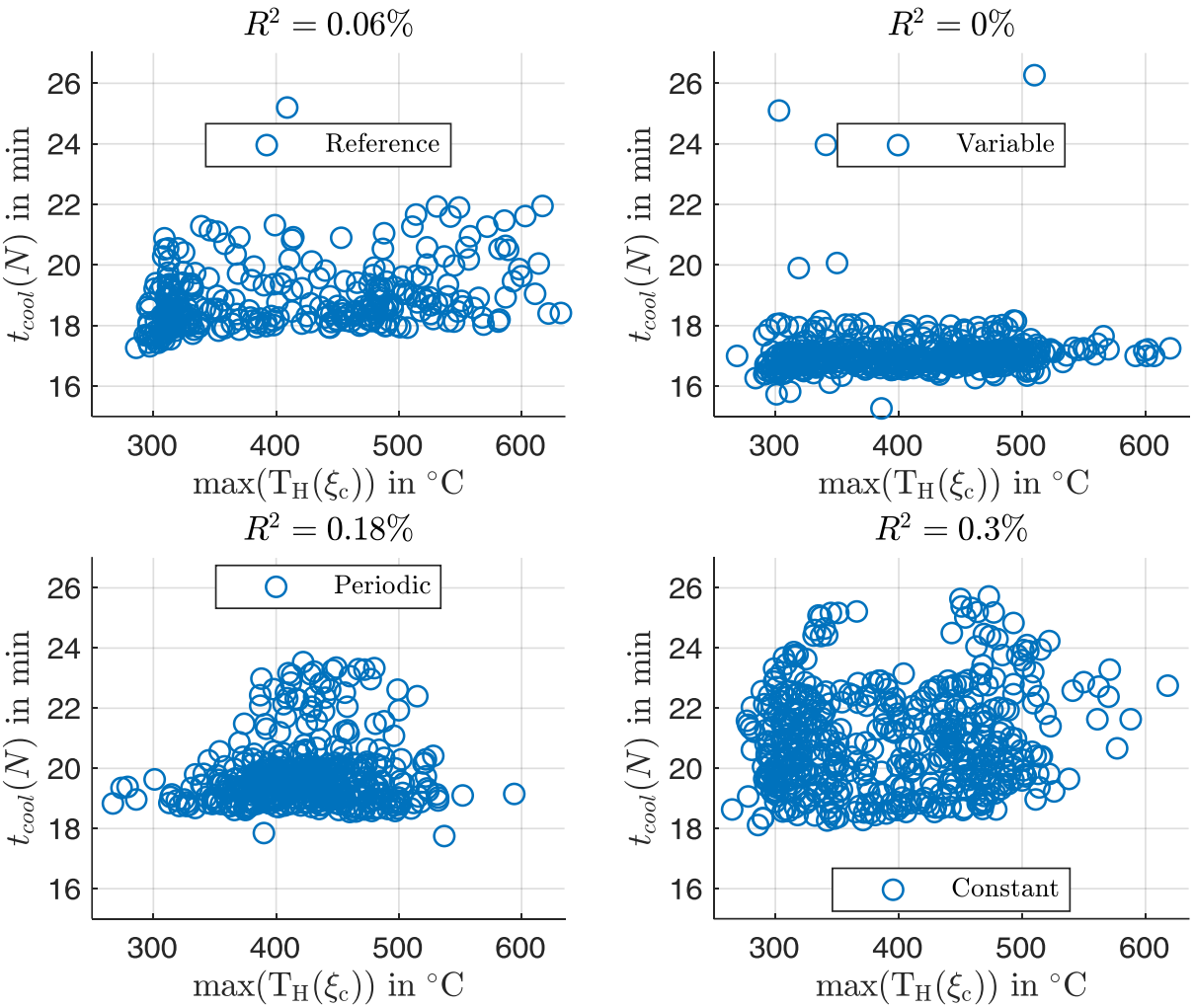

Figure 8-10: Cool-down duration vs. maximum temperature measured by the thermocouple for each brake disc including coefficients of determination

A.2.3 Crack Statistics

For all brake discs, average crack length $\bar{l}(N) = \frac{\Sigma l(\varphi,N)}{k(N)}$ is shown in Figure 8-11. It rises almost linear with increasing heat crack cycle number. For reference, crack count $k(N)$ is shown in Figure 8-12 for all brake discs.

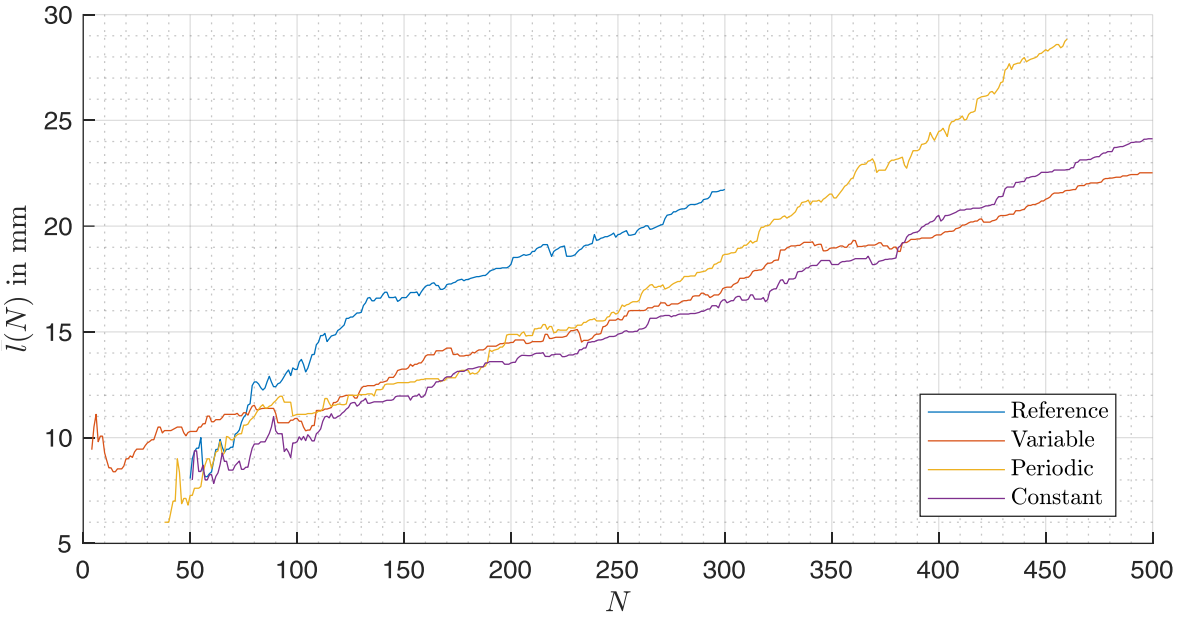

Figure 8-11: Average crack length for all brake discs

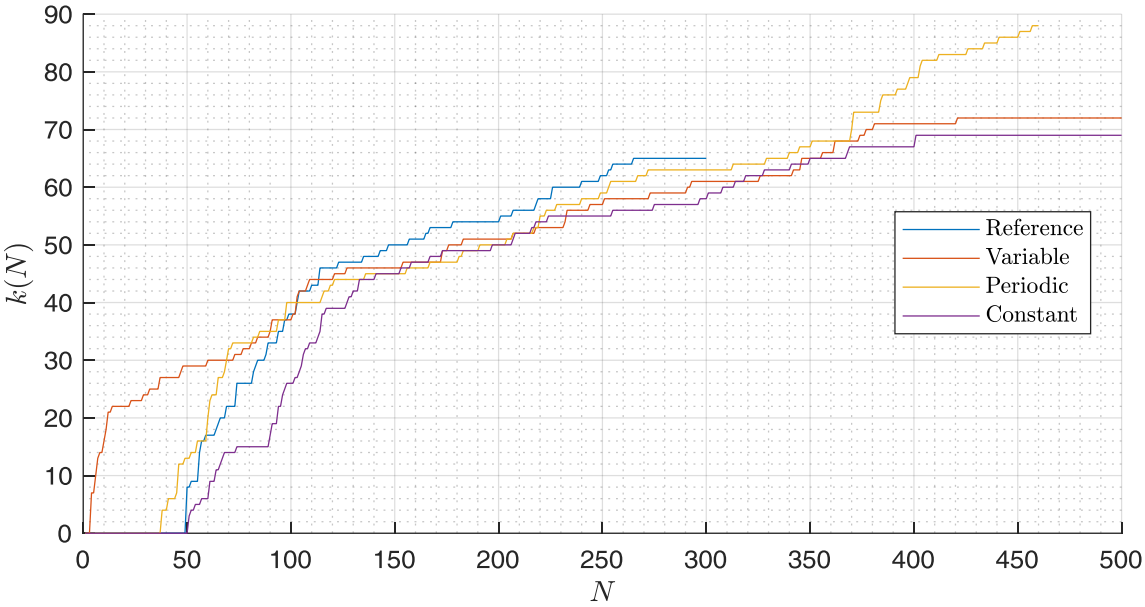

Figure 8-12: Crack count of all brake discs

A.2.4 Evaluation of Crack Length vs. Crack Count

In order to evaluate assumption 1.5 (cf. section 3.1.4), linear regression is applied over $\frac{k^2(N)}{\Sigma l(N)}$ (cf. Figure 5-8) from N_{Start} to N_{End}. While N_{End} is the last cycle of the respective test, N_{Start} is defined as the cycle, when the condition $\frac{k^2(N)}{\Sigma l(N)} = \frac{k^2(N_{\mathrm{End}})}{\Sigma l(N_{\mathrm{End}})}$ is met for the first time. The absolute value of the ascension of the regression straight in the interval $[N_{\mathrm{Start}}\ N_{\mathrm{End}}]$ has to

be smaller or equal to the standard deviation of $\frac{k^2(N)}{\Sigma l(N)}$ in order to fulfill the requirements of the assumption. Values are given in Table 8-1.

Table 8-1: Evaluation of assumption 1.5

Disc	N_{Start}	N_{End}	Absolute Ascension	Standard Deviation	Comment
Reference	104	300	0.196	0.450	Smaller
Variable	91	500	0.316	0.445	Smaller
Periodic	70	460	0.453	0.517	Smaller
Constant	105	500	0.715	0.713	Considered Equal

A.2.5 Phase Shift of Hotspots

Supplementary to Figure 5-2, the filtered phase shift is shown in Figure 8-13 to Figure 8-16 for each brake disc in a separate figure. Moreover, the peak temperature reached in each heat crack cycle $T_{\mathrm{peak,H}}(N)$ taken from Figure 5-1 is plotted over each figure.

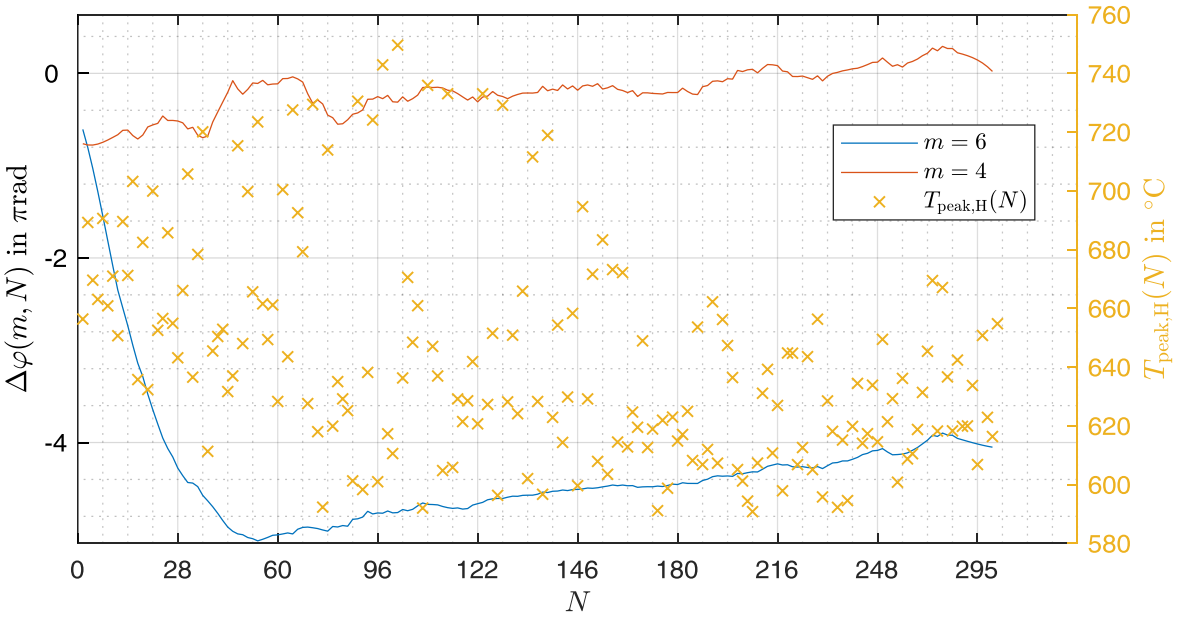

Figure 8-13: Filtered phase shift of the 4th and 6th order hotspots of the *Reference* disc

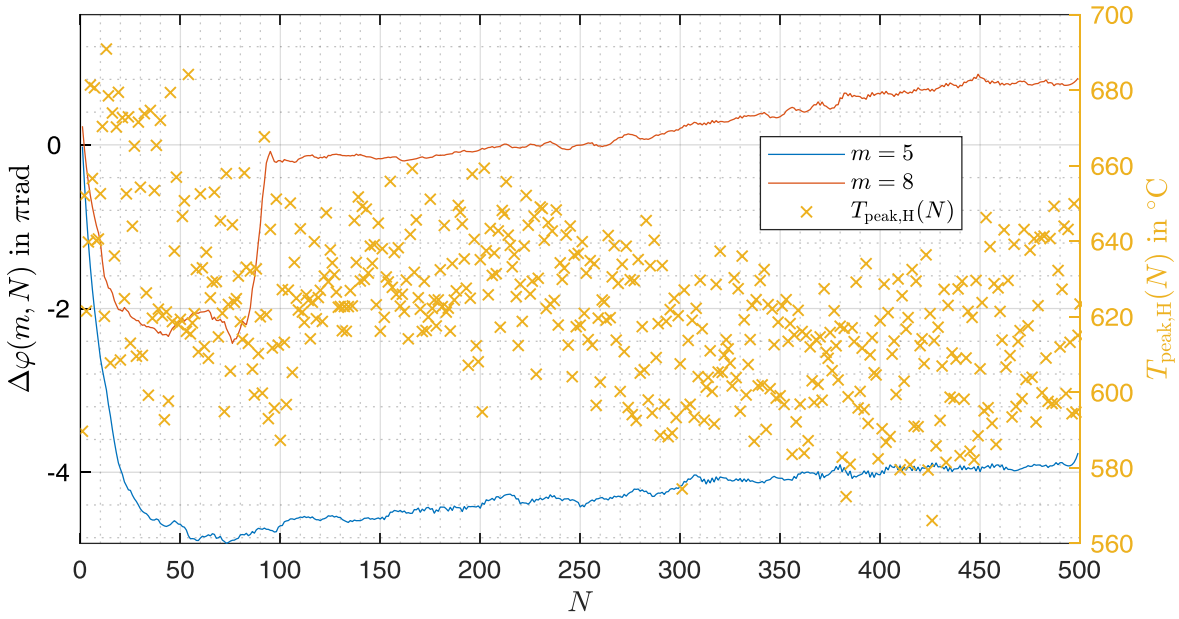

Figure 8-14: Filtered phase shift of the 5th and 8th order hotspots of the *Variable* disc

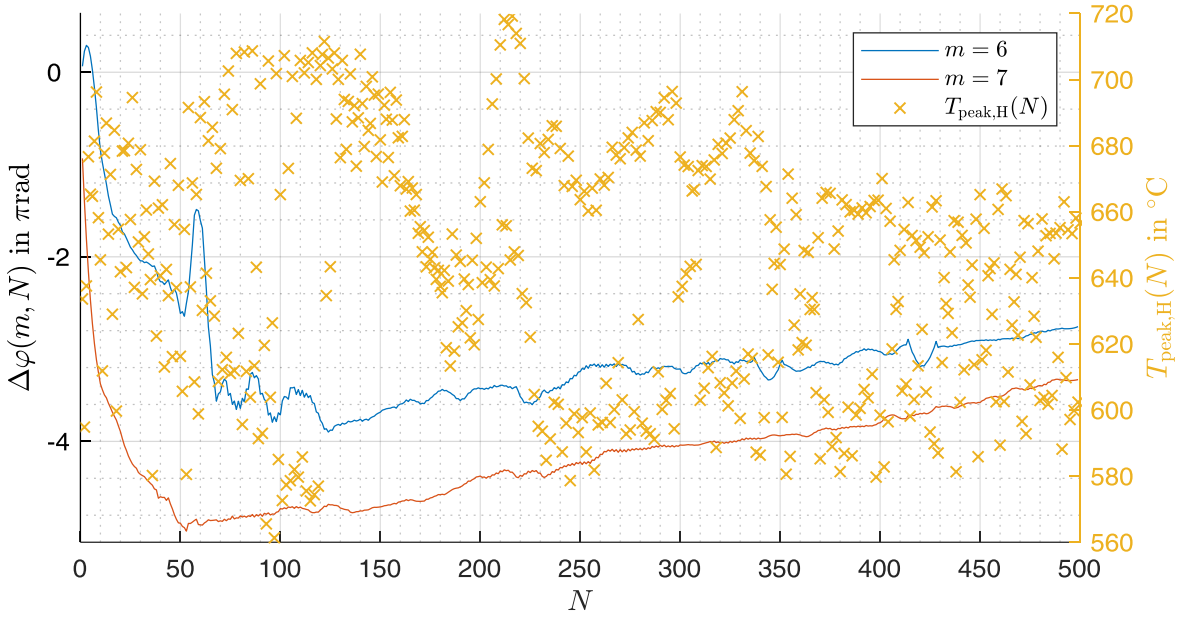

Figure 8-15: Filtered phase shift of the 6th and 7th order hotspots of the *Constant* disc

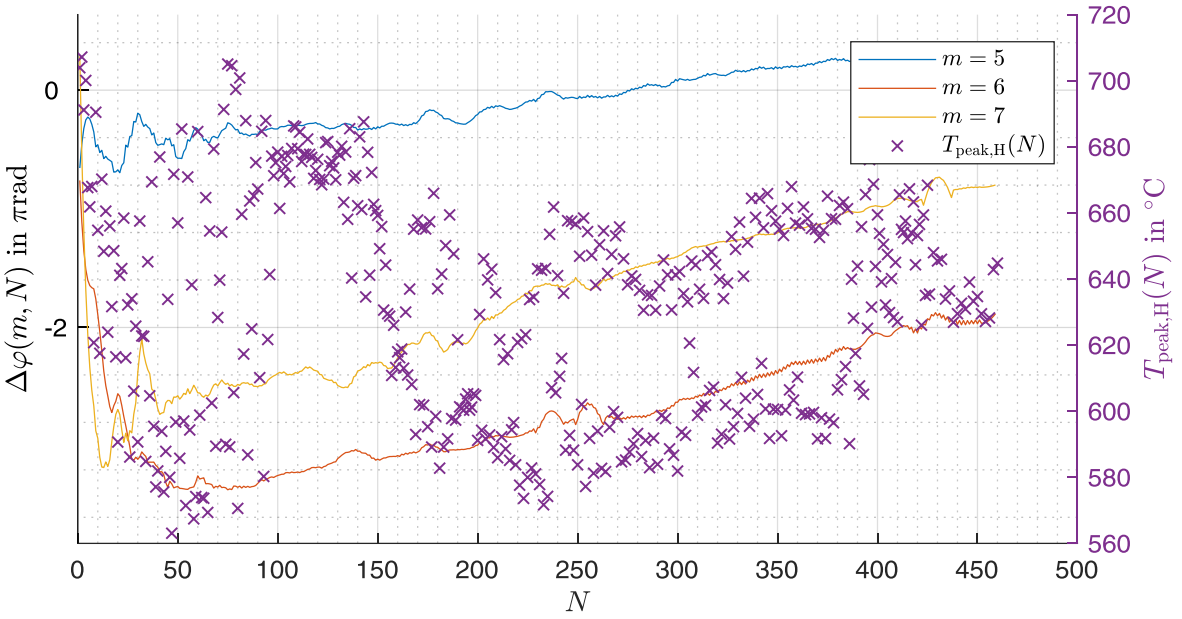

Figure 8-16: Filtered phase shift of the 5th, 6th and 7th order hotspots of the *Periodic* disc

Using the same filtering techniques, phase shift of 6th order hotspots as well as 6th order SRO in hot and cold state is shown in Figure 8-17: Filtered phase shift of the 6th order hotspots as well as 6th order SRO in hot and cold state of the *Reference* disc.

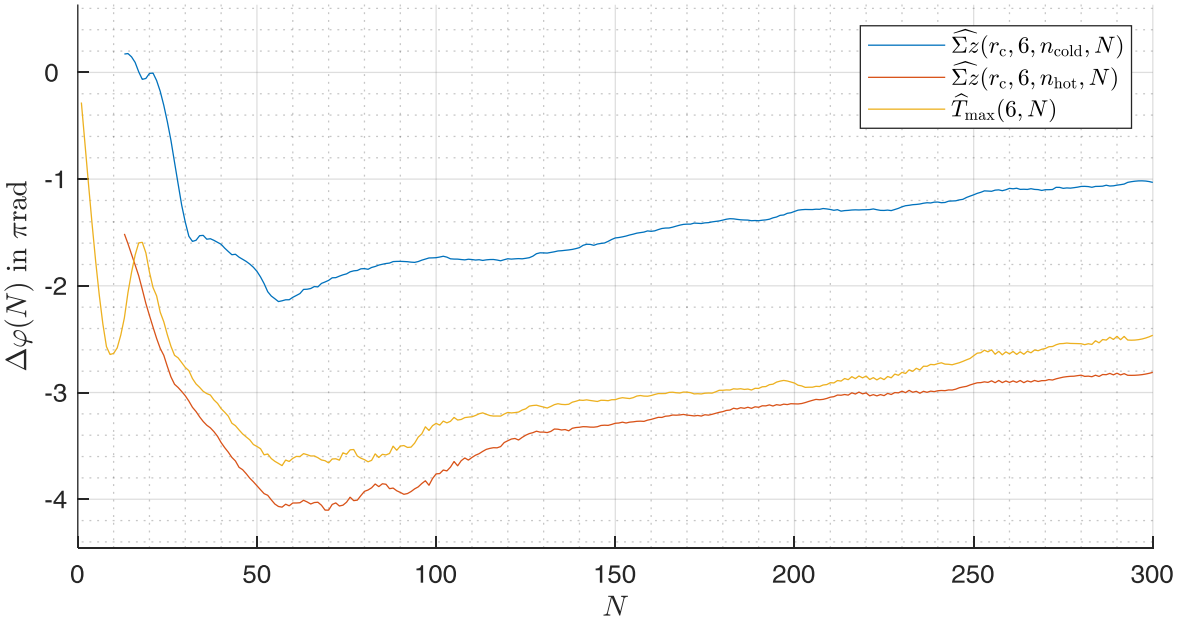

Figure 8-17: Filtered phase shift of the 6th order hotspots as well as 6th order SRO in hot and cold state of the *Reference* disc

A.3 Additional Evaluations Regarding the *Reference* Disc

A.3.1 SRO in Hot and Cold State with Equal Color Scale

In the result chapter, pattern figures of deformation quantities are shown in hot and cold state. A different color scale is used for hot and cold state in order to enhance contrast, although the same quantity is plotted. In Figure 8-3 the effect of low contrast when using the same color scale is visible.

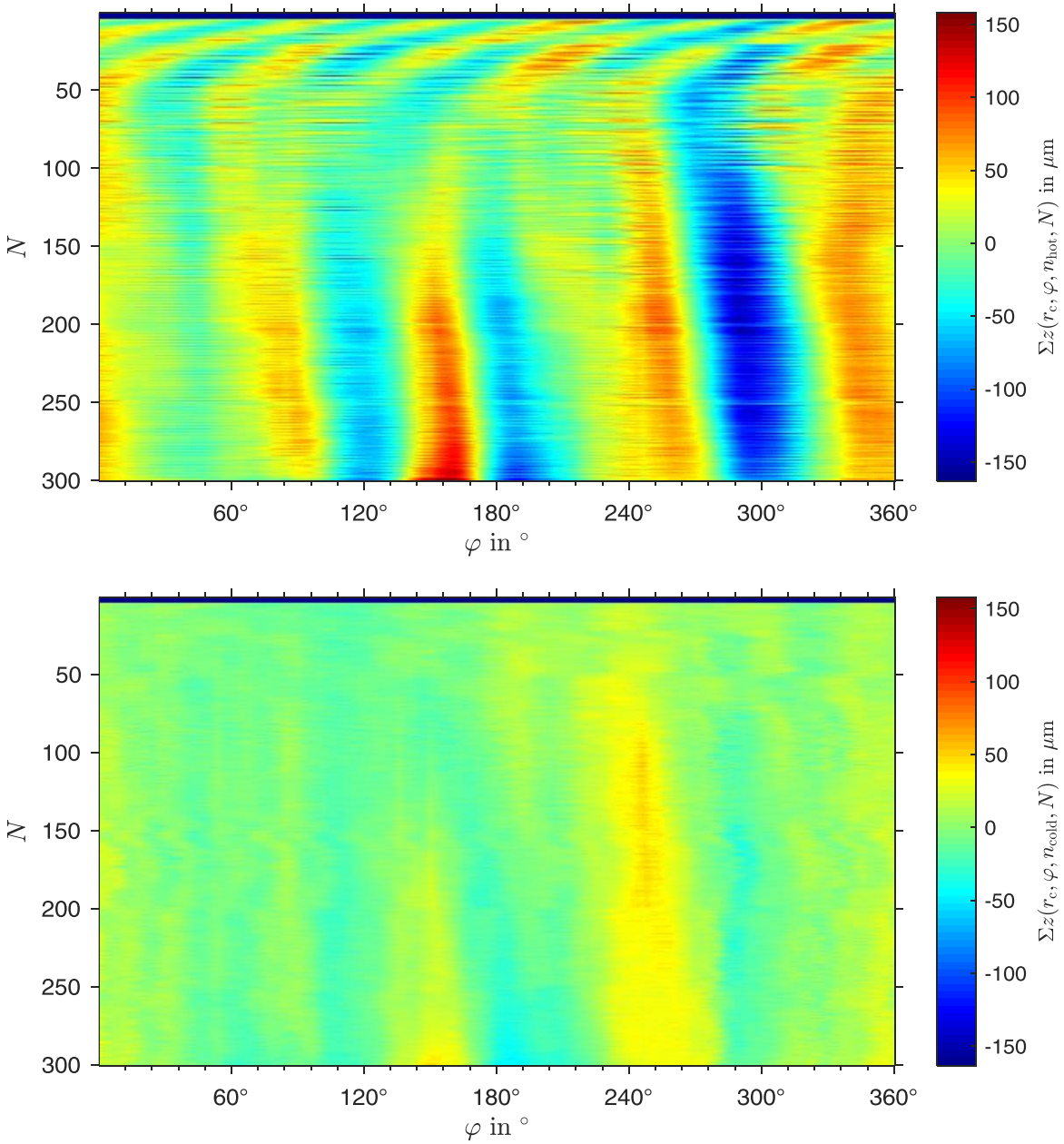

Figure 8-18: SRO in hot (top) and cold (bottom) state of the *Reference* brake disc, corresponding to Figure 5-13 with equal colour scale

A.3.2 Amplitude Spectrum of SRO in Hot and Cold State

For further comparison of SRO in hot and cold state, amplitude spectrums similar to the amplitude spectrum of the hotspots (cf. Figure 5-11) are shown for SRO in hot state in Figure 8-19 and SRO in cold state in Figure 8-20. Dominant orders differ during the entire test.

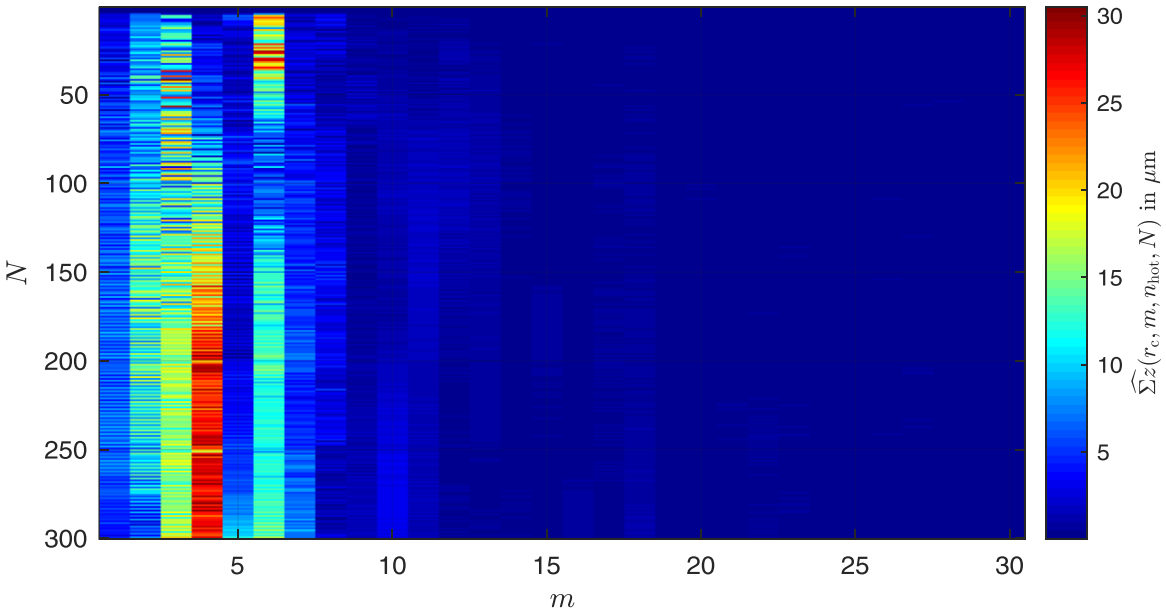

Figure 8-19: Amplitude spectrum of SRO in hot state; *Reference* disc

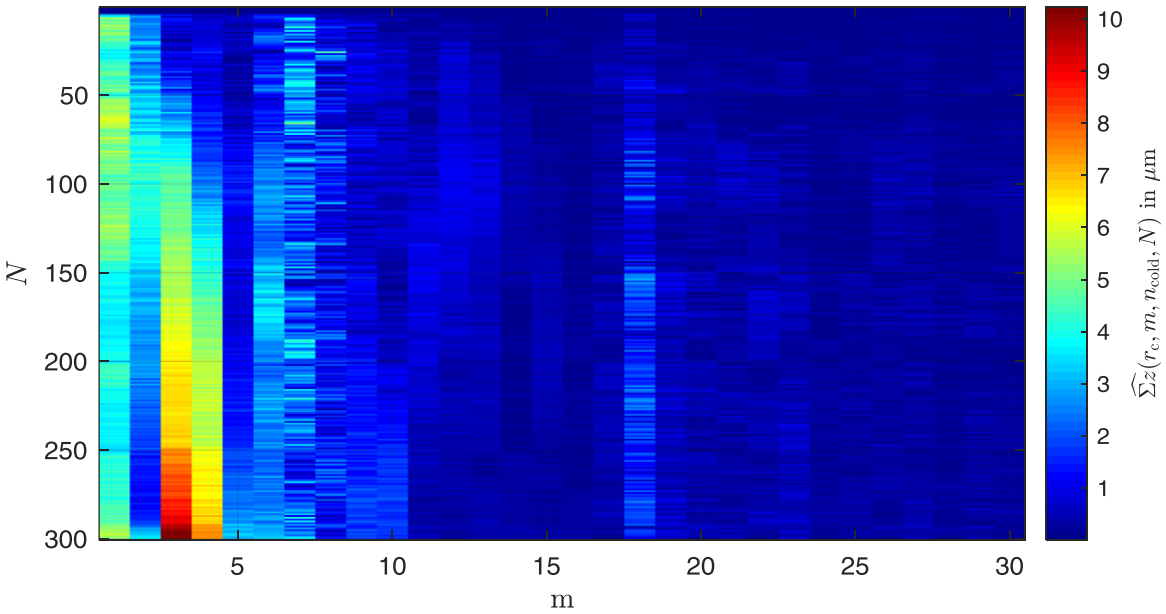

Figure 8-20: Amplitude spectrum of SRO in cold state; *Reference* disc

A.3.3 Cooling Channel Pin Extrusions

As described in section 5.1.2, cooling channel pins cause extrusions on the friction surface resulting in DTV of 30th order. Figure 8-21 is created by averaging the data from Figure 5-14

over all cycles and shows dents at cooling channel pin positions in cold state, i.e. the brake disc is thinner at cooling channel pin positions. In contrast to this, Figure 8-22 shows thicker areas at the cooling channel pin positions at the end of each braking period.

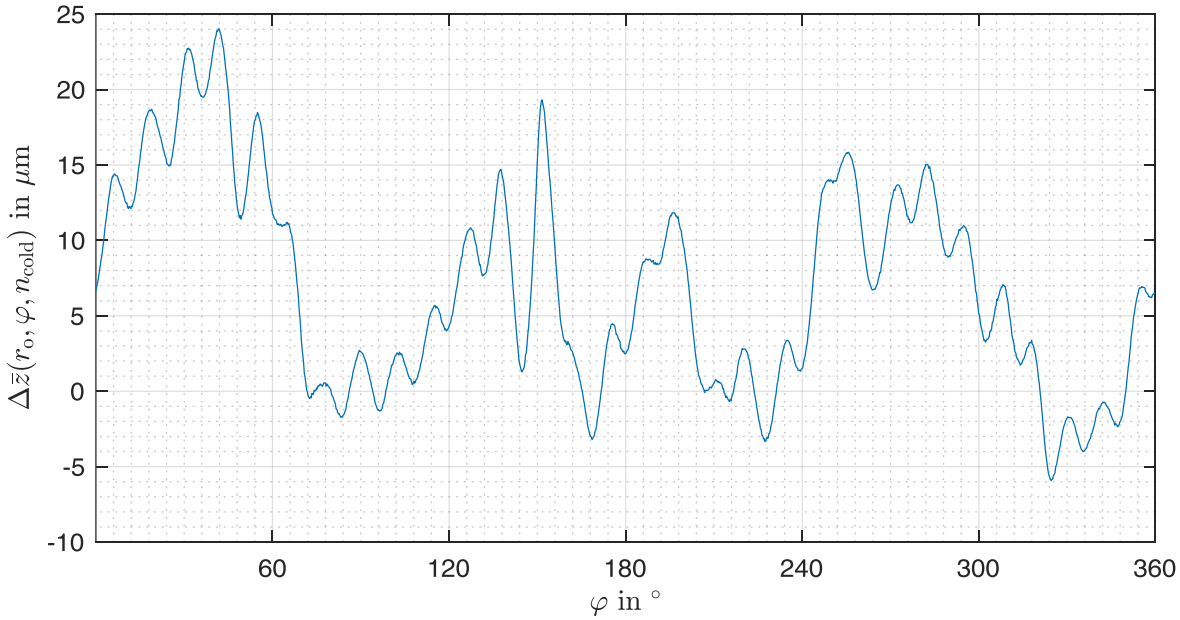

Figure 8-21: Average disc thickness over all cycles at radial outer position in cold state, showing dents/intrusions at the cooling channel pin positions, i.e. at 0°, 12°, 24°, ...

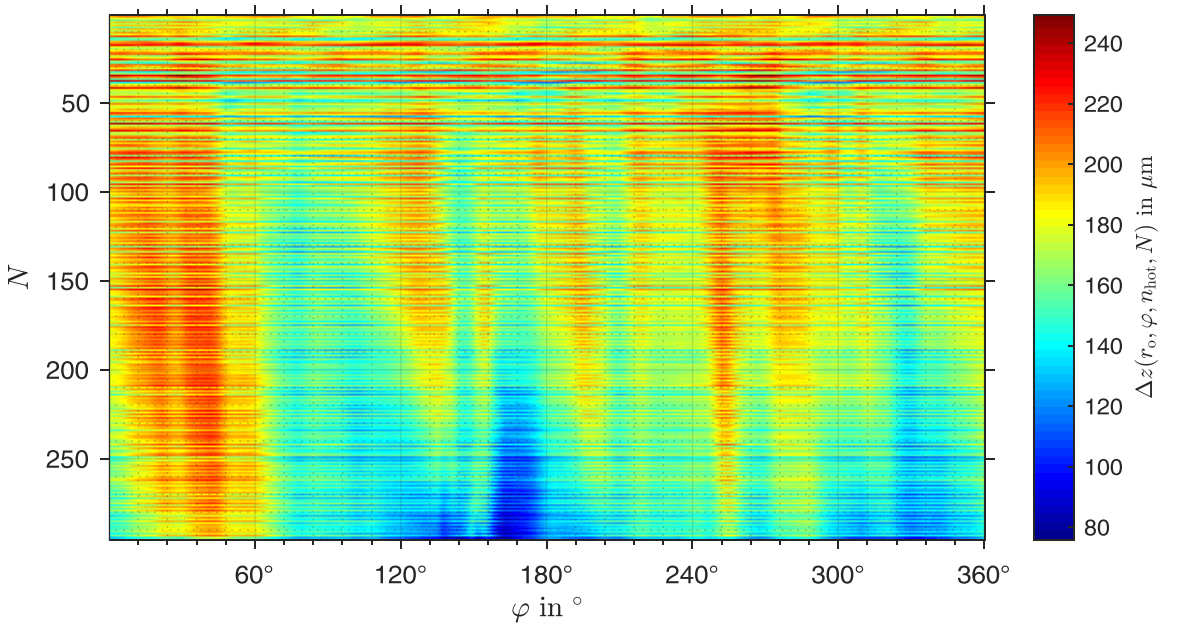

Figure 8-22: Disc thickness in hot state of the *Reference* brake disc, evaluated at radial outer position; grid lines indicate centre points of the cooling channel pins at radial outer position

A.3.4 Crack Length

In order to show the degressive crack propagation rates of the longest cracks, crack lengths of the four longest cracks are plotted in Figure 8-23 on a semi-logarithmic scale. Especially the crack length curve of the through-thickness crack at $\varphi = 150°$ appears as a straight line.

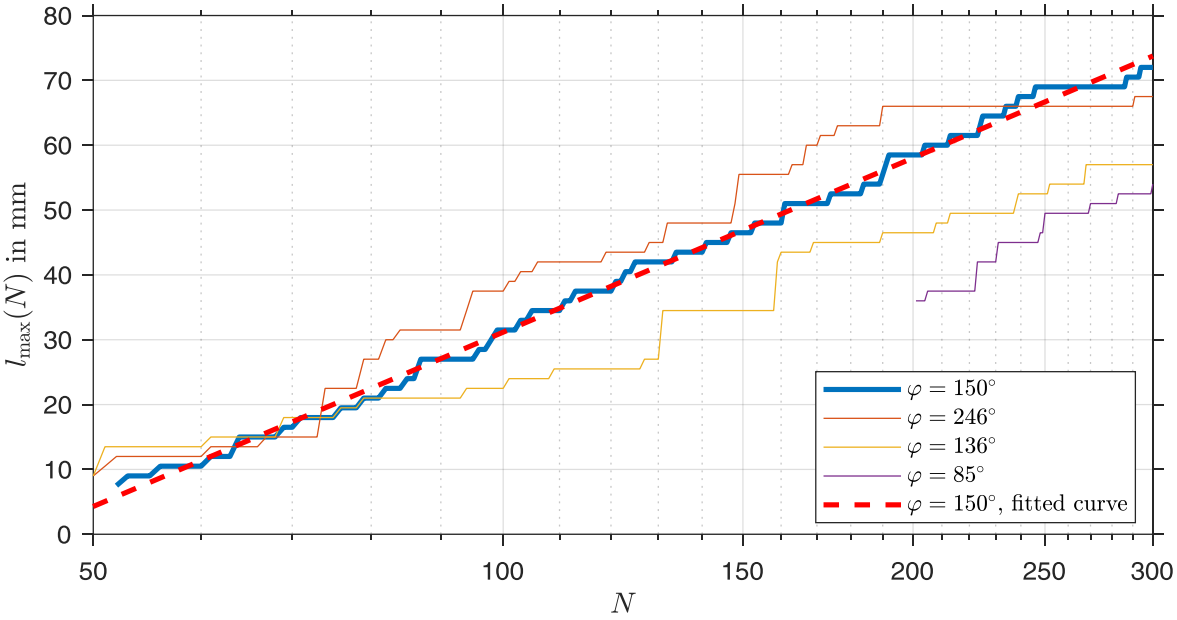

Figure 8-23: Crack length evolution of the four longest cracks of the *Reference* brake disc[125]

Complementing Figure 5-17, crack lengths vs. SRO in cold state is shown in Figure 8-24

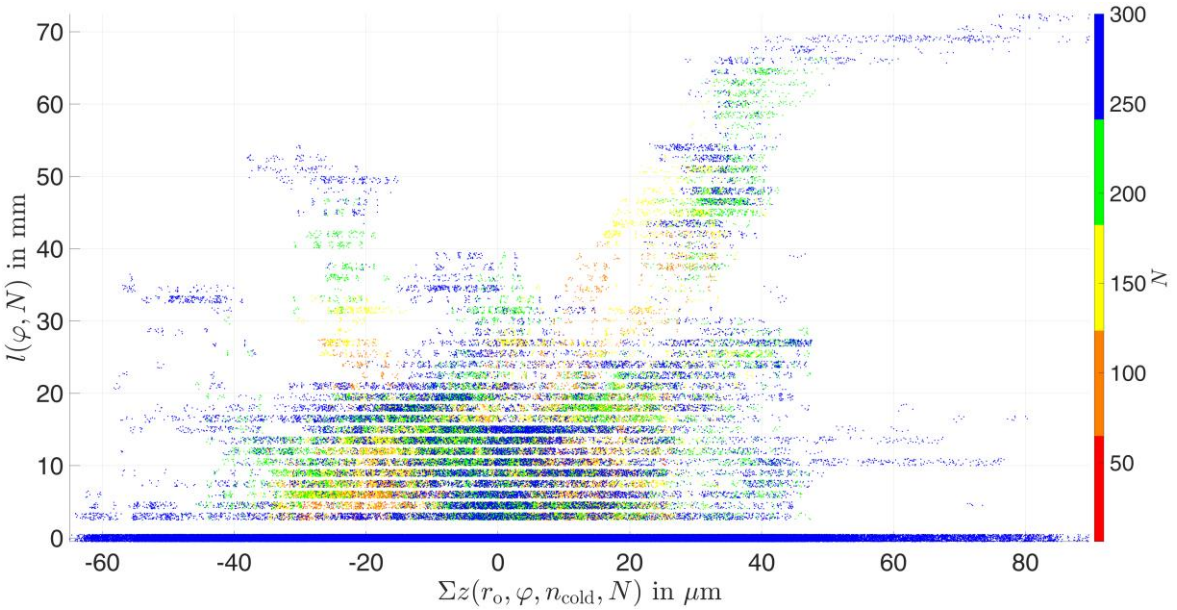

Figure 8-24: Crack lengths vs. SRO at radial outer position in cold state, *Reference* disc

[125] Bilgic Istoc, S.; Winner, H.: The Influence of SRO and DTV (2018).

A.3.5 Photographs of the Specimens for Material Experiments

Figure 8-25: Opened through-thickness crack of the *Reference* brake disc

Figure 8-25 shows the opened through thickness crack of the reference brake disc at sampling area A1/A2 (cf. Figure 8-26). Oxidations are visible and allow for determination of crack depth, which is greater than 5 mm.

Sampling areas for micrograph specimens are shown in Figure 8-26. The disc segment has been chosen because it features the thickness crack (A1/A2) as well as an area where a hotspot has migrated over slowly (B to C). The position of crack initiation of the through-thickness crack is marked in Figure 8-26 as well.

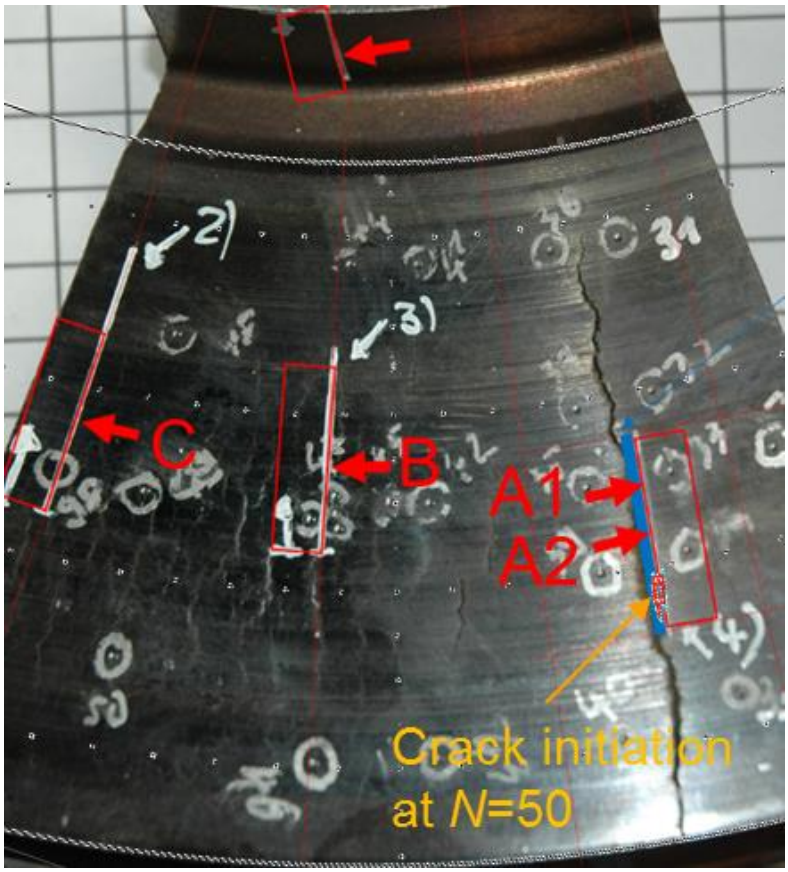

Figure 8-26: Photograph of the sampling segment for micrograph sections of the *Reference* brake disc; initiation point of the future through-thickness crack overlayed

A.3.6 Cyclic Damage

Degradation of maximum stress level at maximum strain during the LCF test is shown in Figure 8-27. It shows cyclic softening of the material, especially at high temperature. At the end of each test, strong degradation indicates macro crack growth.

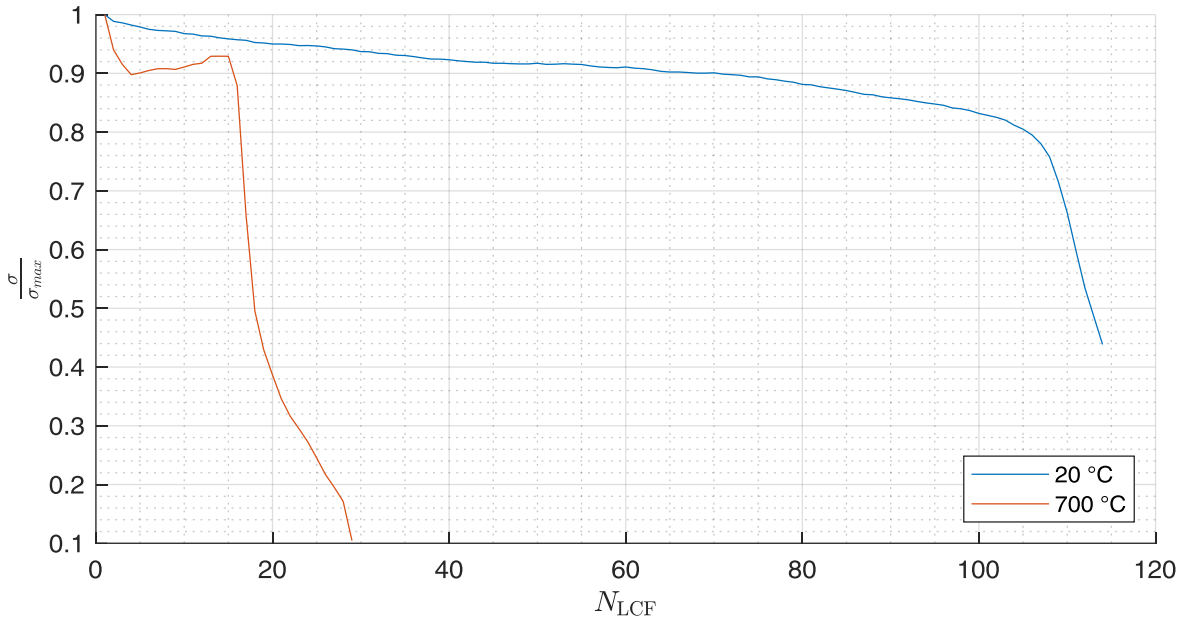

Figure 8-27: Degradation of maximum stress level at maximum strain by cycle number for room temperature and 700 °C

A.4 Additional Evaluations Regarding the Variable Disc

Figure 8-28 corresponds to Figure 5-12 of the *Reference* disc.

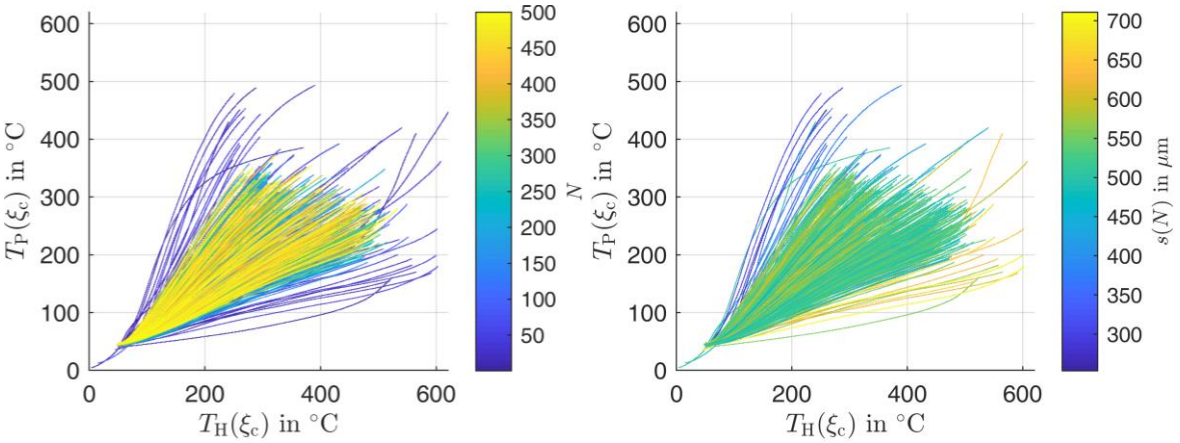

Figure 8-28: Average friction surface temperature of the piston side vs. the hat side during braking; heat crack cycle (left) and coning (right) colour-coded; *Variable* disc

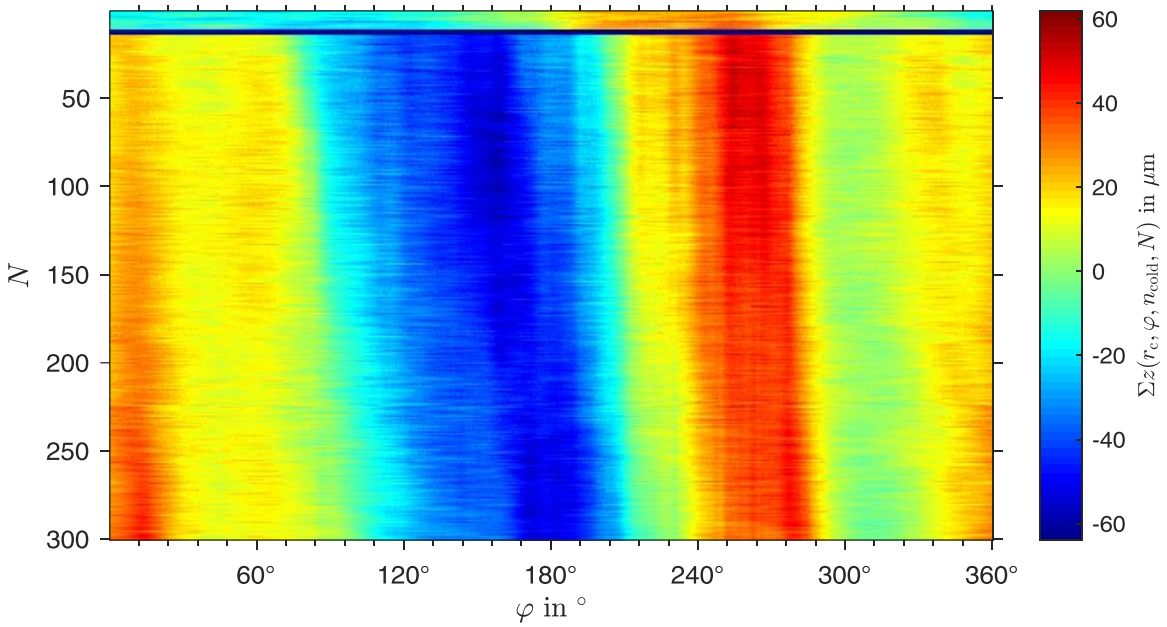

Figure 8-29: SRO pattern of the *Variable* disc, evaluated in cold state at radial centre position

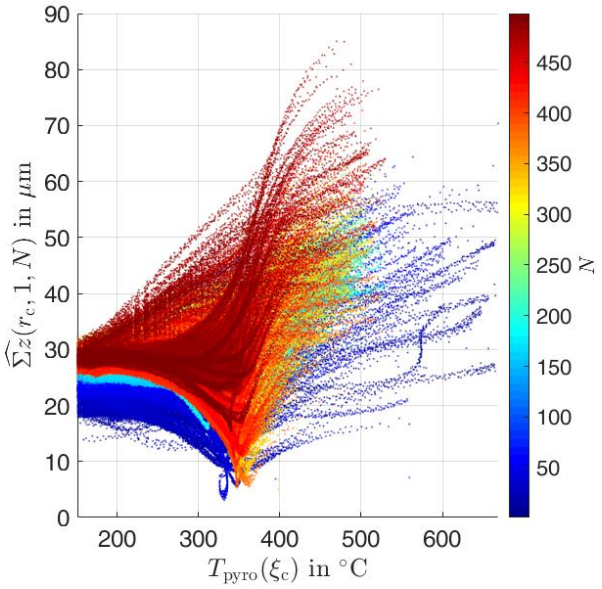

Figure 8-30: SRO of 1st-order; *Variable* disc

Evolution of SRO in cold state is shown in Figure 8-29. It is dominated by 1st-order SRO. Evolution of 1st-order SRO vs. temperature is therefore shown in Figure 8-30.

Figure 8-31 corresponds to Figure 5-17 of the *Reference* disc. Figure 8-32 is generated similarly to Figure 8-31 with DT in cold state instead of SRO in hot state being the data source.

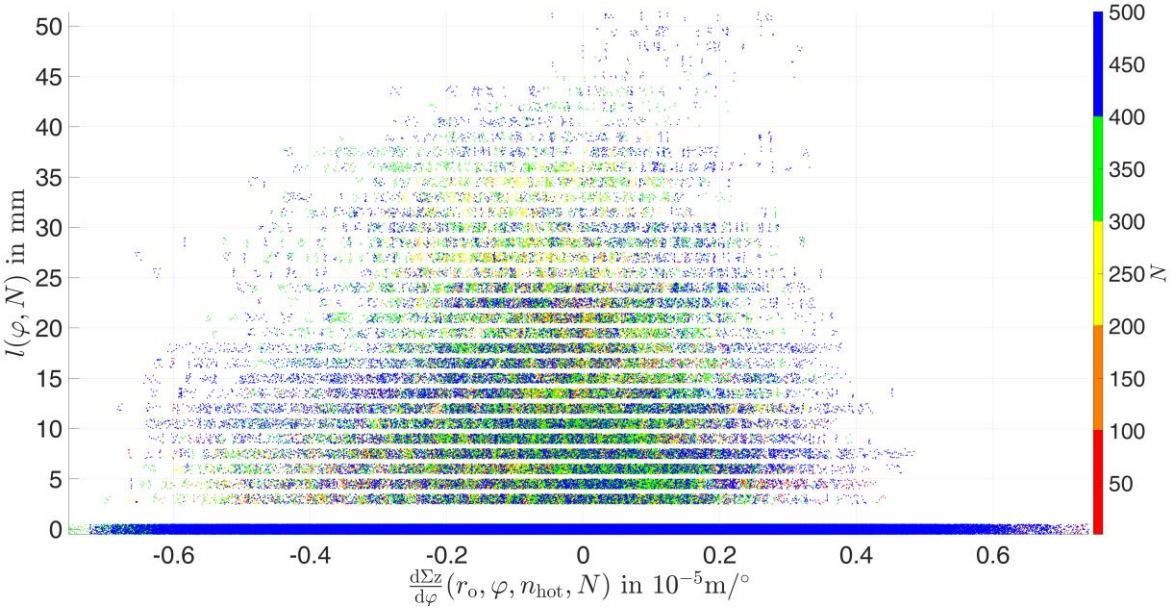

Figure 8-31: Crack lengths vs. SRO gradient, *Variable* disc

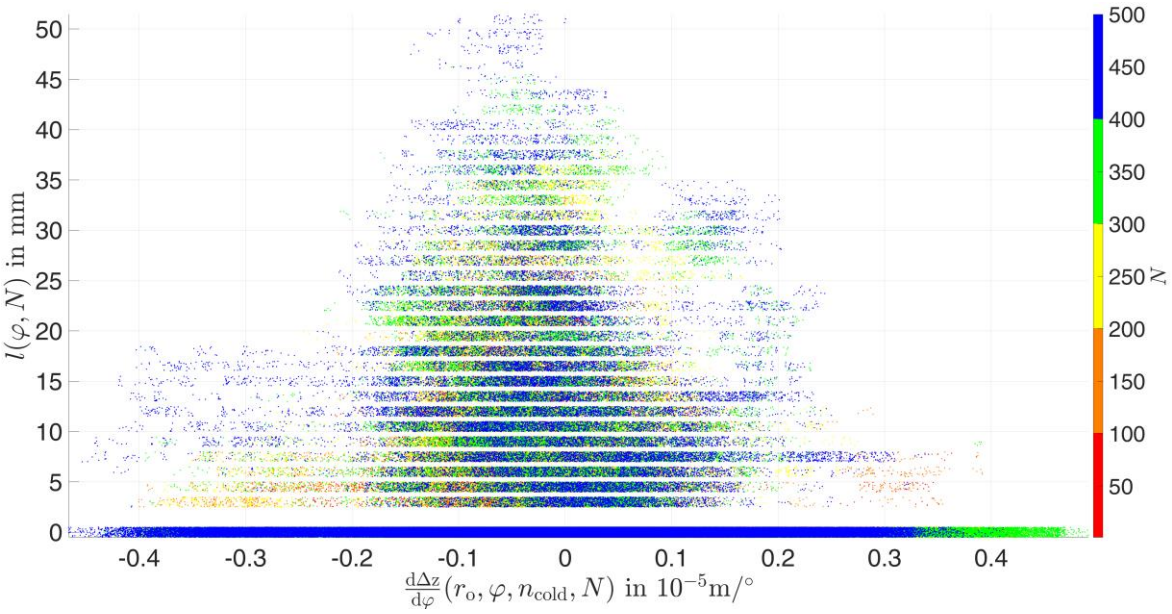

Figure 8-32: Crack lengths vs. gradient of DT in cold state at radial outer position, *Variable* disc

A.5 Additional Evaluations Regarding the Constant and Periodic Disc

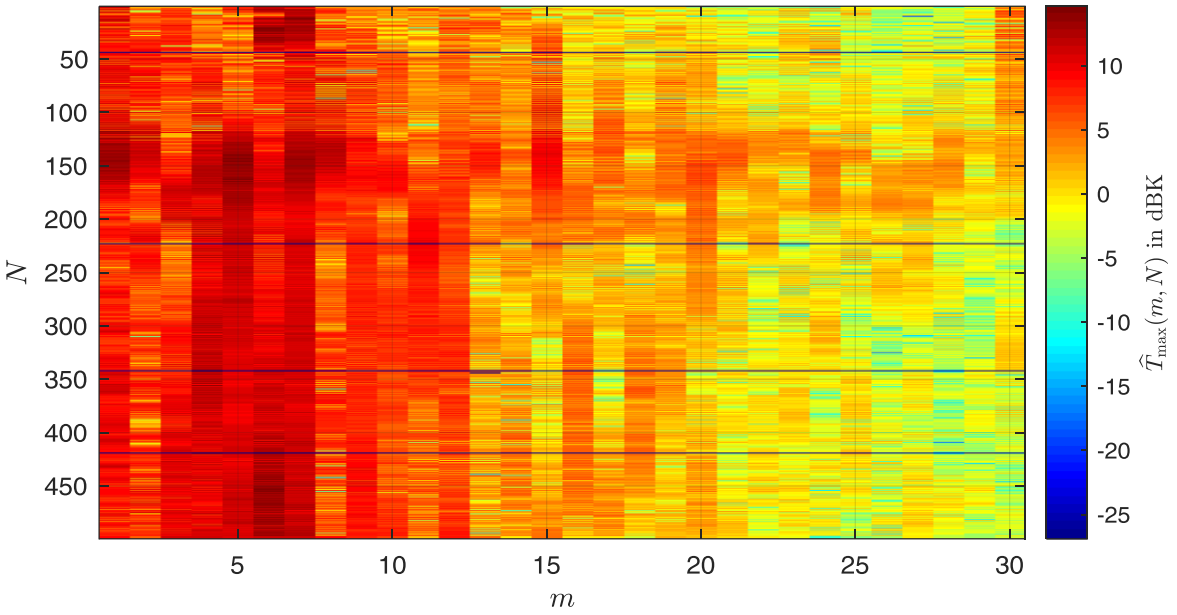

Figure 8-33: Amplitude spectrum of the hotspots of the *Constant* disc; maximum Amplitude: 14.6 dBK (6th order)

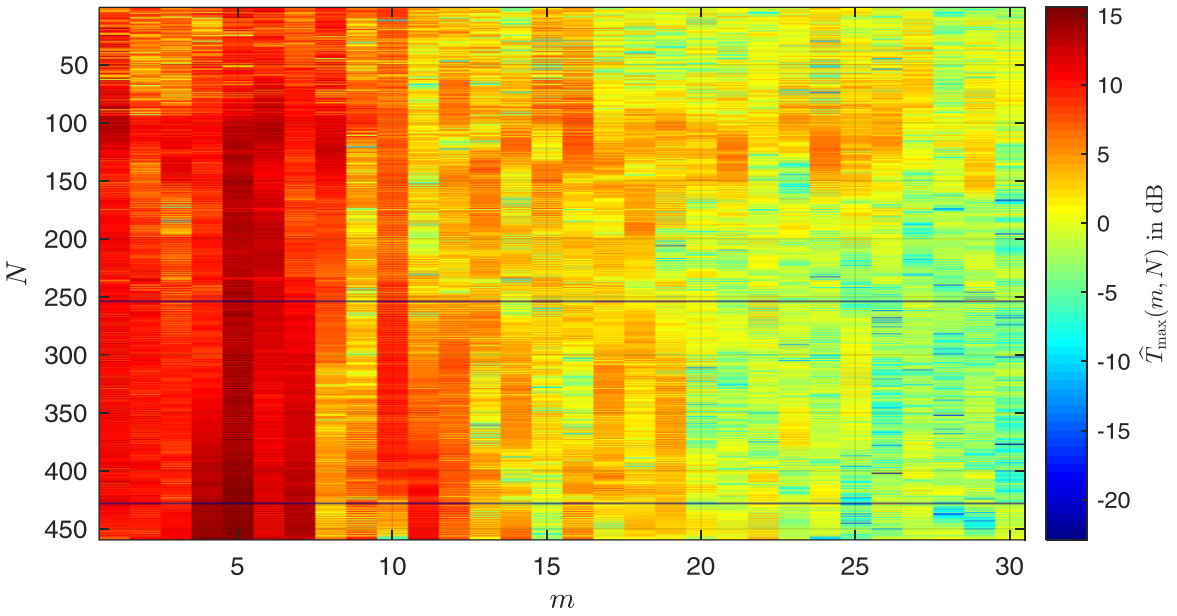

Figure 8-34: Amplitude spectrum of the hotspots of the *Periodic* disc; maximum amplitude: 15.6 dBK (5th order)

Figure 8-33 and Figure 8-34 correspond to Figure 5-11 of the *Reference* disc.

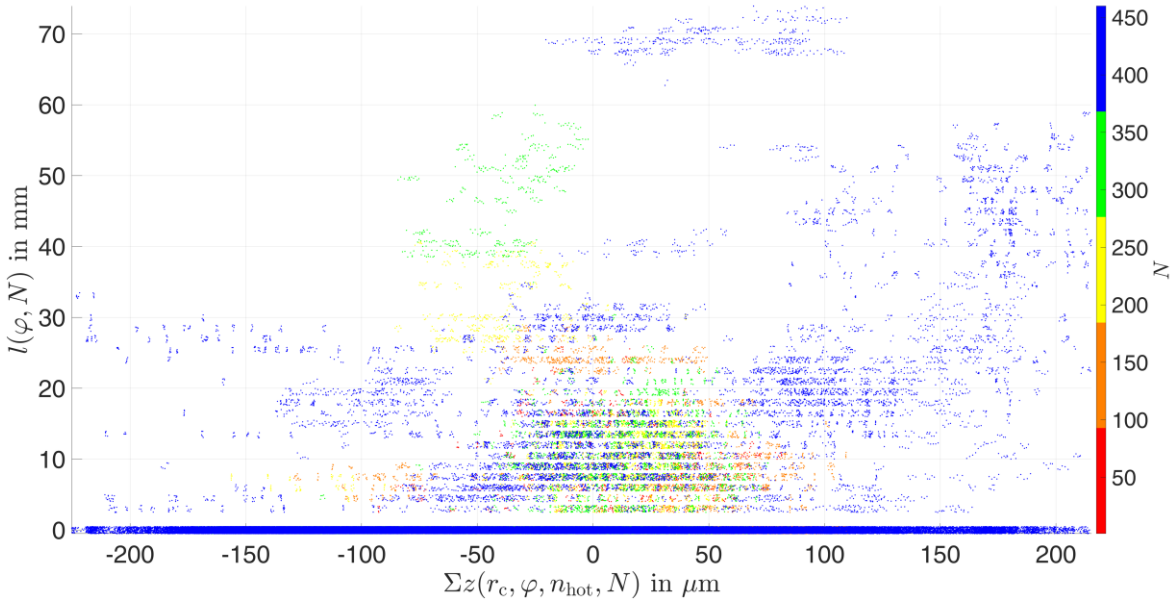

Figure 8-35: Crack lengths vs. SRO in hot state at radial centre position *Periodic* disc

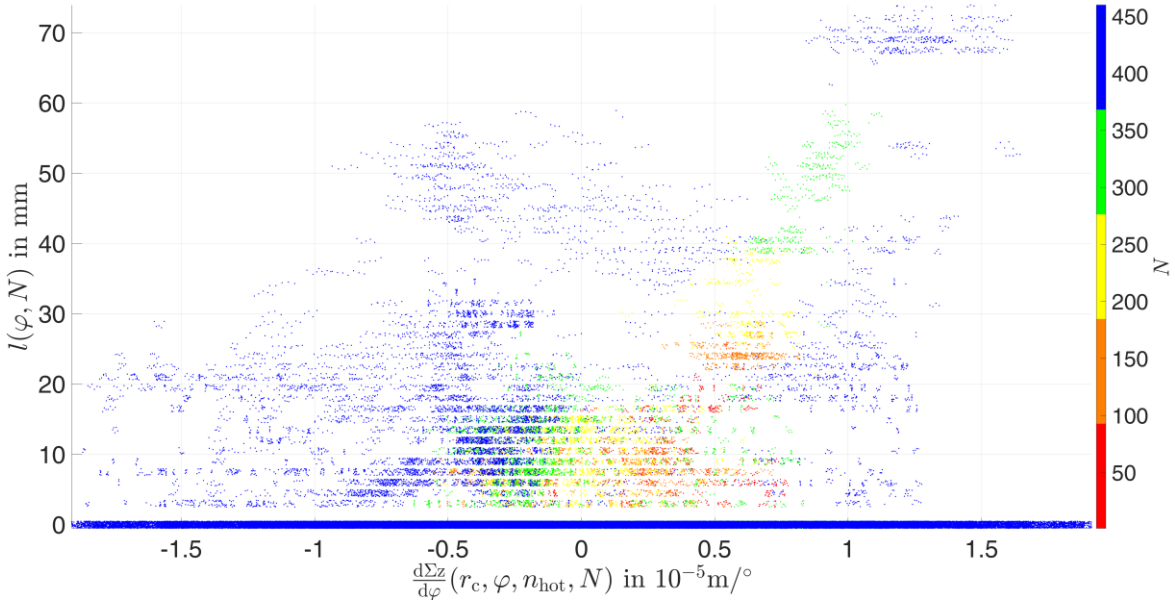

Figure 8-36: Crack lengths vs. gradient of SRO in hot state at radial centre position *Periodic* disc

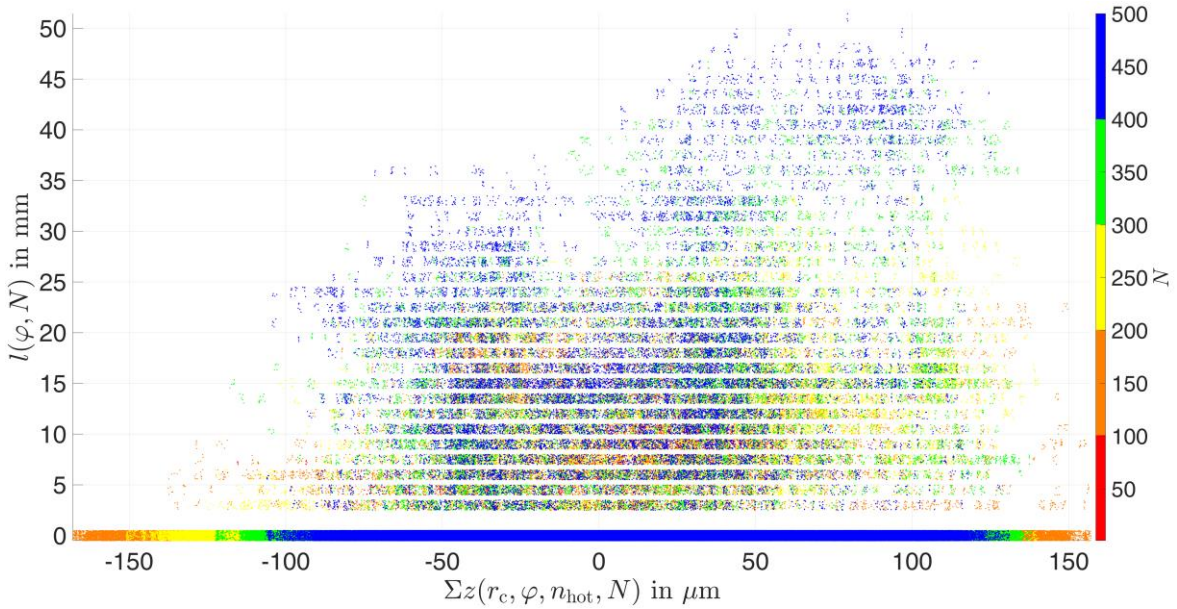

Figure 8-37: Crack lengths vs. SRO in hot state at radial centre position *Constant* disc

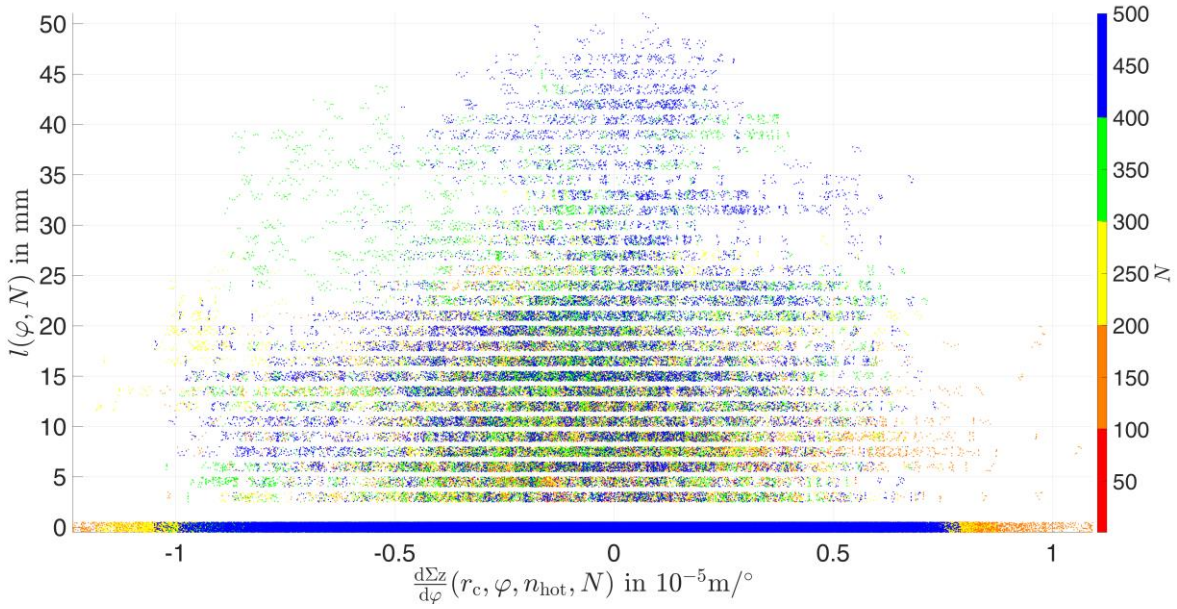

Figure 8-38: Crack lengths vs. gradient of SRO in hot state at radial centre position *Constant* disc, $R^2 = 0.424\,\%$

Figure 8-35 and Figure 8-37 correspond to Figure 5-17 of the *Reference* disc. Figure 8-36 and Figure 8-38 correspond to Figure 5-18 of the *Reference* disc.

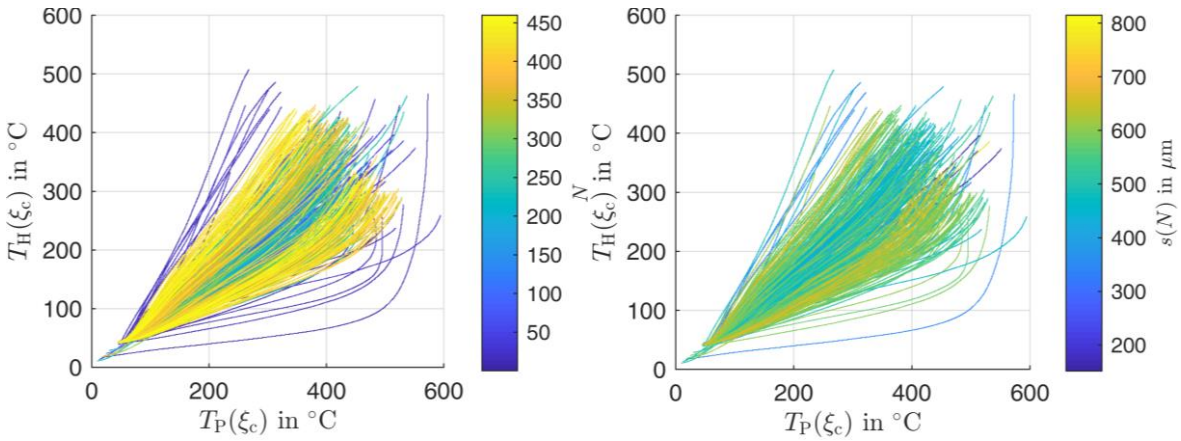

Figure 8-39: Average friction surface temperature of the piston side vs. the hat side during braking; heat crack cycle (left) and coning (right) colour-coded; *Periodic* disc

Figure 8-39 corresponds to Figure 5-12 of the *Reference* disc.

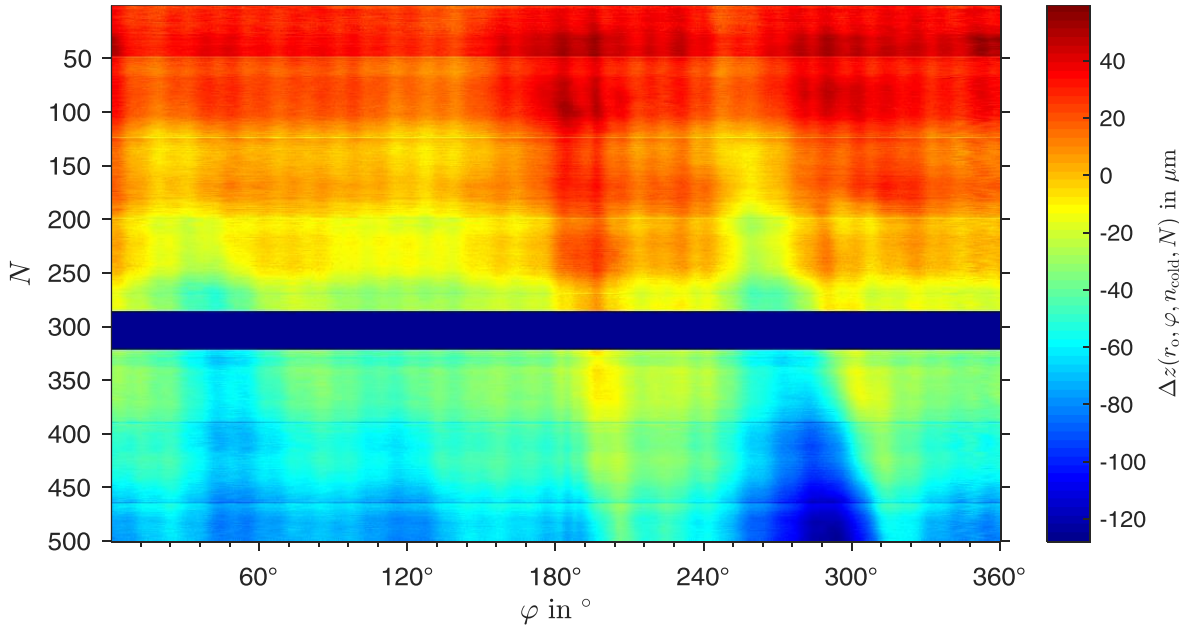

Figure 8-40: DT pattern of the *Constant* disc, evaluated in cold state at radial centre position

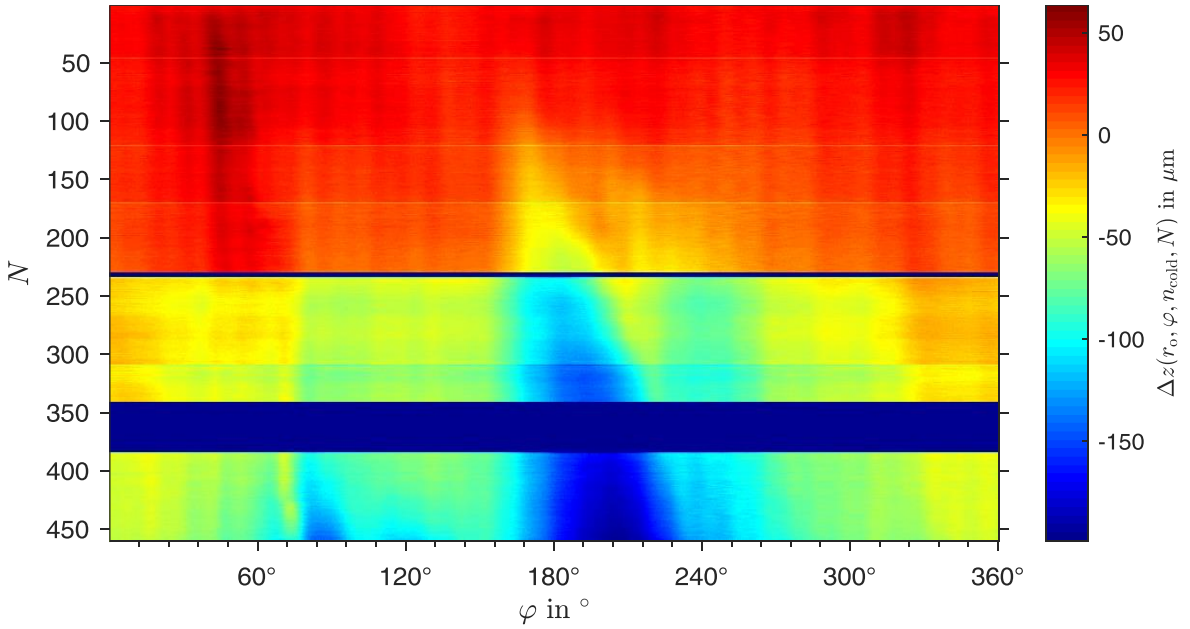

Figure 8-41: DT pattern of the *Periodic* disc, evaluated in cold state at radial centre position

Since the *Periodic* and *Constant* disc get extraordinarily thinner in the course of the test, DT pattern is shown in Figure 8-40 and Figure 8-41. It is unclear, why average DT shrinks greatly after $N > 235$. Probably one of the sensors has been displaced unintentionally during the inspection break, since DT at radial centre position does not shrink at that point (cf. Figure 5-41).

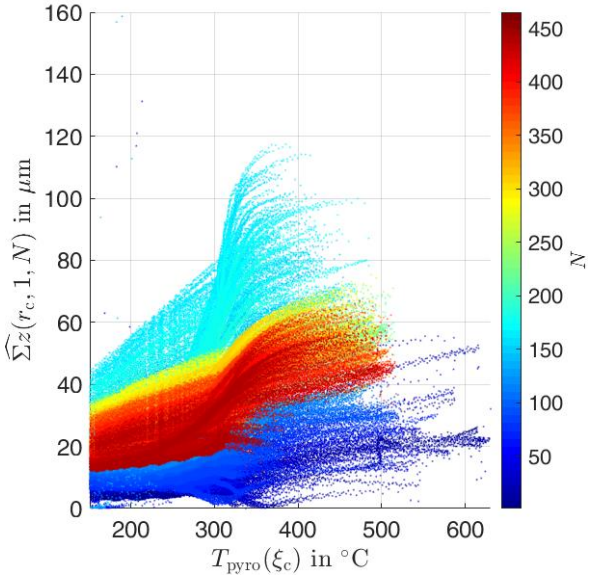

Figure 8-42: SRO of 1st order; *Constant* disc

Figure 8-42 corresponds to Figure 8-30 of the *Variable* disc.

A.5.1 Evolution of Temperature Amplitude of 30th Order

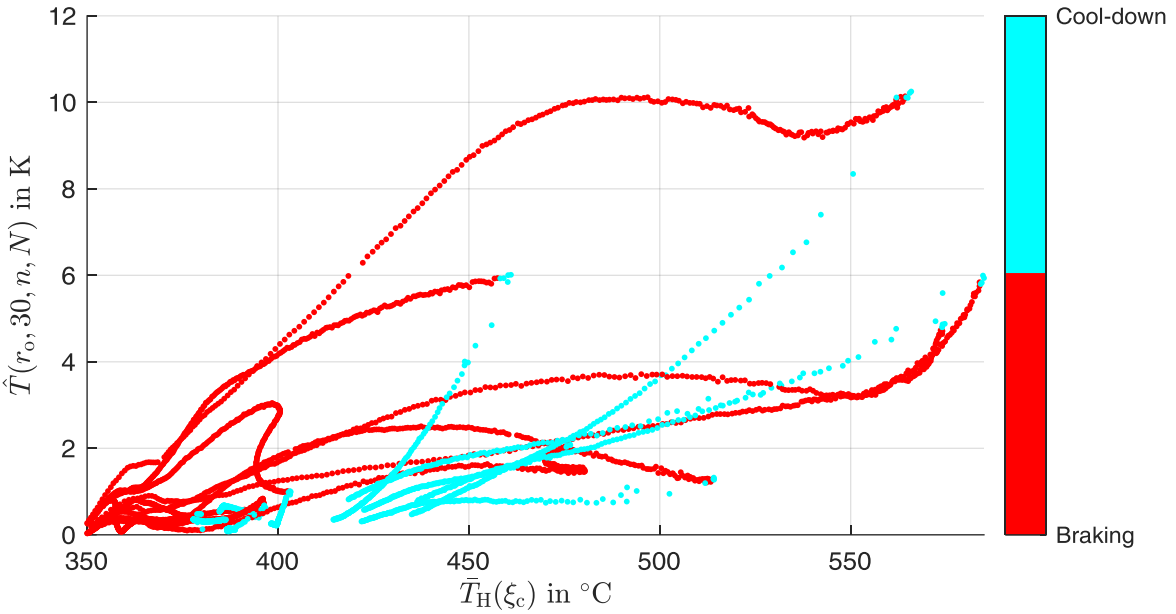

Figure 8-43: Amplitude of 30th order of the temperature at radial outer position during braking and cool-down versus average temperature of the friction surface at radial centre position; first 10 heat crack cycles of the *Constant* disc

Temperature amplitude of 30th order vs. average temperature at radial outer position is shown in Figure 8-43. Amplitude rises during braking with rising average temperature ($R^2 = 29.8$ %), in some cycles strictly monotonically, and falls in all cycles strictly monotonically ($R^2 = 53.5$ %). Data ends 20 seconds after each braking period. At this point, temperature amplitude of 30th order has been fallen under 1 K in all cycles. Plot has been generated in the same way as e.g. Figure 5-42, except for calculation of $\bar{T}_H(\xi_c)$, which is average friction surface temperature at radial centre position measured with the thermographic camera instead of the thermocouple.

A.6 Additional Data Regarding the FE Model

A.6.1 Parameters for Result Generation

The parameters used for generation of the results presented in subchapter 6.3 are listed in Table 8-2.

Table 8-2: Parameters for result generation out of the FE model

Path radius for generation of displacement and stress curves (Figure 6-4, Figure 6-5, Figure 8-44)	$r_o = 205.5$ mm
Step time for extraction of data related to "hot state" (Figure 6-3, Figure 6-4, Figure 6-5, Figure 8-44)	11199.4 s (39.4 s after the beginning of the 10th heat crack cycle
Step time for extraction of data related to "cold state" (Figure 6-4, Figure 6-5, Figure 8-44)	12400 s (end of cool-down period of the 10th heat crack cycle
Average surface displacement (Figure 6-4) in hot state	684 µm
Average surface displacement (Figure 6-4) in cold state	-152 µm

For determination of intrusion depth of hotspots inside the friction surface, temperature gradients at various depths are shown in Figure 8-44.

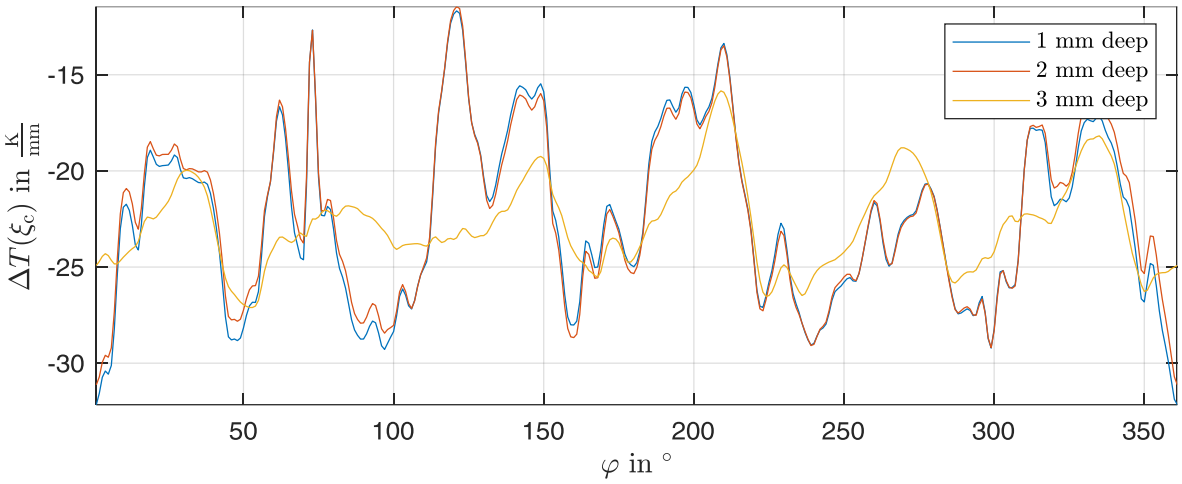

Figure 8-44: Temperature gradient in depth of the friction surface at radial centre position. Evaluated using the FE model.

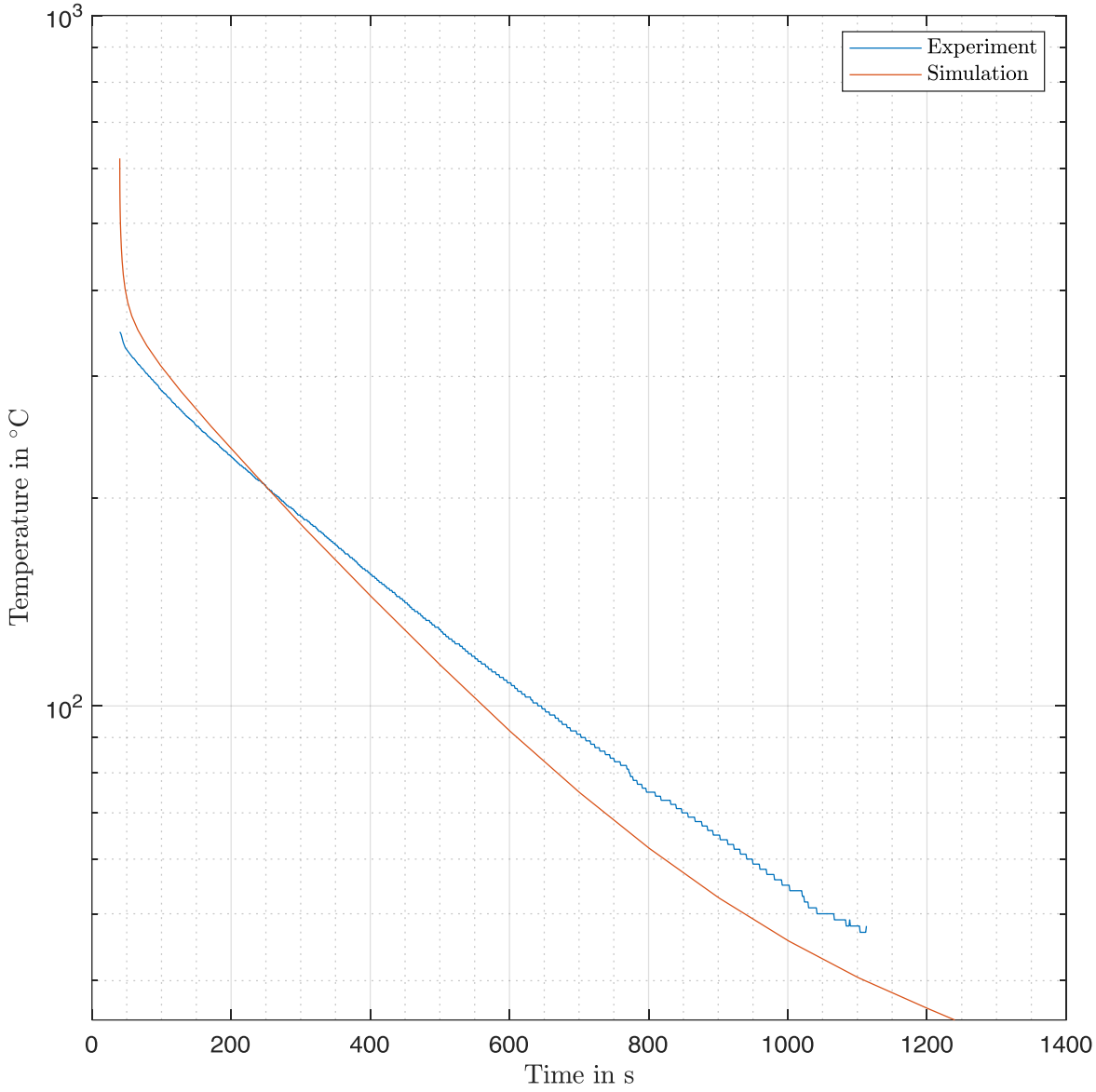

Figure 8-45: Comparison of average friction surface temperature measured by the thermocouple (experiment) with simulated temperature at hotspot position during cool-down; first cool-down period of the *Reference* disc

In order to complement the evaluation of the FE model described in subchapter 7.4, the entire cool-down period is shown in Figure 8-45. Both temperature curves appear as almost straight lines in semi-logarithmic representation. The different gradient shows that convective cooling losses are overestimated by the model, most probably by overestimation of heat transfer coefficients in CFD simulation due to negligence of presence of the brake caliper.

Evaluation of stress-strain response of the mechanical model has been – as well as design and implementation of the mechanical model – conducted by Fraunhofer IWM Freiburg and is shown in Figure 8-46 to Figure 8-49.

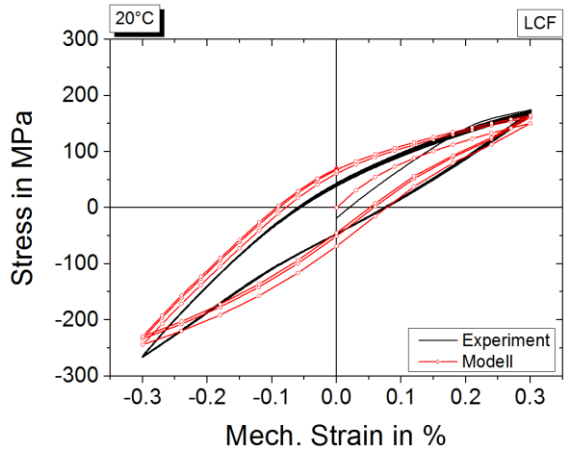

Figure 8-46: Stress-strain response at room temperature; pure LCF[126]

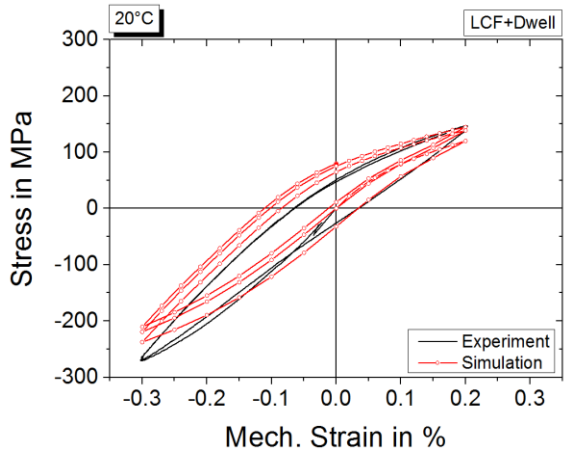

Figure 8-47: Stress-strain response at room temperature; LCF and cycles with dwell periods[126]

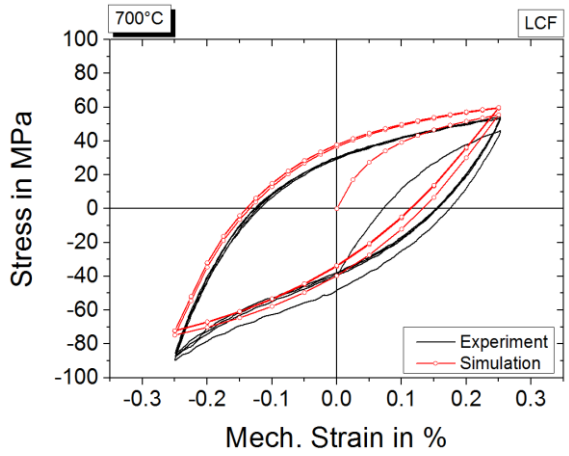

Figure 8-48: Stress-strain response at 700 °C; pure LCF[126]

[126] Metzger, M.: Anpassung und Erweiterung der ThoMat Materialkarte für GJL auf 700°C für die Finite Elemente Software Abaqus (2019).

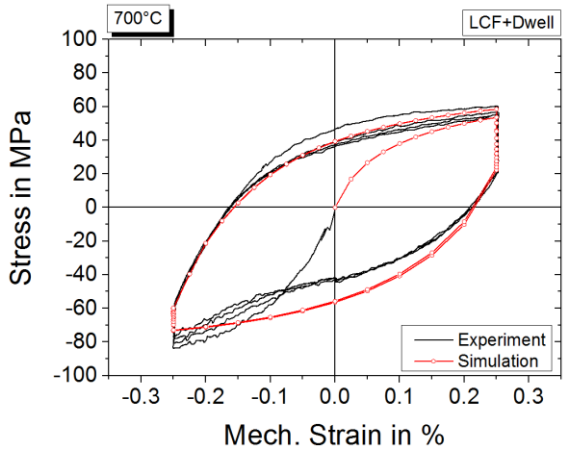

Figure 8-49: Stress-strain response at 700 °C; LCF and cycles with dwell periods[127]

A.6.2 Assessment of the Displacement Sensor Setup

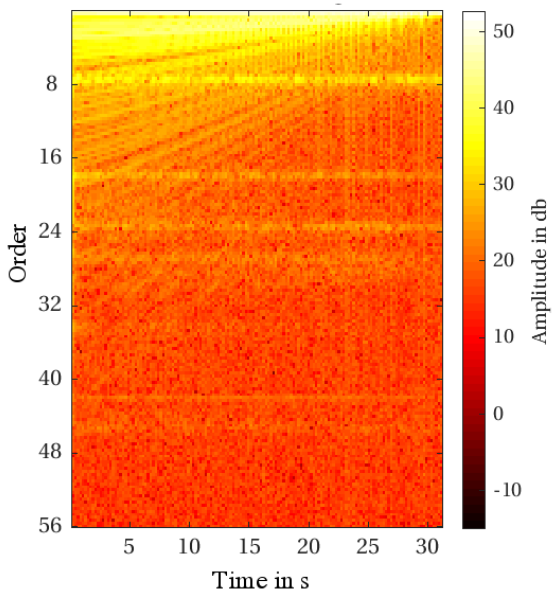

Figure 8-50: Spectrogram of $z_{\mathrm{H}}(r_{\mathrm{c}}, m, t, N_{\mathrm{stop}})$ during stop braking, showing orders/vibrations dependent on rotational speed (diagonal) and independent of rotational speed (horizontal).

Figure 8-50 shows displacement signal amplitudes dependent on time and order. This way, signal parts dependent on rotational speed, i.e. disc displacement, can be distinguished from signal parts independent of rotational speed, i.e. vibrations caused by the dynamometer or the pneumatic system.

[127] Metzger, M.: Anpassung und Erweiterung der ThoMat Materialkarte für GJL auf 700°C für die Finite Elemente Software Abaqus (2019).

List of References

Ankamma, K.: Effect of Trace Elements (2014)
Ankamma, Kandula: Effect of Trace Elements (Boron and Lead) on the Properties of Gray Cast Iron, in: Journal of The Institution of Engineers (India): Series D (1), Issues 95, pp. 19–26, 2014

Augustins, L. et al.: Constitutive model for flake graphite (2016)
Augustins, L.; Billardon, R.; Hild, F.: Constitutive model for flake graphite cast iron automotive brake discs, in: Continuum Mechanics and Thermodynamics (4), Issues 28, pp. 1009–1025, 2016

Bathias, C.; Pineau, A.: Fatigue of materials and structures (2010)
Bathias, Claude; Pineau, A.: Fatigue of materials and structures, ISTE; John Wiley, London, Hoboken, NJ, 2010

Baumgartner, H. et al.: Nutzfahrzeugbremsen (2012)
Baumgartner, Hans; Gerum, Eduard; Pahle, Wolfgang; Siebke, Alf; Pehle, Michael: Nutzfahrzeugbremsen, in: Breuer, Bert; Bill, Karlheinz H. (Eds.): Bremsenhandbuch, Vieweg+Teubner Verlag, Wiesbaden, 2012

Berns, H.; Theisen, W.: Eisenwerkstoffe (2008)
Berns, Hans; Theisen, Werner: Eisenwerkstoffe, 4. Edition, Springer-Verlag, Berlin, Heidelberg, 2008

Bilgic Istoc, S.; Winner, H.: A New Model (2018)
Bilgic Istoc, Sami; Winner, Hermann: A New Model Describing the Formation of Heat Cracks in Brake Discs for Commercial Vehicles, in: 36th SAE Brake Colloquium 2018, Palm Desert, SAE International, 2018

Bilgic Istoc, S.; Winner, H.: Heat cracks in brake discs (2018)
Bilgic Istoc, Sami; Winner, Hermann: Heat cracks in brake discs for heavy vehicles, in: Automotive and Engine Technology, Issues 59, p. 114, 2018

Bilgic Istoc, S.; Winner, H.: Simulationskonzept (2018)
Bilgic Istoc, Sami; Winner, Hermann: Simulationskonzept zur Vorhersage der Hitzerissbildung bei Lkw-Bremsscheiben auf dem Schwungmassenprüfstand, in: VDI-Gesellschaft Fahrzeug- und Verkehrstechnik (Ed.): 19. VDI-Kongress SIMVEC - Simulation und Erprobung in der Fahrzeugentwicklung Nr. 2333, VDI Verlag GmbH, Düsseldorf, 2018

Bilgic Istoc, S.; Winner, H.: The Influence of SRO and DTV (2018)
Bilgic Istoc, Sami; Winner, Hermann: The Influence of SRO and DTV on the Heat Crack Propagation in Brake Discs, in: Eurobrake 2018, The Hague, 2018

Bilgic Istoc, S.; Winner, H.: Influences, Interactions and Prediction Potential (2019)
Bilgic Istoc, Sami; Winner, Hermann: Heat Cracks in Brake Discs for Heavy-Duty Vehicles: Influences, Interactions and Prediction Potential, in: Ralph Mayer (Ed.): XXXVIII. µ-Symposium, Düsseldorf, 2019

Brecht, J.; Egner-Walter, A.: Influence of Material Selection (1998)
Brecht, Jörg; Egner-Walter, Achim: Influence of Material Selection on Stresses in Ventilated Brake Discs, in: International Congress & Exposition, Detroit, SAE International, 1998

Brezolin, A.: Dissertation, Estudo de Geração de Trincas Térmicas (2007)
Brezolin, André: Estudo de Geração de Trincas Térmicas em Discos de Freios de Veículos Comerciais, Dissertation
Universidade de Caixas do Sul, Caixas do Sul, 2007

Brezolin, A.; Soares, M. R.: Influence of Friction Material Properties (2007)
Brezolin, André; Soares, Marcos R. F.: Influence of Friction Material Properties on Thermal Disc Crack Behavior in Brake Systems, in: SAE Brasil 2007 Congress and Exhibit, Sao Paulo, SAE International, 2007

Caprioli, S. et al.: Thermal Cracking of a Railway Wheel Tread (2012)
Caprioli, S.; Vernersson, T.; Ekberg, A.: Thermal cracking of a railway wheel tread due to tread braking - critical crack sizes and influence of repeated thermal cycles, in: Proceedings of the Institution of Mechanical Engineers, Part F: Journal of Rail and Rapid Transit (1), Issues 227, pp. 10–18, 2012

Chaboche, J. L.: Viscoplastic constitutive equations (1977)
Chaboche, J. L.: Viscoplastic constitutive equations for the description of cyclic and anisotropic behaviour of metal, in: Material Science, pp. 33–39, 1977

Chaboche, J. L.: A review (2008)
Chaboche, J. L.: A review of some plasticity and viscoplasticity constitutive theories, in: International Journal of Plasticity (10), Issues 24, pp. 1642–1693, 2008

Collignon, M.: Dissertation, Compréhension des mécanismes de dégradation (2013)
Collignon, Mathilde: Compréhension des mécanismes de dégradation de disques de frein pour véhicule “poids lourd” et définition de nouvelles solutions matériaux, Dissertation Ecole Centrale de Lille, Lille, 2013

Collignon, M. et al.: Failure of truck brake discs (2013)
Collignon, M.; Cristol, A-L.; Dufrénoy, P.; Desplanques, Y.; Balloy, D.: Failure of truck brake discs, in: Tribology International, Issues 59, pp. 114–120, 2013

Cristol, A. et al.: Improvement of truck brake disc lifespan (2014)
Cristol, A; Collignon, M.; Desplanques, Y.; Dufrénoy, P.; Balloy, D.; Regheere, G.: Improvement of truck brake disc lifespan by material design, in: Transport Research Arena, Paris, 2014

DIN: 14577 Instrumentierte Eindringprüfung (2015)
Deutsches Institut für Normung: DIN EN ISO 14577-1 2015: Metallische Werkstoffe - Instrumentierte Eindringprüfung zur Bestimmung der Härte und anderer Werkstoffparameter, Beuth Verlag, Berlin, 2015

Dufrénoy, P. et al.: Damage mechanisms (2002)
Dufrénoy, P.; Bodovillé, G.; Degallaix, G.: Damage mechanisms and thermomechanical loading of brake discs, in: Petit, J.; Rémy, L. (Eds.): Temperature-fatigue interaction, ESIS publication Nr. 29, Elsevier, London, 2002

Fang, L. Y. et al.: Der Elastizitätsmodul von graphitischen Gußeisen (1998)
Fang, L. Y.; Metzloff, K.; Voigt, R.; Loper, C. j.: Der Elastizitätsmodul von graphitischen Gußeisen, in: konstruieren + giessen (4), Issues 23, pp. 8–13, 1998

Gao, C. H. et al.: Stress Analysis of Thermal Fatigue Fracture (2007)
Gao, C. H.; Huang, J. M.; Lin, X. Z.; Tang, X. S.: Stress Analysis of Thermal Fatigue Fracture of Brake Disks Based on Thermomechanical Coupling, in: Journal of Tribology (3), Issues 129, p. 536, 2007

Gesellschaft Verfahrenstechnik und Chemieingenieurwesen: VDI-Wärmeatlas (2013)
VDI-Wärmeatlas, VDI-Buch, 11. Edition, Springer Vieweg, Berlin, 2013

Goo, B.-C.; Lim, C.-H.: Thermal fatigue (2012)
Goo, Byeong-Choon; Lim, Choong-Hwan: Thermal fatigue of cast iron brake disk materials, in: Journal of Mechanical Science and Technology (6), Issues 26, pp. 1719–1724, 2012

Gross, D.; Seelig, T.: Bruchmechanik (2016)
Gross, Dietmar; Seelig, Thomas: Bruchmechanik, 6. Edition, Springer Vieweg, Berlin, Heidelberg, 2016

Gurson, A. L.: Continuum Theory of Ductile Rupture (1977)
Gurson, A. L.: Continuum Theory of Ductile Rupture by Void Nucleation and Growth, in: Journal of Engineering Materials and Technology (1), Issues 99, p. 2, 1977

Hecht, R. L. et al.: The effect of graphite flake morphology (1999)
Hecht, R. L.; Dinwiddie, R. B.; Wang, H.: The effect of graphite flake morphology on the thermal diffusivity of gray cast irons used for automotive brake discs, in: Journal of Materials Science (19), Issues 34, pp. 4775–4781, 1999

ISO: 6310 Compressive strain test methods (2009)
International Organization for Standardization: , ISO 2009: Road vehicles — Brake linings — Compressive strain test methods, 2009

Kim, D.-J. et al.: Thermal stress analysis (2008)
Kim, Dae-Jin; Lee, Young-Min; Park, Jae-Sil; Seok, Chang-Sung: Thermal stress analysis for a disk brake of railway vehicles with consideration of the pressure distribution on a frictional surface, in: Materials Science and Engineering: A483-484, pp. 456–459, 2008

Koetniyom, S. et al.: The development of a material model (2002)
Koetniyom, S.; Brooks, P. C.; Barton, D. C.: The development of a material model for cast iron that can be used for brake system analysis, in: Proceedings of the Institution of Mechanical Engineers, Part D: Journal of Automobile Engineering (5), Issues 216, pp. 349–362, 2002

Könning, M.: Dissertation, Simulation von Heißrubbeln im Gesamtbremssystem (2017)
Könning, Maximilian: Simulation von Heißrubbeln im Gesamtbremssystem, Dissertation Technische Universität Darmstadt, Darmstadt, 2017

Ktari, A. et al.: Numerical computation (2011)
Ktari, A.; Haddar, N.; Koster, A.; Toure, A. M.-L.: Numerical computation of thermal fatigue crack growth of cast iron, in: Fatigue & Fracture of Engineering Materials & Structures (7), Issues 34, pp. 498–509, 2011

Le Gigan, G. et al.: Disc brakes for heavy vehicles (2015)
Le Gigan, G.; Vernersson, T.; Lunden, R.; Skoglund, P.: Disc brakes for heavy vehicles, in: Proceedings of the Institution of Mechanical Engineers, Part D: Journal of Automobile Engineering (6), Issues 229, pp. 684–707, 2015

Le Gigan, G.: Dissertation, On improvement of cast iron brake discs (2015)
Le Gigan, Gaël: On improvement of cast iron brake discs for heavy vehicles, Dissertation Chalmers University of Technology, Gothenburg, Sweden, 2015

Le Gigan, G. et al.: Modelling of grey cast iron (2016)
Le Gigan, G.; Ekh, M.; Vernersson, T.; Lunden, R.: Modelling of grey cast iron for application to brake discs for heavy vehicles, in: Proceedings of the Institution of Mechanical Engineers, Part D: Journal of Automobile Engineering, 2016

Le Gigan, G.: Improvement in the brake disc design (2017)
Le Gigan, Gaël: Improvement in the brake disc design for heavy vehicles by parametric evaluation, in: Proceedings of the Institution of Mechanical Engineers, Part D: Journal of Automobile Engineering (14), Issues 231, pp. 1989–2004, 2017

Lee, Y. M. et al.: Influence of Microstructure (2006)
Lee, Young M.; Huh, Yong; Park, Jae S.; Seok, Chang S.: The Influence of Microstructure and Chemical Composition on the Strength of Cast Iron Used for Railway Vehicles, in: Key Engineering Materials321-323, pp. 1479–1482, 2006

Li, Z. et al.: Analyzing the mechanisms of thermal fatigue (2015)
Li, Zhiqiang; Han, Jianmin; Yang, Zhiyong; Li, Weijing: Analyzing the mechanisms of thermal fatigue and phase change of steel used in brake discs, in: Engineering Failure Analysis, Issues 57, pp. 202–218, 2015

Lim, C.-H.; Goo, B.-C.: Development of compacted vermicular graphite cast iron (2011)
Lim, Choong-Hwan; Goo, Byeong-Choon: Development of compacted vermicular graphite

cast iron for railway brake discs, in: Metals and Materials International (2), Issues 17, pp. 199–205, 2011

Mace, G. et al.: Characterisation of Material Transformation (2006)
Mace, Gael; Bowler, Nicholas; Goddard, Geoff; Morrey, Denise: Characterisation of Material Transformation during Cast Iron Brake Disc Bedding, in: 24th Annual Brake Colloquium and Exhibition, Grapevine, SAE International, 2006

Mackin, T. J. et al.: Thermal cracking in disc brakes (2002)
Mackin, Thomas J.; Noe, Steven C.; Ball, K. J.; Bedell, B. C.; Bim-Merle, D. P.; Bingaman, M. C.; Bomleny, D. M.; Chemlir, G. J.; Clayton, D. B.; Evans, H. A.; Gau, R.; Hart, J. L.; Karney, J. S.; Kiple, B. P.; Kaluga, R. C.; Kung, P.; Law, A. K.; Lim, D.; Merema, R. C.; Miller, B. M.; Miller, T. R.; Nielson, T. J.; O'Shea, T. M.; Olson, M. T.; Padilla, H. A.; Penner, B. W.; Penny, C.; Peterson, R. P.; Polidoro, V. C.; Raghu, A.; Resor, B. R.; Robinson, B. J.; Schambach, D.; Snyder, B. D.; Tom, E.; Tschantz, R. R.; Walker, B. M.; Wasielewski, K. E.; Webb, T. R.; Wise, S. A.; Yang, R. S.; Zimmerman, R. S.: Thermal cracking in disc brakes, in: Engineering Failure Analysis (1), Issues 9, pp. 63–76, 2002

Maluf, O. et al.: Effect of Alloying Elements (2009)
Maluf, O.; Angeloni, M.; Castro, D.B.V.; Bose Filho, W. W.; Spinelli, D.; Ruckert, C.O.F.T.: Effect of Alloying Elements on Thermal Diffusivity of Gray Cast Iron Used in Automotive Brake Disks, in: Journal of Materials Engineering and Performance (7), Issues 18, pp. 980–984, 2009

Metzger, M.: Mikrostruktur- und mechanismusbasierte Werkstoffmodelle (2016)
Metzger, Mario: Mikrostruktur- und mechanismusbasierte Werkstoffmodelle zur Beschreibung des Deformations- und Lebensdauerverhaltens von thermomechanisch beanspruchten Graugusswerkstoffen, Fraunhofer-IWM-ForschungsberichteBand 12, Fraunhofer Verlag, Stuttgart, 2016

Metzger, M.: Anpassung und Erweiterung der ThoMat Materialkarte für GJL auf 700°C für die Finite Elemente Software Abaqus (2019)
Metzger, M.: Anpassung und Erweiterung der ThoMat Materialkarte für GJL auf 700°C für die Finite Elemente Software Abaqus, Freiburg, 2019

Metzger, M.; Seifert, T.: A Mechanism-Based Model (2012)
Metzger, M.; Seifert, T.: A Mechanism-Based Model for LCF/HCF and TMF/HCF Life Prediction: Multiaxial Formulation, Finite-Element Implementation and Application to Cast Iron, in: Technische Mechanik, Issues 32, pp. 435–445, 2012

Metzger, M.; Seifert, T.: Computational assessment (2015)
Metzger, M.; Seifert, T.: Computational assessment of the microstructure-dependent plasticity of lamellar gray cast iron – Part II, in: International Journal of Solids and Structures, Issues 66, pp. 194–206, 2015

Mew, T. D. et al.: Transient thermal response (2015)
Mew, T. D.; Kang, K.-J.; Kienhofer, F. W.; Kim, T.: Transient thermal response of a highly

porous ventilated brake disc, in: Proceedings of the Institution of Mechanical Engineers, Part D: Journal of Automobile Engineering (6), Issues 229, pp. 674–683, 2015

Okamura, T.: Interactive Effects of Thermal Deformation (2016)
Okamura, Toshikazu: Interactive Effects of Thermal Deformation and Wear on Lateral Runout and Thickness Variation of Brake Disc Rotors, in: SAE International Journal of Passenger Cars - Mechanical Systems (3), Issues 9, pp. 1214–1226, 2016

Okamura, T.; Imasaki, M.: Increasing Thermal Strength (2009)
Okamura, Toshikazu; Imasaki, Masanori: Increasing Thermal Strength of Brake Discs by Improving Material Homogeneity, in: SAE 2009 Brake Colloquium and Exhibition, Tampa, SAE International, 2009

Peng, D. et al.: A study into crack growth (2012)
Peng, D.; Jones, R.; Constable, T.: A study into crack growth in a railway wheel under thermal stop brake loading spectrum, in: Engineering Failure Analysis, Issues 25, pp. 280–290, 2012

Pevec, M. et al.: Elevated temperature low cycle fatigue (2014)
Pevec, Miha; Oder, Grega; Potrč, Iztok; Šraml, Matjaž: Elevated temperature low cycle fatigue of grey cast iron used for automotive brake discs, in: Engineering Failure Analysis, Issues 42, pp. 221–230, 2014

Raninger, P. et al.: Understanding the cracking resistance (2016)
Raninger, Peter; Ecker, Werner; Dufrenoy, Philippe; Antretter, Thomas: Understanding the cracking resistance of brake discs: influence of microstructural transformations, in: Eurobrake 2016, Milan, 2016

Rashid, A.; Stromberg, N.: Sequential simulation of thermal stresses (2013)
Rashid, A.; Stromberg, N.: Sequential simulation of thermal stresses in disc brakes for repeated braking, in: Proceedings of the Institution of Mechanical Engineers, Part J: Journal of Engineering Tribology (8), Issues 227, pp. 919–929, 2013

Regheere, G. et al.: Thermocracks (2013)
Regheere, Gilles; Collignon, Mathilde; Cristol, Anne-Lise; Desplanques, Yannick; Dufrenoy, Philippe; Balloy, David: Thermocracks®, a Specific Testing Machine for Evaluation of the Thermal Fatigue Resistance of Materials, in: Fatigue Design 2013, International Conference Proceedings, Issues 66, pp. 250–263, 2013

Remfrey, J. et al.: Aufbau und Komponenten von Pkw-Bremsanlagen (2017)
Remfrey, James; Gruber, Steffen; Sendler, Jan: Aufbau und Komponenten von Pkw-Bremsanlagen, in: Breuer, Bert (Ed.): Bremsenhandbuch, Springer Fachmedien Wiesbaden, Wiesbaden, 2017

Richard, H. A.; Sander, M.: Ermüdungsrisse (2012)
Richard, Hans A.; Sander, Manuela: Ermüdungsrisse, SpringerLink : Bücher, 3. Edition, Springer Vieweg, Wiesbaden, 2012

Sardá, A.: Dissertation, Wirkungskette der Entstehung von Hotspots (2009)
Sardá, Angelo: Wirkungskette der Entstehung von Hotspots und Heißrubbeln in Pkw-Scheibenbremsen, Dissertation
Technische Universität Darmstadt, Darmstadt, 2009

Savitzky, A.; Golay, M. J.: Smoothing and Differentiation of Data (1964)
Savitzky, Abraham.; Golay, M. J. E.: Smoothing and Differentiation of Data by Simplified Least Squares Procedures, in: Analytical Chemistry (8), Issues 36, pp. 1627–1639, 1964

Seifert, T.; Riedel, H.: Mechanism-based fatigue life prediction (2010)
Seifert, T.; Riedel, H.: Mechanism-based thermomechanical fatigue life prediction of cast iron. Part I, in: International Journal of Fatigue (8), Issues 32, pp. 1358–1367, 2010

Shin, M. W. et al.: The Effect of Residual Stress (2013)
Shin, M. W.; Jang, G. H.; Kim, J. K.; Kim, H. Y.; Jang, Ho: The Effect of Residual Stress on the Distortion of Gray Iron Brake Disks, in: Journal of Materials Engineering and Performance (4), Issues 22, pp. 1129–1135, 2013

Tirović, M.: Energy thrift (2009)
Tirović, Marko: Energy thrift and improved performance achieved through novel railway brake discs, in: Applied Energy (3), Issues 86, pp. 317–324, 2009

Ullrich, C.; Bodmer, T.: Thermophysikalische Stoffwerte (2019)
Ullrich, Christian; Bodmer, Thomas: Thermophysikalische Stoffwerte von Metallen und Metalllegierungen, in: Stephan, Peter et al. (Eds.): VDI-Wärmeatlas, Springer Berlin Heidelberg, Berlin, Heidelberg, 2019

Wiegemann, S.-E. et al.: Automatic Heat Crack Detection (2016)
Wiegemann, Sven-Eric; Fecher, Norbert; Merkel, Nora; Winner, Hermann: Automatic Heat Crack Detection of Brake Discs on the Dynamometer, in: Eurobrake 2016, Milan, 2016

Wirth, X.: Bremsbelag (1995)
Wirth, Xaver: Bremsbelag für Teilbelag-Scheibenbremsen, insbesondere von Schienenfahrzeugen, Patent EP0784761B1, Patent application number: PCT/DE96/01139, 1995

Wu, S. C. et al.: Thermal crack growth-based fatigue life prediction (2016)
Wu, S. C.; Zhang, S. Q.; Xu, Z. W.: Thermal crack growth-based fatigue life prediction due to braking for a high-speed railway brake disc, in: International Journal of Fatigue, Issues 87, pp. 359–369, 2016

Xuan, Z.: Masterthesis, Simulation (2017)
Xuan, Zhengjun: Finite-Element-Simulation der Wärme- und Spannungsverteilung in Lkw-Bremsscheiben auf Basis von Messdaten, Masterthesis
Technische Universität Darmstadt, Darmstadt, 2017

Yamabe, J. et al.: Development of Disc Brake Rotors (2003)
Yamabe, Junichiro; Takagi, Masami; Matsui, Toshiharu; Kimura, Takashige; Sasaki, Masanori: Development of Disc Brake Rotors for Heavy- and Medium-Duty Trucks with High

Thermal Fatigue Strength, in: International Truck & Bus Meeting & Exhibition, Fort Worth, 2003, Fort Worth, Texas, USA, 2003

Publications

Bilgic Istoc, Sami; Winner, Hermann: Heat cracks in brake discs for heavy vehicles, in: Automotive and Engine Technology, Ausgabe 3, S. 61-68, 2018

Bilgic Istoc, Sami; Winner, Hermann: The Influence of SRO and DTV on the Heat Crack Propagation in Brake Discs, in: Eurobrake 2018, Den Haag, 2018

Bilgic Istoc, Sami; Winner, Hermann: A New Model Describing the Formation of Heat Cracks in Brake Discs for Commercial Vehicles, in: 36th SAE Brake Colloquium 2018, Palm Desert, 2018

Bilgic Istoc, Sami; Winner, Hermann: Simulationskonzept zur Vorhersage der Hitzerissbildung bei Lkw-Bremsscheiben auf dem Schwungmassenprüfstand, in: VDI-Gesellschaft Fahrzeug- und Verkehrstechnik (ed.): 19. VDI-Kongress SIMVEC - Simulation und Erprobung in der Fahrzeugentwicklung, VDI-Berichte 2333, VDI Verlag GmbH, Düsseldorf, 2018

Bilgic Istoc, Sami; Winner, Hermann: Heat Cracks in Brake Discs for Heavy-Duty Vehicles: Influences, Interactions and Prediction Potential, in: Ralph Mayer (ed.): XXXVIII. µ-Symposium 2019, Düsseldorf, Springer, 2019

Supervised Student Theses

Mosch, Justus: Vergleich und Bewertung von Untersuchungsmethoden zur Rissentstehung bei Lkw-Bremsscheiben. Bachelor-Thesis Nr. 1265/16, 2016

Zhang, Rucheng: Bauformen von Lkw-Bremsscheiben. Forschungsseminar Nr. 154/16, 2016

Sonsalla, Philipp: Vergleich und Anwendung von Algorithmen zur Clusteranalyse von Messdaten. Master-Thesis Nr. 622/16, 2016

Weber, Nico: Untersuchung des thermomechanischen Verhaltens der Reibpaarung Bremsbelag/Bremsscheibe unter Verwendung der Methode der Finiten Elemente. Bachelor-Thesis Nr. 1280/16, 2016

Schlatter, Pascal: Implementierung und Verifikation eines Tools zur automatisierten Erkennung und Vermessung von Rissen mithilfe von Kantenerkennung. Bachelor-Thesis Nr. 1282/16, 2016

Ziegler, Dominik: Analyse von Thermographieaufnahmen von Lkw-Bremsscheiben mittels Bildverarbeitung und statistischer Methoden. Master-Thesis Nr. 631/16, 2016

Altenhofen, Nicolas: Analyse der Hotspot- und Hotbandentwicklung bei Lkw-Bremsscheiben. Bachelor-Thesis Nr. 1289-B/17, 2017

Xuan, Zhengjun: Finite-Element-Simulation der Wärme- und Spannungsverteilung in Lkw-Bremsscheiben auf Basis von Messdaten. Master-Thesis Nr. 660/17, 2017

Reinhard, Tobias: Simulation der Rissbildung bei Lkw-Bremsscheiben unter Verwendung der Finiten Elemente Analyse. Master-Thesis Nr. 632/17, 2017

Seyfried, Merete: Finite-Element-Simulation des Risswachstums in Lkw-Bremsscheiben mit unterschiedlichen Versagensmodellen. Bachelor-Thesis Nr. 1321/18, 2018

Dahal, Diwakar Sharma: Finite-Element-Simulation des Risswachstums in Lkw-Bremsscheiben mit unterschiedlichen Versagensmodellen. Bachelor-Thesis Nr. 1325/18, 2018